Julius-Maximilians Univerisität Würzburg

Thesis submitted for the degree

Dr. rer. nat

Computational Spectroscopic Studies with Focus on Organic Semiconductor Systems

by

Sara Wirsing

Supervisor: **B. Engels**
Co-Supervisor: **V. Engel**

Würzburg, 2022

Computational Spectroscopic Studies with Focus on Organic Semiconductor Systems

Dissertation zur Erlangung des naturwissenschaftlichen Doktorgrades
der Julius-Maximilians-Universität Würzburg

vorgelegt von

Sara Wirsing

aus Mellrichstadt

Würzburg 2022

Eingereicht bei der Fakultät für Chemie und Pharmazie am

06.07.2022

Gutachter der schriftlichen Arbeit

1. Gutachter: Prof. Dr. Bernd Engels

2. Gutachter: Prof. Dr. Petra Tegeder

Prüfer des öffentlichen Promotionskolloquiums

1. Prüfer: Prof. Dr. Bernd Engels

2. Prüfer: Prof. Dr. Petra Tegeder

3. Prüfer: Prof. Dr. Volker Engel

Datum des öffentlichen Promotionskolloquiums

23.08.2022

Doktorurkunde ausgehändigt am

The present work was conducted at the Faculty of Chemistry of the Julius-Maximilians University, Würzburg under the supervision of Prof. Dr. Bernd Engels.

This semi-cumulative thesis contains excerpts of peer-reviewed scientific publications. Please note that the indexation of the references in these excerpts is not identical to the indexation of the references from the additional chapters in this thesis.

Abstract

This work presents excited state investigations on several systems with respect to experimental spectroscopic work. The majority of projects covers the temporal evolution of excitations in thin films of organic semiconductor materials. In the first chapters, thin-film and interface systems are build from diindeno[1,2,3-cd:1',2',3'-lm]perylene (DIP) and N,N'-bis-(2-ethylhexyl)-dicyanoperylene-3,4:9,10-bis(dicarboximide) (PDIR-CN_2) layers, in the third chapter bulk systems consist of 4,4',4"-tris[(3-methylphenyl)phenylamino]triphenylamine (m-MTDATA), 4,7-diphenyl-1,10-phenanthroline (BPhen) and tris-(2,4,6-trimethyl-3-(pyridin-3-yl)phenyl)borane (3TPYMB). These were investigated by aggregate-based calculations. Careful selection of methods and incorporation of geometrical relaxation and environmental effects allows for a precise energetical assignment of excitations. The biggest issue was a proper description of charge-transfer excitations, which was resolved by the application of ionization potential tuning on aggregates. Subsequent characterization of excitations and their interplay condenses the picture. Therefore, we could assign important features of the experimental spectroscopic data and explain differences between systems.
The last chapter in this work covers the analysis of single molecule spectroscopy on methylbismut. This poses different challenges for computations, such as multi-reference character of low-lying excitations and an intrinsic need for a relativistic description. We resolved this by combining complete active space self-consistent field based methods with scalarrelativistic density-functional theory. Thus we were able to confidently assign the spectroscopic features and explain underlying processes.

Acronyms

3TPYMB tris-(2,4,6-trimethyl-3-(pyridin-3-yl)phenyl)borane

ADC(2) algebraic diagrammatic construction method to second order

AIE aggregation-induced emission

AFM atomic force microscope

BDE bond dissociation energy

BO Born-Oppenheimer

BPhen 4,7-diphenyl-1,10-phenanthroline

CAS complete active space

CC2 second-order approximate coupled-cluster singles and doubles model

C-PCM conductor-like polarizable continuum model

CT charge-transfer

D-A donor-acceptor

DFT density-functional theory

DIP diindeno[1,2,3-cd:1',2',3'-lm]perylene

DKH Douglas-Kroll-Hess

EA electron affinity

EFISH electric field induced second harmonic

ELDMR electroluminescence-detected magnetic resonance

EPR electron paramagnetic resonance

ES excited state

E_{xc} exchange-correlation energy

FC Franck-Condon

FET field-effect transistor

GGA generalized gradient approximation

GS ground state

HF Hartree-Fock

HFI hyperfine interaction

HT Herzberg-Teller

HOMO highest occupied molecular orbital

IE ionization energy

IP ionization potential

ISC inter-system crossing

J exchange energy

KS Kohn-Sham

LE local excitation

LED light-emitting diode

LR long-range

LT low-temperature

LUMO lowest unoccupied molecular orbital

MD molecular-dynamics

MR multi-reference

msTPE mass-selected threshold photoelectron

m-MTDATA 4,4',4"-tris[(3-methylphenyl)phenylamino]triphenylamine

NEVPT2 N-electron valence state perturbation theory to second order

NLO non-linear optical

NTO natural transition orbital

ODMR optically detected magnetic resonance

OLED organic light-emitting diode

OPV organic photovoltaic

OSC organic semiconductor

PAH polycyclic aromatic hydrocarbon

PDIR-CN$_2$ N,N'-bis-(2-ethylhexyl)-dicyanoperylene-3,4:9,10-bis(dicarboximide)

PEPICO photoelectron-photoion coincidence

PES potential energy surface

PLDMR photoluminescence-detected magnetic resonance

P$_R$ participation ratio

rISC reverse inter-system crossing

RMSeh root-mean-squared electron-hole distance

RS range-separated

RSH range-separated hybrid

RT room-temperature

SCF self-consistent field

SCS spin-component scaled

SHG second harmonic generation

SI self-interaction

SOC spin-orbit coupling

SR short-range

TA transient absorption

TADF thermally-activated induced fluorescence

TDA Tamm-Dancoff approximation

TD-DFT time-dependent density-functional theory

TR time-resolved

TDMA transition density matrix analysis

trEPR transient electron paramagnetic resonance

trODMR transient optically detected magnetic resonance

TTA triplet-triplet annihilation

xc exchange-correlation

ZORA zeroth-order regular approximation

ZPE zero-point energy

Constants and Notation

$a_0 = \frac{4\pi\epsilon_0\hbar^2}{m_e e^2}$	Bohr radius (5.292×10^{-11} m)
e	elementary charge (1.602×10^{-19} C)
$m_u = m(^{12}C)/12$	atomic mass unit (1.602×10^{-19} C)
m_e	electron mass (9.109×10^{-31} kg)
$\hbar$	Planck constant (1.661×10^{-27} kg)
k_B	Boltzmann constant (1.381×10^{-23} JK^{-1})
ϵ_0	vacuum permittivity (8.854×10^{-12} Fm^{-1})
c	speed of light (2.998×10^8 ms^{-1})

If not denoted otherwise, equations are given in atomic units: $\hbar = e = m_e = \frac{1}{4\pi\epsilon_0} = 1$.

$\vec{a}$	vector a
$F[a]$	functional of a
$\delta_{ab} = \begin{cases} 1, \text{if } a = b. \\ 0, \text{otherwise.} \end{cases}$	Kronecker delta
$(ia\|bj) = \int \mathrm{d}x \psi_i^*(x_1)\psi_b^*(x_2)\psi_a(x_1)\psi_j(x_2)$	Mulliken Notation
$\langle ib\|aj\rangle = \int \mathrm{d}x \psi_i^*(x_1)\psi_b^*(x_2)\psi_a(x_1)\psi_j(x_2)$	Dirac Notation
i, j	occupied orbitals
a, b	virtual orbitals
$\sigma_1 = \begin{pmatrix} 0 & 1 \\ 1 & 0 \end{pmatrix}, \sigma_2 = \begin{pmatrix} 0 & -i \\ i & 0 \end{pmatrix}, \sigma_2 = \begin{pmatrix} 1 & 0 \\ 0 & -1 \end{pmatrix}$	Pauli matrices

Contents

List of Figures

List of Tables

Introduction

Various spectroscopic methods are designed and used by experimentalists in chemistry, physics and biology. These experiments can offer a lot of information on the investigated structures, as well as on processes in those systems, e.g. after excitation by light. The full picture however remains inaccessible in most cases due to restrictions on resolution both in the time and size domain.
Computational investigations can be used to unravel the processes which cause distinct spectroscopic results, bridge observations from different methods and confirm or debunk hypotheses. There are also limits on computational "resolution" though, which need to be circumvented. This can be done by a proper choice of method, model system and calculated properties.
This chapter starts with an overview of all investigated systems and discussed experimental methods, resulting general problems and recurrent challenges for the computational work. Subsequently, the employed computational methods will be discussed. Detailed discussion of each project will be presented in the respective chapters.

0.1 Organic Semiconductors for Optoelectronic Devices

An electronically delocalized structure is the main prerequisite to make use of organic semiconducting materials in optoelectronic devices.[1] This can be achieved using either π-conjugated molecular systems[2–7] or π-conjugated polymers[8] and allows to tune absorption and emission of the materials to the desired part of the UV/VIS spectrum. This region of the electromagnetic spectrum is of particular interest in organic photovoltaic (OPV) and organic light-emitting diode (OLED) devices. Similar materials are also employed in and investigated for field-effect transistors (FETs),[9] but those will not be discussed in the course of this work. OPVs and OLEDs present some similarities which favour their investigation in a unified computational framework. Both consist of at least one electron donating and one electron accepting material. In OPVs,

light creates excitons which can result in CT states if the energy reaches a donor-acceptor (D-A) interface. Carefully tuned energy levels and intermolecular geometries can then allow for the generation of free charge-carriers and ultimately result in a current flow. OLEDs basically work in the reverse. Charge-carriers are injected, can combine at a D-A interface to a CT state, eventually end up in an emissive state and generate light.
While each application also comes with their own intricate challenges, some important generalizations can be made. It is obvious that investigation and fine-tuning of molecular properties is not sufficient to unleash the maximum potential of the devices.[1] Intermolecular arrangements need to be included in the considerations. This leads to extra difficulties if polymers are used, which are not part of the research presented in this work. But small molecules which form crystal like structures pose challenges as well, which will be discussed in the following sections and the respective computational chapters 1, 2 and 3.

0.1.1 Spectroscopic Methodology

Absorption and emission measurements often serve as a basis in the spectroscopic investigation of OPVs and OLEDs. These methods are conceptually rather easy to apply on the devices as well as on single-material films, crystals or single molecules (in solution).[6;7;10] This can provide information about the energetic levels in the materials as well as the influence of aggregate effects in materials in comparison to pure compounds. An extension to time-resolved measurements as in transient absorption (TA) spectroscopy allows i.a. for the monitoring of CT processes,[11] generation and transport of charge-carriers in the bulk[12] and even for probing of relative arrangements at interfaces with polarization-selective measurements.[13]
Whenever open-shell species are involved, but especially in OLEDs where the majority of charge-carriers initially ends up in triplet states, electron paramagnetic resonance (EPR) based methods can add valuable insights.[5–7;10;14;15] Chapter 3 discusses results of various time-resolved methods namely transient electron paramagnetic resonance (trEPR)[16;17], time-resolved photoluminescence-detected magnetic resonance (PLDMR) and time-resolved electroluminescence-detected magnetic resonance (ELDMR).[5–7;10;14;15] The combination of these methods gives deep insights into the dynamics of involved triplet states. Details on their strength and weaknesses are given in the respective chapter.
Interfaces play an important role in the functionality of OPVs as they facilitate the build up of CT states and subsequent generation of free charge carriers. Spectroscopic

methods based on second harmonic generation (SHG) are especially suited to monitor processes at interfaces since it takes anisotropy to allow for phase matching and a second-order signal.[2;18] SHG signals are further enhanced by electric fields (electric field induced second harmonic (EFISH)), which makes a time-resolved variant of the methodology a perfect fit for the observation of CT state dynamics.[2;19] Further details are presented in chapter 1 and 2.

0.1.2 Computational Challenges

Computational investigation of excitations and dynamics of charge-carriers are complicated due to several reasons: First, there is the size and the complexity of the system. A full description of the situation in a thin film system would need to include at least several hundreds of molecules, or tens of thousands of atoms. This is not feasible for excited state calculations in density-functional theory (DFT); on the available machines we are restricted to several hundreds of atoms at the required accuracy. Cheaper methods are not an option due to the character of the excitations as discussed later in this section and in section 0.3.2. This problem can be circumvented by the use of model systems and/or multi-scale approaches.[20–22] Both require the selection of important regions which requires a high-level understanding of the systems and the involved processes. In addition to their size, the investigated systems all show more or less pronounced disorder. This could be simulated by molecular-dynamics (MD), a methodology widely used for proteins and increasingly in materials chemistry.[21;23] However this entails its own drawbacks, such as insufficient description of the systems by the applied low-level methods, and especially high computational cost. In these projects we chose a different approach and work with limiting and exemplary cases.
A second difficulty lies in the non-trivial character of the involved excitations which prohibits the use of cheap methods such as semi-empirics and standard, non-hybrid DFT functionals. Especially CT excitations are a notorious problem for cheap methods (compare section section 0.3.2). Additionally, open-shell states and delocalization of excitons demand a very careful choice of method as is discussed in detail in chapters 1, 2 and 3.
Finally, the experimental results at hand can only be interpreted with regard to intersystem crossing (ISC), spin-orbit coupling (SOC) and non-linear optical (NLO) effects. With the framework and ressources at hand it was not possible to directly calculate all these observables. Instead, it is madatory to carefully build a model from the accessible information and connect it to the results given by the experiments.

0.2 Biradicals

Biradicals[1] are molecules with an even number of electrons that nonetheless form an open-shell ground state due to two energetically degenerate frontier orbitals.[26] This unusual behaviour makes them interesting for research in materials science and plays an important role in atmospheric chemistry and combustion. This open-shell configuration has triplet multiplicity in most cases but can also adapt singlet configuration under special circumstances. This was found e.g. for extended polycyclic aromatic hydrocarbons (PAHs),[27] where a singlet open-shell configuration can expand the aromatic system, and cAAC-stabilized boron-containing species[28]. Species which still exhibit biradical character although having a (small) HOMO-LUMO gap are termed biradicaloids.[26]

0.2.1 Spectroscopic Methodology

EPR based methods are always of interest for the investigation of open-shell species as discussed in section 0.1.2. They are particularly often used in studies of aggregated biradical systems in materials science (e.g. investigations on singlet fission)[29;30] or on biological systems[31;32].
Biradicals in general, but especially small, isolated ones are often very reactive which complicates spectroscopic studies.[26] This obstacle can be circumvented by top down approaches, where a more stable species is fragmented in the course of the experiment. The species of interest is then among the fragments and can be measured with photoelectron-photoion coincidence (PEPICO) techniques.[33] These can yield mass-selected threshold photoelectron (msTPE) spectra and thereby information about the ionization energy (IE), bond dissociation energys (BDEs) and structural information from the vibrational structure in combination with computational studies.[24;25;34]

0.2.2 Computational Challenges

The prerequisite for biradicals and biradicaloids, two frontier orbitals of similar energy, result in several close-lying singlet and triplet states. This induces several complications which lower the quality and usefulness of DFT based descriptions for such species. Firstly, the Tamm-Dancoff approximation (TDA) has to be employed if DFT functionals are used for several excited states to avoid problems due to triplet instabilities.[35]

[1] IUPAC differentiates between diradicals and biradicals, with biradicals being a sub-group of diradicals with a non-Kekulé structure. In this work and further related studies we use diradical and biradical synonymously.[24;25]

This reduces the accuracy of time-dependent density-functional theory (TD-DFT) further, which might be too low to calculate the correct order of excited states in a crowded configuration space to begin with. Secondly, several energetically close-lying orbitals and states can result in states with multi-reference (MR) character. And finally, open-shell singlets are not included in a standard TD(A)-DFT calculation since they can only be described in an at least two-determinant picture.[36]
While the last issue can be avoided by the use of spin-flip DFT,[37] the issues regarding accuracy and MR states remain. In this work we tried to navigate this by careful applications of (TDA-)DFT for computationally expensive frequencies, while relying on N-electron valence state perturbation theory to second order (NEVPT2)[38–40] calculations for energies and gradients.

0.3 Technical Aspects of the Quantum Chemical Treatment

Computational examination of spectroscopic results requires the consideration of various, partly conflicting aspects.
The investigation of excitations, both vibrationally and electronically, calls for high-level quantum chemical methods. Contrarily, the environment or sheer size of the system in question sets limits to the cost-efficiency and therefore accuracy of the method. Another problem lies in the complexity of the experiments. It is not possible to directly recalculate the whole experiment. Instead the main processes have to be identified and separately calculated on chosen model systems. This section strives to highlight the aspects of the quantum chemical treatment which are special to this work. It cannot and does not attempt to give a full overview of the framework and the applied methods which are already discussed in innumerable textbooks. The interested reader can find basics on quantum chemistry given in a very conscise manner in reference [41], and basics on DFT in reference [42]. Further literature is given wherever methods are introduced or applied throughout this work.

0.3.1 Investigation of Excitations by Linear-Response Theory Exemplified by TD-DFT

Generally, observables in spectroscopy can be calculated from the eigenstates of the initial system using response theory.[43] A system in its ground state consisting of interacting particles is affected by an external potential $v_{ext}(\vec{r}, t)$ which can include a

perturbation ($\delta v_{ext}(\vec{r},t)$) switched on at t=0.[44] In a realistic case however, the eigenstates of the unperturbed system are not exactly known. States are usually approximated by a combination of slater determinants, or - as in the case of DFT - by a single slater determinant.[43] In the DFT realm the focus is on an energy functional $E^0[\rho]$ which has a minimum value for $\rho^0(\vec{r})$, the exact ground state density.[45;46] Runge and Gross proved that the biunique one-to one mapping of densities and external potentials can be extended to time-dependent cases even for fully interacting systems.[44;47] The resulting TD-DFT framework is nowadays intensely used to study excitation energies and corresponding observables. The response of observables, e.g. the density, to a pertubation ($\delta v_{ext}(\vec{r},t)$) can then be expressed as a Taylor series.[44] Applying this to the density ($\rho(\vec{r},t) = \rho_{GS}(\vec{r},t) + \rho_1(\vec{r},t) + \rho_2(\vec{r},t) + ...$) the first-order term can be calculated as

$$\rho_1(\vec{r},t) = \int_0^\infty \mathrm{d}t' \int \mathrm{d}^3r' \chi(\vec{r}t, \vec{r}'t')\delta v_{ext}(\vec{r}',t') \tag{1}$$

in standard response theory.[44]

$$\chi(\vec{r}t, \vec{r}'t') = \left.\frac{\delta\rho(\vec{r},t)}{\delta v_{ext}(\vec{r}',t')}\right|_{v_{ext,0}} \tag{2}$$

is the linear density-density response function, which can be transformed by perturbation theory under the assumption of $\delta v_{ext}(\vec{r},t)$ being small enough.[44;45] Most commonly, only the first-order term is investigated ("linear response"), while higher-order terms are essential for the calculation of certain observables such as the direct investigation of non-linear spectra involving hyperpolarizabilities.[48] This is often done via time-propagation.[44;49] A Fourier-transformation with respect to $t - t'$ subsequently results in the spectral ("Lehmann") representation of the response function[43;44;50]

$$\chi(\vec{r}, \vec{r}', \omega) = \lim_{\eta\to 0^+} \sum_I \frac{\langle\Psi^0|\hat{\rho}(\vec{r})|\Psi^I\rangle\langle\Psi^I|\hat{\rho}(\vec{r}')|\Psi^0\rangle}{\omega - \Omega_I + i\eta} - \frac{\langle\Psi^0|\hat{\rho}(\vec{r}')|\Psi^I\rangle\langle\Psi^I|\hat{\rho}(\vec{r})|\Psi^0\rangle}{\omega + \Omega_I + i\eta}. \tag{3}$$

The sum runs over all interacting excited states (Ψ^I) which fulfill the completeness relation ($\sum_I |\Psi^I\rangle\langle\Psi^I| = \hat{1}$).[44] Formally, energies of the excited states Ψ_I can be directly calculated as $E_I = E_0 + \Omega_I$, where E_0 denotes the energy of the exact ground state (Ψ^0) of the fully interacting system.[44] The density operator is defined as $\hat{\rho} = \sum_{i=1}^N \delta(\vec{r} - \hat{r}_i)$.[44]

In practice, equation 3 is very hard to evaluate, which motivates the derivation and application of TD-DFT. In these paragraphs some of the most important equation are given and discussed to sketch the logic behind the TD-DFT framework. Proofs and a detailed derivation can be found in the literature, such as references [43; 44; 46; 47; 50]:

Analogously to equation 1, $\rho_1(\vec{r},t)$ can also be defined in terms of the first order change of the TD Kohn-Sham (KS) potential ($\delta v_s(t)$) of a non-interacting reference state.[50] The Lehmann representation of the KS density response function is given by

$$\chi_{KS}(\vec{r},\vec{r}',\omega) = \lim_{\eta\to 0^+}\sum_{k,j} = (f_k - f_j)\delta_{\sigma_k\sigma_j}\frac{\psi_k^{(0)*}(\vec{r})\psi_j^{(0)}(\vec{r})\psi_j^{(0)*}(\vec{r}')\psi_k^{(0)}(\vec{r}')}{\omega - (\epsilon_j - \epsilon_k) + i\eta}, \quad (4)$$

where f_k denote Fermi occupation factors (considered to be 0 and 1 only in the following) and σ_k the spin orientation of the kth orbital.[44;50] Equation 4 has poles at the energy differences of the KS single-particle orbitals, not at the true excitation energies (poles of equation 3)![44] But the true-density response can be obtained from the KS systems by the use of the exact time-dependent exchange-correlation (xc) kernel[44;50]

$$f_{xc}[\rho_{GS}](\vec{r}t,\vec{r}'t') = \left.\frac{\delta v_{xc}[\rho](\vec{r},t)}{\delta\rho(\vec{r}',t')}\right|_{\rho=\rho_{GS}}. \quad (5)$$

Using these prerequisites, the first-order change in the TDKS potential (δv_{KS}) for a given δv_{ext} can be formulated as[44]

$$\delta v_{KS}(\vec{r},t) = \delta v_{ext}(\vec{r},t) + \int \mathrm{d}^3r'\frac{\rho_1(\vec{r}',t)}{|\vec{r}-\vec{r}'|} + \int \mathrm{d}t'\int \mathrm{d}^3 f_{xc}[\rho_{GS}](\vec{r}t,\vec{r}'t')\rho_1(\vec{r}'t'). \quad (6)$$

Equation 6 together with the definition of the exact density response ρ_1 in terms of the non-interacting KS system

$$\rho_1(\vec{r}t) = \int_0^\infty \mathrm{d}t'\int \mathrm{d}^3r'\chi_{KS}(\vec{r}t,\vec{r}'t')\delta v_{KS}(\vec{r}'t') \quad (7)$$

result in an exact representation of the linear density response.[44;51;52] This connection - the possibility of reformulating the exact linear density response ρ_1 of an interacting system in terms of the linear density response of a non-interacting system to a perturbation δv_{KS} - was used from the late seventies[53] but only proven in 1996 by Petersilka et al.[44;51;52] By inserting equation 6 in equation 7 and equating this to equation 1, a Dyson-like equation for the response function of the interacting system can be obtained.[44] A Fourier-transformation takes us back to the frequency domain and results in a framework which allows for the direct extraction of excitation energies and oscillator strengths of the full interacting system in question from the non-interacting KS system.[44;50] The Dyson-like equation in the frequency domain is commonly written as

$$(\hat{1} - \chi_{KS}(\omega) * f_{Hxc}(\omega))\chi(\omega) = \chi_{KS}(\omega), \quad (8)$$

where a few new notations are introduced. The spatial indices (r) are dropped and the corresponding integrals are shortened to $*$ as in

$$\chi_{KS}(\omega) * f_{Hxc}(\omega) = \int \mathrm{d}^3 r_1 \chi_{KS}(\vec{r}, \vec{r}_1, \omega) f_{Hxc}(\vec{r}_1, \vec{r}', \omega). \tag{9}$$

Furthermore, a Hartree-xc kernel

$$f_{Hxc}(\vec{r}, \vec{r}', \omega) = \frac{1}{|\vec{r} - \vec{r}'|} + f_{xc}(\vec{r}, \vec{r}', \omega) \tag{10}$$

was introduced.[44;50] Expanding this equation in a KS spin orbital basis, finally leads to the well known Casida matrix equation,[44;54]

$$\begin{bmatrix} \mathbf{A}(\omega) & \mathbf{B}(\omega) \\ \mathbf{-B^*}(\omega) & \mathbf{-A^*}(\omega) \end{bmatrix} \begin{bmatrix} \mathbf{X}(\omega) \\ \mathbf{Y}(\omega) \end{bmatrix} = \omega \begin{bmatrix} \mathbf{X}(\omega) \\ \mathbf{Y}(\omega) \end{bmatrix} \tag{11}$$

which heavily masks its response character. $\mathbf{A}(\omega)$, $\mathbf{B}(\omega)$, $\mathbf{X}(\omega)$ and $\mathbf{Y}(\omega)$ are matrices themselves and defined as[54]

$$A_{ia,jb}(\omega) = \delta_{ij}\delta_{ab}(\epsilon_a - \epsilon_b) + (ia|\hat{f}_{Hxc}(\omega)|bj), \tag{12}$$

$$B_{ia,jb}(\omega) = (ia|\hat{f}_{Hxc}(\omega)|bj), \tag{13}$$

$$X_{ia}(\omega) = -\{\sum_{jb} \frac{f_j - f_b}{\omega - \omega_{jb}} (ia|\hat{f}_{Hxc}(\omega)|bj)\} \frac{1}{\omega - \omega_{ia}} \tag{14}$$

and

$$Y_{ia}(\omega) = -X_{ai}(\omega) \tag{15}$$

The extension of these matrices for hybrid and range-separated (RS) functionals can be found in reference [55]. The deduced framework is formally exact. However, for real world applications a few approximations have to be introduced. Those are mainly the adiabatic approximation of the TD xc model and the approximation of the xc functional.[50] The former results in frequency-independent xc terms and therefore makes LR-TD-DFT a linear eigenvalue problem. On the downside, this causes the loss of all information attributed to double or higher excitations.[50] The adiabatic approximation also enforces the approximation of the xc functional. This can heavily deteriorate the quality of excitation energies, especially when Rydberg or CT character

is involved.[50] One approach to tackle these problems in applications is discussed in the next section. TDA is a further, often used approximation. In this approximation, the B-matrix is set to zero which makes computations faster.[35] For this reason it is still the default method in ORCA 5.0[56] and QChem 5.3[57]. We found however quite large errors for systems such as pentacene in comparison to full TD-DFT.[58;59] It is therefore advisable to use full TD-DFT if only singlet excitations are investigated. If triplets are investigated, however, TDA is absolutely necessary due to instabilities in the B-Matrix.[35]

0.3.2 Range-separation and IP-tuning in DFT

The majority of calculations in this work was performed using DFT. This approach is based on the theorems by Hohenberg and Kohn[46], which state that the ground state of a N-electron system is biuniquely determined by its external one-body potential[60]. In combination with the equations implemented by Kohn and Sham[61], which are based on a fictitious non-interacting system, this allows in principle for an exact solution of the many-body problem. Although the exact functional remains elusive, DFT is a highly popular method due to the massive reduction in the dimensionality of calculations in comparison to wavefunction based methods at comparable accuracy.[62] Analogous theorems were formulated by Runge and Gross[47] which facilitate for the deduction of excited state properties from the time-dependent ground state density via TD-DFT.

One persistent problem of common functionals in spectroscopic TD-DFT applications is their poor description of CT excitations. This is due to the lack of derivative discontinuities in the exchange-correlation energy which results in an underestimation of the fundamental gap by the Kohn-Sham gap.[63]

An idea to mitigate the derivative discontinuity problem, was the incorporation of a non-local operator such as the Hartree-Fock (HF) exchange operator which results in so-called hybrid-functionals. Equation 16 shows the division of the exchange energy (E_x) in such a functional in its simplest form. Here, λ denotes the coupling-strength parameter and E_x^{HF} and E_x^{GGA} are the fractions of the exchange energy calculated by Hartree-Fock or the DFT functional respectively which is classically a generalized gradient approximation (GGA)-functional.

$$E_x = \int_0^1 d\lambda E_x^{\lambda} \approx E_x^{GGA} + \lambda(E_x^{HF} - E_x^{GGA}) \tag{16}$$

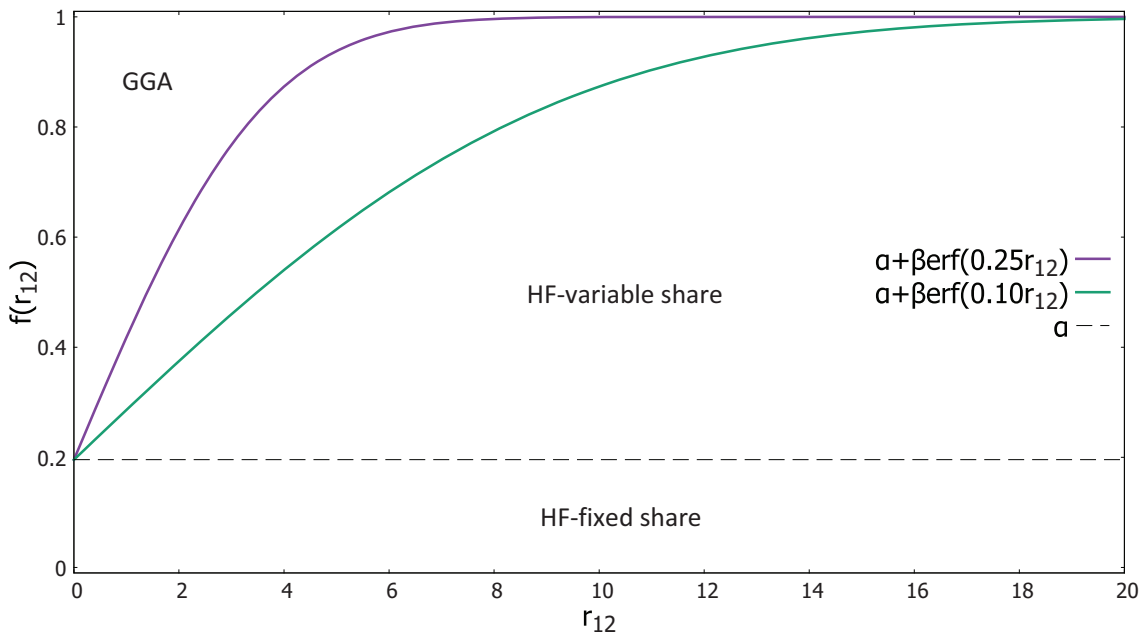

Figure 1: Plot of the error-function to illustrate the effect of different ω-factors. ω=0.25 equates to the standard formulation of ωB97X-D3[67], ω=0.10 is a realistic approximation to the tuned value of an extended molecular organic system. Additionally, the parameters which control the amount of HF exchange in the limiting cases are adopted from ωB97X-D3 (α=0.195728, $\beta = 1 - \alpha$)[67]. The x-axis is given in atomic units. 10 a.u. equal approximately 5.29 Å.

Strictly speaking, this extension does not fit into the original Kohn-Sham framework since the HF exchange integral is not based on the electron density but is covered by the generalized Kohn-Sham method as formulated by Seidl et al.[64]. Hybrid functionals use a fixed amount of HF exchange which reduces the self-interaction error of approximate DFT functionals but has also to be balanced to keep an accurate enough description of correlation effects.[64]

More flexibility is provided by RS hybrid-functionals,[65] which allow particularly for the correction of the asymptotic behaviour of the exchange potential to match the exact value of $-r_{12}^{-1}$. This can greatly improve the description of Rydberg and CT states.[66] In this group of functionals one range-separation parameter (denoted as ω throughout this work) controls the proportion of HF-exchange at a given inter-electron distance (r_{12}) as an argument of the error function (erf) as shown in figure 1. This leads to the division of the two electron operator ($\frac{1}{r_{12}}$) as follows:[68]

$$\frac{1}{r_{12}} = \frac{1 - \mathrm{erf}(\omega r_{12})}{r_{12}} + \frac{\mathrm{erf}(\omega r_{12})}{r_{12}} \tag{17}$$

When combined with a hybrid functional with a fixed percentage α of HF-exchange at all distances, the maximum share of HF at long distances is given by $\alpha+\beta$. With this, equation 17 can be expanded to

$$\frac{1}{r_{12}} = \frac{1-[\alpha+\beta\,\mathrm{erf}(\omega r_{12})]}{r_{12}} + \frac{\alpha+\beta\,\mathrm{erf}(\omega r_{12})}{r_{12}} \tag{18}$$

where $\alpha+\beta=1$ is often enforced to ensure an asymptotically correct behaviour. A famous exception to this rule is the CAM-B3LYP functional, with standard values of α=0.19 and β=0.33.[66] The first term of the operator is applied to the underlying (GGA) DFT exchange terms, the second to the exact HF-exchange. This is more apparent in the reformulation in energy terms, here formulated analogously to the expression $E_{xc} = E_{c,GGA} + E_{x,GGA}$ of the exchange-correlation energy (E_{xc}) of the pure GGA functional.[59]

$$E_{xc}^{RSH} = \alpha E_{x,HF}^{SR} + (\alpha+\beta)E_{x,HF}^{LR} + (1-\alpha)E_{x,GGA}^{SR} + (1-\alpha-\beta)E_{x,GGA}^{LR} + E_{c,GGA} \tag{19}$$

Here, the E_x and E_c terms denote contributions to the exchange energy and the correlation energy, respectively. The superscripts denote whether the terms are part of the long-range (LR) or short-range (SR) description of the range-separated hybrid (RSH) functional. An optimal value for ω can be either defined by fitting to empirical data or by imposing physical conditions which should be met by an ideal functional.
The latter motivates a procedure called non-empirical or ionization potential (IP)-tuning.[69] It is based on the ionization potential theorem which states that in exact Kohn-Sham theory, the energy of the highest occupied molecular orbital (HOMO) (ε_{HOMO}) is equal to the IP and opposite in sign.[70]

$$-\varepsilon_{HOMO} = E_{gs}(N-1) - E_{gs}(N) \tag{20}$$

In this equation E_{gs} denotes the ground state (GS) energy of the N (neutral) and N-1 (cation) electron system. The tuned value of ω for extended organic systems is often substantially smaller than the standard for the functional. A smaller value for ω results in a smaller proportion of HF-exchange at all distances which might be less ideal in terms of self-interaction (SI)-errors. It does, however, incorporate substantial DFT exchange at longer inter-electron distances which can enhance the description of delocalized and CT-excitations in extended systems.
The tuning procedure itself is done to meet not only one but two requirements. There is no analogue to the IP theorem for the electron affinity (EA) and the lowest unoccupied molecular orbital (LUMO). Instead, this is circumvented by the application of

the theorem to the HOMO of the anion at the geometry of the neutral system as a reliable approximation for the vertical EA. Since only one parameter (ω) is varied, both conditions cannot be perfectly satisfied simultaneously. Therefore the sum of the deviations from the requirements ($J(\omega)$) is minimized.

$$J(\omega) = \sum_{i=neutral,anionic} (\varepsilon_{HOMO}^{\omega,i} + E_{gs}^{i}(N_i - 1;\omega) - E_{gs}^{i}(N_i;\omega))^2 \tag{21}$$

0.3.3 Description of Vibronic Spectra in the Franck-Condon Framework

The Franck-Condon (FC) principle provides a handy starting point for the analysis of vibronic spectra. Its basis will be shortly reviewed in this section following the reasoning by Norman et al.[43] and Condon himself.[71] In the realm of the Born-Oppenheimer (BO) approximation, the transition dipole moment between a vibronically excited (final) state and an initial state can be written as $\langle f, F|\hat{\mu}|i, I\rangle$. In this section lowercase letters denote vibrational states, uppercase letters electronic states. The transition dipole operator can be divided in parts depending exclusively on electronic and nuclear coordinates ($\hat{\mu} = \hat{\mu}_e(r) + \hat{\mu}_K(R)$). Integration over electronic coordinates results in

$$\langle f(R), F(r;R)|\hat{\mu}(r,R)|i(R), I(r;R)\rangle = \langle f(R)|\mu_e^{FI}(r;R)|i(R)\rangle \tag{22}$$

where μ_e^{FI} denotes a matrix element of the dipole moment where nuclear coordinates are assumed to be parametric.[71] μ_e^{FI} is hard to interpret in a general manner, but supposed to be a smooth or slowly varying function over the interval of R in question.[71] For a further evaluation of the integral, it is beneficial to switch from cartesian coordinates R to mass-weighted normal coordinates in which the electronic ground state can be expanded.[43] The electronic dipole moment can then be represented by a Taylor-Expansion around the nuclear equilibrium configuration ($Q = 0$). Cutting this expansion after the first order results in the following terms:

$$\langle f|\mu_e^{FI}(r;Q)|i\rangle = \mu_e^{FI}(0)\langle f|i\rangle + \sum_i (\frac{\delta\mu_e^{FI}}{\delta Q_i})_0 \langle f|Q_i|i\rangle + ... \tag{23}$$

The Franck-Condon approximation assumes the parametric dependence in the electronic states to be constant ($R = R_0$).[43] Therefore only the zeroth order element of the expansion survives and μ_e^{FI} is constant. The intensity (I) of a transition is then

solely dependent on the overlap integral of the nuclear wavefunctions $\langle f|i\rangle$ scaled by a Boltzmann distribution and is conventionally defined as[72]

$$I = \langle f|i\rangle^2 e^{-E^i/k_B T}, \tag{24}$$

where E^i denotes the energy of the vibrational state of the initial electronic state relative to the ground state of the respective electronic state. The second term of equation 23 is known as the Herzberg-Teller (HT) correction.[43] This term allows for symmetry forbidden transitions to gain intensity through vibrational coupling.
Calculation of FC integrals and HT corrections is implemented in various program packages.[57;72–74] The preferred package for FC spectra throughout this work due to its robustness was ezFCF by Krylov and co-workers as described in [72] employing Dushinsky rotations.

0.3.4 Treatment of Relativistic Effects

This chapter intends to sketch the framework of relativity used in quantum mechanical calculations and closely follows the rationale of Norman et al.[43] For a more in-depth introduction please refer to the literature, e.g. references [23; 75–77]. Calculations in a full relativistic treatment are based on the one-electron stationary Dirac equation:[77]

$$h_D\Psi = \begin{bmatrix} V & c(\boldsymbol{\sigma}\cdot\boldsymbol{p}) \\ c(\boldsymbol{\sigma}\cdot\boldsymbol{p}) & V - 2mc^2 \end{bmatrix} \Psi = E\Psi \tag{25}$$

Here h_D denotes the one-electron stationary Dirac Hamiltonian and Ψ is a spinor which includes a large (L) and a small component (S) $\Psi = \begin{bmatrix} \Psi^L \\ \Psi^S \end{bmatrix}$. The interested reader can follow the derivation in reference [77]. V is the potential induced by clamped nuclei and $\boldsymbol{\sigma}\cdot\boldsymbol{p}$ the dot product of the Pauli spin matrices with the relativistic momentum.[77] While a full relativistic treatment of quantum chemical calculations is expensive and poses a lot of challenges for the non-expert user, there are several aspects which can be incorporated at a somewhat lower level. Although these techniques still have to be handled with care, they can greatly improve the quality of calculations when e.g. heavy atoms are handled or spin-forbidden transitions are of interest.[76]

Scalar Relativistic Effects

Relativistic effects become apparent for particles moving close to the speed of light. Electrons in the vicinity of heavy nuclei are among those particles. The kinetic energy

of an electron (K) rises with the square of the nuclear charge (Z), as can be seen from the relation for a 1s-electron and its kinetic energy (K) in a hydrogen-like ion:[43]

$$K = \frac{Z^2\hbar^2}{2m_e n^2 a_0^2} \tag{26}$$

$\hbar$ denotes the reduced Planck constant, n and m_e the quantum number and mass of the electron and a_0 the Bohr radius. In the limit of high kinetic energies - where classical expressions break down - K is connected to speed as follows:[43]

$$K = \left(\frac{1}{\sqrt{1-(v/c)^2}} - 1\right) mc^2 = (\gamma - 1)\, mc^2 \tag{27}$$

Equation 27 includes the Lorentz factor γ. In the non-relativistic limit the relation $\gamma = 1$ holds. Noticeable deviations from this value can therefore serve as an indicator of the extent of relativistic effects. A 1s-electron of a gold atom for example, corresponds to $\gamma = 1.15$.[43] The Lorentz factor feeds back into the relativistic mass $m = \gamma m_e$ which in turn is inversely proportional to a_0. As a direct effect, this contracts and stabilizes (s-)orbitals. In fact, the contracting effect mostly predominates for s- and p-orbitals. For the outer shells this effect is opposed by the stronger screening effect of the inner shells which leads to an expansion of d- and f-orbitals.[43]

To practically include scalar relativistic effects in a standard self-consistent field (SCF) treatment, the full (4-component) relativistic Hamiltonian as described in equation 25 has to be approximated. ORCA[74;78] provides i.a. the Douglas-Kroll-Hess (DKH)[79] and zeroth-order regular approximation (ZORA)[80–82] framework. As ZORA Hamiltonians were employed in chap. 4, I focus on this framework in the following. Approximative relativistic two-component Hamiltonians (to which the DKH and the ZORA Hamiltonian belong) rely on different approximations to the exact coupling (R). R connects the large and small components of Ψ ($\Psi_+^S = R\Psi_+^L$). In the ZORA framework it is approximated as $R \approx \frac{c}{2mc^2 - V}\boldsymbol{\sigma}\cdot\boldsymbol{p}$.[77] Using this approximation it is possible to arrive at an equation for a variationally stable ZORA Hamiltonian:[77]

$$\hat{H}^{ZORA} = V + T^{ZORA} \tag{28}$$

The effective energy operator (T^{ZORA}) is defined in such a way that it approaches to the non-relativistic limit for $V \to 0$, which mirrors the situation far from the nuclei.[77]

$$T^{ZORA} = \frac{1}{2m}\boldsymbol{\sigma}\cdot\boldsymbol{p}\frac{2mc^2}{2mc^2 - V}\boldsymbol{\sigma}\cdot\boldsymbol{p} \tag{29}$$

Further simplification was achieved by van Wüllen et al.[82] who proposed a procedure for DFT which relates to a spin-free variant of ZORA in a model potential:

$$\left[\boldsymbol{p}\frac{c^2}{2c^2 - V}\boldsymbol{p} - V_{eff}\right]\psi_i = \epsilon_i\psi_i \tag{30}$$

Replacing V_{eff} with a non-relativistic KS potential resembles a standard DFT treatment were only the kinetic operator is replaced by the ZORA variant. However, since this would require a costly recalculation of the kinetic energy in each SCF cycle, van Wüllen introduced a model potential which is constructed from a model density ($\rho_{model}(\boldsymbol{r}) = \sum_A \rho^A(\boldsymbol{r})$). This is calculated by summing over the spherically symmetric atomic densities (ρ^A).[82]

The resulting SCF equations (30) are currently often used not only for DFT but are also adapted for HF based methods such as complete active space (CAS)-SCF and its perturbation theory based additions.[78]

Spin-Orbit interaction

SOC is rooted in magnetic induction and describes the interaction of the spin of the electron ($\hat{\boldsymbol{s}}$) with a magnetic field, which arises of the relative motion of a charged particle, such as a nucleus or electron.[43] This effect becomes important for phenomena such as phosphorescence and ISC and is indispensable for the calculation of the anisotropy of the g-tensor in EPR.[43;83] Full description of this coupling would require a more involved treatment than scalar-relativistics, this means at least a two-component approximative Dirac operator.[43] Therefore, it is often added to non-relativistic frameworks in a pertubative manner.[83] In this framework the composition of a perturbed triplet wavefunction $|\Psi_{T_i}^{SOC}\rangle$ can be expressed as[84]

$$|\Psi_{T_i}^{SOC}\rangle = |\Psi_{T_i}\rangle + \sum_n \frac{\langle\Psi_{S_n}|\hat{H}_{SOC}|\Psi_{T_i}\rangle}{E(T_i) - E(S_n)}|\Psi_{S_n}\rangle. \tag{31}$$

This expansion of triplet states allows e.g. for the use of Fermi's Golden Rule

$$k(\omega)_{if} = \frac{4\omega^3 n^2}{3\hbar c^3}\left|\langle\Psi_i|\hat{\mu}|\Psi_f\rangle\right|^2 \delta(E_i - E_f \pm \hbar\omega) \tag{32}$$

to approximate radiative transitions between states of different multiplicity.[83] Plugging a pure triplet as initial state (Ψ_i) and a pure singlet as final state (Ψ_f) would yield a zero transition dipole moment ($\langle\Psi_i|\hat{\mu}|\Psi_f\rangle$). Using $|\Psi_{T_1}^{SOC}\rangle$ together with the FC approximation permits for example the calculation of phosphorescence rates.[83]

Chapter 1

Excited States in Perylene-Based Thin Film Systems

This chapter covers investigations on thin film systems of PDIR-CN_2 and DIP. The molecules are perylene derivatives and are pictured in figure 1.1. Due to their relative position of frontier orbitals, these materials are candidates for organic photovoltaics.[3;4] The functionality of organic photovoltaics is based on the interplay between a donor- and an acceptor-material, which in this case are deposited as thin film layers with DIP acting as donor and PDIR-CN_2 as acceptor. In this chapter two publications are presented, each preceded by a short summary and attribution of contributions to the co-authors. These publications cover the processes in single thin films after excitation by light.[4] While the former discusses relaxation effects only approximately, those effects were investigated in the second publication.[85] The processes taking place at the interface between two thin films will be discussed in the next chapter.

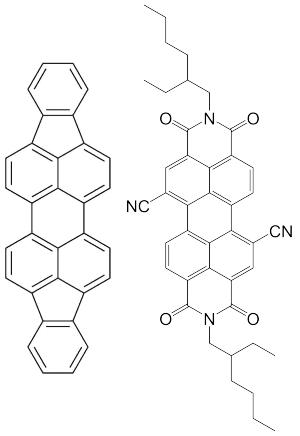

Figure 1.1: Molecular structure of DIP (left) and PDIR-CN_2 (right).

1.1 Excited-State Dynamics in Perylene-Based Organic Semiconductor Thin Films: Theory Meets Experiment

This publication is a collaborative work with physical chemists from Heidelberg and physicists from Tübingen, with contributions as stated in the following and detailed in the submitted documents. All calculations were done by myself, additionally I contributed to the composition of the article and the writing itself in a leading position.
The NLO-experiments, conducted by Hänsel et al.[2–4] showed significant differences for thin film systems of DIP prepared at room-temperature (RT) (DIP_{RT}), at low-temperature (LT) (DIP_{LT}) and PDIR-CN_2. We investigated these effects focusing on excited states of monomers and aggregates. TD-DFT, namely the RS-functional ωB97X-D was the method of choice since it finely balances the ability to calculate excitations on systems of several hundred atoms while providing a proper balance of Frenkel and CT states.
Firstly, an extensive benchmark of the quality of monomer calculations was done to attach error-margins to our calculations. As benchmark data we used wavefunction based methods such as the spin-component scaled (SCS)-second-order approximate coupled-cluster singles and doubles model (CC2) and the SCS-algebraic diagrammatic construction method to second order (ADC(2)) as well as experimental absorption spectra of the monomers. All experimental absorption spectra in this work were measured by Belova, Broch and Schreiber. We investigated the influence of different environments (conductor-like polarizable continuum model (C-PCM), point-charges and vacuum), the importance of relaxation and vibrational effects, the error margin correlated to the choice of method and basis-set and lastly the difference induced by using a model system instead of full PDIR-CN_2. Dealing with PDIR-CN_2 in this work posed two difficulties. Firstly, in the crystal structure the perylene-body is kept flat while full optimization in vacuum or approximate environments results in a twist of its body. This was avoided by restricting the respective dihedrals in the optimization. Secondly, PDIR-CN_2 possesses big alkyl-chains which result in high computational costs while the influence on the excitations of interest is low. Since those alkyl-chains are also tough to optimize in a sensible manner which mirrors the crystal environment, we replaced them with a methyl-groups in the aggregate calculations.
To approximate the configuration of the thin films, optimized monomers were placed on the respective positions in cutouts of the experimentally known crystal structures and were surrounded by layers of point charges. Atomic point charges were calculated for

single optimized molecules and placed at the positions of the atoms in the crystal. Most calculations were done on tetramers in point-charge environment. The effect of bigger aggregates on the excited states was approximated by semi-empirical calculations on DIP for which ZINDO(S) showed reliable results. The resulting excited state calculations were investigated in terms of character and expansion of the excitons. These data was set in context to experimental absorption spectra of the thin film systems to determine the character of the excitons which can be created by the pump-pulses in the NLO measurements by Hänsel and Tegeder. We found a clear difference in the size of excitons between DIP_{LT} and PDIR-CN_2. Further investigations confirmed, that this is no artifact of symmetry but a real effect which can explain the different build-up times of the signals in NLO measurements. The difference in the decay time of the signal could be attributed to the varying sequences when looking at the brightness of states in DIP and PDIR-CN_2. This is induced partly by the difference in the crystal structures, but greatly enhanced by the higher level of disorder in the first layers of PDIR-CN_2. These aspects further the build-up of J-aggregate like structures in PDIR-CN_2 and therefore a longer decay time back to the ground state in comparison to DIP. The remaining feature of the time-resolved (TR)-SHG spectra is similar in both systems and was attributed to exciton trapping on lower-lying (disordered) sites. Vibrations which modulate the signals, could be assigned to vibrations of the monomers.
In conclusion, we were able to assign processes after light-induced excitation in the thin film systems by calculations on aggregates taken from crystal structures by additionally considering effects of the environment, disorder and relaxations on individual monomers.

This paper was published in S. Wirsing, M. Hänsel, V. Belova, F. Schreiber, K. Broch, B. Engels, and P. Tegeder, *Excited-State Dynamics in Perylene-Based Organic Semiconductor Thin Films: Theory Meets Experiment*, The Journal of Physical Chemistry C **123**, 27561–27572 (2019). Reprinted from reference [4] with permission from 2021 American Chemical Society.

THE JOURNAL OF PHYSICAL CHEMISTRY C
Article
Cite This: J. Phys. Chem. C 2019, 123, 27561−27572
pubs.acs.org/JPCC

Excited-State Dynamics in Perylene-Based Organic Semiconductor Thin Films: Theory Meets Experiment

Sara Wirsing,[†] Marc Hänsel,[‡] Valentina Belova,[§] Frank Schreiber,[§] Katharina Broch,[§] Bernd Engels,*[,†] and Petra Tegeder*[,‡]

[†]Institut für Physikalische und Theoretische Chemie, Universität Würzburg, Emil-Fischer-Straße 42, 97074 Würzburg, Germany
[‡]Physikalisch-Chemisches Institut, Universität Heidelberg, Im Neuenheimer Feld 253, 69120 Heidelberg, Germany
[§]Institut für Angewandte Physik, Universität Tübingen, Auf der Morgenstelle 10, 72076 Tübingen, Germany

Supporting Information

ABSTRACT: Perylene-based organic semiconductors are widely used in organic electronic devices. Here, we studied the ultrafast excited-state dynamics in diindenoperylene (DIP) and dicyanoperylene-bis(dicarboximide) (PDIR-CN_2) thin films, respectively, after optical excitation using femtosecond (fs) time-resolved second harmonic generation in combination with large scale quantum chemical calculations. In DIP, the initial optical excitation leads to the formation of delocalized excitons, which localize on dimers on a ultrafast time scale of <50−150 fs depending on the excitation energy. In contrast, in PDIR-CN_2, the optical excitation directly generates localized excitons on monomers or dimers. In both DIP and PDIR-CN_2, localized excitons decay within hundreds of fs into Frenkel-like trap sites. The relaxation to the ground state occurs in DIP on a time scale of 600 ± 110 ps. In PDIR-CN_2, this relaxation time is 1 order of magnitude faster (62 ± 1.8 ps). The differences in the exciton formation and decay dynamics in DIP and PDIR-CN_2 are attributed to differences in the aggregation as well as to the respective structural and energetic disorder within the materials. Our study provides important insights into the exciton formation and decay dynamics in perylene-based organic compounds, which is essential for the understanding of the photophysics of these molecules in thin films.

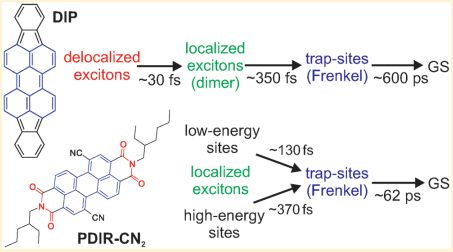

INTRODUCTION

Understanding photoinduced processes in thin films of functionalized polycyclic aromatic molecules is a prerequisite for the design of optoelectronic devices such as organic solar cells or light emitting diodes.[1−7] In organic solar cells, separation of optically excited electron−hole pairs and long-range charge transport play an important role for the efficiency.[2] Both are largely influenced by the film structure and the molecular orientation at interfaces between electron donor (D) and acceptor (A) molecules.[8,9]

To characterize the various photoinduced processes, which take place on different time scales, sufficiently sensitive methods are needed. While time-resolved photoluminescence and transient absorption spectroscopy have been frequently used to investigate the excited-state dynamics in organic films ranging from the femtosecond (fs) to the nanosecond time scale, fs time-resolved second harmonic generation (TR-SHG) studies are less common.[10−13] The SHG signal is generated by the second-order nonlinear susceptibility of the sample and is therefore especially sensitive to electronic excitations.[14−16] For centrosymmetric materials, the signal is dominated by surface processes, since the bulk contributions vanish, which results in the surface or interface sensitivity of this method.[14−21] TR-SHG spectroscopy has been applied, for instance, to investigate the role of hot excitons on charge transfer (CT) yields at D/A interfaces[13] or to characterize the ultrafast decay dynamics of excitons in diindenoperylene (DIP) thin films prepared at room temperature (DIP_{RT}) on sapphire and SiO_2 substrates.[22] DIP is a perylene derivative (see Figure 1a) which plays an

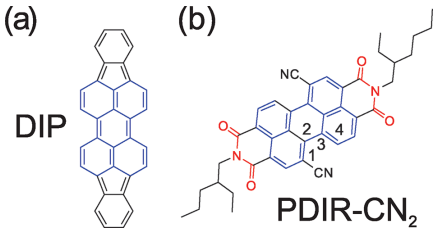

Figure 1. Molecular structures of (a) DIP and (b) PDIR-CN_2.

Received: August 7, 2019
Revised: October 20, 2019
Published: October 22, 2019

DOI: 10.1021/acs.jpcc.9b07511
J. Phys. Chem. C 2019, 123, 27561−27572

important role as a donor material in organic semiconductor devices.[23−28] On the basis of the fs TR-SHG data obtained from DIP_{RT} films, it has been proposed that the initial optical excitation induces the generation of delocalized excitons. Depending on the excitation energy, they localize on a time scale of 140 fs at an excitation energy of 2.03 eV and approximately 20 fs for an excitation at 2.23 eV. Such localizations are also known for other organic materials.[29−31] A drawback of the TR-SHG method is that the time-dependent signal contains very little information about the character of the involved states. Thus, the nature of the involved states in DIP could not be fully determined, even taking into account time-resolved photoluminescence and transient absorption data.[32]

In the present study, we extend the scope to TR-SHG measurements on DIP films prepared at low temperatures (DIP_{LT}) and to the electron acceptor *N*,*N*′-bis(2-ethylhexyl)-1,7-dicyanoperylene-3,4:9,10-bis(dicarboximide) (PDIR-CN_2, see Figure 1b). The former is of interest in order to investigate the influence of the film morphology (e.g., increased disorder or decreased size of nucleation sites) on localization and exciton transfer processes. While DIP_{RT} forms highly ordered films in which the molecules are arranged in a standing upright (edge-on) geometry (σ-phase), DIP_{LT} exhibits additional lying down (face-on) domains, the λ-phase.[25] On the other hand, studying PDIR-CN_2, a compound also widely used in organic electronic devices,[9,33−36] allows insights to be gained into the influence of variations in both the electronic structure and the film morphology on the ultrafast photoinduced processes. Note that PDIR-CN_2 films are less ordered compared to DIP_{RT} films.[9]

Previous investigations showed that reliable interpretation of spectroscopic measurements necessitates input from theoretical simulations of the spectra because the overall shapes of the measured spectra result from an intimate interplay of various effects. Approaches based on the Frenkel−Holstein model Hamiltonian[37−41] have very successfully been used to interpret the absorption spectra of perylene-based systems.[42−44] However, for emission spectra, difficulties exist because the parameters for the absorption may differ from the parameters needed for the emission. Improvements of this approach were suggested by Martinez and co-workers[45] and Kühn and co-workers.[46,47] In the present work, we performed large scale quantum chemical calculations on the energetics and the characters of the involved states, using our dimer- or aggregate-based approach.[46] This approach has been proven to be reliable for the investigations of the excited-state dynamics after optical excitations of DIP and other substituted perylene derivatives.[48−51] Further information about exciton diffusion processes in amorphous films is adopted from recent work on DIP films and DIP−C_{60} interfaces.[52−54] Moreover, these data are combined with experimental information about the thin-film structures.[55−58]

We found that the initial optical excitation in DIP_{LT} results in the formation of delocalized excitons in agreement with previous studies.[22] Depending on the excitation energy, these excitons localize on an ultrafast time scale (<50 fs) on DIP dimers. In contrast, for PDIR-CN_2, the initial excitation leads directly to the generation of localized excitons on monomers and dimers. In both compounds, the localized excitons relax within hundreds of fs into Frenkel-like trap states. The final relaxation to the ground state occurring on the picosecond time scale is an order of magnitude faster in PDIR-CN_2 compared to DIP_{LT}. The differences in the exciton formation and decay dynamics are mainly based on the different film morphologies of both compounds.

■ METHODS SECTION

Sample Preparation. Thin films of DIP_{LT} and PDIR-CN_2 were prepared by organic molecular beam deposition in an ultrahigh vacuum chamber on sapphire substrates (CrysTec, single crystal, (0001) surface, both sides polished). During deposition, the substrate temperature was kept at 220 ± 10 K for DIP_{LT}, while it was room temperature for PDIR-CN_2 at a base pressure of 1×10^{-9} mbar. The deposition rate of 0.3 nm/min during growth was controlled by a quartz crystal microbalance calibrated by X-ray reflectivity (XRR). The nominal thickness of each layer was 20 nm. For the deposition method used, PDIR-CN_2 forms films in an edge-on geometry, while, in DIP, the deposition at 220 ± 10 K led to molecular orientations which consist of edge-on and face-on domains.[57,59] The film structures were studied by XRR measurements.[9]

SHG Experiments. For the TR-SHG measurements, a Ti:sapphire laser system with a repetition rate of 300 kHz, a pulse length of 50 fs, and a spectral width of 25 nm was used. The initial beam was split into a pump and probe beam. The wavelength of the pump beam was varied between 650 and 550 nm, while the probe beam was kept at 800 nm, resulting in a SHG signal of 400 nm. The measurements were taken in reflection mode under an angle of 45° with respect to the surface normal. The SHG signal was filtered by a monochromator and detected by a photomultiplier tube. The beams were p-polarized, leading to a perpendicular and a parallel component of the light with respect to the surface normal. In addition, measurements with s-polarized light were performed, which exhibits only a parallel component of the light.[13,15,16,21,60] A probe beam intensity of 360 $\mu J/cm^2$ and a pump intensity of 135 $\mu J/cm^2$ were used. For an improved signal-to-noise ratio, at least 10 measurements were summed up on one spot and at least four different spots on the sample were used for each signal trace. The sapphire substrate was used, since sapphire generates a SHG signal close to zero. All experiments were performed under an inert gas atmosphere (N_2) and at room temperature. To describe the TR-SHG data, we utilized different models for DIP and PDIR-CN_2. In the case of DIP, a three-step first-order kinetic model with the amplitude *A* set to zero and overlaid with an oscillating part (see ref 22 and the Supporting Information) was used. For PDIR-CN_2, a two-step (A to B) combined with a single exponential decay and the oscillating term first-order kinetic model was used (see the Supporting Information). The signal decaying on the picosecond time scale in DIP and PDIR-CN_2 was modeled by a single exponential decay function.

Computational Details and Estimates of Theoretical Error Bars. The aggregate systems in the present study pose various challenges for a thorough computational investigation. Since the intermolecular arrangement of the molecules in the thin films was found to have an essential impact on the charge-carrier qualities of the system,[55,56,61] intermolecular degrees of freedoms need to be investigated. The electronic screening induced by the environment also has to be accounted for, since it significantly affects the processes after excitation. Another property of the thin-film structures is their high anisotropy with regard to the propagation direction which reduces the

DOI: 10.1021/acs.jpcc.9b07511
J. Phys. Chem. C 2019, 123, 27561−27572

The Journal of Physical Chemistry C Article

accuracy of a description of the environment through continuum models.

To account for the various effects, the model structures for the calculations on DIP aggregates were built from optimized monomers and arranged according to experimentally determined X-ray structures. For PDIR-CN_2 aggregates, some additional effects had to be considered. X-ray experiments indicate that PDIR-CN_2 is planar in single crystals and thin films, while an optimization of a monomer in solvent or vacuum predicts a twisted form (dihedral(1234) = 17°, the enumeration of the centers is given in Figure 1). In a vacuum, the twisted equilibrium structure is about 7 kJ/mol more stable than the corresponding planar structure. In contrast, a tetramer built up from four twisted monomers is about 250 kJ/mol less stable than the tetramer built up from four planar monomers. Differences between the monomer and the tetramer result, since the van der Waals interactions are considerably higher between planar monomers than between twisted ones. Additionally, steric interactions may also play a role. However, due to the difference between monomer and tetramer, one cannot exclude that single molecules are slightly twisted within defect regions. To investigate the influence of such possible distortions, we also computed mixed tetramers, which consist of three planar monomers and one twisted monomer. The twisted monomers were taken from a full ground-state optimization starting from the crystal structure. To obtain minimized planar structures, we performed a constrained optimization in which the dihedral angles are kept frozen at 0 or 180°. To test the influence of possible defect structures on the electronic structure, we also calculated distorted tetramers in which one monomer is tilted by 10° around its short axis. This was also done for the DIP tetramer. The nomenclature used for the aggregates is sketched in Figures 2 and 3. For DIP,

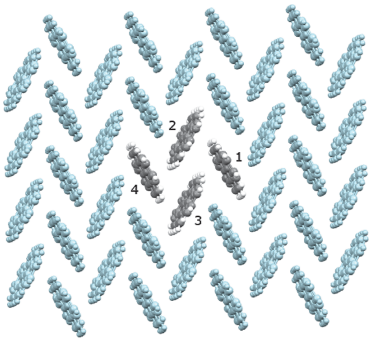

Figure 2. One layer of the crystal structure of the DIP σ-phase, with a highlighted tetramer. In the following discussion, the dimers will be enumerated according to this scheme.

we used the single crystal structure of the high temperature σ-phase which is in good agreement with the unit cell of DIP films on sapphire.[57,62] The structure of PDIR-CN_2 was adopted from a powder X-ray diffraction analysis.[55] This structure was used to model that of the solution-processed annealed films of PDIR-CN_2 which is also in accordance with the structure of the vacuum deposited films used in this work.[55,56] Necessary geometry optimizations of monomers

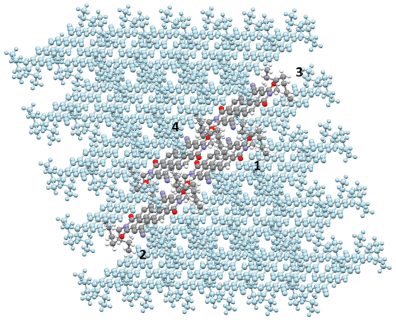

Figure 3. One layer of the crystal structure of PDIR-CN_2, with a highlighted tetramer. In the following discussion, the dimers will be enumerated according to this scheme.

were conducted with the density functional theory (DFT) functional ωB97X-D[63] in combination with the cc-pVDZ basis set[64] if not denoted otherwise. This method was tested to perform very well in combination with a double-ζ basis-set plus polarization in a former benchmark study including perylene derivatives and is still sufficiently cheap to describe larger clusters.[65]

Excited-state properties were mostly calculated using time-dependent (TD)-DFT theory employing ωB97X-D/cc-pVDZ. As a range-separated and dispersion-corrected functional, ωB97X-D allows for a reliable description of excited states of Frenkel and CT character.[63] This functional was furthermore found to qualitatively reproduce the potential energy surfaces (PES) of perylene dimers along an intermolecular coordinate when the respective monomers were optimized with the same method.[66] Accounting for the size of the systems, SCS-CC2/cc-pVTZ[64,67−73] and SCS-ADC(2)/cc-pVTZ[64,68−71,73−76] calculations could only be used to test the quality of the TD-DFT calculations. All (TD-)DFT calculations in this work were conducted with Gaussian 16,[77] while SCS-CC2 and SCS-ADC(2) calculations were performed with Turbomole7.1.[78] For the investigation of bigger aggregates of DIP, consisting of up to 10 monomers, we employed ZIndo(S).[79−81] Although it is a semiempirical method, ZIndo(S) has been proven to produce reliable results for perylenetetracarboxylic dianhydride (PTCDA) aggregates in earlier studies.[48] Benchmarks with respect to TD-DFT showed that this also holds for the DIP films, while it turned out to not accurately reproduce the character of the excitations in PDIR-CN_2 (see the Supporting Information).

To account for environmental effects, a supercell of the crystal structure was mimicked by a point-charge field fit to the electrostatic potential (ESP).[82,83] The supercells are built up by three layers, where each layer consists of 28 (DIP)/30 (PDIR-CN_2) monomers (Table S1). The lying domains (λ-phase) in DIP_{LT} were approximated by the same unit cell as the standing domains but were rotated manually by 90° to mimic the neighborhood between lying and upright standing DIP molecules. This is a valid assumption according to investigations by Dürr et al.[58] For further details on the supercell, see the Supporting Information (Table S1).

Calculated excitations are investigated regarding the following parameters: The delocalization of a system is

DOI: 10.1021/acs.jpcc.9b07511
J. Phys. Chem. C 2019, 123, 27561−27572

quantified by the participation ratio (P_R) which depicts the mean delocalization of the hole and the particle (electron) in terms of involved fragments.[84] For the investigation of the systems at hand, monomers were defined as fragments. Hence, the quantity of P_R directly mirrors how many monomers of the calculated aggregate are involved in the excitation. The CT character of an excitation is calculated from all configurations with the hole and the particle located on different fragments.[84] A CT value of 1 corresponds to a fully charge-separated state, and a value of 0, to a pure Frenkel excitation. For the determination of P_R and CT, the program package TheoDORE was employed.[84−86]

The quantum chemical cluster computations on aggregates allow for an even treatment of CT and Frenkel excitations and offer detailed insights into photoinduced processes. Thus, the assignment of the measured spectra and the interpretation of the TR-SHG signals can be based on these results. Nevertheless, the computations include some approximations the accompanying errors of which have to be carefully estimated to allow for a reliable interpretation of the experimental data. The corresponding benchmark calculations are described in the Supporting Information. Due to the size of the model systems, only vertical excitation energies can be evaluated for the aggregates. Vibrationally resolved monomer computations on DIP, which agree excellently with their experimental counterparts (deviation <0.05 eV), indicate that the vertical excitation energies obtained with ωB97X-D/cc-pVDZ are blue-shifted by about 0.4 eV. ZIndo/S calculations predict an additional error of 0.1 eV when restricting the aggregate to a tetramer. An additional estimate is made by the utilization of perfect crystal structures. Work by Hertel and Bässler and by Brückner et al. indicates that the disorder in the thin films induces an averaged broadening of 0.1 eV.[52−54] These studies also show the existence of trap states which lie 0.2−0.3 eV lower in energy than the average of states. Corresponding benchmark calculations of PDIR-CN_2 (Table S7) indicate that the vertical energies calculated on the tetramer (Table 3) are blue-shifted by about 0.4−0.5 eV.

■ RESULTS AND DISCUSSION

In the case of DIP, we can build up on our previous study, in which we investigated the ultrafast excited-state dynamics in DIP films generated at room temperature (DIP_{RT}).[22] The preparation at low temperature (220 ± 10 K, DIP_{LT}), leads to a different film structure. The well-ordered structure with the molecules oriented perpendicular to the substrate (edge-on) is disturbed in a way that some molecules adopt a more parallel (face-on) orientation.[57] The optical extinction of the DIP and PDIR-CN_2 films is displayed in Figure 4. In addition, the excitation photon energies of 556 nm (2.23 eV), 580 nm (2.14 eV), and 610 nm (2.03 eV) are marked.

TR-SHG Experiments on DIP Films. The excited-state dynamics of DIP_{LT} films after optical excitation at 580 nm are shown in Figure 5a. They are very similar to the TR-SHG data of DIP_{RT}.[22] A strong intensity increase of the SHG signal is observed due to the electronic excitation by the pump pulse. The signal contains two components, a fast and a slow one (feature labeled as B and C). In addition, as has been found for DIP_{RT} films,[22] the rise of the pump pulse is steeper compared to the signal rise, and the signal still increases after the pump pulse has passed. This indicates that the initial optical excitation does not induce a signal change. The initially created excited species is labeled as A. The TR-SHG data can

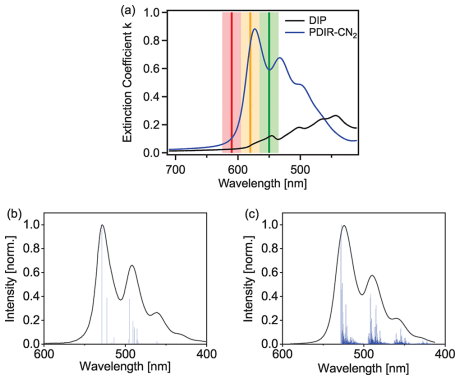

Figure 4. Extinction spectra of both materials on a glass substrate (a) and in solution (b and c). (a) The vertical lines mark the excitation wavelengths (556, 580, and 610 nm) used for the TR-SHG experiments, and the colored area around the respective central wavelength indicates the energy width of the excitation pulse. (b) DIP in acetone. (c) PDIR-CN_2 in chloroform. The black lines indicate the experiment. The stick spectra were calculated with ωB97X-D/cc-pVTZ and the Franck−Condon−Herzberg−Teller formalism in IEF-PCM. Both are red-shifted by 0.04 eV (DIP)/0.05 eV (PDIR-CN_2) for a better comparison with the experiment. For details, see the Supporting Information, Computational Details.

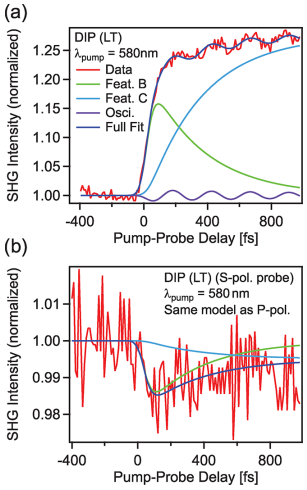

Figure 5. Time-resolved second harmonic generation (TR-SHG) measurement of DIP_{LT} films on sapphire. (a) TR-SHG signal for the p-polarized probe beam overlaid with the results of a three-step first-order kinetic model (see the Supporting Information and ref 22). (b) TR-SHG result in which an s-polarized probe beam has been used.

be perfectly modeled by the first-order kinetic three-step model (see the Supporting Information) used previously.[22] From the fit, we get times of 30 ± 10 fs for the transfer from A

DOI: 10.1021/acs.jpcc.9b07511
J. Phys. Chem. C 2019, 123, 27561−27572

The Journal of Physical Chemistry C Article

to B and 350 ± 100 fs for that from B to C, in agreement with our previous study.[22] The decay of C occurs on longer time scales, namely, within 600 ± 110 ps (see the Supporting Information). In addition, we observe an oscillation on the TR-SHG signal. It has a period of 247 ± 3 fs, which corresponds to a frequency of 135 ± 2 cm^{-1} (16.7 ± 0.2 meV). The measured values are summarized in Table 1 together with the decay times observed for different excitation energies. Note that, in contrast to measurements on the DIP_{RT}, we observe for DIP_{LT} a clear time-dependent SHG signal with s-polarized light (see Figure 5b). This can be attributed to the more parallel oriented DIP_{LT} molecules with respect to the surface plane.

Table 1. Summary of the Observed TR-SHG Features in DIP and PDIR-CN_2 Films, Respectively[a]

feature	rate constants determined for different excitation energies (nm)		
	610	580	556
DIP			
1a (A1 to B)		30 ± 10 fs	20 ± 10 fs
1b (A2 to B)	150 ± 90 fs		
2 (B to C)	350 ± 100 fs	350 ± 100 fs	350 ± 100 fs
3 (decay of C)	600 ± 110 ps	600 ± 110 ps	600 ± 110 ps
oscillation	247 fs	247 fs	247 fs
PDIR-CN_2			
1 (A to C)	130 ± 30 fs	130 ± 30 fs	130 ± 30 fs
2 (B to C)		370 ± 30 fs	370 ± 30 fs
3 (decay of C)	62 ± 2 ps	62 ± 2 ps	62 ± 2 ps
4 (decay of D)	20 ± 10 fs	20 ± 10 fs	20 ± 10 fs
oscillation	271 fs	271 fs	271 fs

[a]The associated nomenclature used in Figures 5 and 6 is given in parentheses.

TR-SHG Experiments on PDIR-CN_2 Films. In a next step, we present and discuss the data obtained from PDIR-CN_2 films on sapphire. As observed for DIP_{LT}, we detect an oscillation on the TR-SHG signal (see Figure 6a). For the PDIR-CN_2 film, the oscillation period is 271 ± 2 fs, corresponding to a frequency of 123 ± 1 cm^{-1} (15.3 ± 0.1 meV). In PDIR-CN_2, the optical excitation leads to a direct (within the temporal width of the pump pulse) and steep increase of the SHG signal. In order to describe the data, we used a two-step first-order kinetic model combined with a single exponential decay (including an oscillating term), as detailed in the Supporting Information. The data obtained at a pump photon energy of 556 nm indicate that an excitation of electrons into different vibronic levels is possible (see Figure 4); therefore, we included this in the modeling. This results in two different components A and B. The dependence of the TR-SHG signal on the excitation energy is shown in Figure 6b. For an excitation of 610 nm, only one feature can be observed, which resembles the fast relaxation component (A) of the spectrum obtained with a pump energy of 556 nm. Increasing the excitation energy leads to a rise of a second decay component (B). Feature A is decaying on a time scale of 130 ± 30 fs and feature B within 370 ± 30 fs. For delay times in the picosecond regime, another feature labeled as C can be observed (see Figure 6c). The decay time of C is 62 ± 2 ps. In addition, a further component labeled as D decaying on the ultrafast time scale of 20 ± 10 fs could be detected. Feature D has a different dependency on the pump intensity compared to feature C (see Figure 6d); thus, we assume that D belongs to a process which is independent of the process involving feature C as well as features A and B (data not shown here), since they possess the same pump intensity dependence as feature C. Thus, we suppose that feature D is related to polarization effects in the molecules due to the electric field of the laser light. The measured decay times are summarized in Table 1.

Calculations—Absorption Spectra. Before discussing the observed SHG features, we will first focus on the assignment of the absorption spectra of the DIP and PDIR-CN_2 thin films given in Figure 4. Subtracting a blue-shift of 0.4 eV resulting from the use of vertical energies instead of 0−0 energies (Table S2) from the computed excitation energy of 2.63 eV for the lowest state of the DIP tetramer in the point-charge field (Table 2), we predict the lowest absorption band of the DIP thin film at 2.2−2.3 eV. This matches the lowest band of the absorption spectrum (≈2.25 eV). The strongest peak in the spectrum (≈2.8 eV) is assigned to the highest electronic state of the tetramer in the point-charge field (2.94 eV, see Table 2). In agreement with the experiment, our calculations predict considerably higher transition dipole moments for this state compared to the lower lying states. The computations seem to underestimate this excitation by about 0.2 eV if we assume the same error bars as used for the lower states. Note that the highest peak is not relevant for the present study, since the highest excitation energy used in the SHG experiments is 2.23 eV.

The thin-film absorption spectra of PDIR-CN_2 exhibit the most intense absorption band at 2.16 eV. This agrees with the computed second state of the PDIR-CN_2 tetramer in the point-charge field located at 2.66 eV (see Table 3), if it is corrected by the blue-shift of vertical excitation energies discussed in the Supporting Information (Table S9) of 0.4−0.5 eV. In addition, the intensity pattern of the computed four states matches excellently that of the experimental spectrum, because the second state possesses by far the highest electronic transition dipole. The corrected energy of the lowest electronic state of the tetramer is about 2.0 eV; i.e., only this state will be populated by the lowest excitation energy of 2.01 eV used in the SHG experiments. The energy of the second absorption maximum at 2.34 eV fits to the corrected energy of the computed fourth state of the tetramer (≈2.3 eV). Whether the peak at higher energies (2.48 eV) belongs to an even higher electronic excitation or a combination of the electronic state at 2.36 eV plus an excited vibrational state remains unclear. However, this state is not relevant for the present study. Our cluster computations also nicely reflect that both materials exhibit inverted intensity patterns. This variation results because the absorption spectrum of the DIP film is dominated by H-aggregates (e.g., Dimer12 in Table S4), while for PDIR-CN_2 the second lowest state possesses the highest transition dipole moment. This is in line with the experimentally found aggregation structure in PDIR-CN_2 which is an intermediate between H- and J-type.[56] A comparison of our calculations with a previous theoretical study on DIP[44] shows agreement with respect to the relative energetic positions of Frenkel and CT states as well as a minor mixing of Frenkel and CT states.

Assignment of the TR-SHG Features. The assignment of TR-SHG features demands for further experimental and theoretical information. Therefore, we combine our computations of DIP and PDIR-CN_2 aggregates discussed above with (i) experimental data from the thin-film structures,[55−58] (ii) previous simulations on trapping effects in organic semiconductors such as perylene diimide (PDI), PTCDA, and

DOI: 10.1021/acs.jpcc.9b07511
J. Phys. Chem. C 2019, 123, 27561−27572

The Journal of Physical Chemistry C Article

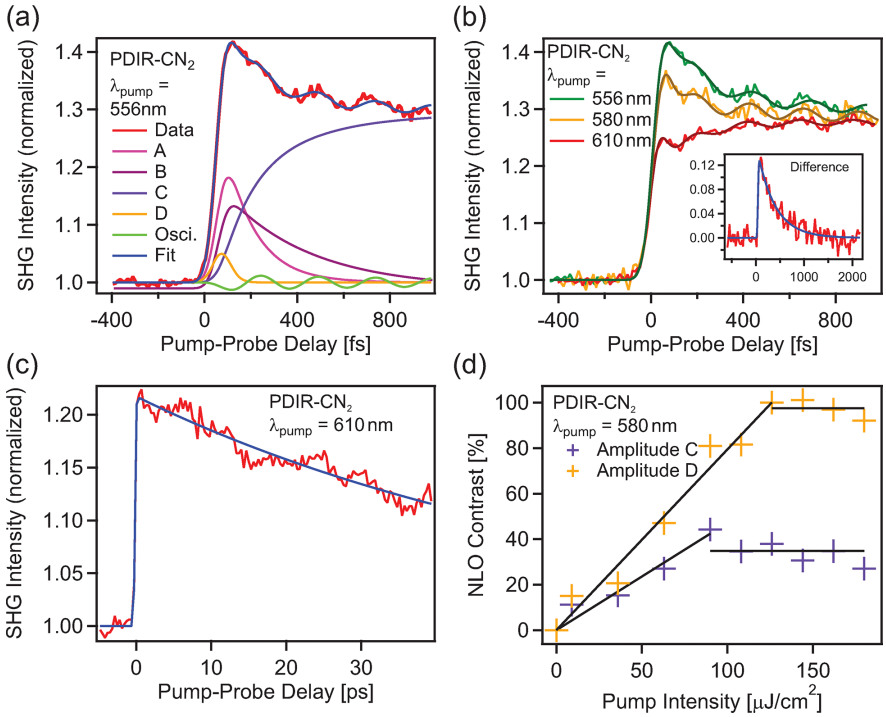

Figure 6. (a) TR-SHG measurements of PDIR-CN_2 on sapphire for delay times of up to 1 ps overlaid with the results of our model (see text). (b) Dependence of the TR-SHG trace on the pump wavelength. Inset: Difference in the TR-SHG response for a pump wavelength of 556 and 610 nm. (c) Decay of the signal for decay times of 40 ps. (d) Pump intensity dependence of features C and D.

Table 2. Comparison of TD-ωB97X-D/cc-pVDZ Calculations of the Effects of Possible Environments and Distortions on DIP Tetramers in the σ-Phase[a]

(a) in vacuum			(b) in point-charge field			(c) in vacuum, tilted		
ΔE	f	P_R	ΔE	f	P_R	ΔE	f	P_R
2.62	0.00	3.97	2.63	0.00	4.00	2.60	0.01	3.80
2.68	0.00	2.03	2.70	0.00	2.04	2.67	0.00	2.14
2.73	0.00	2.03	2.73	0.00	2.04	2.72	0.02	2.09
2.90	1.97	4.00	2.94	2.33	4.00	2.90	2.00	3.89

[a]All energy differences (ΔE) are given in eV and depict vertical excitation energies. f denotes the oscillator strength and P_R the participation ratio (see the Methods Section). Note that the CT character for all excitations is below 0.1 (compare Tables S3 and S4); thus, we did not include the CT values here. "Tilted" refers to the aggregate described in the Computational Details, in which one monomer is tilted by 10° along its short axis to disturb the symmetry of the aggregate.

DIP,[48,49,87] as well as (iii) information about the exciton diffusion in DIP films and at a DIP/fullerene interface.[29,53] Various experimental investigations indicate that, due to the structural disorder in thin films, the generated excitons localize very fast on smaller subunits; i.e., shortly after their generation by the pump pulse, the excitons are only delocalized over a few monomers[30] or even on dimers.[88,89] The exciton energies and the delocalization of the excitons depend on the excitation energy, the organic material, and its degree of disorder.[90,91] Microscopically, the relative orientation of the monomer determines these exciton characteristics.[29,52,53]

In general, TR-SHG signals, which monitor the population or depopulation of a given electronic state, can be attributed to two pathways. They can originate from local processes on a subunit, e.g., due to the transition from a higher to a lower lying electronic state as well as from the accumulation of excitons on energetically favorable sites. Such accumulations are induced by the exponential decrease of the jump probability of an exciton with the energy difference between the respective sites according to Marcus theory.[92,93] Since both processes occur on similar time scales, an unambiguous assignment of the TR-SHG signals is difficult.[49] Sites for which the jump probabilities vanish, act as traps from which the excitons cannot escape but can only decay into the electronic ground state.[49,66] Such traps often result from a combination of intra- and intersite effects. For example, for perylene-based dyes, experimental studies indicate that excitons localize on dimers on a femtosecond time scale.[94] Nevertheless, further hopping would still be possible for most

DOI: 10.1021/acs.jpcc.9b07511
J. Phys. Chem. C 2019, 123, 27561−27572

The Journal of Physical Chemistry C Article

Table 3. Comparison of TD-ωB97X-D/cc-pVDZ Calculations of the Effects of Possible Environments and Distortions on PDIR-CN_2 Tetramers[a]

(a) in vacuum			(b) in point-charge field			(c) in vacuum, tilted			(d) in vacuum, twisted		
ΔE	f	P_R	ΔE	f	P_R	ΔE	f	P_R	ΔE	f	P_R
2.57	0.00	2.17	2.57	0.00	2.13	2.61	0.08	2.19	2.58	0.01	2.15
2.67	3.06	4.00	2.66	2.97	3.67	2.67	2.89	3.20	2.68	2.57	2.41
2.70	0.00	2.14	2.70	0.10	3.52	2.71	0.07	1.48	2.71	0.00	2.74
2.71	0.01	3.99	2.71	0.00	2.22	2.71	0.01	2.48	2.74	0.41	1.10

[a]All energy differences (ΔE) are given in eV and depict vertical excitation energies. f denotes the oscillator strength and P_R the participation ratio (see the Methods Section). Note that the CT character for all excitations is low (compare Tables S11 and S12); thus, we did not include the CT values here. "Tilted" refers to the aggregate described in the Computational Details, in which one monomer is tilted by 10° along its short axis to disturb the symmetry of the aggregate, and "twisted" refers to an aggregate in which one of the monomers is fully ground-state optimized and therefore twisted.

sites.[29,53,54] For H-aggregates, the final trapping occurs due to the relaxation from the upper to the lower Frenkel state[48,49] sometimes mediated through CT states.[50,87]

The TR-SHG signals for DIP_{LT} and PDIR-CN_2 thin films show two main differences: First, the signal of the DIP_{LT} film arises after optical excitation with a specified, pump-energy-dependent delay, while the TR-SHG trace of PDIR-CN_2 increases instantaneously with the pump pulse. Second, the decay time of the feature C is 10 times faster in PDIR-CN_2 than in DIP_{LT}. These differences arise most likely from intermonomer effects rather than from variations in the photophysics of the monomers (intramonomer effects), because the monomer spectra strongly resemble each other (Figures S1 and S2). This resemblance is owed to transitions within the perylene core, which dominate both monomer spectra.

The differences in the intermonomer effects result from the different aggregation structures (H- vs J-aggregates) and from the respective structural and energetic disorders within the materials. For example, experiments show that PDIR-CN_2 thin films are less-ordered than DIP thin films.[56,57] This is likely caused by the branched alkyl chains or the CN substituents of the PDIR-CN_2 molecule. However, it is an open question if this higher structural disorder leads to significant differences in the electronic structures of DIP and PDIR-CN_2 thin films. To test such effects, we compared the electronic structure of tetramers in a vacuum with the electronic structure of tetramers embedded in spatially limited point-charge fields, thus mimicking a slightly disturbed single crystal environment (Table S1). To investigate the influence of defects, we computed tetramers in which one monomer is tilted by 10° around its short axis. Finally, we computed PDIR-CN_2 tetramers, which are composed of three planar monomers and one twisted monomer. Such a twisting may happen at defects because PDIR-CN_2 molecules possess a twisted structure in a vacuum or solvents but are planarized due to the intermolecular interactions in a single crystal. For DIP, we did not perform computations with nonplanar monomers because DIP is always planar. The data are summarized in Table 2 (DIP) and Table 3 (PDIR-CN_2). Both tables summarize the excitation energies of the four lowest lying states (ΔE), the oscillator strengths (f), and the P_R value. The latter gives a measure of the delocalization of the exciton in the tetramer; i.e., a value of 4 indicates a completely delocalized exciton, while a value of 1 characterizes the exciton as localized on one monomer. A comparison between DIP and PDIR-CN_2 crystal properties on the basis of tetramer data is only valid if the transition from crystals to tetramers does not introduce different symmetry reductions. Figure 7 shows the various inversion symmetries (yellow points), 2-fold rotational axes

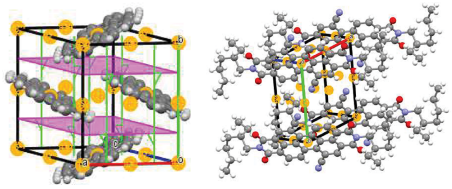

Figure 7. Schematic representation of the symmetry elements in the thin-film systems of DIP (left) and PDIR-CN_2 (right).

(green), and mirror planes (purple plane) which are present in the DIP crystal. For the tetramer, the inversion center in the middle of the tetramer remains. For PDIR-CN_2, the various inversion centers of the crystal structure also reduce to one in the middle of the tetramer. Additionally, the translational equivalents within both crystals disappear in the tetramers. Because the reduction of symmetry going from the full crystal to a tetramer is similar for both compounds, a comparison based on differences in the tetramers seems to be valid. For the distorted tetramers (one monomer tilted by 10°), the symmetry reduces for both compounds. For PDIR-CN_2, the symmetry additionally lowers if one planar monomer is replaced by a twisted one.

The computations predict strongly delocalized excitons for the computations in a vacuum. For PDIR-CN_2 (Table 3a), the second and fourth states are delocalized over all four units, while the first and third states are only delocalized over two units. For DIP (Table 2a), a complete delocalization is found for the first and fourth states, while a delocalization over two monomers is predicted for the two middle states. Differences between both compounds arise if the high symmetry of the nondisturbed tetramers is lifted. In the slightly distorted environment of the point-charge fields, the P_R values for PDIR-CN_2 lower to 3.5−3.6, while the corresponding values for DIP remain 4.0. Please note that the excitation energies and the oscillator strengths do not change considerably for both compounds. For the distorted tetramer (one monomer tilted by 10°), the differences are even stronger. For PDIR-CN2, the P_R values for the strongly delocalized states decrease further (P_R = 3.20 and 2.48, respectively), while again nearly no change is found for DIP (P_R = 3.80 and 3.89). In the mixed cluster consisting of three planar molecules and one twisted

DOI: 10.1021/acs.jpcc.9b07511
J. Phys. Chem. C 2019, 123, 27561−27572

PDIR-CN_2 molecule, the P_R values for the most delocalized states are only 2.41 and 2.74; i.e., on average, the exciton is localized on dimers. In summary, our computations indicate that distortions in the crystal structures influence the localization of excitons less strongly in DIP than in PDIR-CN_2. Hence, we conclude that the experimentally found higher structural disorder in PDIR-CN_2 films will lead to considerably stronger localized excitons.

Taking these differences into account, we can assign the various TR-SHG signals. We first focus on the oscillations found for both compounds. To get deeper insights into the physical nature of these oscillations, their dependence on the pump energy and intensity was investigated. For both compounds, the amplitude depends on excitation energy and pump intensity, while the oscillation period is independent of both (see Figure S4). A more detailed discussion is given in the Supporting Information. Based on these observations, the oscillations can be explained as a coherent excited-state wave packet motion of the molecular core of the molecules induced by the pump pulse,[95−98] i.e., a combined electronic-vibration excitation generated by the pump pulse. Since the excitations start from the lowest vibrational state of the electronic ground state, excited vibrations of the electronically excited states and the corresponding Franck−Condon factors are relevant for the assignment of these oscillations. In principle, the assignment should include the modes taken from a larger cluster. However, since calculations for the larger model system failed due to hardware and software limitations, we approximate the vibrations by monomer vibrations. This includes several assumptions. First, intermolecular modes are not taken into account; however, they should lie at even lower energies. Second, we assume that interactions between the monomers will not influence the modes. This should also be approximately valid, since the intramonomeric interactions are considerably stronger than the interactions between the monomers. Finally, the vibrational motions computed for a monomer could be hindered because the molecule is embedded in the thin films. However, as seen in Tables S16 and S17 (unscaled vibrations), the displacements of the perylene cores are very small, and thus probably not hindered.

For DIP_{LT}, the oscillation has a period of 247 ± 3 fs, which corresponds to a frequency of 135 ± 2 cm^{-1}. Based on Franck−Condon intensities (see Table S15), we assign this oscillation to the excitation of mode 4 (154 cm^{-1}), which is a kind of twist mode around the molecular center (Table S16). The corresponding oscillation for PDIR-CN_2 has a period of 271 ± 3 fs, which corresponds to a frequency of 123 ± 1 cm^{-1}. The Franck−Condon calculations for the full PDIR-CN_2 molecule did not converge. If the alkyl chains are replaced by methyl groups, the computations predict two modes with strong Franck−Condon factors in this energy region (Table S15). The one with the highest intensity (122 cm^{-1}, intensity 183 dm^3 cm^{-1} mol^{-1}) represents a combination mode of the first, second, and fifth modes, which are all singly excited. The second (123 cm^{-1}, intensity 58 dm^3 cm^{-1} mol^{-1}) represents an excitation of mode 10 (Table S17, upper part). The nonconverged computations for the full PDIR-CN_2 also predict a buckling mode along the long axis, whose motion in the perylene part is similar to mode 10 of the model system with methyl groups (Table S17, bottom) but also involves a significant movement of the alkyl chains. Besides the uncertainty arising from the nonconverged computation, this mode might be hindered within the solid state because the alkyl substituents are much more closely packed than the perylene cores. Based on the higher intensity, we assign this oscillation to the combination mode. Nevertheless, in contrast to the DIP situation, this assignment is quite precarious.

A schematic representation of the remaining TR-SHG features is given in Figures 8 and 9, including the nomenclature

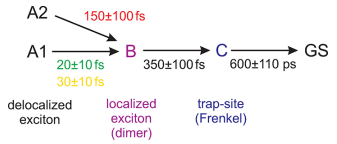

Figure 8. Scheme of the processes observed by TR-SHG spectroscopy in DIP_{LT} films. Colored transfer times indicate the energy of the pump pulse (red, 610 nm (2.03 eV); yellow, 580 nm (2.14 eV); green, 556 nm (2.23 eV)).

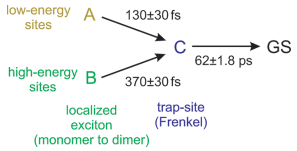

Figure 9. Scheme of the excited-state dynamics observed by TR-SHG spectroscopy in PDIR-CN_2 films as well as the assignment to the involved processes (see text).

introduced in Table 1. We first discuss the processes in the ps time regime, since these can be described by the same phenomenon in both materials. The signals are assigned to the final decay from the energetic sinks (trap states), in which the excitons accumulate to the ground state (C to GS). The factor 10 between the rate constants can be explained by the variations in the transition intensities to the ground state found for DIP (Table 2, Figure 8) and PDIR-CN_2 (Table 3, Figure 9) thin films. As a consequence, the emission from the lowest electronic state is allowed for PDIR-CN_2, while it is formally forbidden for DIP. This explanation is in line with photoluminescence measurements for DIP and PDIR-CN_2,[9,56] which show a considerably stronger luminescence for PDIR-CN_2. These measurements also indicate the presence of trap states. From the experimental data, it is impossible to conclude whether these trap states possess Frenkel or CT character. Our computations clearly indicate (see Tables 2 and 3 and Tables S2, S4, and S10) that they exhibit Frenkel character because the lowest lying states with distinct CT character are predicted to appear above 3 eV.

For DIP, the excitation pulses at 580 and 556 nm induce very fast processes with rate constants of 30 ± 10 and 20 ± 10 fs (Figure 8) which are completely missing for PDIR-CN_2. For the probe pulse at 610 nm, the process happens on a longer time scale of 150 ± 100 fs in DIP. Combining the above-discussed different localization behavior of excitons in DIP and PDIR-CN_2 films with the experimentally determined higher structural order of DIP thin films, we propose that the pump pulses at 580 and 556 nm initially excite delocalized excitons which induce no signal change due to their high isotropy. The signal rise is then caused by the localization of these excitons on smaller aggregates, e.g., tetramers or dimers ($A1_{DIP}$ to B_{DIP}).

DOI: 10.1021/acs.jpcc.9b07511
J. Phys. Chem. C 2019, 123, 27561−27572

Such localization effects were already described in our previous DIP_{RT} study[22] but also in other perylene-based dyes.[88,94,99] Since these localization processes are faster than energy dissipation, which occurs on the 100−1000 fs time scale,[100] the resulting excitons still possess enough energy for diffusion. This diffusion process leads to a final population of even lower lying trap states and takes place on a time scale of around 350 fs (B_{DIP} to C_{DIP}). For the excitation at 610 nm, we monitor basically the same effects. Since this excitation energy lies considerably below the first absorption maximum (see Figure 4), the generated excitons exhibit almost no excess energy, which slows down the localization process to 150 fs ($A2_{DIP}$ to B_{DIP}). In extreme cases, the localization can only take place on trap sites, which corresponds to a direct relaxation ($A1_{DIP}$ to C_{DIP}).

Based on the TR-SHG results, both DIP_{RT} (pure σ-phase) and DIP_{LT} (including domains of the λ-phase) behave very similar.[22] This is also mirrored in our calculations (compare Table 2 and Tables S4−S7) from which we can conclude that the shorter relaxation times in DIP_{LT} compared to DIP_{RT} thin films should mainly result from smaller nucleation sites and the resulting higher degree of disorder. Furthermore, they indicate that the λ-domains in DIP_{LT} exhibit the same relaxation processes as the pure σ-phase. The direction of exciton diffusion in DIP_{LT} is of course flipped by 90°.

For PDIR-CN_2 (Figure 9), the fast processes (<100 fs) are missing for all excitation energies. This can be explained by a stronger exciton localization as indicated by our computations (Table 3) in combination with the higher structural disorder of PDIR-CN_2 thin films found experimentally. Therefore, the excitons in PDIR-CN_2 are instantaneously localized. Hence, for the pump pulses at 580 and 556 nm, the first TR-SHG signal change already monitors the population of the trap states ($B_{PDIR\text{-}CN_2}$ to $C_{PDIR\text{-}CN_2}$) which was assigned to the second signal of the DIP system. The rate constant for this process is 370 ± 30 fs for excitation energies of 580 and 556 nm but only 130 ± 30 fs for the excitation at 610 nm. This difference can be attributed to the mobility of the generated excitons. According to Förster's theory, these mobilities depend on the transition dipole moment of the populated state as well as on the excess energy of the exciton. The excitons generated by the 610 nm (2.03 eV) pump pulse can only populate the lowest electronically excited state (S_1), which has a low transition dipole moment. In combination with the low excess energy, the mobility of these excitons is expected to be rather small, leading to fast trapping processes. Conversely, the excitons generated at higher excitation energies (580 and 556 nm) inhibit a considerably higher mobility, because the S_2-state is mainly populated. The S_2-state has a higher transition dipole moment which is accompanied by a higher mobility. If these excitons relax to the S_1-state through, e.g., intrasite relaxation processes, they still possess rather high excess energies; consequently, their trapping occurs on a longer time scale.

■ CONCLUSION

We have investigated the excited-state dynamics in diindeno-perylene (DIP_{LT}) and dicyano-perylene-bis(dicarboximide) (PDIR-CN_2) thin films after optical excitation utilizing femtosecond (fs) time-resolved second harmonic generation and large scale quantum chemical calculations. DIP_{LT} prepared at low temperatures leads to the formation of face-on domains compared to the edge-on geometry formed at room temperature (DIP_{RT}). In DIP_{LT}, optical excitation (at 556, 580, and 610 nm) resulted in the formation of delocalized excitons. Depending on the excitation energy and accordingly on the excess energy, a localization on dimers occurred on a time scale between 20 and 150 fs. Afterward, the excitons are trapped within 350 ± 100 fs on Frenkel-like trap sites, followed by a decay into the ground state on the time scale of 600 ± 110 ps. In PDIR-CN_2, the fast processes (<100 fs) are not observed at all, since the initial excitation induced the creation of localized excitons located on either monomers or dimers. These excitons relax into Frenkel-like trap states within around 100−400 fs depending on their excess energy. The decay to the ground state happened within 62 ± 1.8 ps. The differences between DIP_{LT} and PDIR-CN_2 in the primary exciton generation process (delocalized vs localized) and the 1 order of magnitude difference in the exciton decay times into the final ground state are assigned on the one hand to differences in the aggregation structures (J- vs H-aggregates). On the other hand, they are attributed to differences in the respective structural and energetic disorders within the thin films. Our combined experimental and theoretical study has elucidated the so far unresolved processes and decay times of electronically excited states on the femtosecond time scale in perylene-based semiconductors.

■ ASSOCIATED CONTENT

Supporting Information

The Supporting Information is available free of charge on the ACS Publications website at DOI: 10.1021/acs.jpcc.9b07511.

> Computational details, benchmark of the theoretical approaches, visualization of vibrational modes, coordinates of computationally evaluated compounds, models used to describe the TR-SHG data, and additional TR-SHG data (PDF)

■ AUTHOR INFORMATION

Corresponding Authors

*E-mail: bernd.engels@uni-wuerzburg.de. Phone: (+49) 931 31 85394. Fax: (+49) 931 31 85331.

*E-mail: tegeder@uni-heidelberg.de. Phone: +49 (0) 6221 548475. Fax: +49 (0) 6221 456199.

ORCID

Valentina Belova: 0000-0002-8142-2090

Bernd Engels: 0000-0003-3057-389X

Petra Tegeder: 0000-0002-5071-9385

Notes

The authors declare no competing financial interest.

■ ACKNOWLEDGMENTS

Funding by the German Research Foundation (DFG) through the collaborative research center SFB 1249 (project B06) is gratefully acknowledged (P.T. and M.H.). M.H. acknowledges financial support from the Heidelberg Graduate School of Fundamental Physics. K.B. and F.S. acknowledge financial support from the DFG (BR4869/1-1 and SCHR700/20-1). B.E. and S.W. acknowledge financial support via the GRK 2112 "Molekulare Biradikale".

DOI: 10.1021/acs.jpcc.9b07511
J. Phys. Chem. C 2019, 123, 27561−27572

REFERENCES

(1) Bredas, J. L.; Norton, J. E.; Cornil, J.; Coropceanu, V. Molecular Understanding of Organic Solar Cells: The Challenges. *Acc. Chem. Res.* **2009**, *42*, 1691−1699.

(2) Clarke, T. M.; Durrant, J. R. Charge Photogeneration in Organic Solar Cells. *Chem. Rev.* **2010**, *110*, 6736−6767.

(3) May, V.; Kühn, O. *Charge and Energy Transfer Dynamics in Molecular Systems*; Wiley-VCH: 2011.

(4) Beljonne, D.; Cornil, J.; Muccioli, L.; Zannoni, C.; Brédas, J. L.; Castet, F. Electronic Processes at OrganicâĹŠOrganic Interfaces: Insight from Modeling and Implications for Opto-electronic Devices. *Chem. Mater.* **2011**, *23*, 591−609.

(5) Ruhle, V.; Lukyanov, A.; May, F.; Schrader, M.; Vehoff, T.; Kirkpatrick, J.; Baumeier, B.; Andrienko, D. Microscopic Simulations of Charge Transport in Disordered Organic Semiconductors. *J. Chem. Theory Comput.* **2011**, *7*, 3335−3345.

(6) Bakulin, A. A.; Rao, A.; Pavelyev, V. G.; van Loosdecht, P. H. M.; Pshenichnikov, M. S.; Niedzialek, D.; Cornil, J.; Beljonne, D.; Friend, R. H. The Role of Driving Energy and Delocalized States for Charge Separation in Organic Semiconductors. *Science* **2012**, *335*, 1340−1344.

(7) Köhler, A.; Bässler, H. *Electronic Processes in Organic Semiconductors*; Wiley-VCH: 2015.

(8) D'Avino, G.; Muccioli, L.; Castet, F.; Poelking, C.; Andrienko, D.; Soos, Z. G; Cornil, J.; Beljonne, D. Electrostatic Phenomena in Organic Semiconductors: Fundamentals and Implications for Photovoltaics. *J. Phys.: Condens. Matter* **2016**, *28*, 433002.

(9) Belova, V.; et al. Evidence for Anisotropic Electronic Coupling of Charge Transfer States in Weakly Interacting Organic Semiconductor Mixtures. *J. Am. Chem. Soc.* **2017**, *139*, 8474−8486.

(10) Chan, W.-L.; Ligges, M.; Jailaubekov, A.; Kaake, L.; Miaja-Avila, L.; Zhu, X.-Y. Observing the Multiexciton State in Singlet Fission and Ensuing Ultrafast Multielectron Transfer. *Science* **2011**, *334*, 1541−1545.

(11) Jailaubekov, A. E.; Willard, A. P.; Tritsch, J. R.; Chan, W.-L.; Sai, N.; Gearba, R.; Kaake, L. G.; Williams, K. J.; Leung, K.; Rossky, P. J.; Zhu, X.-Y. Hot Charge-Transfer Excitons Set the Time Limit for Charge Separation at Donor/Acceptor Interfaces in Organic Photovoltaics. *Nat. Mater.* **2013**, *12*, 66−73.

(12) Wu, X.; Park, H.; Zhu, X.-Y. Probing Transient Electric Fields in Photoexcited Organic Semiconductor Thin Films and Interfaces by Time-Resolved Second Harmonic Generation. *J. Phys. Chem. C* **2014**, *118*, 10670−10676.

(13) Schulze, M.; Hänsel, M.; Tegeder, P. Hot Excitons Increase the Donor/Acceptor Charge Transfer Yield. *J. Phys. Chem. C* **2014**, *118*, 28527−28534.

(14) McGilp, J. F. A Review of Optical Second-Harmonic and Sum-Frequency Generation at Surfaces and Interfaces. *J. Phys. D: Appl. Phys.* **1996**, *29*, 1812−1821.

(15) Schulze, M.; Utecht, M.; Moldt, T.; Przyrembel, D.; Gahl, C.; Weinelt, M.; Saalfrank, P.; Tegeder, P. Nonlinear Optical Response of Photochromic Azobenzene-Functionalized Self-Assembled Monolayers. *Phys. Chem. Chem. Phys.* **2015**, *17*, 18079−18086.

(16) Schulze, M.; Utecht, M.; Hebert, A.; Rück-Braun, K.; Saalfrank, P.; Tegeder, P. Reversible Photoswitching of the Interfacial Nonlinear Optical Response. *J. Phys. Chem. Lett.* **2015**, *6*, 505−509.

(17) Shen, Y. R. Surface Studies by Optical Second Harmonic Generation: An Overview. *J. Vac. Sci. Technol., B: Microelectron. Process. Phenom.* **1985**, *3*, 1464−1466.

(18) Guyot-Sionnest, P.; Chen, W.; Shen, Y. R. General Considerations on Optical Second-Harmonic Generation from Surfaces and Interfaces. *Phys. Rev. B: Condens. Matter Mater. Phys.* **1986**, *33*, 8254−8263.

(19) Shen, Y. R. Surface Properties Probed by Second-Harmonic and Sum-Frequency Generation. *Nature* **1989**, *337*, 519−525.

(20) Shen, Y. R. Surface Probed by Nonlinear Optics. *Surf. Sci.* **1994**, *299-300*, 551−562.

(21) Hänsel, M.; Barta, C.; Rietze, C.; Utecht, M.; Rück-Braun, K.; Saalfrank, P.; Tegeder, P. 2-Dimensional Nonlinear Optical Switching Materials: Molecular Engineering towards High Nonlinear Optical Contrasts. *J. Phys. Chem. C* **2018**, *122*, 25555−25564.

(22) Hänsel, M.; Belova, V.; Hinderhofer, A.; Schreiber, F.; Broch, K.; Tegeder, P. Ultrafast Excited State Dynamics in Diindenoperylene Films. *J. Phys. Chem. C* **2017**, *121*, 17900−17906.

(23) Wagner, J.; Gruber, M.; Hinderhofer, A.; Wilke, A.; Bröker, B.; Frisch, J.; Amsalem, P.; Vollmer, A.; Opitz, A.; Koch, N.; Schreiber, F.; Brütting, W. High Fill Factor and Open Circuit Voltage in Organic Photovoltaic Cells with Diindenoperylene as Donor Material. *Adv. Funct. Mater.* **2010**, *20*, 4295.

(24) Heinemeyer, U.; Broch, K.; Hinderhofer, A.; Kytka, M.; Scholz, R.; Gerlach, A.; Schreiber, F. Real-time Changes in the Optical Spectrum of Organic Semiconducting Films and their Thickness Regimes During Growth. *Phys. Rev. Lett.* **2010**, *104*, 257401.

(25) Kowarik, S.; Gerlach, A.; Sellner, S.; Schreiber, F.; Cavalcanti, L.; Konovalov, O. Real-Time Observation of Structural and Orientational Transitions During Growth of Organic Thin Films. *Phys. Rev. Lett.* **2006**, *96*, 125504.

(26) Hörmann, U.; et al. Voc from a Morphology Point of View: The Influence of Molecular Orientation on the Open Circuit Voltage of Organic Planar Heterojunction Solar Cells. *J. Phys. Chem. C* **2014**, *118*, 26462.

(27) Zhou, Y.; Taima, T.; Kuwabara, T.; Takahashi, K. Efficient Small-Molecule Photovoltaic Cells Using a Crystalline Diindenoperylene Film as a Nanostructured Template. *Adv. Mater.* **2013**, *25*, 6069−6075.

(28) Gruber, M.; Wagner, J.; Klein, K.; Hörrmann, U.; Opitz, A.; Stutzmann, M.; Brütting, W. Thermodynamic Efficiency Limit of Molecular Donor-Acceptor Solar Cells and its Application to Diindenoperylene/C60-Based Planar Heterojunction Devices. *Adv. Energy Mater.* **2012**, *2*, 1100−1108.

(29) Brückner, C.; Würthner, F.; Meerholz, K.; Engels, B. Atomistic Approach To Simulate Processes Relevant for the Efficiencies of Organic Solar Cells as a Function of Molecular Properties. II. Kinetic Aspects. *J. Phys. Chem. C* **2017**, *121*, 26−51.

(30) Spano, F. C.; Yamagata, H. Vibronic Coupling in J-Aggregates and Beyond: A Direct Means of Determining the Exciton Coherence Length from the Photoluminescence Spectrum. *J. Phys. Chem. B* **2011**, *115*, 5133−5143.

(31) Hestand, N. J.; Spano, F. C. Molecular Aggregate Photophysics beyond the Kasha Model: Novel Design Principles for Organic Materials. *Acc. Chem. Res.* **2017**, *50*, 341−350.

(32) Nichols, V. M.; Broch, K.; Schreiber, F.; Bardeen, C. J. Excited-State Dynamics of Diindenoperylene in Liquid Solution and Solid Films. *J. Phys. Chem. C* **2015**, *119*, 12856−12864.

(33) Lee, J.; Jadhav, P.; Reusswig, P. D.; Yost, S. R.; Thompson, N. J.; Congreve, D. N.; Hontz, E.; Voorhis, T. V.; Baldo, M. A. Singlet Exciton Fission Photovoltaics. *Acc. Chem. Res.* **2013**, *46*, 1300−1311.

(34) Oh, J. H.; Sun, Y.-S.; Schmidt, R.; Toney, M. F.; Nordlund, D.; Könemann, M.; Würthner, F.; Bao, Z. Interplay Between Energetic and Kinetic Factors on the Ambient Stability of n-Channel Organic Transistors Based on Perylene Diimide Derivatives. *Chem. Mater.* **2009**, *21*, 5508−5518.

(35) Kim, J.-H.; Han, S.; Jeong, H.; Jang, H.; Baek, S.; Hu, J.; Lee, M.; Choi, B.; Lee, H. S. Thermal Gradient During Vacuum-Deposition Dramatically Enhances Charge Transport in Organic Semiconductors: Toward High-Performance N-Type Organic Field-Effect Transistors. *ACS Appl. Mater. Interfaces* **2017**, *9*, 9910−9917.

(36) Reusswig, P. D.; Congreve, D. N.; Thompson, N. J.; Baldo, M. A. Enhanced External Quantum Efficiency in an Organic Photovoltaic Cell via Singlet Fission Exciton Sensitizer. *Appl. Phys. Lett.* **2012**, *101*, 113304.

(37) Holstein, T. Studies of Polaron Motion: Part II. The "Small" Polaron. *Ann. Phys.* **1959**, *8*, 343−389.

(38) Barford, W.; Marcus, M. Theory of Optical Transitions in Conjugated Polymers. I. Ideal Systems. *J. Chem. Phys.* **2014**, *141*, 164101.

(39) Schröter, M.; Ivanov, S.; Schulze, J.; Polyutov, S.; Yani, Y.; Pullerits, T.; Kühn, O. Exciton-Vibrational Coupling in the Dynamics

DOI: 10.1021/acs.jpcc.9b07511
J. Phys. Chem. C 2019, 123, 27561−27572

and Spectroscopy of Frenkel Excitons in Molecular Aggregates. *Phys. Rep.* **2015**, *567*, 1−78.
(40) Spano, F. C. The Spectral Signatures of Frenkel Polarons in H- and J-Aggregates. *Acc. Chem. Res.* **2010**, *43*, 429−439.
(41) Spano, F. C. Excitons in Conjugated Oligomer Aggregates, Films, and Crystalls. *Annu. Rev. Phys. Chem.* **2006**, *57*, 217−243.
(42) Pochas, C. M.; Kistler, K. A.; Yamagata, H.; Matsika, S.; Spano, F. C. Contrasting Photophysical Properties of Star-Shaped vs Linear Perylene Diimide Complexes. *J. Am. Chem. Soc.* **2013**, *135*, 3056−3066.
(43) Plötz, P.-A.; Polyutov, S. P.; Ivanov, S. D.; Fennel, F.; Wolter, S.; Niehaus, T.; Xie, Z.; Lochbrunner, S.; Würthner, F.; Kühn, O. Contrasting Photophysical Properties of Star-Shaped vs Linear Perylene Diimide Complexes. *Phys. Chem. Chem. Phys.* **2016**, *18*, 25110−25119.
(44) Gisslén, L.; Scholz, R. Crystallochromy of Perylene Pigments: Interference between Frenkel Excitons and Charge-Transfer States. *Phys. Rev. B: Condens. Matter Mater. Phys.* **2009**, *80*, 115309.
(45) Li, X.; Parrish, R. M.; Liu, F.; Schumacher, S. I. L. K.; Martínez, T. J. An Ab Initio Exciton Model Including Charge-Transfer Excited States. *J. Chem. Theory Comput.* **2017**, *13*, 3493−3504.
(46) Plötz, P.-A.; Megow, J.; Niehaus, T.; Kühn, O. Spectral Densities for Frenkel Exciton Dynamics in Molecular Crystals: A TD-DFTB Approach. *J. Chem. Phys.* **2017**, *146*, 084112.
(47) Plötz, P.-A.; Megow, J.; Niehaus, T.; Kühn, O. All-DFTB Approach to the Parametrization of the System-Bath Hamiltonian Describing Exciton-Vibrational Dynamics of Molecular Assemblies. *J. Chem. Theory Comput.* **2018**, *14*, 5001−5010.
(48) Bellinger, D.; Pflaum, J.; Brüning, C.; Engel, V.; Engels, B. The Electronic Character of PTCDA Thin Films in Comparison to Other Perylene-Based Organic Semi-Conductors: Ab Initio-, TD-DFT and Semi-Empirical Computations of the Opto-Electronic Properties of Large Aggregates. *Phys. Chem. Chem. Phys.* **2017**, *19*, 2434−2448.
(49) Settels, V.; Schubert, A.; Tafipolski, M.; Liu, W.; Stehr, V.; Topczak, A. K.; Pflaum, J.; Deibel, C.; Fink, R. F.; Engel, V.; et al. Identification of Ultrafast Relaxation Processes as a Major Reason for Inefficient Exciton Diffusion in Perylene-Based Organic Semiconductors. *J. Am. Chem. Soc.* **2014**, *136*, 9327−9337.
(50) Schubert, A.; Falge, M.; Kess, M.; Settels, V.; Lochbrunner, S.; Strunz, W. T.; Würthner, F.; Engels, B.; Engel, V. Theoretical Analysis of the Relaxation Dynamics in Perylene Bisimide Dimers Excited by Femtosecond Laser Pulses. *J. Phys. Chem. A* **2014**, *118*, 1403−1412.
(51) Fink, R. F.; Seibt, J.; Engel, V.; Renz, M.; Kaupp, M.; Lochbrunner, S.; Zhao, H.-M.; Pfister, J.; Würthner, F.; Engels, B. Exciton Trapping in π-Conjugated Materials: A Quantum-Chemistry-Based Protocol Applied to Perylene Bisimide Dye Aggregates. *J. Am. Chem. Soc.* **2008**, *130*, 12858−12859.
(52) Hertel, D.; Bässler, H. Photoconduction in Amorphous Organic Solids. *ChemPhysChem* **2008**, *9*, 666−688.
(53) Brückner, C.; Würthner, F.; Meerholz, K.; Engels, B. Structure-Property Relationships from Atomistic Multiscale Simulations of the Relevant Processes in Organic Solar Cells. I. Thermodynamic Aspects. *J. Phys. Chem. C* **2017**, *121*, 4−25.
(54) Brückner, C.; Stolte, M.; Würthner, F.; Pflaum, J.; Engels, B. QM/MM Calculations Combined with the Dimer Approach on the Static Disorder at Organic-Organic Interfaces of Thin-Film Organic Solar Cells Composed of Small Molecules. *J. Phys. Org. Chem.* **2017**, *30*, e3740.
(55) Ferlauto, L.; Liscio, F.; Orgiu, E.; Masciocchi, N.; Guagliardi, A.; Biscarini, F.; Samorì, P.; Milita, S. Enhancing the Charge Transport in Solution-Processed Perylene Di-imide Transistors via Thermal Annealing of Metastable Disordered Films. *Adv. Funct. Mater.* **2014**, *24*, 5503−5510.
(56) Belova, V.; Wagner, B.; Reisz, B.; Zeiser, C.; Duva, G.; Rozbořil, J.; Novák, J.; Gerlach, A.; Hinderhofer, A.; Schreiber, F. Real-Time Structural and Optical Study of Growth and Packing Behavior of Perylene Diimide Derivative Thin Films: Influence of Side-Chain Modification. *J. Phys. Chem. C* **2018**, *122*, 8589−8601.
(57) Kowarik, S.; Gerlach, A.; Sellner, S.; Cavalcanti, L.; Konovalov, O.; Schreiber, F. Real-Time X-Ray Diffraction Measurements of Structural Dynamics and Polymorphism in Diindenoperylene Growth. *Appl. Phys. A: Mater. Sci. Process.* **2009**, *95*, 233−239.
(58) Dürr, A. C.; Koch, N.; Kelsch, M.; Rühm, A.; Ghijsen, J.; Johnson, R. L.; Pireaux, J.-J.; Schwartz, J.; Schreiber, F.; Dosch, H.; Kahn, A. Interplay Between Morphology, Structure, and Electronic Properties at Diindenoperylene-Gold Interfaces. *Phys. Rev. B: Condens. Matter Mater. Phys.* **2003**, *68*, 115428.
(59) Jones, B. A.; Facchetti, A.; Wasielewski, M. R.; Marks, T. J. Tuning Orbital Energetics in Arylene Diimide Semiconductors. Material Design for Ambient Stability of n-Type Charge Transport. *J. Am. Chem. Soc.* **2007**, *129*, 15259−15278.
(60) Moldt, T.; Przyrembel, D.; Schulze, M.; Bronsch, W.; Boie, L.; Brete, D.; Gahl, C.; Klajn, R.; Tegeder, P.; Weinelt, M. Differing Isomerization Kinetics of Azobenzene-Functionalized Self-Assembled Monolayers in Ambient Air and in Vacuum. *Langmuir* **2016**, *32*, 10795−10801.
(61) Krause, S.; Schöll, A.; Umbach, E. Interplay of Geometric and Electronic Structure in Thin Films of Diindenoperylene on Ag(111). *Org. Electron.* **2013**, *14*, 584−590.
(62) Heinrich, M. A.; Pflaum, J.; Tripathi, A. K.; Frey, W.; Steigerwald, M. L.; Siegrist, T. Enantiotropic Polymorphism in Diindenoperylene. *J. Phys. Chem. C* **2007**, *111*, 18878−18881.
(63) Chai, J.-D.; Head-Gordon, M. Long-Range Corrected Hybrid Density Functionals with Damped Atom−Atom Dispersion Corrections. *Phys. Chem. Chem. Phys.* **2008**, *10*, 6615.
(64) Dunning, T. H. Gaussian Basis Sets for Use in Correlated Molecular Calculations. I. The Atoms Boron Through Neon and Hydrogen. *J. Chem. Phys.* **1989**, *90*, 1007.
(65) Brückner, C.; Engels, B. Benchmarking Ground-State Geometries and Vertical Excitation Energies of a Selection of P-Type Semiconducting Molecules with Different Polarity. *J. Phys. Chem. A* **2015**, *119*, 12876−12891.
(66) Engels, B.; Engel, V. The Dimer-Approach to Characterize Opto-Electronic Properties of Exciton Trapping, Diffusion in Organic Semiconductor Aggregates and Crystals. *Phys. Chem. Chem. Phys.* **2017**, *19*, 12604−12619.
(67) Christiansen, O.; Koch, H.; Jørgensen, P. The Second-Order Approximate Coupled Cluster Singles and Doubles Model CC2. *Chem. Phys. Lett.* **1995**, *243*, 409−418.
(68) Hellweg, A.; Grün, S. A.; Hättig, C. Benchmarking the Performance of Spin-Component Scaled CC2 in Ground and Electronically Excited States. *Phys. Chem. Chem. Phys.* **2008**, *10*, 4119−4127.
(69) Hättig, C.; Weigend, F. CC2 Excitation Energy Calculations on Large Molecules Using the Resolution of the Identity Approximation. *J. Chem. Phys.* **2000**, *113*, 5154−5161.
(70) Hättig, C.; Köhn, A. Transition Moments and Excited-State First-Order Properties in the Coupled-Cluster Model CC2 Using the Resolution-of-the-Identity Approximation. *J. Chem. Phys.* **2002**, *117*, 6939−6951.
(71) Weigend, F.; Köhn, A.; Hättig, C. Efficient use of the Correlation Consistent Basis Sets in Resolution of the Identity MP2 Calculations. *J. Chem. Phys.* **2002**, *116*, 3175−3183.
(72) Hättig, C. Geometry Optimizations with the Coupled-Cluster Model CC2 using the Resolution-of-the-Identity Approximation. *J. Chem. Phys.* **2003**, *118*, 7751−7761.
(73) Hättig, C.; Hellweg, A.; Köhn, A. Distributed Memory Parallel Implementation of Energies and Gradients for Second-Order Møller−Plesset Perturbation Theory with the Resolution-of-the-Identity Approximation. *Phys. Chem. Chem. Phys.* **2006**, *8*, 1159−1169.
(74) Schirmer, J. Beyond the Random-Phase Approximation: A New Approximation Scheme for the Polarization Propagator. *Phys. Rev. A: At., Mol., Opt. Phys.* **1982**, *26*, 2395−2416.
(75) Trofimov, A. B.; Schirmer, J. An Efficient Polarization Propagator Approach to Valence Electron Excitation Spectra. *J. Phys. B: At., Mol. Opt. Phys.* **1995**, *28*, 2299.

DOI: 10.1021/acs.jpcc.9b07511
J. Phys. Chem. C 2019, 123, 27561−27572

(76) Hättig, C. Structure Optimizations for Excited States with Correlated Second-Order Methods: CC2 and ADC (2). *Adv. Quantum Chem.* **2005**, *50*, 37−60.
(77) Frisch, M. J.; et al. *Gaussian 16*, revision A.01; Gaussian, Inc.: Wallingford, CT, 2016.
(78) TURBOMOLE V7.1 2016, a Development of University of Karlsruhe and Forschungszentrum Karlsruhe GmbH, 1989−2007, TURBOMOLE GmbH, since 2007; available from http://www.turbomole.com.
(79) Ridley, J.; Zerner, M. An Intermediate Neglect of Differential Overlap Technique for Spectroscopy: Pyrrole and the Azines. *Theor. Chim. Acta* **1973**, *32*, 111−134.
(80) De Mello, P. C.; Hehenberger, M.; Zernert, M. C. ConvergingSCF Calculations on Excited States. *Int. J. Quantum Chem.* **1982**, *21*, 251−258.
(81) Zerner, M. C. *Reviews in Computational Chemistry*; John Wiley & Sons, Inc.: 2007; pp 313−365.
(82) Besler, B. H.; Merz, K. M.; Kollman, P. A. Atomic Charges Derived from Semiempirical Methods. *J. Comput. Chem.* **1990**, *11*, 431−439.
(83) Singh, U. C.; Kollman, P. A. An Approach to Computing Electrostatic Charges for Molecules. *J. Comput. Chem.* **1984**, *5*, 129−145.
(84) Plasser, F.; Lischka, H. Analysis of Excitonic and Charge Transfer Interactions from Quantum Chemical Calculations. *J. Chem. Theory Comput.* **2012**, *8*, 2777−2789.
(85) Plasser, F.; Wormit, M.; Dreuw, A. New Tools for the Systematic Analysis and Visualization of Electronic Excitations. I. Formalism. *J. Chem. Phys.* **2014**, *141*, 024106.
(86) Plasser, F.; Bäppler, S. A.; Wormit, M.; Dreuw, A. New Tools for the Systematic Analysis and Visualization of Electronic Excitations. II. Applications. *J. Chem. Phys.* **2014**, *141*, 024107.
(87) Schubert, A.; Settels, V.; Liu, W.; Würthner, F.; Meier, C.; Fink, R. F.; Schindlbeck, S.; Lochbrunner, S.; Engels, B.; Engel, V. Ultrafast Exciton Self-Trapping upon Geometry Deformation in Perylene-Based Molecular Aggregates. *J. Phys. Chem. Lett.* **2013**, *4*, 792−796.
(88) Schlosser, M.; Lochbrunner, S. Exciton Migration by Ultrafast Förster Transfer in Highly Doped Matrixes. *J. Phys. Chem. B* **2006**, *110*, 6001−6009.
(89) West, B. A.; Womick, J. M.; McNeil, L.; Tan, K. J.; Moran, A. M. Ultrafast Dynamics of Frenkel Excitons in Tetracene and Rubrene Single Crystals. *J. Phys. Chem. C* **2010**, *114*, 10580−10591.
(90) Erwin, P.; Thompson, M. E. Elucidating the Interplay Between Dark Current Coupling and Open Circuit Voltage in Organic Photovoltaics. *Appl. Phys. Lett.* **2011**, *98*, 223305.
(91) Kamm, V.; Battagliarin, G.; Howard, I. A.; Pisula, W.; Mavrinskiy, A.; Li, C.; Müllen, K.; Laquai, F. Polythiophene: Perylene Diimide Solar Cells−the Impact of Alkyl-Substitution on the Photovoltaic Performance. *Adv. Energy Mater.* **2011**, *1*, 297−302.
(92) Stehr, V.; Fink, R. F.; Engels, B.; Pflaum, J.; Deibel, C. Singlet Exciton Diffusion in Organic Crystals Based on Marcus Transfer Rates. *J. Chem. Theory Comput.* **2014**, *10*, 1242−1255.
(93) Stehr, V.; Fink, R.; Tafipolski, M.; Deibel, C.; Engels, B. Comparison of Different Rate Constant Expressions for the Prediction of Charge and Energy Transport in Oligoacenes. *Wiley Interdisciplinary Reviews: Computational Molecular Science* **2016**, *6*, 694−720.
(94) Howard, I. A.; Laquai, F.; Keivanidis, P. E.; Friend, R. H.; Greenham, N. C. Perylene Tetracarboxydiimide as an Electron Acceptor in Organic Solar Cells: A Study of Charge Generation and Recombination. *J. Phys. Chem. C* **2009**, *113*, 21225−21232.
(95) Rosker, M. J.; Wise, F. W.; Tang, C. L. Femtosecond Relaxation Dynamics of Large Molecules. *Phys. Rev. Lett.* **1986**, *57*, 321−324.
(96) Nelson, K. A.; Williams, L. R. Femtosecond Time-Resolved Observation of Coherent Molecular Vibrational Motion. *Phys. Rev. Lett.* **1987**, *58*, 745.
(97) Son, M.; Park, K. H.; Yoon, M.-C.; Kim, P.; Kim, D. Excited-State Vibrational Coherence in Perylene Bisimide Probe by Femtosecond Broadband Pump-Probe Spectroscopy. *J. Phys. Chem. A* **2015**, *119*, 6275−6282.
(98) Lee, G.; Kim, J.; Kim, S. Y.; Kim, D. E.; Joo, T. Vibrational Spectrum of an Excited State and Huang-Rhys Factor by Coherent Wave Packets in Time-Resolved Fluoresence Spectroscopy. *ChemPhysChem* **2017**, *18*, 670−676.
(99) Engel, E.; Koschorreck, M.; Leo, K.; Hoffmann, M. Ultrafast Relaxation in Quasi-One-Dimensional Organic Molecular Crystals. *Phys. Rev. Lett.* **2005**, *95*, 157403.
(100) Tapping, P. C.; Kee, T. W. Optical Pumping of Poly (3-hexylthiophene) Singlet Excitons Induces Charge Carrier Generation. *J. Phys. Chem. Lett.* **2014**, *5*, 1040−1047.

DOI: 10.1021/acs.jpcc.9b07511
J. Phys. Chem. C 2019, 123, 27561−27572

1.2 Geometry Relaxation-Mediated Localization and Delocalization of Excitons in Organic Semiconductors: A Quantum Chemical Study

This publication is a collection of quantum chemical investigations by my colleagues and me with contributions as stated in the following and detailed in the submitted documents. I did all calculations on DIP and PDIR-CN_2, and provided input to the discussion of the impact of results on all systems featured in this paper.
Following the implications of former publications[4;86–89] we wanted to elucidate the effect of and interplay between inter- and intramonomer relaxations on the character and position of excited states in organic semiconductor materials. This also covers the question to which extent the investigation of monomer relaxations can be used to model relaxations which take place in spatially extended systems.
In the first part of the paper we show that the used DFT functionals pose a good compromise between cost and accuracy and are well suited for the description of excitation levels in the systems at hand. This was followed up by the extension of the methodology to aggregates, mostly tetramers. Previous calculations on DIP showed that an initial delocalization of the exciton to at least four (but potentially up to nine monomers) is possible in a crystal like thin film structure.[4] Following this, the question arises whether such a delocalized exciton could potentially be more stable than a localization on a single monomer when relaxation of nuclear coordinates (R) is taken into account. Based on the outcome, one could explain trapping effects and potentially guide the development of materials with an improved behaviour in this regard.
Full relaxation of potential energy surfaces (PESs) of aggregates cannot be used to study this question due to (a) artificial boundaries which are introduced by the extraction of aggregates from approximately periodic systems and (b) limits on computational resources. We employed the hypothesis that relaxation of a monomer in the aggregate will follow the direction of relaxation in vacuum as long as packing structures do not hinder the geometric change. Delocalization of the exciton might then favour a geometry which is not fully relaxed to the excited state (ES) minimum of the monomer ($R(S_1)$) but can be seen as an intermediate between the GS geometry of the monomer ($R(S_0)$) and $R(S_1)$. Indeed, we found that a fully delocalized exciton in DIP is most stable in a tetramer where all monomers are at a $\frac{1}{4}R(S_1)$ geometry. The minimum of the PES of the first excited state of the tetramer in DIP is however found when one monomer can fully relax resulting in a localized excitation. This is contrasted by the second and third ES of the aggregate which clearly favour a delocalized geometry.

In conclusion, we found that the effect of geometric relaxation on excited state energies in aggregates can exceed several tenths of eV and therefore should not be overlooked. Additionally, the effect on distinct excitations stemming from the same monomer excitation can vary greatly. This last effect might be even more pronounced when CT excitations become more important in donor:acceptor systems. This is investigated in ongoing work and will be detailed following this paper.

This paper was published in M. Deutsch, S. Wirsing, D. Kaiser, R. Fink, P. Tegeder, and B. Engels, *Geometry relaxation-mediated localization and delocalization of excitons in organic semicon-ductors: A quantum chemical study*, The Journal of Chemical Physics **153**, 224104(2020). Reprinted from reference [85] with permission from 2021 American Chemical Society.

The Journal of Chemical Physics ARTICLE scitation.org/journal/jcp

Geometry relaxation-mediated localization and delocalization of excitons in organic semiconductors: A quantum chemical study

Cite as: J. Chem. Phys. **153**, 224104 (2020); doi: 10.1063/5.0028943
Submitted: 9 September 2020 • Accepted: 13 November 2020 •
Published Online: 8 December 2020

View Online Export Citation CrossMark

M. Deutsch,[1] S. Wirsing,[1] D. Kaiser,[1] R. F. Fink,[2] P. Tegeder,[3] and B. Engels[1,a)]

AFFILIATIONS

[1] Institut für Physikalische und Theoretische Chemie, Universität Würzburg,, Emil-Fischer-Str. 42, D-97074 Würzburg, Germany
[2] Institut für Physikalische und Theoretische Chemie, Universität Tübingen, Auf der Morgenstelle 18, 72076 Tübingen, Germany
[3] Physikalisch-Chemisches Institut, Universität Heidelberg, Im Neuenheimer Feld 253, 69120 Heidelberg, Germany

Note: This paper is part of the JCP Special Topic on Excitons: Energetics and Spatio-temporal Dynamics.
[a)] Author to whom correspondence should be addressed: bernd.engels@uni-wuerzburg.de

ABSTRACT

Photo-induced relaxation processes leading to excimer formations or other traps are in the focus of many investigations of optoelectronic materials because they severely affect the efficiencies of corresponding devices. Such relaxation effects comprise inter-monomer distortions in which the orientations of the monomer change with respect to each other, whereas intra-monomer distortions are variations in the geometry of single monomers. Such distortions are generally neglected in *quantum chemical* investigations of organic dye aggregates due to the accompanied high computational costs. In the present study, we investigate their relevance using perylene-bisimide dimers and diindenoperylene tetramers as model systems. Our calculations underline the importance of intra-monomer distortions on the shape of the potential energy surfaces as a function of the coupling between the monomers. The latter is shown to depend strongly on the electronic state under consideration. In particular, it differs between the first and second excited state of the aggregate. Additionally, the magnitude of the geometrical relaxation decreases if the exciton is delocalized over an increasing number of monomers. For the interpretation of the vibronic coupling model, pseudo-Jahn–Teller or Marcus theory can be employed. In the first part of this paper, we establish the accuracy of density functional theory-based approaches for the prediction of vibrationally resolved absorption spectra of organic semiconductors. These investigations underline the accuracy of those approaches although shortcomings become obvious as well. These calculations also indicate the strength of intra-monomer relaxation effects.

INTRODUCTION

Functionalized polycyclic aromatic molecules are in the focus of a multitude of experimental and theoretical investigations because they are promising materials in the field of organic semiconductors.[1–5] In this context, perylene-based dyes have been frequently investigated as they exhibit favorable properties.[1] In particular, 3,4,9,10-perylene tetracarboxylic acid bisimides (PBIs) have been explored as a replacement for fullerenes in organic photovoltaics as they possess higher electron mobilities[6,7] and high extinction coefficients in the visible region.[8] Furthermore, they are relatively inexpensive and remarkably stable toward light as well as air.[1] Eventually, their electronic properties and the packing geometries can be tuned by varying the substitution pattern.[9,10] However, despite all these advantages, PBI containing photovoltaic devices show reduced efficiencies in comparison to fullerene analogs.[11] Reasons for these shortcomings were attributed to morphological issues[12] and to trapping processes, which arise due to the formation of excimer states.[13,14] For PBI thin films, a fast relaxation of excitons leading to long-lived immobile states was identified.[14] For α-perylene, the formation of excimers induced by motions of two monomers with respect to each other was indicated by Raman spectroscopy.[15] Recent investigations on excimer formation by Hoche and co-workers,[16] as well as Kennehan and co-workers,[17] also

The Journal of Chemical Physics ARTICLE scitation.org/journal/jcp

indicated a similar mechanism. For amorphous systems, additional traps are due to the strongly varying excitation energies due to the relative orientation of the molecules with respect to each other.[18,19] Actually, it was shown that the energetic disorder is mostly caused by these orientation effects and only to a smaller degree by environmental effects. In this investigation, the energetical disorder predicted by using the Bässler model[20,21] could only be reproduced if a delocalization of excimers is assumed.[22]

A detailed understanding of possible relaxation pathways is very important for the rational design of materials with improved functionality.[1,23] However, while the mentioned studies agree with the fact that exciton trapping occurs rather frequently, the details of the underlying processes are still under debate. Within H-aggregates, trapping can occur because the exciton is initially excited to the higher lying Frenkel state (in a dimer system, this is the S_2 state). If the relaxation to the lowest Frenkel state (S_1) is faster than the competing hopping process, the exciton gets trapped because hopping to the higher lying S_2 state is no longer possible due to the energy loss accompanied with the relaxation to the S_1 state. Furthermore, hopping between the lower Frenkel states—which is energetically feasible—is very inefficient due to the vanishing transition dipoles of these states.

Non-negligible contributions of charge transfer (CT) states result in an even more complex situation. Using the dimer M–M (M ≡ Monomer) as the most simple aggregate, Frenkel configurations arise from linear combinations of the locally excited M^*M and MM^* determinants, while the CT-type configurations stem from linear combinations of the electron exchanging determinants M^+M^- and M^-M^+. Due to significant couplings between locally excited- and CT-configurations, the adiabatic states determined by common quantum-chemistry excited state calculations are generally strong mixtures of these configurations. The ratio of Frenkel and CT characters depends on a subtle interplay of the energy difference and the electronic coupling between the diabatic states.[21,24–26] Hence, a rugged potential energy surface (PES) with various conical intersections results, which may provide very efficient decay pathways to lower lying states.[27–30] Going to larger aggregates, the number of CT states increases considerably (trimer: 3 Frenkel, 6 CT; tetramer: 4 Frenkel, 12 CT), resulting in a decreased energy spacing between the states. Consequently, transitions into lower lying states become even more efficient. Note that due to the couplings between states, CT states can influence the position of conical intersections even if they are higher in energy than the Frenkel states.

Photo-induced relaxation processes in PBI aggregates represent one example for the complicated interplay of various electronic states and geometrical relaxations and distortions.[29–32] Model calculations predict that excimer formation is the reason for the measured strong red shift in the emission spectra of PBI dimers in the minimum structure of the ground state. This red shift is obtained by twisting one of the two monomers of an eclipsed arrangement by 30° about the symmetry axis parallel to the molecular plane [$R_L = R_T = 0$ Å, $R_z = 3.4$ Å, and $\varphi = 30°$ according to the dimer structure parameters in Fig. 3(a)].[33] According to these model calculations, the excimer formation starts with an exciton relaxation from the initially populated S_2 Frenkel state to the lower lying S_1 Frenkel state. However, this first step is not a direct transfer but is mediated by a CT state, which crosses the initially populated S_2 state, resulting in a fast population transfer. The transition between the transiently populated CT state and the S_1 Frenkel state is non-radiative and also very efficient due to the strong coupling between both states. The final emission then takes place from the S_1 state.[29–32] The computations show that intra-monomer (e.g., variations of interatomic distances) and inter-monomer (e.g., the torsional angle between both monomers) relaxation effects have to be taken into account. The relaxation effects not only strongly influence the efficiencies of the relaxation processes but also induce strong red shifts in the emission. On the basis of these processes, it was possible to assign the known spectra of PBI aggregates as well as femtosecond time-resolved experiments.[30,31,33] Recently, the model was also successfully employed to explain the ambient-stable, bright, steady-state photoluminescence from long-lived excitons of H-aggregated PBI crystals.[34] Another important example for localization effects is due to intra-chain dynamics.[35,36]

While intra-monomer relaxations leading to the CT geometry were included in the description of the PBI trapping processes, possible geometry relaxations of the Frenkel states themselves were omitted. Their importance became apparent through our monomer computations, which indicated relaxation effects of about 0.3 eV–0.4 eV. This is in the range of the Davydov splittings found for aggregates of these organic semiconductors. The pronounced impact of geometry relaxation raises the question of how their explicit consideration for Frenkel states may change predictions for aggregate clusters. The inclusion of such relaxation effects might not only induce a change in the energetic position of the excited states but may also affect the individual character of the electronic states. For example, the nuclear relaxation of a single monomer in an aggregate could lead to a localization of the exciton on that monomer. The energetics associated with this situation is sketched in Fig. 1 using a dimer as the simplest model for a molecular aggregate. For clarity, we neglect possible influences of CT states. Figure 1 depicts the coupling between the two localized S_1 states of the monomers if both monomers adopt the same geometry (blue) or if one monomer adopts a structure leading to a lower energy of its localized S_1 state (red). If both monomers adopt the same geometry (blue), the exciton is completely delocalized over both monomers due to simple symmetry considerations. Going to the case given in red, one monomer is relaxed to the

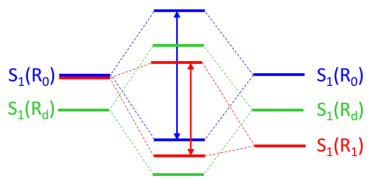

FIG. 1. Comparison of different relaxations. Blue: Both monomers remain in the geometry of the ground state of the monomer (R_0). Red: One monomer is relaxed to the geometry of the excited state of the monomer (R_1) while the second one remains in the ground state geometry of the monomer (R_0). Green: Both monomers relaxed by the same amount (R_d = optimal geometry for S_1-state of dimer).

The Journal of Chemical Physics ARTICLE scitation.org/journal/jcp

optimal geometry of its localized S_1 state (R_1), while the other remains in the geometry of the ground state (R_0). Because the energy of the localized S_1 state in the optimal S_1 geometry is lower, both interacting localized states differ not only in their geometry but also in their associated energies. Due to these inequalities, the splitting decreases, and the exciton starts to localize on the monomer in the S_1 geometry for the lower Frenkel state. For the exciton in a dimer, it could also be that both monomers relax by the same amount (green situation, R_d is the optimal geometry for the S_1 state of the dimer). Then, the energy of the exciton would also decrease, but the exciton remains delocalized over the whole dimer. Which situation is most appropriate to characterize the molecular aggregate depends on the relative energies of the resulting Frenkel states. It might also be that the exciton becomes localized for the lowest Frenkel state but stays delocalized for the second Frenkel state. Since CT states are always delocalized, the degree of delocalization of an exciton may vary strongly during complex relaxation processes involving several electronic states.

Localization effects in self-assembled perylene helices were investigated by Segalina and co-workers.[37] Their study offers valuable insights into the behavior of such aggregates, but localization effects resulting from geometrical changes in monomers were omitted. Such localization effects were investigated by Talipov and co-workers.[38] They investigated relaxation effects in polychromophoric assemblies using covalently linked cofacially arrayed polyfluorenes as model systems. Their computations show that for these systems, excitons always localize on dimers irrespective of the number of chromophores. This behavior is explained by very strong geometry relaxation effects of the highest occupied and lowest unoccupied molecular orbitals (HOMO and LUMO) in this specific case. Thus, it remains unclear whether these systems can serve as real model systems.

Possible models were already worked out by Fulton and Gouterman who successfully described these excitonic effects with vibronic coupling theory.[39,40] They also showed that this theory is formally equivalent with the pseudo Jahn–Teller (pJT) framework and similar to the potential energy model used in Marcus theory. The vibronic coupling theory was later employed by Diehl and co-workers[41] to assign the spectra for a homologous series of oligo(*p*-phenylene) bridged PBI dimers with intermolecular center-to-center distances ranging from 1.3 nm to 2.6 nm. For these dimer systems, the reorganization effects are in the range of 0.3 eV–0.4 eV, while the coupling between monomers is small by a factor of 5 or even more. Consequently, a double minimum potential arises in which the exciton is either localized on one or the other monomer. In simulations, the monomer on which the exciton remains adopts the S_1 equilibrium geometry, while the other monomer stays in the S_0 structure. For the fully delocalized situation, both monomers were assumed to adopt the S_0 geometry (blue case in Fig. 1).

Dreuw and co-workers employed the pJT framework to model relaxation effects in CO and in the benzene dimer.[42,43] In both cases, they varied inter-monomer geometries of the dimers to modify the coupling between both monomers. They showed that for larger monomer distances, the coupling is weaker than the relaxation, which results in a double-minimum potential. For smaller distances, a parabolic shape is found because the coupling is stronger than the relaxation. More details in relation to our study will be given below.

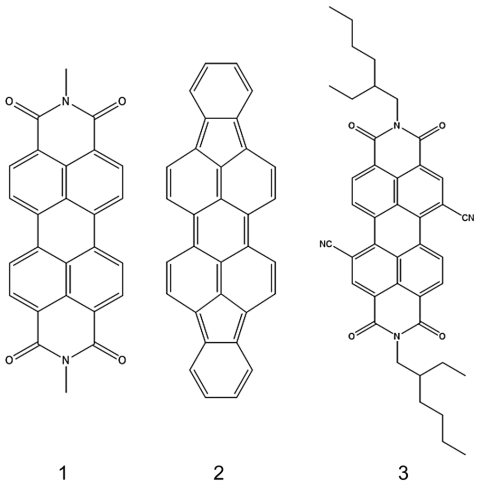

FIG. 2. Lewis structures of the investigated monomer systems. (1) 3,4,9,10-perylene tetracarboxylic acid bisimides (PBIs), (2) diindenoperylene (DIP), and (3) dicyanoperylene-bis(dicarboximide) (PDIR-CN_2).

In the present study, we will extend these previous investigations of the interplay of geometry relaxation and exciton localization. Whether an exciton is delocalized or localized depends on the subtle interplay between the coupling strength between the units of the aggregate and the decrease in the associated energy due to the intra-monomer relaxation of one unit into its S_1 geometry. While the former favors a delocalization of the exciton, the latter induces its localization. We start the investigations with perylene dimers [Figs. 2 and 3(a)] and vary the inter-monomer geometries (e.g., the longitudinal shift or the distance) and the intra-monomer geometry of one monomer. In a second step, we investigate the diindenoperylene (DIP) tetramer as an example for larger clusters. Variations in the electronic character are monitored by computing the localization of the exciton.

This paper is organized as follows: After briefly describing the details of the used theoretical approaches, we first establish expected error bars for different quantum chemical approaches by comparing computed vibrationally resolved excitation energies of the PBI monomer (1) (Fig. 2) with measurements of Klebe *et al.*[44] and Wewer and Stienkemeier.[45,46] For DIP (2) and PDIR-CN_2 (3), we extend these investigations to solvent effects. After establishing the accuracies of our approaches, we turn to the dimer and trimer computations to investigate the interplay of exciton localization and delocalization effects.

TECHNICAL DETAILS

Multi-reference approaches would yield ideal reference results for benchmarks because they provide very accurate results for

The Journal of Chemical Physics ARTICLE scitation.org/journal/jcp

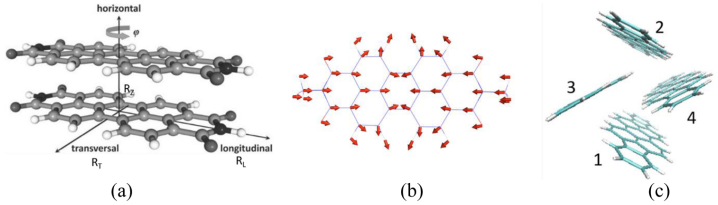

FIG. 3. (a). Description of the varied inter-monomer coordinates for the computed PBI dimer. The coordinates include transversal (R_T) and longitudinal (R_L) shifts, the distance between both monomers R_Z, and the rotation of the upper monomer around φ. (b) Enlarged sketch of the geometry change between the equilibrium structures of the S_0 to the S_1 states of the PBI monomer. The sum of the variations is <0.005 Å. (c) Arrangement of the DIP tetramer.

excited states,[47–50] potential energy surfaces,[51,52] as well as other molecular properties.[53] For the size of the present system, however, they are computationally too expensive. Hence, we test the accuracy of time-dependent density functional theory (TD-DFT) calculations against SCS-CC2[54,55] in combination with the SVP (split valence plus polarization)[56,57] and the TZVPP basis sets.[56,58] We compared the TD-DFT-based approaches with respect to SCS-CC2 to keep the computational costs feasible. SCS-CC2 predicted adiabatic excitation energies with a mean absolute error (MAE) of 0.05 eV and a standard deviation of 0.06 eV for a test set of 0–0 transitions in medium-sized and large organic molecules.[59] In this work, SCS-CC2 was shown to perform slightly better than its parent approach CC2 (MAE = 0.09 eV). Furthermore, it improves the description of CT states.[60] For the "low-cost" TD-DFT approach, we mainly used the modern range-separated hybrid ωB97X-D functional[61] in combination with SVP, TZVP, cc-pVDZ, cc-pVTZ, and def2-SVP basis sets.[56,58,62,63] This method is sufficiently efficient to compute aggregates up to tetramers.[32,64,65] For the benchmark, we optimized the ground state and the first excited states within the given approximation unless stated otherwise. Vibrational effects were computed using the Franck–Condon approximation alone or in combination with the Herzberg–Teller correction as implemented in the Gaussian16 program package.[66] For the vibrational effects, we used not only the standard time-independent approach[67] but also the time-dependent formalism.[68] For excited state calculations in solution, we used the equilibrium and non-equilibrium options in the IEF-PCM (Integral Equation Formalism version of Polarizable Continuum Model) approach implemented in the Gaussian program suite.[69–71] In the non-equilibrium option, only ultrafast solvent processes (e.g., polarization of the electron cloud of the solvent) are considered.[72] In the equilibrium option, also slower effects (e.g., the reorientation of solvent molecules) are included.[73] An equilibrium calculation describes a situation where the solvent has had time to fully respond to the solute. A non-equilibrium calculation is appropriate for processes that are too rapid for the solvent to have time to fully respond, e.g., for the energy of the 0–0 excitation in an absorption spectrum. The vibrational propagation had to be estimated based on frequencies in the equilibrium model due to technical limitations.

To mimic intra-monomer relaxation effects, we modulated the monomer geometry linearly from the monomer ground state geometry $[\vec{R}(S_0)]$ to the monomer geometry in its S_1 state $[\vec{R}(S_1)]$ using

$$\vec{R}_\chi = \vec{R}(S_0) + \chi\Delta\vec{R}, \text{ with } \Delta\vec{R} = \vec{R}(S_0) - \vec{R}(S_1). \quad (1)$$

We varied χ from −0.5 to 1.5 in 0.5 steps for each monomer of the dimer. According to Eq. (1), χ = 0.0 gives $\vec{R}(S_0)$, while $\vec{R}(S_1)$ is obtained with χ = 1.0. An enlarged description of the difference between $\vec{R}(S_0)$ and $\vec{R}(S_1)$ for PBI is given in Fig. 3(b). The resulting 2D surfaces for energy and properties were obtained by spline interpolation between the resulting 25 points. We only include relaxations to the equilibrium geometry of the S_1 state of the monomer because higher electronic states of the monomer units are normally not relevant for the photo-induced behavior of crystals, thin films, or amorphous systems.[18,19,74] To investigate the interplay between inter-monomer and intra-monomer changes, we computed the intra-monomer variations for the longitudinal shifts (R_L = 0.0 Å, 0.5 Å, 1.0 Å, 1.4 Å, 1.7 Å, and 2.5 Å) and the distances between both monomers (R_Z = 3.1 Å, 3.31 Å, 3.5 Å, 4.0 Å, 5.0 Å, and 10.0 Å). Beside the energies, we also computed the oscillator strengths, the P_R value, and the CT value. The P_R values give the delocalization of the exciton, i.e., $P_R = 2$ denotes the situation in which the exciton is completely delocalized between the two monomers in a dimer, while $P_R = 1$ characterizes an exciton that solely resides on one monomer. The CT value gives the percentage of CT character, i.e., CT = 0 corresponds to a pure Frenkel state, and CT = 1 corresponds to a pure CT state. To determine the P_R and CT values, we employed the TheoDORE program package.[75,76]

Benchmark for vibrationally resolved absorption spectra of perylene-based organic semi-conductors

In order to computationally model the relevant processes in organic semiconductor thin films, sufficiently large molecular clusters have to be used to mimic the high density of states, their energy shifts, and the important mixing of CT and Frenkel states. Additionally, the experimental absorption and emission spectra exhibit distinct vibrational progressions, i.e., vibrational effects should also be considered. Finally, the influence of the environment on the energy position of the different states can also be important because the

The Journal of Chemical Physics ARTICLE scitation.org/journal/jcp

position of conical intersections or even the energetic order of states might change due to polarizable environments. Obviously, the computational modeling of large molecular clusters and very accurate electronic descriptions exclude each other. Computations of such cluster models are only possible with DFT or even simpler methods because the system size excludes costly high-level multi-reference approaches.[77–79] The inclusion of vibrational effects—even solely on the harmonic level—necessitates geometry optimizations and the determination of the Hessian of the excited state, which is generally too costly for more accurate approaches.

Table I estimates the error bars arising from the use of TD-DFT and neglect of the vibrational effects by comparing the computed results for the PBI monomer (1) with measurements of Klebe *et al.*[44] as well as Wever and Stienkemeier.[45] Klebe *et al.* noted that the first band peak of PBI monomers dispersed in, e.g., polystyrene appears at 530 nm (2.339 eV), while Wever and Stienkemeier measured the 0–0 transition of N–N-dimethyl PBI in He-droplets at 486 nm (2.553 eV). The difference of about 0.2 eV within the experimental spectra may result from the different temperatures, solvent effects, or the influence of substituents. Because we performed the computations of single molecules without considering environmental (solvent) effects, we chose the values of Wever and Stienkemeier as our reference, i.e., a 0–0 transition at 2.553 eV. In the following, we focus on the $S_0 \rightarrow S_1$ transition because the vertical energy of the S_2 state is about 1 eV higher. Furthermore, the corresponding transition moment vanishes.

From our experience, also the range-separated ωB97X-D functional should give reliable results for perylene systems.[74,80–82] In contrast, the B3LYP functional that is very often used for the computations of excited states was less accurate and tends to underestimate the excitation energies of CT states.[28,81,83] Comparing computed vertical excitation energies obtained for vacuum with measured 0–0 energies in He-droplets, B3LYP/TZVP deviates by only −0.122 eV. The discrepancies for SCS-CC2/SVP (+0.418 eV) and ωB97X-D/cc-pVDZ (+0.287 eV) are considerably larger. The picture changes if vibrational effects are included and the transitions between the lowest vibrational states of ground and excited states (0–0 transition) are compared. While the discrepancies between the SCS-CC2/SVP and ωB97X-D/cc-pVDZ values and their experimental counterparts decrease to +0.143 eV and +0.008 eV, respectively, the values obtained with B3LYP/TZVP are too low by about 0.3 eV.

The error found for SCS-CC2 decreases to −0.010 eV if the larger TZVPP basis is employed, i.e., SCS-CC2 shows a much improved description with larger basis sets. In contrast, for ωB97X-D/cc-pVDZ, we find an error compensation because the agreement to the experimental result of 2.553 eV slightly deteriorates if the basis sets are enlarged (Table II). Comparing the results obtained with the cc-pVDZ basis with those computed with the improved aug-cc-pVDZ basis sets, the 0–0 excitation energy decreases to 2.49 eV, i.e., the deviation from the experimental result increases to about 0.06 eV. The same trend is also found for other larger basis sets. Hence, at least for PBI, ωB97X-D/cc-pVDZ represents an excellent choice for the description of the electronic states. The agreement is much better than expected because various benchmarks indicate larger error bars for the computations of excitation energies of organic molecules.[84,85]

The variations going from vertical to vibrationally-resolved excited state estimations mainly result from the relaxation energies of the first excited state $[E_{S_1}(R_{S_1}) - E_{S_1}(R_{S_0})]$, which amount to 0.14 eV–0.21 eV depending on the employed method. This explains the distinct vibrational progression found in experimental absorption and emission spectra. Figure 3(b) gives an enlarged description of the geometrical structure difference between the equilibrium geometry of the S_0 state to that of the S_1 state. Note that the sum of all variations is less than 0.005 Å. Table I clearly shows that the small deviations between theoretical B3LYP/TZVP vertical energies and experimental 0–0 energies stem from error compensation. In comparison to the more accurate approaches, B3LYP underestimates the excitation energies by about 0.4 eV–0.5 eV. This error is partly compensated by the neglect of the relaxation energy of the excited state (0.15 eV–0.2 eV). For SCS-CC2/SVP, the

TABLE I. Comparison of computed and measured excitation energies for a PBI monomer.

	B3LYP/ TZVP	ωB97X-D/ cc-pVDZ	SCS-CC2/ SVP	SCS-CC2/ TZVPP	Reference 44	Reference 45
E_{vert} (eV)[a]	2.431	2.840	2.971	2.810[b]		
E_{adi} (eV)[c]	2.289	2.631	2.766	2.613[b]		
E_{relax} (eV)[d]	0.143	0.209	0.205	0.197		
ZPE (eV)[e]	0.030	0.070				
0–0 (eV)[f]	2.259	2.561	2.696[g]	2.543[g]	2.339	2.553
E_{corr} (eV)[h]	0.172	0.279	0.275			

[a]Vertical excitation energy.
[b]Single point computation on the SCS-CC2/SVP geometrical structure.
[c]Adiabatic excitation energy.
[d]Relaxation energy of the excited state ($E_{vert}-E_{adi}$).
[e]Energy correction due to zero-point vibrational effects.
[f](0–0) excitation energy.
[g]Using the ZPE of ωB97X-D/cc-pVDZ.
[h]Total correction ($E_{vert}-E_{0-0}$).

The Journal of Chemical Physics ARTICLE scitation.org/journal/jcp

TABLE II. Influence of functionals and basis sets on the computed excitation energies for the S_1 state of a PBI monomer. For more explanations, see Table I and the text.

	ωB97X-D/ cc-pVDZ	ωB97X-D/ aug-cc-pVDZ	ωB97X-D/ 6–311++G(d,p)	ωB97X-D/ def2-TZVP	ωB97X-D/ def2-TZVPP
E_{vert} (eV)[a]	2.840	2.763	2.801	2.814	2.811
E_{adi} (eV)[b]	2.631	2.554	2.587	2.596	2.593
0–0 (eV)[c]	2.561	2.494	2.511	2.510	2.512

	B3LYP/ cc-pVDZ	CAM-B3LYP/ cc-pVDZ	M06-2X/ cc-pVDZ	LC-ωHPBE/ cc-pVDZ
E_{vert} (eV)[a]	2.414	2.803	2.820	3.160
E_{adi} (eV)[b]	2.297	2.602	2.620	2.878
0–0 (eV)[c]	2.226	2.531	2.546	2.803

	B3LYP/ def2-TZVPP	CAM-B3LYP/ def2-TZVPP	M06-2X/ def2-TZVPP	LC-ωHPBE/ def2-TZVPP
E_{vert} (eV)[a]	2.383	2.766	2.789	3.118
E_{adi} (eV)[b]	2.262	2.556	2.580	2.831
0–0 (eV)[c]	2.174	2.468	2.489	2.744

[a]Vertical excitation energy.
[b]Adiabatic excitation energy.
[c](0–0) excitation energy.

vertical excitation energies do not coincide with the experimental 0–0 transition because no error compensation takes place. Remaining deficiencies in the basis set (SVP vs TZVPP) even lead to an overestimation of the vertical energies by about 0.1 eV–0.2 eV. Assuming SCS-CC2/TZVPP results as a reference value, the ωB97X-D functional overestimates the vertical excitation energies by less than +0.1 eV. These estimates are in good agreement with previous investigations of perylenetetracarboxylic dianhydride (PTCDA) single crystals.[29,32,64]

Table S1 shows the results of extended computations employing additional functionals and basis sets, and Table II summarizes the influence of the basis set size for ωB97X-D and the influence of the functionals for the smallest (cc-pVDZ) and the largest basis sets (def2-TZVPP). Comparing the vertical excitation energies obtained for the def2-TZVPP basis sets, B3LYP (2.383 eV) gives the lowest value. The B3LYP excitation energy differs by about 0.74 eV from the excited state energy obtained for LC-ωHPBE (3.118 eV). The ωB97X-D functional, which seemed to be quite accurate according to the comparisons given in Table I, predicts a value of 2.811 eV, which is 0.045 eV higher than that of CAM-B3LYP (2.766 eV), the long-range corrected version of B3LYP. The M06-2X functional lies in between (2.789 eV). Comparing the 0–0 transitions with the corresponding experimental values (Table I, 2.553 eV), ωB97X-D/def2-TZVPP shows the best agreement (−0.041 eV deviation from the experimental value of Ref. 45). CAM-B3LYP/def2-TZVPP and M06-2X/def2-TZVPP give comparable deviations (−0.085 eV and −0.064 eV, respectively). As already discussed above, B3LYP/def2-TZVPP considerably underestimates the experimental value by 0.379 eV, and PBE0 behaves rather similar, while LC-ωHPBE/def2-TZVPP overestimates the experimental value by 0.191 eV.

Tables II and S1 also show interesting trends with respect to basis sets' selection. Going from larger basis sets to the double-zeta cc-pVDZ basis set, which represent the smallest employed basis sets, the computed 0–0 excitation energies increase irrespective of the used functionals. However, the increments are less than 0.1 eV in all cases. This shows that the neglect of vibrational effects is a more severe approximation than the use of smaller basis sets. The aug-cc-pVDZ basis sets are well adapted to the description of electronically excited states, and indeed, the corresponding 0–0 excitation energies are slightly lower than the ones obtained with the def2-TZVPP basis sets. However, for the most reliable functionals (ωB97X-D, CAM-B3LYP, and M06-2X), the predicted values become too low in comparison to the experimental value of 2.553 eV. In summary, the best agreement is found for M06-2X/cc-pVDZ, which only deviates by 56 cm^{-1} (0.007 eV). ωB97X-D/cc-pVDZ underestimates the experimental value by 65 cm^{-1} (0.008 eV).

Note that while ωB97X-D/cc-pVDZ predicts the 0–0 excitation energy rather accurately, a comparison with the SCS-CC2 benchmark values indicates that it seems to overestimate the relaxation energy by about 4%. As indicated by the even larger relaxation energies obtained with larger basis sets (Table II), the choice of the relatively small cc-pVDZ basis set again tends to improve the performance of the method.

Figure 4 depicts a comparison of computationally modeled and experimental absorption spectra. We present the spectrum obtained

The Journal of Chemical Physics ARTICLE scitation.org/journal/jcp

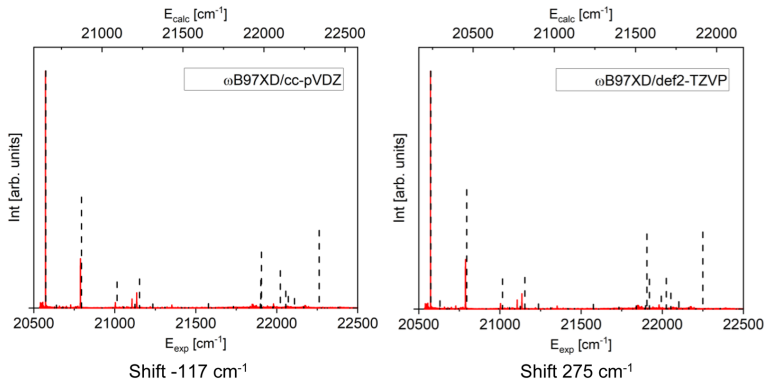

FIG. 4. Comparison of the experimental (red full lines) and computed (black dashed line) S_0–S_1 absorption spectra of the PBI monomer. The computed spectra were shifted by −117 cm^{-1} and 275 cm^{-1}, respectively, so that the 0–0 lines of experiment and theory coincide. The computed intensities are adjusted with respect to the experimental 0–0 transition intensity; however, the intensities cannot be compared due to experimental reasons. For more information, see the text.

within the ωB97X-D/cc-pVDZ ansatz as an example. To simplify the comparison, the computed spectra were shifted so that the 0–0 lines of experiment and theory coincide. Furthermore, the computed intensities were adjusted with respect to the experimental 0–0 transition intensity. The overall agreement in the energetic positions of the quantized absorption peaks is excellent. As mentioned by Wewer and Stienkemeier,[45] the intensities in their laser induced fluorescence spectra do not agree with absorption spectra, which are simulated in our theoretical approach. It is obvious that the sizes of the employed AO basis sets do not have a relevant influence on the accuracy of the computational prediction.

Table III and Fig. 5 extend our investigations to the DIP molecule. Table III summarizes the computed data and compares the 0–0 band of the $S_0 \rightarrow S_1$ transition with the energy of the lowest band of the experimental absorption spectrum, measured in acetone at room temperature.[87] Figure 5 compares the stick spectrum and a convoluted version of the computed vibrational transitions with the measured absorption spectrum. The computed data are shifted by 0.04 eV to match the maximum of the energetically lowest peak in the absorption spectrum. More information is given in the supplementary material. For the DIP monomer, the S_2 state is only slightly higher in energy than the S_1 state. Nevertheless, it can be omitted in regard to the assignment of the absorption spectrum as the $S_0 \rightarrow S_2$ transition is symmetry forbidden.[88] S_3 will also not contribute because it is too high in energy and the computed transition dipole moment vanishes.[88] We combine the ωB97X-D/cc-pVTZ approach with a (non-equilibrium) continuum-solvation approach to account for solvent effects (acetone) in the absorption spectrum. We predict the 0–0 band of the S_0–S_1 excitation at 2.38 eV, which is in excellent agreement with the energetically lowest peak of the experimental absorption spectrum of the monomer (2.35 eV). The corresponding vertical energies are predicted at about 2.7 eV, underlining that the neglect of vibrational effects leads to a blue shift in the absorption spectrum of 0.32 eV in vacuum and 0.34 eV in acetone. Table III shows that for vacuum and acetone, the strongest contributions to the difference between vertical excitation energies and the 0–0 peak result from the geometrical relaxation into the S_1 geometry (0.24 eV–0.25 eV). Variations in the zero-point energies (ZPEs) of both electronic states are about 0.1 eV, i.e., they further decrease the excitation energy. All other contributions to the

TABLE III. Monomer calculations on the $S_0 \rightarrow S_1$ transition of DIP. All energies are given in eV. For more explanations, see Table I and the text.

				Acetone		
Solvent	Vacuum			Eq.	Non-eq.	
Method	ωB97X-D		SCS-CC2	ωB97X-D		
Basis sets	cc-pVDZ		cc-pVTZ			Experiment
E_{vert} (eV)[a]	2.80	2.77	2.72		2.72	
E_{adi} (eV)[b]	2.59	2.53		2.29	2.47	
E_{relax} (eV)[c]	0.21	0.24		0.42	0.24	
ZPE (eV)[d]	0.11	0.10		0.09		
0–0 (eV)[e]	2.48	2.43		2.20	2.38[f]	2.35
E_{corr} (eV)[g]	0.32	0.34		0.51	0.34	

[a]Vertical excitation energy.
[b]Adiabatic excitation energy.
[c]Relaxation energy of the excited state (E_{vert}−E_{adi}).
[d]Energy correction due to zero-point vibrational effects.
[e](0–0) excitation energy.
[f]Calculated with the equilibrium ZPE since frequency calculations are not feasible in non-equilibrium solvation.
[g]Total correction (E_{vert}−E_{0-0}).

The Journal of Chemical Physics ARTICLE scitation.org/journal/jcp

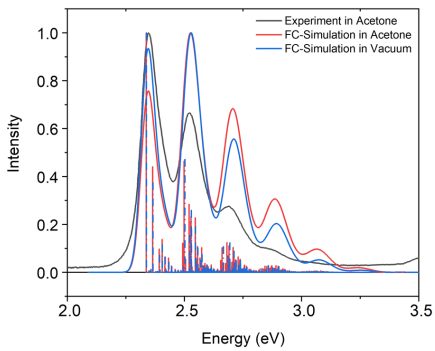

FIG. 5. The monomer $S_0 \rightarrow S_1$ absorption spectrum of DIP (ωB97X-D/cc-pVTZ): The black full line shows the experimental data (in acetone).[86] The computational estimate in acetone is given in red (stick spectrum and its Gaussian convolution, FWHM = 500 cm^{-1}). For a better comparison, these theoretical data were shifted by 0.04 eV so that the energetically lowest peak of the theoretical and experimental spectra coincides. The corresponding data in blue give the computational results in vacuum. These datapoints are shifted by 0.14 eV.

0–0 energies are smaller. The reduction in the basis set's size from valence triple-zeta (cc-pVTZ) to valence double-zeta (cc-pVDZ) seems to introduce an error of 0.06 eV. In contrast to PBI, an increase in the basis sets slightly improves the agreement with the experimental values for DIP. Using the wave function based SCS-CC2 approach in combination with the cc-pVTZ basis set, the computed excitation energies change by only about 0.05 eV. In summary, as for PBI, the explicit consideration of the photo-induced relaxation of the geometry (vertical excitation vs adiabatic excitation) introduces the strongest shift in the computed excitation energies.

Figure 5 shows the vibrational structure of the theoretical absorption spectra in acetone (red) or vacuum (blue) at T = 0 K and the experimental spectrum.[86] For the corresponding convolution with a Gaussian, we used a FWHM of 500 cm^{-1} because it seemed to reflect the overall shape of the bands better than, for example, a FWHM of 270 cm^{-1}, which is the default option in the Gaussian16 program. Decreasing the FWHM introduces additional features in the envelope of the first band, which are not found in the experimental spectra (Figs. S1 and S2). However, while the computed energy spacings between the first two bands and their widths agree quite nicely with the experimental results, the intensity ratio between the two lowest energy (highest intensity) bands is predicted less well (Fig. 5). The experimental measurements find a decrease in intensity with an increase in energy. In contrast, the lowest band has less intensity than the next higher one in the computed spectrum. This erratic intensity ratio is found for the theoretical spectra in vacuum and even stronger in acetone. Thus, while ωB97X-D/cc-pVTZ reproduces the excitation energy quite accurately, it overestimates the relaxation of the DIP molecule due to excitation in the S_1 state. The amount of which the relaxation of the excited state is overestimated can be assessed by approximating the potentials of the ground end excited states by shifted harmonics. Then, the intensity I_n of the vibrational line n is given by a Poisson distribution $\left(I_n = \frac{S^n}{n!}e^{-S}\right)$, with the Huang–Rys parameter $S = \frac{1}{2}(\Delta u)^2$. Here, Δu is the difference between the equilibrium distances in dimensionless coordinates.[89] With the observed intensity patterns, it results that ωB97X-D/cc-pVTZ overestimates the structural change in the excited state (Δu) by about 20%. This seems sufficiently small to employ this model for the qualitative analysis of the excited states shown below. Furthermore, as discussed in the supplementary material, the shape of the theoretical spectrum changes by modifying the FWHM of the Gaussian convolution or by including temperature effects (Fig. S2), while the Herzberg–Teller correction is hardly significant (Fig. S3).

The corresponding data for the PDIR-CN_2 molecule are given in the supplementary material (Table S2, Fig. S4). We find the same trends as already discussed for PBI and DIP. Similar performance of the quantum chemical models for these molecules could be expected since the electronic excitations are dominated by the perylene core.[28,65] However, in a recent study, we also find comparable relaxation effects for tetracene, which represents a considerably larger molecule.[90]

Intra-monomer relaxation effects in aggregate structures

The above-mentioned monomer relaxation effects of 0.2 eV –0.4 eV raise the question how distortions of the monomer geometry (intra-monomer relaxation) influence the photophysical behavior of organic semiconductors. The Davidov splitting in such molecular aggregates is often in a similar range. Previous computational investigations often neglect intra-monomer relaxation effects since full optimizations of aggregates are too time-consuming if sufficiently accurate approaches are employed. Hence, to make the computations feasible, the frozen-monomer approximation has often been used. In this approximation, the geometries of the monomers are fixed to their S_0 equilibrium structures. Using these frozen monomers, the potential energy surfaces are computed as a function of the inter-monomer geometrical parameters to model inter-monomer relaxation effects. The inter-monomer parameters are shown in Fig. 3(a). To investigate how inclusion of intra-monomer effects changes the figure, we utilized the PBI-dimer for model calculations. For this model, we took various relative orientations of the monomers in the dimer and characterized the intra-monomer relaxation by distorting each monomer independently from the equilibrium structure of the ground state of the monomer $\vec{R}(S_0)$ to the equilibrium structure of the first excited state of the monomer $\vec{R}(S_1)$. We performed the computations for the vacuum case, an almost nonpolar environment with a high refractive index (ε = 5 and ε_{inf} = 4.45) and water (ε = 78.355 and ε_{inf} = 1.776) to investigate the influences of polarizable environments. However, since the comparison of the corresponding PESs (Fig. S5) shows very small changes when changing the polarity of the environment, we focus the discussion on the values obtained for the almost nonpolar medium.

Figure 6 summarizes the PESs of the various states as a function of distortions of the monomers. To differentiate between the

The Journal of Chemical Physics ARTICLE scitation.org/journal/jcp

electronic dimer and monomer states, the dimer states are abbreviated as D_0–D_3, where D_0 represents the singlet ground state of the dimer, while D_n stands for its n-th excited singlet state. The white lines are given for a better overview. Within the figures, the abscissa and ordinate depict the distortion of the monomers. Moving along the lowest horizontal white line of the PESs, one monomer remains fixed at its ground state geometry, while the other monomer varies its geometry from $\vec{R}_{-0.5} = \vec{R}(S_0) + (-0.5)\Delta\vec{R}$ to $\vec{R}_{1.5} = \vec{R}(S_0) + 1.5\Delta\vec{R}$ [Eq. (1)]. In Eq. (1), $\Delta\vec{R} = \vec{R}(S_0) - \vec{R}(S_1)$ represents the difference between the equilibrium structures of the monomer in its ground and first excited singlet states. Consequently, $\vec{R}(S_0)$ is related to $\chi = 0.0$, while $\vec{R}(S_1)$ corresponds to $\chi = 1.0$. Along the left vertical white line, the structure of the other monomer changes. The PES must be symmetric due to the symmetry of the system [Fig. 3(a)]. Along the diagonal, both monomers are equally distorted so that the exciton must be completely delocalized over the whole dimer. In the outer diagonal parts, both monomers are differently distorted so that the exciton can localize on one monomer. Single points on the PESs are designated as $[\vec{R}_A; \vec{R}_B]$ where the structure of the first monomer is $\vec{R}(S_0) + A\Delta\vec{R}$, while the second monomer's geometry is $\vec{R}(S_0) + B\Delta\vec{R}$.

To make the small variations visible, we choose contour lines with an energy difference of only 0.02 eV. All energies are given with respect to the equilibrium geometry of the ground state, and all dimer structures have a vertical (molecular plane to plane) distance of R_Z = 3.31 Å [Fig. 3(a)]. All calculations were performed with the ωB97X-D/def2-TZVP approach. Previous investigations show that the dimer is additionally stabilized by small transversal shifts (R_L) or alternatively by a torsion of both monomers with respect to each other.[13,27] Nevertheless, in the scope of the present work, we only vary the longitudinal shift and the distance between the two monomers. Figures 6 and 7 compare the energies and the properties of the various dimer states at their optimal R_L orientations. Note that the optimal R_Z value is 3.31 Å for all states. This comparison allows us to differentiate between intra- and inter-monomer relaxation effects. Figures 8 and 9 focus on the differences in the behavior of the D_1 and D_2 states for the same inter-monomer orientations (the same R_L and R_Z values).

As expected, the minimum of the D_0 surface (Fig. 6, top left) is found if both monomers adopt essentially the monomer ground state geometry. The small elongation of the equilibrium bond distance in the direction of the excited state indicates that the

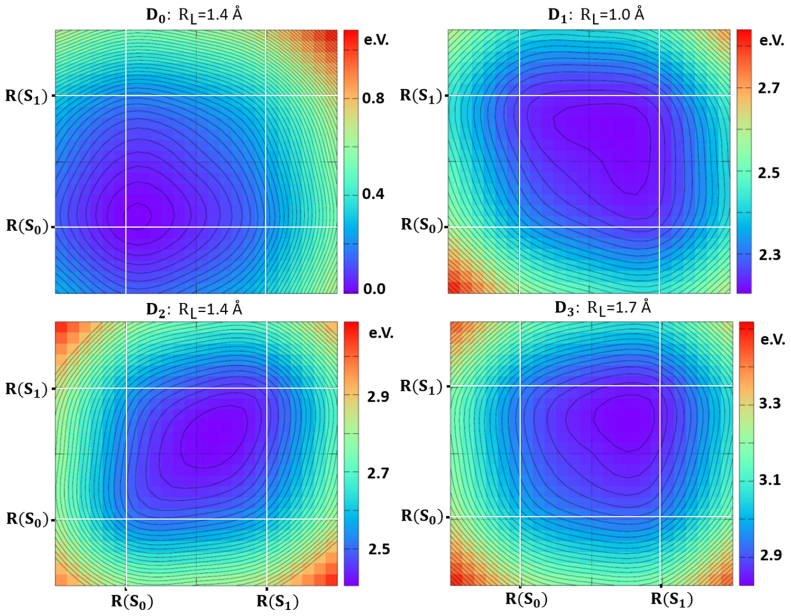

FIG. 6. PES as a function of the monomer distortions computed for a monomer distance of 3.31 Å and the optimal longitudinal shift R_L for the respective electronic state. The energy color code is given on the left side of each PES. The energy difference between two contour lines is 0.02 eV. $R(S_0)$ and $R(S_1)$ denote equilibrium geometries for the monomer in its ground (S_0) and first excited states (S_1), respectively. The white lines are given for a better overview. For more information, see the text.

The Journal of Chemical Physics ARTICLE scitation.org/journal/jcp

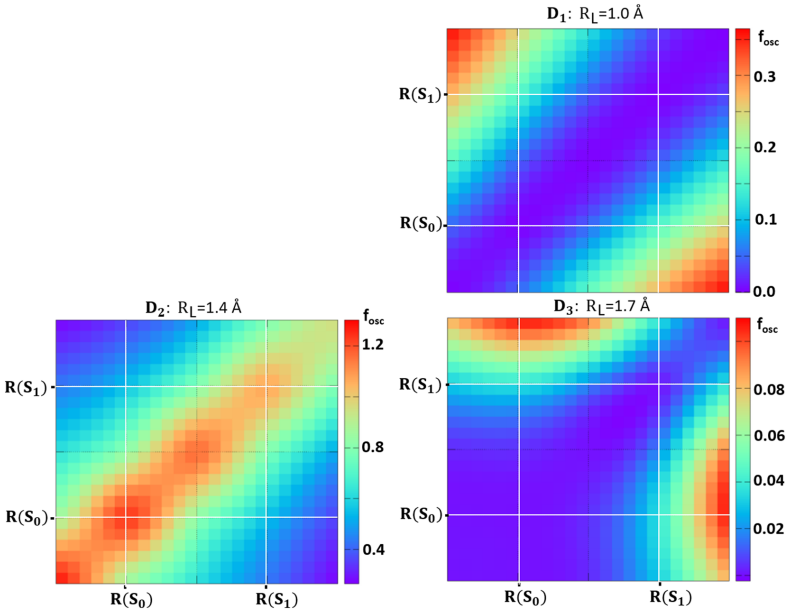

FIG. 7. Variation in the oscillator strength f_{osc} (a.u.) as a function of the monomer distortions computed for a monomer distance of 3.31 Å and the optimal longitudinal shift R_L for the given electronic state. The color code for f_{osc} is given on the left side of each surface. $R(S_0)$ and $R(S_1)$ denote equilibrium structures for the monomer in its ground and first excited states, respectively. The white lines are given for a better overview. For more information, see the text.

interaction of the two monomers tends to promote electrons from the HOMO of one monomer into the LUMO of the other one and vice versa. Thus, both monomers are partially excited due to the interaction with the other one, which introduces the observed departure of the dimer equilibrium geometry from the monomer values. However, the energy lowering with respect to the monomer structure amounts to only about 0.02 eV, which is hardly significant. For the D_1 state, our computations predict different inter- and intra-monomer geometries compared to the ground state. The optimal inter-monomer orientation for the ground state is found at R_L = 1.4 Å, whereas R_L = 1.0 Å gives the lowest computed energy for the first excited state. In the D_1 state, the optimal intra-monomer geometry is at $[\vec{R}_{0.7}; \vec{R}_{0.7}]$. This indicates that an exciton that is delocalized over a dimer influences the geometry of the single monomers less than it is found for the S_1 state of the monomer. This is in line with the work of Harbach and Dreuw on the CO dimer.[42] In the CO dimer, the CO distance of the dimer D_1 state is 1.1875 Å, which lies between the distance found for S_0 (1.126 Å) and S_1 (1.222 Å) of the monomer. In terms of the χ-parameter, they obtain a value of 0.65, which is surprisingly close to our value of 0.7. Figure 6 also reveals that the D_1-PES shows a curved valley ranging from $[\vec{R}_{0.7}; \vec{R}_{0.3}]$ over $[\vec{R}_{0.7}; \vec{R}_{0.7}]$ to $[\vec{R}_{0.3}; \vec{R}_{0.7}]$. In this range, the energy varies by less than 0.02 eV, i.e., all structures are virtually isoenergetic. For the vertical energy of the D_1 state at the structure $[\vec{R}_{0.0}; \vec{R}_{0.0}]$ and R_L = 1.0 Å, we compute an excitation energy of 2.452 eV. Intermolecular relaxation along the longitudinal axis to R_L = 1.0 Å decreases the excitation energy to 2.360 eV (E_{relax}^{inter} = 0.09 eV). Adding the intra-monomer relaxation ($[\vec{R}_{0.0}; \vec{R}_{0.0}]$ to $[\vec{R}_{0.7}; \vec{R}_{0.7}]$) for R_L = 1.0 Å, the excitation energy drops to 2.225 eV, i.e., E_{relax}^{intra} amounts to 0.135 eV. Hence, the intra-monomer relaxations are slightly larger than the inter-monomer ones. However, for the former, we only included one degree of freedom, while all possible relaxations are included in the latter. Note that E_{relax}^{intra} computed for the dimer (0.135 eV) is smaller than the variation found for the monomer (Table I; 0.201 eV).

For the D_2 state, inter- and intra-monomer effects differ from those computed for the D_1 state. The optimal R_L value for D_0 and D_2 is equal, i.e., inter-monomer relaxation effects vanish. Furthermore, the minimum of the D_2-PES lies along the diagonal, i.e., structures with equally distorted monomers are favored with respect to those with unequally distorted monomers. The intra-monomer relaxation effects for the D_2 state are computed to be 0.13 eV. As

The Journal of Chemical Physics ARTICLE scitation.org/journal/jcp

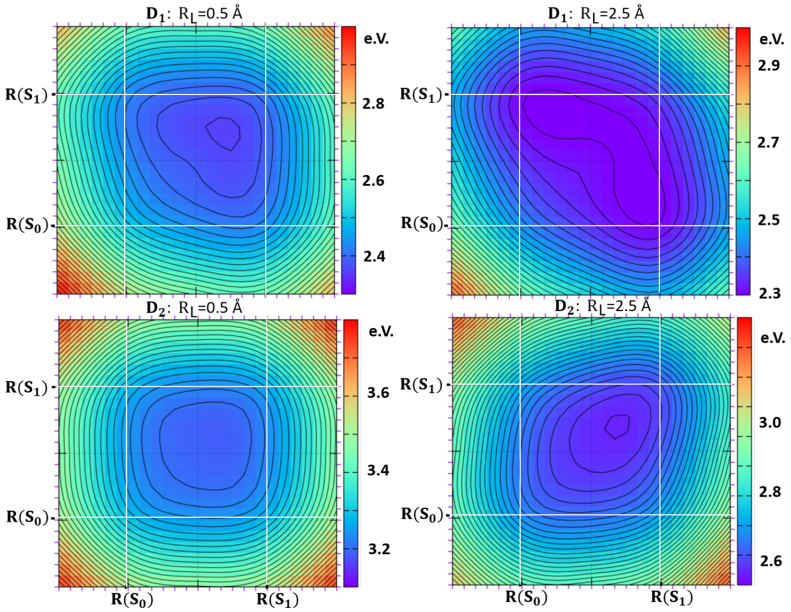

FIG. 8. Comparison of the PESs obtained for the longitudinal shifts R_L = 0.5 and 2.5 Å. The horizontal distance between both monomers is always 3.31 Å. The energy color code is given on the left side of each PES. The energy difference between two contour lines is 0.02 eV. $R(S_0)$ and $R(S_1)$ denote equilibrium structures for the monomer in its ground and first excited states, respectively. The white lines are given for a better overview. For more information, see the text.

for the D_1 state, the monomers do not fully relax to the S_1 geometry of the monomer. The minimum ranges from about $[\vec{R}_{0.5}; \vec{R}_{0.5}]$ to $[\vec{R}_{0.7}; \vec{R}_{0.7}]$ instead.

The shape of the intra-monomer PES of the D_3 state seems to be a mixture of shapes of the D_1 and D_2 states. However, while D_1 and D_2 possess mainly Frenkel character, the D_3 represents a CT state. Hence, to describe its intra-monomer relaxation effects, we would have to distort the monomers to the anionic and cationic structures rather than to the S_1 structures of the monomers. Since these additional variations are out of the scope of the present work, we will focus in the following on D_1 and D_2 states of the dimer.

The PES of the D_1 states possesses a broad minimum, which comprises unequally distorted monomers and equally distorted monomers. For the latter, the exciton must be completely delocalized due to symmetry reasons. Since unequally distorted monomers can induce exciton localization, it is of interest to investigate the variation in the P_R value obtained from the TheoDORE program. The P_R value differentiates between completely delocalized (P_R = 2.0) and localized (P_R = 1.0) excitons. Hence, for equally distorted monomers, P_R = 2 is obtained due to the symmetry. The P_R value for $[\vec{R}_{0.3}; \vec{R}_{0.7}]$ is about 1.9, showing that excitons remains mainly delocalized in the range of the curved valley of the D_1 state. For the D_2 state, the minimum runs along the diagonal, and therefore, the excitons are also delocalized.

Another property that differentiates between localized and delocalized excitons is the oscillator strength f_{osc}. For a completely delocalized exciton, f_{osc} should vary roughly between twice the monomer value and zero. For completely localized excitons, all oscillator strengths should resemble the monomer values. For example, for an H-aggregate, the D_1 state should be dark (f_{osc} = 0) if the exciton is delocalized. If the exciton starts to localize, the oscillator strength of D_1 should increase to the limit of the oscillator strength of the S_1 monomer state. The corresponding data are summarized in Fig. 7. Indeed, for the D_1 state, f_{osc} vanishes for equally distorted monomers. For unequally distorted ones, the values smoothly increase. For the D_2 state, the opposite is found. The variations found for D_3 resemble the behavior expected for a CT state.

In the vibronic coupling theory, the relative size of the Davydov splitting with respect to the monomer relaxation energy determines whether an asymmetrical distortion of both monomers will take place or not. The monomer relaxation energy within the pJT framework is related to the size of the vibronic interactions.[42,43]

The Journal of Chemical Physics ARTICLE scitation.org/journal/jcp

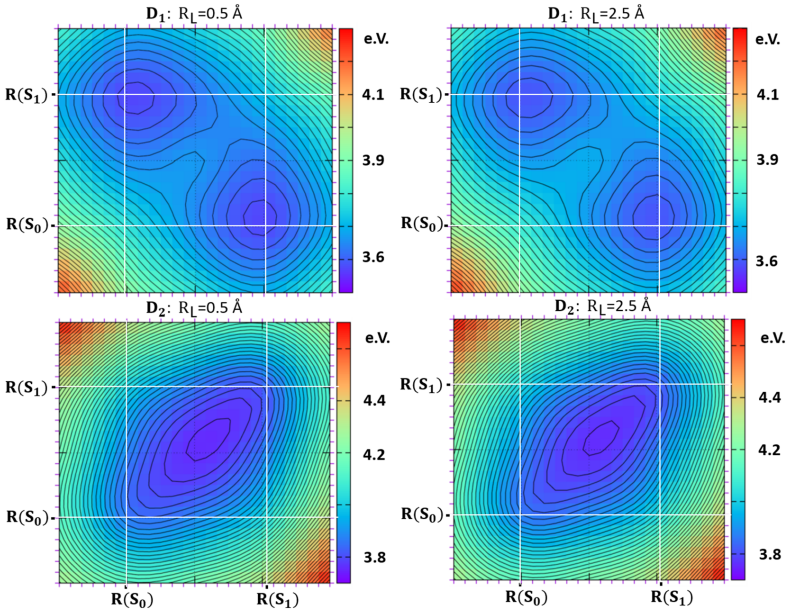

FIG. 9. Comparison of the PESs obtained for the longitudinal shifts of R_L = 0.5 and 2.5 Å. The horizontal distance between both monomers is always 5.0 Å. The energy color code is given on the left side of each PES. The energy difference between two contour lines is 0.02 eV. $R(S_0)$ and $R(S_1)$ denote equilibrium structures for the monomer in its ground and first excited states, respectively. For more information, see the text.

Figures 8 and 9 investigate these interplays. We compare the situations obtained for R_L = 0.5 Å and R_L = 2.5 Å in Figs. 8 and 9. The horizontal distance between both monomers (R_Z) is 3.31 Å in Fig. 8. Thus, the coupling is stronger but should vary due to the variation in R_L. The coupling J is given as half of the energy difference between D_1 and D_2 ($\Delta E = 2$ J) for equally distorted monomers. Using this relationship, for R_Z = 3.31 Å and R_L = 0.5 Å, our computations predict a coupling of 0.43 eV for $[\vec{R}_{0.0}; \vec{R}_{0.0}]$ and 0.39 eV $[\vec{R}_{1.0}; \vec{R}_{1.0}]$. We compute a coupling of 0.12 eV for both monomer relaxations for R_Z = 3.31 Å and R_L = 2.5 Å, i.e., the coupling is indeed smaller. Figure 8 shows that this variation in the coupling influences the shapes of the PESs, but the overall energy variations are small. Figure S6 gives the f_{osc} values. They show that even for $[\vec{R}_{0.5}; \vec{R}_{1.0}]$, f_{osc} behaves as expected for an H-aggregate (R_L = 0.5 Å) or a J-aggregate (R_L = 2.5 Å), showing the excitons to be still delocalized.

For R_Z = 5.0 Å, the coupling is only 0.04 eV–0.05 eV for R_L = 0.5 Å and 0.03 eV for R_L = 2.5 Å. The considerably smaller couplings are reflected in the PES shapes, as given in Fig. 9. The PESs of the D_1 state possess two distinct minima at $[\vec{R}_{1.0}; \vec{R}_{0.0}]$ and $[\vec{R}_{0.0}; \vec{R}_{1.0}]$ for which one monomer remains at the ground state structure, while the other relaxes to the S_1 monomer structure. The exciton is strongly localized in these positions at the relaxed monomer as shown by the computed P_R value of 1.08. Hence, the system represents a localized exciton on the relaxed monomer, which is weakly perturbed by the non-excited PBI monomer at the distance of 5 Å for both minima. For R_L = 0.5 Å, the intra-monomer relaxation energy (E_{relax}) is 0.204 eV, while 0.216 eV is computed for R_L = 2.5 eV. We included environmental effects for these calculations. The corresponding vacuum environment data are 0.143 eV for R_L = 0.5 Å and 0.155 eV for R_L = 2.5 Å. Both values are smaller than E_{relax} calculated for the monomer in vacuum (0.218 eV in Table II; ωB97X-D/def2-TZVP). This implies that the disturbed, non-excited monomer slightly decreases the relaxation energy, while a polarizable environment leads to a small increase. Our computations show the well-known double-well potential of the Marcus theory or of a pJT-surface with a strong vibronic coupling for the PESs of the D_1 state. The computations also show that an estimate of the barrier height based on the unrelaxed geometry $[\vec{R}_{0.0}; \vec{R}_{0.0}]$ leads to an overestimation thereof. The barrier height is estimated at 0.20 eV for R_L = 0.5 Å if $[\vec{R}_{0.0}; \vec{R}_{0.0}]$ is taken as top of the barrier. The value reduces to only about 0.09 eV if the optimal arrangement ($\approx[\vec{R}_{0.7}$;

The Journal of Chemical Physics ARTICLE scitation.org/journal/jcp

$\vec{R}_{0.7}$]) is used. The corresponding values for R_L = 2.5 Å are 0.22 eV (via [$\vec{R}_{0.0}$; $\vec{R}_{0.0}$]) and 0.08 eV (via [$\vec{R}_{0.7}$; $\vec{R}_{0.7}$]).

The shapes of the PESs of D_1 and D_2 differ considerably for R_Z = 3.31 Å and 5.0 Å. Especially the computed shapes for 5.0 Å nicely reflect the 1D potential curves given by Marcus theory for ground and excited states of weakly interacting monomers or that of a pJT effect with strong vibronic coupling. In Fig. 9, the D_1 state exhibits the double-well potential if both minima are connected, while the shape of D_2 along this coordinate is harmonic. A very similar potential was obtained by Garcia-Fernandez *et al.* for the benzene dimer in D_{6h} symmetry at a distance of 5 Å, emphasizing the generality of our results.[43] As in the Marcus theory picture, the difference between D_1 and D_2 in our model results from the required orthogonality between two solutions of a Hermitian operator such as the electronic Hamilton operator. The exciton is localized on the relaxed monomer for the minimum of the D_1 state at [$\vec{R}_{0.0}$; $\vec{R}_{1.0}$]. Due to the required orthogonality, a localized exciton would reside on the unrelaxed monomer for D_2. If it is localized on the relaxed monomer, it would populate the S_2 state of the monomer, which is considerably higher in energy. However, if the exciton localized on the unrelaxed monomer, both monomers exhibit unfavorable geometries for this localization. Hence, the symmetrical relaxation of both monomers leading to a delocalized exciton represents the energetically most stable situation for D_2.

For our investigations on a larger cluster, we selected DIP tetramers in which the monomers take the position of the crystal structure as a first example. While the monomer positions were taken from the experimental crystal structure (CCDC code 642482),[91,92] the intra-monomer coordinates were determined by full optimizations for the S_0 and S_1 states of the DIP monomer. As for the PBI dimer, the intra-monomer geometries were varied by changing the monomer structures linearly from $\vec{R}(S_0)$ to $\vec{R}(S_1)$. The energy variations obtained for the four lowest electronic states of the tetramer (T_1–T_4) as a function of varying monomer geometries are collected in Fig. 10. The abscissa gives the distortion of the respective monomers toward $\vec{R}(S_1)$. To simplify the abbreviations, we introduce a different nomenclature for the tetramers. If all monomers are equally distorted, the distortion is indicated only once. For example, "1" denotes the structure in which all monomers are in the S_1 geometry, while "0.25" abbreviates the structure in which all monomers are distorted to $\vec{R}_{0.25}$ ([$\vec{R}_{0.25}$; $\vec{R}_{0.25}$; $\vec{R}_{0.25}$; $\vec{R}_{0.25}$] in dimer notation). For differently distorted monomers, the abbreviation denotes which one is distorted (Fig. 3). For the [0.5 0 0 0.5] monomer, 1 and 4 are distorted to $\vec{R}_{0.5}$, while 1000 and 0001 abbreviate the clusters in which monomer 1 or 4 adopts the S_1 geometry. For the cluster computations, these geometries have different energies because the corresponding monomers are not transferred into each other by a symmetry operation. Symmetrically equivalent are only monomers 1 and 2 as well as 3 and 4.

As expected, the global minimum of the tetramer ground state T_0 is obtained for "0." Distortions of the monomers toward $\vec{R}(S_1)$ increase the ground state energies. For example, for "0.25," the energy slightly increases by 0.05 eV, while an energy increase of 0.81 eV is obtained for "1." For "1000," the energy raises by 0.2 eV. The minimum of the first electronically excited tetramer state T_1 is found for the structure "0001," i.e., if monomer 4 (Fig. 3) adopts the S_1 geometry, while all other monomers remain in the ground state geometry. The excitation energy with respect to the energy of the

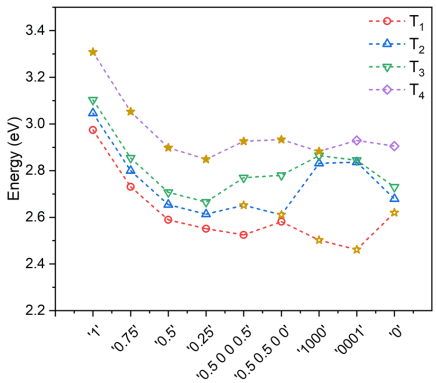

FIG. 10. Energies of the four lowest excited states of the DIP tetramer (T_1 in red, T_2 in blue, T_3 in green, and T_4 in purple) as a function of the monomer geometries (for details see text). All energies are given with respect to the energy of the equilibrium geometry of the ground state. * indicates states with considerable oscillator strengths. A full * denotes f_{osc} > 0.5, while an empty one gives f_{osc} > 0.2.

equilibrium geometry of T_0 (E_{adi}) is 2.46 eV, and the corresponding value for "1000" is 2.50 eV. The computed P_R values of 1.04 and 1.13 indicate that the unequal distortions lead to a nearly complete localization of the exciton on the distorted monomer. If all monomers are equally distorted by a quarter of the difference between S_0 and S_1 ("0.25"), E_{adi} increases to 2.55 eV. For a tetramer, P_R varies between 4 (exciton delocalized over all 4 monomers) and 1 (exciton localized on one monomer). For "0.25," the P_R value is 3.97. The P_R value differs from 4 because not all monomers are symmetrically equivalent. The comparison of the "1000," "0001," and "0.25" structures shows that for the T_1 state of the DIP tetramer, the localized structures are about 0.1 eV lower in energy than the delocalized ones. The partially localized structures "0.5 0.5 0 0" (E_{adi} = 2.58 eV) and "0.5 0 0.5 0" (E_{adi} = 2.52 eV) are similar in energy to the delocalized structures "0.25." For "0.5 0 0.5 0," we compute a P_R value of 2.09, while 3.17 was computed for "0.5 0.5 0 0." The difference arises because the exciton is delocalized over two neighbors for "0.5 0 0.5 0" but not for "0.5 0.5 0 0." The structure "0.25" is slightly lower in energy than "0.5" (E_{adi} = 2.59 eV). If the distortion increases to "0.75" and "1," the E_{adi} increases to 2.73 eV and 2.97 eV. In all cases, the P_R values are near to 4.

As for the PBI dimer, the T_2 state of the DIP tetramer adopts equally distorted structures. The same holds for the T_3 and T_4 states. For the T_2 state, the adiabatic excitation energies of the equally distorted structure "0.25" and of the partially unequally distorted structure "0.5 0.5 0 0" are 2.61 eV. However, the corresponding P_R values are only around 2, indicating that for "0.25," the exciton is not completely delocalized as found for the corresponding structure of the T_1 state. A closer inspection, indeed, showed that for the T_2 state, the exciton is only delocalized over the monomers 3 and 4. For T_3, it is delocalized over the monomers 1 and 2. Such a localization

The Journal of Chemical Physics ARTICLE scitation.org/journal/jcp

is possible because only 1 and 2 as well as 3 and 4 are symmetrically equivalent. For T_4, the exciton is again completely delocalized for "0.25." Note that the unit cell of the DIP crystal contains two monomers, i.e., also for the crystal, not all monomers are identical. The P_R value computed for the "0.5 0.5 0 0" structure of the T_2 is also lower than the corresponding value obtained for T_1. For T_3 and T_4, the "0.25" structures represent the respective minima (2.67 eV and 2.85 eV). For the T_3 state, this equally distorted structure lies about 0.2 eV below the "1000" or "0001" structures and still 0.1 eV below the structures in which only two monomers are distorted. Even the "0.5" structure is still lower than the unequally distorted structures. For the T_4 state, energy variations are smaller. The "1000" structure is in the same energy range (E_{adi} = 2.88 eV) as the equally distorted structure "0.25" (2.85 eV), while the partially unequally distorted structures "0.5 0.5 0 0" and "0.5 0 0.5 0" lie slightly higher in energy (E_{adi} = 2.93).

For the T_1 state of the DIP tetramer, the unsymmetrical distortion is clearly favored over the symmetrical one, while for the D_1 state of the PBI dimer, both structures were isoenergetic. This can be explained by the couplings for the DIP tetramer, which are expected to be smaller because the molecular planes of the monomers are tilted with respect to each other. To check if differences in the electronic structure of both molecules also contribute, we performed test computations for DIP dimers in which both monomers lie on top of each other. Based on previous investigations of the minimum structures of such dimers, we choose R_L = 1.5 Å and R_Z = 3.6 Å.[93] For this dimer, the symmetrically distorted $[\vec{R}_{0.5}; \vec{R}_{0.5}]$ structure (E_{adi} = 2.47 eV) and unsymmetrically distorted $[\vec{R}_{0.0}; \vec{R}_{1.0}]$ (E_{adi} = 2.46 eV) are again virtually identical. The corresponding values for the PBI dimer with R_L = 1.4 Å and R_Z = 3.5 Å are 2.41 eV ($[\vec{R}_{0.5}; \vec{R}_{0.5}]$) and 2.35 eV $[\vec{R}_{1.0}; \vec{R}_{0.0}]$, i.e., the variations are similar. Other structures like $[\vec{R}_{0.0}; \vec{R}_{0.0}]$ and $[\vec{R}_{1.0}; \vec{R}_{1.0}]$ are higher in energy for DIP (E_{adi} = 2.60 eV and 2.55 eV) and for PBI (E_{adi} = 2.53 eV and 2.45 eV). In both dimers, symmetrically distorted structures are favored with respect to unsymmetrical ones in the D_2 state (DIP: $[\vec{R}_{0.5}; \vec{R}_{0.5}]$ E_{adi} = 2.65 eV; $[\vec{R}_{0.0}; \vec{R}_{1.0}]$ E_{adi} = 2.75 eV; PBI: $[\vec{R}_{0.5}; \vec{R}_{0.5}]$ E_{adi} = 2.51 eV; $[\vec{R}_{0.0}; \vec{R}_{1.0}]$ E_{adi} = 2.69 eV). This comparison indicates that the favored unsymmetrically distorted monomers for the DIP tetramer mainly result from the different orientations of monomers, while differences between the electronic structure of DIP and PBI are of minor importance.

Comparing the optimized geometries of the first excited states of monomer, dimer, and tetramer, respectively, shows that the distortion relative to the ground state structure decreases. Taking the factor of 1.0 for the difference found for the monomer, for PBI, DIP, and the CO-dimer, the delocalized exciton leads to smaller distortions of 0.7, 0.65, and about 0.5. For the DIP tetramer, the structure in which each monomer is distorted by a factor of "0.25" is already lower in energy than the "0.5" geometry. This trend indicates that for the first excited states, the size of the photo-induced geometry distortions decreases with an increase in delocalization of the exciton. Indeed, the trend is supported by test calculations for a cluster consisting of 14 tetracene. In this system, the vertical excitation energy (factor 0.0) is already lower than the excitation energy to the geometry in which all monomers are equally distorted by a factor of 1/14. Computations to investigate if this is a general trend are under way.

CONCLUSIONS

In the first part of the present publication, we show that DFT-based descriptions of vibrationally resolved absorption spectra of perylene-based organic semiconductor monomers such as PBI, DIP, and PDIR-CN_2 are very accurate. The computations show that photo-induced geometrical relaxation effects are quite important and have to be included for an accurate description of the spectra. The ZPE also contributes but is of minor influence. For solvent effects, the non-equilibrium option is important. The most intensive band mainly represents the 0–0 transition. Small errors in the ratio of the intensities of the various bands indicate that the photo-induced relaxation effects are slightly overestimated. The Franck–Condon and harmonic approximations are essentially appropriate, but the inclusion of temperature (hot bands) is in some case significant.

The size of the photo-induced relaxation effects found for monomers suggested that the inclusion of intra-monomer relaxation effects is also important for the description of spectra of aggregates. Our investigations of the PBI dimer, indeed, underline their importance. The D_1 state shows the expected double well shape for larger distances for which the coupling is weaker than the intra-monomer relaxation. Therefore, the exciton localizes on one monomer. However, even in this situation, the D_2 PES exhibits the harmonic form, i.e., the exciton remains localized. The strong dependence on the state under consideration results because the wavefunctions of both states have to be orthogonal to each other for each geometry. For the optimal distance between both monomers (R_Z = 3.31 Å), the coupling is sufficiently strong that the excitons remain mainly delocalized for the D_1 as well as for D_2 states, but the differences in the shapes of both PES are obvious. Additionally, the optimal longitudinal shifts (R_L) of both states also differ. The results can be modeled by the vibronic coupling, the Marcus theory or by pJT-effect. All models represent a two-state system in which the eigenvalues are determined by an interplay between energy difference of the diagonal elements and size of the outer-diagonal elements. The pJT is closer to the physical nature of the effect. In the delocalized situation for the dimer, both monomers adopt the same structures, which lie somewhere between the S_0 and S_1 structures of the monomer. The relaxation to a localized exciton is then induced by a force, which drives one monomer toward the S_1 geometry and the other toward the S_0 geometry. Obviously, this force leads to the antisymmetric motion, which is also obtained from symmetry considerations. The Marcus theory also allows for a description of these effects; however, the underlying forces remain more abstract as only one coordinate is considered.

For the DIP tetramer, the coupling strength is smaller so that for the lowest electronically excited state T_1, the localized structure is the global minimum. In this structure, one monomer adopts the equilibrium geometry of the S_1 state of the monomer, while all other monomers remain undisturbed. Structures in which all monomers are equally distorted are more stable for the T_2–T_4 states. However, even for these states, the amount of delocalization varies. For T_2 and T_3, the exciton is only delocalized over two monomers, while it is completely delocalized for T_4. This finding emphasizes that intra-monomer relaxation effects strongly depend not only on the ratio of intra-monomer relaxation and coupling but also on the electronic state under consideration. Note that the photo-induced

The Journal of Chemical Physics ARTICLE scitation.org/journal/jcp

geometry distortions decrease if the exciton is delocalized over more and more monomers. For dimers, the distortion is smaller by a factor of 0.5–0.7 than the distortion found for the monomer. The distortions shrink to about $\frac{1}{4}$ if the exciton is delocalized over a tetramer.

AUTHORS' CONTRIBUTIONS

M.D., S.W., and D.K. performed all computations and contributed equally to this work. B.E. supervised the calculations. P.T., R.F.F., and B.E. wrote this manuscript. B.E., S.W., and P.T. thank the DFG (B.E. and S.W. in the framework of the GRK2112, P.T. for the project TE479/6-1) and D.K. thanks the Fonds der chemischen Industrie for funding.

SUPPLEMENTARY MATERIAL

See the supplementary material for further information.

DATA AVAILABILITY

The data that support the findings of this study are available from the corresponding author upon reasonable request.

REFERENCES

[1] F. Würthner, C. R. Saha-Möller, B. Fimmel, S. Ogi, P. Leowanawat, and D. Schmidt, "Perylene bisimide dye assemblies as archetype functional supramolecular materials," Chem. Rev. **116**, 962–1052 (2016).
[2] H. E. Katz, A. J. Lovinger, J. Johnson, C. Kloc, T. Siegrist, W. Li, Y.-Y. Lin, and A. Dodabalapur, "A soluble and air-stable organic semiconductor with high electron mobility," Nature **404**, 478–481 (2000).
[3] S. E. Shaheen, G. E. Jabbour, B. Kippelen, N. Peyghambarian, J. D. Anderson, S. R. Marder, N. R. Armstrong, E. Bellmann, and R. H. Grubbs, "Organic light-emitting diode with 20 lm/W efficiency using a triphenyldiamine side-group polymer as the hole transport layer," Appl. Phys. Lett. **74**, 3212–3214 (1999).
[4] C. W. Tang, "2-layer organic photovoltaic cell," Appl. Phys. Lett. **48**, 183–185 (1986).
[5] M. A. Green and S. P. Bremner, "Energy conversion approaches and materials for high-efficiency photovoltaics," Nat. Mater. **16**, 23–34 (2017).
[6] P. E. Hartnett, A. Timalsina, H. S. S. R. Matte, N. Zhou, X. Guo, W. Zhao, A. Facchetti, R. P. H. Chang, M. C. Hersam, M. R. Wasielewski, and T. J. Marks, "Slip-stacked perylenediimides as an alternative strategy for high efficiency nonfullerene acceptors in organic photovoltaics," J. Am. Chem. Soc. **136**, 16345–16356 (2014).
[7] X. W. Zhan, A. Facchetti, S. Barlow, T. J. Marks, M. A. Ratner, M. R. Wasielewski, and S. R. Marder, "Rylene and related diimides for organic electronics," Adv. Mater. **23**, 268–284 (2011).
[8] C. Huang, S. Barlow, and S. R. Marder, "Perylene-3,4,9,10-tetracarboxylic acid diimides: Synthesis, physical properties, and use in organic electronics," J. Org. Chem. **76**, 2386–2407 (2011).
[9] H. Langhals, S. Demmig, and T. Potrawa, "The relation between packing effects and solid-state fluorescence of dyes," J. Prakt. Chem. **333**, 733–748 (1991).
[10] M. C. R. Delgado, E.-G. Kim, D. A. da Silva Filho, and J.-L. Bredas, "Tuning the charge-transport parameters of perylene diimide single crystals via end and/or core functionalization: A density functional theory investigation," J. Am. Chem. Soc. **132**, 3375–3387 (2010).
[11] S. Shoaee, F. Deledalle, P. S. Tuladhar, R. Shivanna, S. Rajaram, K. S. Narayan, and J. R. Durrant, "A comparison of charge separation dynamics in organic blend films employing fullerene and perylene diimide electron acceptors," J. Phys. Chem. Lett. **6**, 201–205 (2015).
[12] S. Rajaram, R. Shivanna, S. K. Kandappa, and K. S. Narayan, "Nonplanar perylene diimides as potential alternatives to fullerenes in organic solar cells," J. Phys. Chem. Lett. **3**, 2405–2408 (2012).
[13] R. F. Fink, J. Seibt, V. Engel, M. Renz, M. Kaupp, S. Lochbrunner, H.-M. Zhao, J. Pfister, F. Würthner, and B. Engels, "Exciton trapping in π-conjugated materials: A quantum-chemistry-based protocol applied to perylene bisimide dye aggregates," J. Am. Chem. Soc. **130**, 12858–12859 (2008).
[14] I. A. Howard, F. Laquai, P. E. Keivanidis, R. H. Friend, and N. C. Greenham, "Perylene tetracarboxydiimide as an electron acceptor in organic solar cells: A study of charge generation and recombination," J. Phys. Chem. C **113**, 21225–21232 (2009).
[15] B. A. West, J. M. Womick, L. E. McNeil, K. J. Tan, and A. M. Moran, "Influence of vibronic coupling on band structure and exciton self-trapping in α-perylene," J. Phys. Chem. B **115**, 5157–5167 (2011).
[16] J. Hoche, H.-C. Schmitt, A. Humeniuk, I. Fischer, R. Mitrić, and M. I. S. Röhr, "The mechanism of excimer formation: An experimental and theoretical study on the pyrene dimer," Phys. Chem. Chem. Phys. **19**, 25002–25015 (2017).
[17] E. R. Kennehan, C. Grieco, A. N. Brigeman, G. S. Doucette, A. Rimshaw, K. Bisgaier, N. C. Giebink, and J. B. Asbury, "Using molecular vibrations to probe exciton delocalization in films of perylene diimides with ultrafast mid-IR spectroscopy," Phys. Chem. Chem. Phys. **19**, 24829–24839 (2017).
[18] C. Brückner, F. Würthner, K. Meerholz, and B. Engels, "Structure-property relationships from atomistic multiscale simulations of the relevant processes in organic solar cells. I. Thermodynamic aspects," J. Phys. Chem. C **121**, 4–25 (2017).
[19] C. Brückner, F. Würthner, K. Meerholz, and B. Engels, "Atomistic approach to simulate processes relevant for the efficiencies of organic solar cells as a function of molecular properties. II. Kinetic aspects," J. Phys. Chem. C **121**, 26–51 (2017).
[20] H. Bässler, "Charge transport in disordered organic photoconductors—A Monte-Carlo simulation study," Phys. Status Solidi B **175**, 15–56 (1993).
[21] D. Hertel and H. Bässler, "Photoconduction in amorphous organic solids," ChemPhysChem **9**, 666–688 (2008).
[22] C. Brückner, M. Stolte, F. Würthner, J. Pflaum, and B. Engels, "QM/MM calculations combined with the dimer approach on the static disorder at organic-organic interfaces of thin-film organic solar cells composed of small molecules," J. Phys. Org. Chem. **30**, e3740 (2017).
[23] T. M. Clarke and J. R. Durrant, "Charge photogeneration in organic solar cells," Chem. Rev. **110**, 6736–6767 (2010).
[24] W. L. Liu, S. Canola, A. Köhn, B. Engels, F. Negri, and R. F. Fink, "A model Hamiltonian tuned toward high level *ab initio* calculations to describe the character of excitonic states in perylenebisimide aggregates," J. Comput. Chem. **39**, 1979–1989 (2018).
[25] W. L. Liu, B. Lunkenheimer, V. Settels, B. Engels, R. F. Fink, and A. Kohn, "A general ansatz for constructing quasi-diabatic states in electronically excited aggregated systems," J. Chem. Phys. **143**, 084106 (2015).
[26] N. J. Hestand, R. V. Kazantsev, A. S. Weingarten, L. C. Palmer, S. I. Stupp, and F. C. Spano, "Extended-charge-transfer excitons in crystalline supramolecular photocatalytic scaffolds," J. Am. Chem. Soc. **138**, 11762–11774 (2016).
[27] H.-M. Zhao, J. Pfister, V. Settels, M. Renz, M. Kaupp, V. C. Dehm, F. Würthner, R. F. Fink, and B. Engels, "Understanding ground- and excited-state properties of perylene tetracarboxylic acid bisimide crystals by means of quantum chemical computations," J. Am. Chem. Soc. **131**, 15660–15668 (2009).
[28] V. Settels, W. Liu, J. Pflaum, R. F. Fink, and B. Engels, "Comparison of the electronic structure of different perylene-based dye-aggregates," J. Comput. Chem. **33**, 1544–1553 (2012).
[29] V. Settels, A. Schubert, M. Tafipolski, W. Liu, V. Stehr, A. K. Topczak, J. Pflaum, C. Deibel, R. F. Fink, V. Engel, and B. Engels, "Identification of ultrafast relaxation processes as a major reason for inefficient exciton diffusion in perylene-based organic semiconductors," J. Am. Chem. Soc. **136**, 9327–9337 (2014).
[30] A. Schubert, M. Falge, M. Kess, V. Settels, S. Lochbrunner, W. T. Strunz, F. Würthner, B. Engels, and V. Engel, "Theoretical analysis of the relaxation

The Journal of Chemical Physics ARTICLE scitation.org/journal/jcp

dynamics in perylene bisimide dimers excited by femtosecond laser pulses," J. Phys. Chem. A **118**, 1403–1412 (2014).
[31] A. Schubert, V. Settels, W. L. Liu, F. Würthner, C. Meier, R. F. Fink, S. Schindlbeck, S. Lochbrunner, B. Engels, and V. Engel, "Ultrafast exciton self-trapping upon geometry deformation in perylene-based molecular aggregates," J. Phys. Chem. Lett. **4**, 792–796 (2013).
[32] B. Engels and V. Engel, "The dimer-approach to characterize opto-electronic properties of and exciton trapping and diffusion in organic semiconductor aggregates and crystals," Phys. Chem. Chem. Phys. **19**, 12604–12619 (2017).
[33] Z. J. Chen, V. Stepanenko, V. Dehm, P. Prins, L. D. A. Siebbeles, J. Seibt, P. Marquetand, V. Engel, and F. Würthner, "Photoluminescence and conductivity of self-assembled π–π stacks of perylene bisimide dyes," Chem.-Eur. J. **13**, 436–449 (2007).
[34] S. Samanta, S. K. Ray, S. Deolka, S. Saha, K. R. Pradeep, R. Bhowal, N. Ghosh, and D. Chaudhuri, "Safeguarding long-lived excitons from excimer traps in H-aggregated dye-assemblies," Chem. Sci. **11**, 5710–5715 (2020).
[35] W. Popp, M. Polkehn, R. Binder, and I. Burghardt, "Coherent charge transfer exciton formation in regioregular P3HT: A quantum dynamical study," J. Phys. Chem. Lett. **10**, 3326–3332 (2019).
[36] R. Binder and I. Burghardt, "First-principles quantum simulations of exciton diffusion on a minimal oligothiophene chain at finite temperature," Faraday Discuss. **221**, 406–427 (2020).
[37] A. Segalina, X. Assfeld, A. Monari, and M. Pastore, "Computational modeling of exciton localization in self-assembled perylene helices: Effects of thermal motion and aggregate size," J. Phys. Chem. C **123**, 6427–6437 (2019).
[38] M. R. Talipov, M. V. Ivanov, and R. Rathore, "Inclusion of asymptotic dependence of reorganization energy in the modified Marcus-based multistate model accurately predicts hole distribution in poly-*p*-phenylene wires (vol 120, pg 6402, 2016)," J. Phys. Chem. C **120**, 10720 (2016).
[39] R. L. Fulton and M. Gouterman, "Vibronic coupling. 1. Mathematical treatment for 2 electronic states," J. Chem. Phys. **35**, 1059 (1961).
[40] R. L. Fulton and M. Gouterman, "Vibronic coupling. 2. Spectra of dimers," J. Chem. Phys. **41**, 2280 (1964).
[41] F. P. Diehl, C. Roos, A. Duymaz, B. Lunkenheimer, A. Köhn, and T. Basché, "Emergence of coherence through variation of intermolecular distances in a series of molecular dimers," J. Phys. Chem. Lett. **5**, 262–269 (2014).
[42] P. H. P. Harbach and A. Dreuw, "A fresh look at excitonically coupled chromophores from a Jahn-Teller perspective," Chem. Phys. **377**, 78–85 (2010).
[43] P. Garcia-Fernandez, L. Andjelkovic, M. Zlatar, M. Gruden-Pavlovic, and A. Dreuw, "A simple monomer-based model-Hamiltonian approach to combine excitonic coupling and Jahn-Teller theory," J. Chem. Phys. **139**, 174101 (2013).
[44] G. Klebe, F. Graser, E. Hädicke, and J. Berndt, "Crystallochromy as a solid-state effect—Correlation of molecular-conformation, crystal packing and color in perylene-3,4-9,10-bis(dicarboximide) pigments," Acta Crystallogr., Sect. B: Struct. Sci. **45**, 69–77 (1989).
[45] M. Wewer and F. Stienkemeier, "Laser-induced fluorescence spectroscopy of *N*,*N*′-dimethyl 3,4,9,10-perylene tetracarboxylic diimide monomers and oligomers attached to helium nanodroplets," Phys. Chem. Chem. Phys. **7**, 1171–1175 (2005).
[46] B. Fimmel, M. Son, Y. M. Sung, M. Grüne, B. Engels, D. Kim, and F. Würthner, "Phenylene ethynylene-tethered perylene bisimide folda-dimer and folda-trimer: Investigations on folding features in ground and excited states," Chem.-Eur. J. **21**, 615–630 (2015).
[47] M. Peric, B. Engels, and S. D. Peyerimhoff, "*Ab initio* investigation of the vibronic structure of the C_2H spectrum—Calculation of the hyperfine coupling-constants for the 3 lowest-lying electronic states," J. Mol. Spectrosc. **150**, 56–69 (1991).
[48] M. Peric, B. Engels, and S. D. Peyerimhoff, "*Ab initio* investigation of the vibronic structure of the C_2H spectrum—Computation of the vibronically averaged values for the hyperfine coupling-constants," J. Mol. Spectrosc. **150**, 70–85 (1991).
[49] M. R. Silva-Junior, M. Schreiber, S. P. A. Sauer, and W. Thiel, "Benchmarks of electronically excited states: Basis set effects on CASPT2 results," J. Chem. Phys. **133**, 174318 (2010).
[50] M. R. Silva-Junior, M. Schreiber, S. P. A. Sauer, and W. Thiel, "Benchmarks for electronically excited states: Time-dependent density functional theory and density functional theory based multireference configuration interaction," J. Chem. Phys. **129**, 104103 (2008).
[51] M. Schmittel, J.-P. Steffen, M. Maywald, B. Engels, H. Helten, and P. Musch, "Ring size effects in the C^2-C^6 biradical cyclisation of enyne-allenes and the relevance for neocarzinostatin," J. Chem. Soc., Perkin Trans. 2 **2**, 1331–1339 (2001).
[52] V. Pless, H. U. Suter, and B. Engels, "*Ab initio* study of the energy difference between the cyclic and linear-forms of the C_6 molecule," J. Chem. Phys. **101**, 4042–4048 (1994).
[53] H. U. Suter, V. Pless, M. Ernzerhof, and B. Engels, "Difficulties in the calculation of electron-spin-resonance parameters using density-functional methods," Chem. Phys. Lett. **230**, 398–404 (1994).
[54] A. Hellweg, S. A. Grün, and C. Hättig, "Benchmarking the performance of spin-component scaled CC2 in ground and electronically excited states," Phys. Chem. Chem. Phys. **10**, 4119–4127 (2008).
[55] O. Christiansen, H. Koch, and P. Jørgensen, "The second-order approximate coupled-cluster singles and doubles model CC2," Chem. Phys. Lett. **243**, 409–418 (1995).
[56] A. Schäfer, C. Huber, and R. Ahlrichs, "Fully optimized contracted Gaussian-basis sets of triple zeta valence quality for atoms Li to Kr," J. Chem. Phys. **100**, 5829–5835 (1994).
[57] F. Weigend, M. Häser, H. Patzelt, and R. Ahlrichs, "RI-MP2: Optimized auxiliary basis sets and demonstration of efficiency," Chem. Phys. Lett. **294**, 143–152 (1998).
[58] K. Eichkorn, O. Treutler, H. Öhm, M. Häser, and R. Ahlrichs, "Auxiliary basis-sets to approximate Coulomb potentials," Chem. Phys. Lett. **240**, 283–289 (1995).
[59] N. O. C. Winter, N. K. Graf, S. Leutwyler, and C. Hättig, "Benchmarks for 0–0 transitions of aromatic organic molecules: DFT/B3LYP, ADC(2), CC2, SOS-CC2 and SCS-CC2 compared to high-resolution gas-phase data," Phys. Chem. Chem. Phys. **15**, 6623–6630 (2013).
[60] O. Oeltermann, C. Brand, B. Engels, J. Tatchen, and M. Schmitt, "The structure of 5-cyanoindole in the ground and the lowest electronically excited singlet states, deduced from rotationally resolved electronic spectroscopy and *ab initio* theory," Phys. Chem. Chem. Phys. **14**, 10266–10270 (2012).
[61] J.-D. Chai and M. Head-Gordon, "Long-range corrected hybrid density functionals with damped atom-atom dispersion corrections," Phys. Chem. Chem. Phys. **10**, 6615–6620 (2008).
[62] T. H. Dunning, "Gaussian basis sets for use in correlated molecular calculations. I. The atoms boron through neon and hydrogen," J. Chem. Phys. **90**, 1007–1023 (1989).
[63] E. R. Davidson, "Comment on Dunning's correlation-consistent basis sets—Comment," Chem. Phys. Lett. **260**, 514–518 (1996).
[64] D. Bellinger, J. Pflaum, C. Brüning, V. Engel, and B. Engels, "The electronic character of PTCDA thin films in comparison to other perylene-based organic semi-conductors: *Ab initio*-, TD-DFT and semi-empirical computations of the opto-electronic properties of large aggregates," Phys. Chem. Chem. Phys. **19**, 2434–2448 (2017).
[65] S. Wirsing, M. Hänsel, V. Belova, F. Schreiber, K. Broch, B. Engels, and P. Tegeder, "Excited-state dynamics in perylene-based organic semiconductor thin films: Theory meets experiment," J. Phys. Chem. C **123**, 27561–27572 (2019).
[66] M. J. Frisch, Gaussian 16, Revision A.01, Gaussian, Inc., Wallingford, CT, 2016.
[67] J. Bloino, M. Biczysko, F. Santoro, and V. Barone, "General approach to compute vibrationally resolved one-photon electronic spectra," J. Chem. Theory Comput. **6**, 1256–1274 (2010).
[68] A. Baiardi, J. Bloino, and V. Barone, "General time dependent approach to vibronic spectroscopy including Franck-Condon, Herzberg-Teller, and Duschinsky effects," J. Chem. Theory Comput. **9**, 4097–4115 (2013).
[69] S. Miertus, E. Scrocco, and J. Tomasi, "Electrostatic interaction of a solute with a continuum—A direct utilization of *ab initio* molecular potentials for the prevision of solvent effects," Chem. Phys. **55**, 117–129 (1981).
[70] S. Miertus and J. Tomasi, "Approximate evaluations of the electrostatic free-energy and internal energy changes in solution processes," Chem. Phys. **65**, 239–245 (1982).

The Journal of Chemical Physics ARTICLE scitation.org/journal/jcp

[71] J. L. Pascual-ahuir, E. Silla, and I. Tuñon, "GEPOL—An improved description of molecular-surfaces. 3. A new algorithm for the computation of a solvent-excluding surface," J. Comput. Chem. **15**, 1127–1138 (1994).
[72] B. Mennucci, R. Cammi, and J. Tomasi, "Excited states and solvatochromic shifts within a nonequilibrium solvation approach: A new formulation of the integral equation formalism method at the self-consistent field, configuration interaction, and multiconfiguration self-consistent field level," J. Chem. Phys. **109**, 2798–2807 (1998).
[73] J. Tomasi, B. Mennucci, and R. Cammi, "Quantum mechanical continuum solvation models," Chem. Rev. **105**, 2999–3093 (2005).
[74] C. Brückner and B. Engels, "Benchmarking singlet and triplet excitation energies of molecular semiconductors for singlet fission: Tuning the amount of HF exchange and adjusting local correlation to obtain accurate functionals for singlet-triplet gaps," Chem. Phys. **482**, 319–338 (2017).
[75] F. Plasser, M. Wormit, and A. Dreuw, "New tools for the systematic analysis and visualization of electronic excitations. I. Formalism," J. Chem. Phys. **141**, 024106 (2014).
[76] F. Plasser, S. A. Bappler, M. Wormit, and A. Dreuw, "New tools for the systematic analysis and visualization of electronic excitations. II. Applications," J. Chem. Phys. **141**, 024107 (2014).
[77] B. Engels and S. D. Peyerimhoff, "The hyperfine coupling-constants of the $X^3\Sigma^-$ states of NH influence of polarization functions and configuration space on the description of spin polarization," Mol. Phys. **67**, 583–600 (1989).
[78] B. A. Engels, "Detailed study of the configuration selected multireference configuration-interaction method combined with perturbation-theory to correct the wave-function," J. Chem. Phys. **100**, 1380–1386 (1994).
[79] B. O. Roos, R. Lindh, P. A. Malmqvist, V. Veryazov, and P.-O. Widmark, *Multiconfigurational Quantum Chemistry* (John Wiley & Sons, Hoboken, NJ, 216).
[80] C. Brueckner and B. Engels, "Benchmarking ground-state geometries and vertical excitation energies of a selection of P-type semiconducting molecules with different polarity," J. Phys. Chem. A **119**, 12876–12891 (2015).
[81] C. Walter, V. Kramer, and B. Engels, "On the applicability of time-dependent density functional theory (TDDFT) and semiempirical methods to the computation of excited-state potential energy surfaces of perylene-based dye-aggregates," Int. J. Quantum Chem. **117**, e25337 (2017).
[82] J. Auerswald, B. Engels, I. Fischer, T. Gerbich, J. Herterich, A. Krueger, M. Lang, H.-C. Schmitt, C. Schon, and C. Walter, "The electronic structure of pyracene: A spectroscopic and computational study," Phys. Chem. Chem. Phys. **15**, 8151–8161 (2013).
[83] W. Liu, V. Settels, P. H. P. Harbach, A. Dreuw, R. F. Fink, and B. Engels, "Assessment of TD-DFT- and TD-HF-based approaches for the prediction of exciton coupling parameters, potential energy curves, and electronic characters of electronically excited aggregates," J. Comput. Chem. **32**, 1971–1981 (2011).
[84] A. Fihey and D. Jacquemin, "Performances of density functional tight-binding methods for describing ground and excited state geometries of organic molecules," J. Chem. Theory Comput. **15**, 6267–6276 (2019).
[85] C. Suellen, R. G. Freitas, P.-F. Loos, and D. Jacquemin, "Cross-comparisons between experiment, TD-DFT, CC, and ADC for transition energies," J. Chem. Theory Comput. **15**, 4581–4590 (2019).
[86] U. Heinemeyer, R. Scholz, L. Gisslén, M. I. Alonso, J. O. Ossó, M. Garriga, A. Hinderhofer, M. Kytka, S. Kowarik, A. Gerlach, and F. Schreiber, "Exciton-phonon coupling in diindenoperylene thin films," Phys. Rev. B **78**, 085210 (2008).
[87] E. M. Huber, G. de Bruin, W. Heinemeyer, G. Paniagua Soriano, H. S. Overkleeft, and M. Groll, "Systematic analyses of substrate preferences of 20S proteasomes using peptidic epoxyketone inhibitors," J. Am. Chem. Soc. **137**, 7835–7842 (2015).
[88] V. Stehr, R. F. Fink, B. Engels, J. Pflaum, and C. Deibel, "Singlet exciton diffusion in organic crystals based on Marcus transfer rates," J. Chem. Theory Comput. **10**, 1242–1255 (2014).
[89] M. Malagoli, V. Coropceanu, D. A. da Silva Filho, and J. L. Brédas, "A multimode analysis of the gas-phase photoelectron spectra in oligoacenes," J. Chem. Phys. **120**, 7490–7496 (2004).
[90] U. Müller, L. Roos, M. Frank, M. Deutsch, S. Hammer, M. Krumrein, A. Friedrich, T. B. Marder, B. Engels, A. Krueger, and J. Pflaum, "Role of intermolecular interactions in the excited-state photophysics of tetracene and 2,2′-ditetracene," J. Phys. Chem. C **124**, 19435 (2020).
[91] S. Kowarik, A. Gerlach, S. Sellner, L. Cavalcanti, O. Konovalov, and F. Schreiber, "Real-time X-ray diffraction measurements of structural dynamics and polymorphism in diindenoperylene growth," Appl. Phys. A **95**, 233–239 (2009).
[92] M. A. Heinrich, J. Pflaum, A. K. Tripathi, W. Frey, M. L. Steigerwald, and T. Siegrist, "Enantiotropic polymorphism in di-indenoperylene," J. Phys. Chem. C **111**, 18878–18881 (2007).
[93] C. Brückner, "The electronic structure and optoelectronic processes at the interfaces in organic solar cells composed of small organic molecules—A computational analysis of molecular, intermolecular, and aggregate aspects," Ph.D. thesis, Universität Würzburg, 2016.

Chapter 2

Interface Effects in Perylene-Based Organic Semiconductor Thin Films

This chapter expands the publications in chapter 1 to investigations of interfaces between DIP and PDIR-CN_2 thin film systems. In an introductory section I will give an overview covering the motivation for this research, the materials at hand and some experimental results which were to be explained in the course of this work. This will be followed by computational details which build on section 0.3. Afterwards I will present the results and give a short discussion of implications for each key point before I combine all important points in a separate discussion section. Concluding remarks complete this chapter.

2.1 Introduction and Experimental Data

This chapter heavily focusses on the energetic position of excitations with CT character in relation to local excitations. CT excitons are a central element in photovoltaics with a strong influence on the device performance.[90;91] They are desirable as precursors for the generation of free charge carriers but can also have negative effects and e.g. channel geminate recombination.[92] For this reason, Hänselt et al.[2–4] investigated different interface systems (compare figure 2.10) with TR-SHG spectroscopy; a method which is especially sensitive to CT excitations as discussed in the following. These experimental studies strongly indicate that the population of CT excited states is only possible at very specific interface geometries (compare table 2.1).[3] Furthermore, energy and polarization dependent effects were found and described,[2–4] but could not be fully explained. Further investigations of the energetics of this interface systems with emphasis on the CT character of the involved energetic levels were needed. In

this work this is done with aggregate based TD-DFT calculations and transition density matrix analysis (TDMA) as implemented in TheoDORE.[93;94] Interweaving these new insights on energetic position and CT character of the involved excited states allowed us to create an extended and more reliable illustration of the processes present in charge generation in such organic semiconductor (OSC) interfaces.

2.2 Charge Transfer at Organic Interfaces

Efficient conversion of photoenergy via excited excitons to free charge carriers is a key process in the utilization of renewable energy in photovoltaic devices.[90;95;96] In organic semiconductor materials, this can be facilitated by fine tuning of the energetic position of frontier orbitals of donor (D) and acceptor (A) molecules.[97;98] These orbitals are of vital importance for the buildup of CT states at interfaces, which can then dissociate and supply free energy carriers.[90;97] While the relative position of HOMO (D) and LUMO (A) is important for the energetics of CT states and is often used to approximate the latter, it is not the only factor which should be considered.[90;97–99] The excitation energy (EE) required to populate a CT state at large internuclear distances (R_{DA}) can be approximated by[100]

$$EE = IP(D) - EA(A) - \frac{e^2}{R_{DA}}. \tag{2.1}$$

To further simplify this, the IP/EA is often approximated by the HOMO/LUMO which follows the reasoning of Koopmans' Theorem. From this equation it is obvious that not only the molecular properties but also the intermolecular arrangement determines the energetics of a CT state.

The correlation between interface geometries and the involvement of CT states in the exciton dynamics after photoexcitation played an essential role in the work of Hänsel et al.[2;3]. In the following I will give a short overview of employed materials, the experimental methods and results of the aforementioned experimental work, before I detail my computational work and its implications for the field.

2.2.1 Materials and Spectroscopic Methods

Thin films of DIP and PDIR-CN_2 on sapphire substrates as prepared by Belova et al.[101;102] form well defined structures.[102–107] Of particular interest here is the tendency of DIP to form two different phases depending on the deposition structure. While at high temperatures all molecules take up a standing configuration (long axis

approximately perpendicular to the surface, σ-phase)[103], a second phase arises by deposition at lower temperatures. This second configuration is denoted λ-phase and has a similar unit cell to the σ-phase but with the long axis parallel to the surface.[104;105] In the case of PDIR-CN_2 different temperature-dependent phases were also found, but all experiments discussed here were done in the range of the RT phase of PDIR-CN_2.[102] Nevertheless, PDIR-CN_2 thin films are less uniform than those of DIP with especially the first layers on a non-interacting substrate exhibiting significant disorder.[102] Atomic force microscope (AFM) measurements of PDIR-CN_2 on DIP indicate that PDIR-CN_2 is more ordered in this case and partly adopts the structure of the underlying DIP film.[101] Experiments by Hänsel et al.[2–4] were done with a technique called TR-SHG which is especially sensitive to interfaces and CT excitations. Since SHG, as a second order non-linear property, is forbidden in centrosymmetric media, it is extremely well suited to study disturbances of the electronic structure of a material.[108–110]A static electric field can greatly enhance this effect. It can be induced by the separation of charges at the interface which happens when a CT state is populated. This is called EFISH generation[111–113] and is of great importance for the experiments on prospective photovoltaic materials.[3] The interface combinations investigated by Hänsel et al.[3] consist of (a) DIP_{RT} on PDIR-CN_2 on sapphire, (b) PDIR-CN_2 on DIP_{RT} on sapphire and (c) PDIR-CN_2 on DIP_{LT} on sapphire. The subscript of DIP indicates the temperature at which it was deposited, where RT is room temperature and LT refers to a temperature of 220±10 K. RT produces the aforementioned high-temperature phase of DIP, LT the low-temperature phase with lying (σ-phase) domains.[3] Since the long axis of PDIR-CN_2 in the thin films is aligned rather vertically with respect to the surface/interface, interface compositions with DIP_{RT} lead to an edge-on configuration in between layers and compounds. DIP deposited at lower temperature however allows for domains where the perylene planes of DIP and PDIR-CN_2 are facing each other at a smaller angle. Some of the main features of the TR-SHG measurements on the interface structures could be attributed to its distinct components as discussed in chapter 1. The remaining ones (compare table 2.1) indicate an interaction of the layers and will be discussed in combination with the computational results of this chapter.

Table 2.1: Summary of the main features of the TR-SHG measurements on the interface structures which cannot be explained by the exciton dynamics in the sole films. All data is reproduced from the thesis of Marc Hänsel.[3]

	enhancement of the main signal (p-pol.)	excited state decay (p-pol.)	ultra-short feature (s-pol.)
DIP_{RT}: PDIR-CN_2	-	-	-
PDIR-CN_2: DIP_{RT}	-	Excited state decay at long times (> 500 ps) mirrors the behaviour of DIP but not PDIR-CN_2.	-
PDIR-CN_2: DIP_{LT}	Enhancement depends on the energy of the pump-pulse: 2.25 eV: doubled 2.14 eV: +50 % 2.03 eV: no effect	Excited state decay at long times (> 500 ps) mirrors the behaviour of DIP but not PDIR-CN_2.	Visible for a pump energy of 2.25 eV.

2.3 Computational Details

To create a guess for the configuration at the interface, several layers of crystal structures for both materials were extracted. The crystallographic data was obtained from the Crystallographic Data Centre (CCDC)[114] via `www.ccdc.cam.ac.uk/structures/` with the CCDC code 642482 for DIP and 982087 for PDIR-CN_2. The DIP layers were then moved with respect to PDIR-CN_2 in x-, y- and z-direction and additionally rotated around the z-axis as sketched figure 2.1 to find the most stable relative position by use of the OPLSAA force field within our programm package CAST[115]. For the lying domains as found in interfaces with DIP_{LT}, the DIP layers were additionally rotated by 90° around the x-axis. From the most stable configuration, aggregates (dimers and tetramers) were selected manually and replaced by optimized monomers. The optimization was done using ωB97X-D3/def2-TZVP in ORCA 4.2 without environment. For PDIR-CN_2 we cut the alkyl-chains and replaced them with methyl-groups to make computations less costly. The validity of this approach is discussed in reference[4]. Furthermore, the perylencore of PDIR-CN_2 was restricted to be flat, as this is the case in the crystal environment. In a full vacuum optimization, PDIR-CN_2 is twisted about 4° as is also discussed in reference[4]. To investigate stabilization of Frenkel and CT excited states by relaxation we used an approach as in reference[85], were the ground

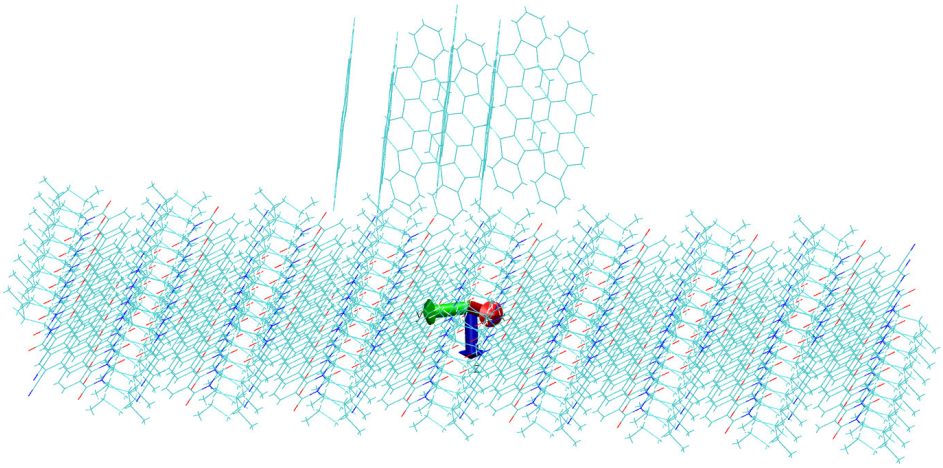

Figure 2.1: Extracts of the crystal structures of DIP and PDIR-CN_2 with the axes along which the DIP aggregate is moved to find the most stable position with respect to the PDIR-CN_2 layer.

state optimized monomers are replaced by partly or fully relaxed S_1, anionic or cationic geometries.

Excited state calculations were performed on these model aggregates. Tetramers were preferred to include both the interactions in the respective layers and the interactions at the interface (compare figure 2.2). The limiting case of high-disorder regions was also investigated by a fully optimized heterodimer, which consists of one DIP and one PDIR-CN_2 molecule. An even description of Frenkel- and CT-excitations poses a challenge for TD-DFT calculations but can be achieved by range-separated (RS) hybrid functionals, as discussed in chapter0.3. To this end we employed an IP-tuned version of ωB97X-D3[67] in combination with the def2-SVP[116] basis set if not denoted otherwise. IP tuning, as formulated by Stein et al.[69] employs the fact that in exact Kohn-Sham theory the energy of the highest occupied molecular orbital (HOMO) is equal to the inverse of the ionization potential. Depending on the definition of the "system" the tuning procedure can be done for the monomers, or for the full aggregates[59]. In this work we used both, optimal values are listed in table 2.2.
The choice of functional is in line with our work on the pure thin film systems[4]. The differences stemming from the tuning procedure, choice of basis set and description of the environment are shortly discussed in the following section. Calculations were done in ORCA 4.2 and 5.0.0[56;74;78] as well as in QChem 5.3[57]. To account for the screening effects of the environment, the conductor-like polarizable continuum model (C-PCM)[117] with a static and optical dielectric constant ($\epsilon = \epsilon_{\text{inf}} = 3$) suitable for an organic semiconductor system was employed. The CT character of excitations was determined by TDMA employing TheoDORE2.4.[93;94]

Table 2.2: Optimal values for the range-separation factor ω for different systems.

σ_c (model)^a	0.12
σ_c (full)	0.12
λ_b (model)^a	0.11
λ_b (full)	0.10
DIP monomer	0.14
DIP tetramer	0.09
PDIR-CN$_2^b$ monomer (model)^a	0.14
PDIR-CN$_2^b$ monomer (full)	0.13
PDIR-CN$_2^b$ tetramer (full)	0.08

^{a}If not denoted otherwise, we used a model system for PDIR-CN$_2$ throughout this work for all energy calculations, were the alkylchain was cut and replaced by a methylgroup. This does not influence the excitation behaviour as was verified in former works[4]. ^{b}As described in the Computational Details part of the SI, PDIR-CN$_2$ had to be kept flat during the optimization to mimic the crystal environment.

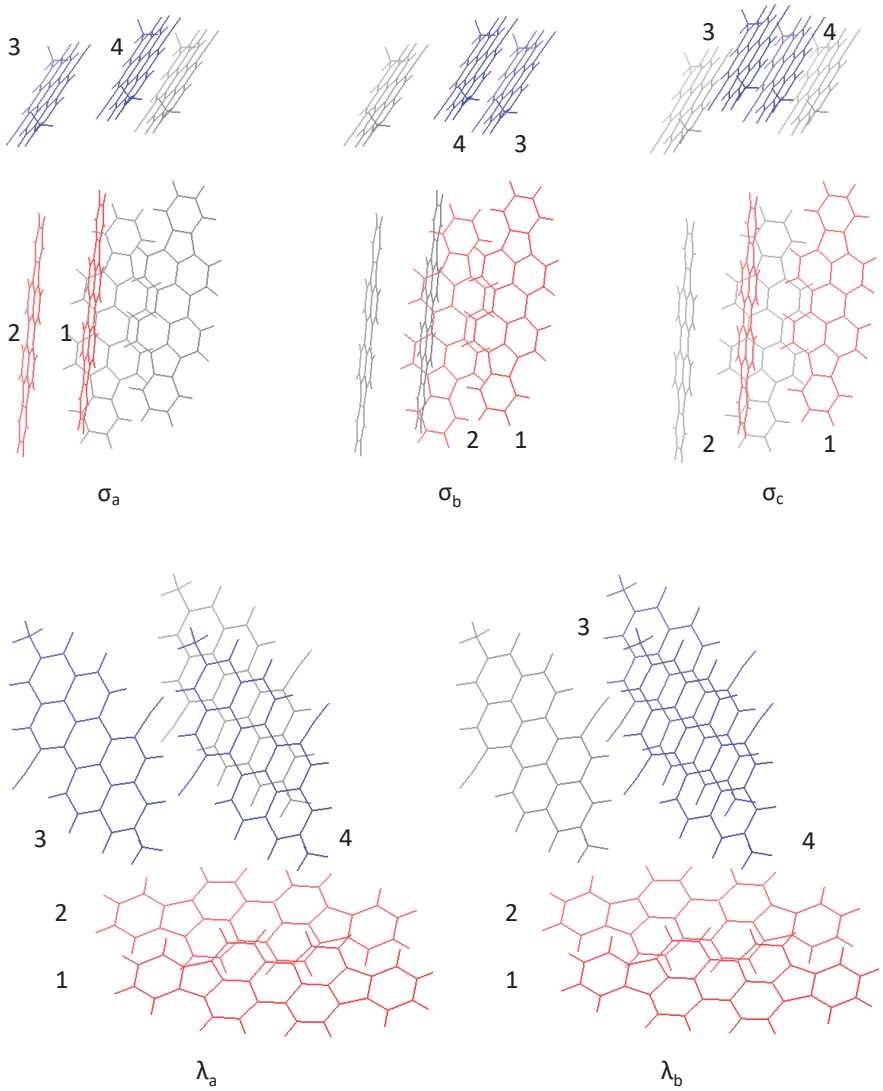

Figure 2.2: Chosen tetramers to model the interface with DIP in standing-up (σ) and lying (λ) configuration. σ-geometries are found in bilayer systems consisting of DIP$_{RT}$:PDIR-CN$_2$ and DIP$_{LT}$:PDIR-CN$_2$. λ only in DIP$_{LT}$:PDIR-CN$_2$. DIP monomers are highlighted in red, PDIR-CN$_2$ in blue. Grey molecules are included to display the surroundings in crystal layers.

2.4 Results and Implications

2.4.1 Benchmark of Calculated Excitation Energies in Comparison to Pure Thin Film Absorption Spectra

In reference [4] (called Paper I in the following) we assigned the thin film absorption spectra using tetramers cut from the crystal structure and replaced the monomers with optimized monomer structures in a point-charge model of the environment. Excited states were calculated using ωB97X-D/cc-pVDZ. This could be done quite confidently for low-lying states which are important for the following investigations. We observed an overall, consistent shift between theory and experiment, though. The charge environment had almost no effect on the position of the excited states in the pure film, but greatly influenced the position of CT states in this work which we deemed unphysical. Therefore a different approach was adopted for the investigation of interface effects.

Table 2.3: Assignment of features of the absorption spectra of the DIP thin film to vertical excitations calculated on tetramers. Energies are given in eV, followed by the oscillator strength (f).

state	exp.[4]	Paper I[4]	this work[b]
S_1	2.25 (first peak)	2.63/0.00[a]	2.38/0.00[a]
S_2		2.70/0.00	2.44/0.00
S_3		2.73/0.00	2.52/0.00
S_4		2.94/2.33	2.52/0.00
...			
S_{10}	2.48 (second peak)		2.63/0.69

a: The oscillator strength becomes non-zero for this state as soon as the system is slightly disordered.[4] b: ωB97X-D/def2-SVP/ω=0.09

Table 2.4: Assignment of features of the absorption spectra of the PDIR-CN_2 thin film to vertical excitations calculated on tetramers of full PDIR-CN_2 monomers with a flat perylene core. Energies are given in eV, followed by the oscillator strength (f).

state	exp.[4]	Paper I[4]	this work[a]
S_1		2.57/0.00	2.09/0.00
S_2	2.16 (first peak)	2.66/2.97	2.22/2.70
S_3	2.30 (second peak)	2.70/0.10	2.27/0.00
S_4	2.30 (second peak)	2.71/0.00	2.27/0.35

a: ωB97X-D/def2-SVP/ω=0.09

In the course of this work we also recalculated the excitation energies for the pure aggregates. We used a version of ωB97X-D/def2-SVP which is IP-tuned to the respec-

tive tetramers and simulated the environment with C-PCM. While the old calculations overestimated the excitation energies by up to 0.4-0.5 eV this is reduced in the new approach to less than 0.15 eV. The remaining difference between theory and experiment can be either attributed to relaxation effects as discussed in reference[85] which amount to 0.16 eV for DIP or to the limited size of the aggregate (amounts to about 0.1 eV in DIP)[4]. Investigations of the same fashion on PDIR-CN_2 were not feasible since it is not known if and how much its perylene-core and the alkyl-chains can relax in a crystalline environment. Furthermore ZINDO(S) as employed for the calculations on bigger aggregates of DIP did not produce reliable results for PDIR-CN_2.[4]

2.4.2 Interface Calculations

All calculations in this chapter are done on the tetramers in figure 2.2 or a fully optimized DIP:PDIR-CN_2 (ωB97X-D3/def2-SVP) dimer.

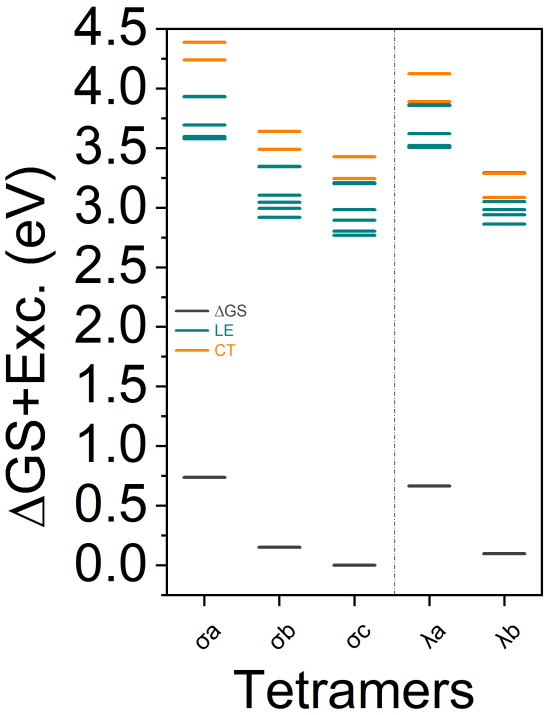

Figure 2.3: Excited states calculated (ωB97X-D3/def2-SVP) on the tetramer structures defined in figure 2.2 with PDIMe-CN_2. The colors indicate the character of the excited state.

Necessity for IP tuning. Application of the standard DFT approach, yielded no low-lying CT states at all (compare figure 2.3). Additionally, the lowest vertical excitation energy of any state on any structure lies above 2.7 eV for this method. The experiments were done with pump energies of 2.03 to 2.25 eV. While a shift of 0.4-0.5 eV might be explained by aggregate and relaxation effects,[4] the observed deviation of >0.7 eV and the absence of the experimentally found CT states indicate fundamental problems with this method.

IP tuning is a promising approach to balance the description of CT and local excitations.[59;69] The results in vacuum with the range-separation factor obtained from IP-tuning on the monomers (ω=0.14) are pictured in figure 2.4. This allows for an energetic comparison between aggregates. In this description, CT states are stabilized for λ structures as expected from the experiments. Additionally, local excitation (LE) states are shifted towards the correct energetic range, albeit still being too high in energy. However, σ_c shows CT character in its lowest excited state, which does not mirror the differences between σ and λ structures in the experiments (table 2.1).[3] This indicates that more environmental effects need to be taken into account.

Effect of C-PCM. Figure 2.5 shows the effect of a polarizable environment on the excitation energies. Frenkel excitations, especially those with high oscillator strengths, are stabilized in a polarizable environment as observed by Bellinger et al.[87;118] The destabilization of CT states with spatially separated donor and acceptor moieties was rather unexpected. However, it persisted in the C-PCM implementations of all big program packages (ORCA 5.0.0, QChem 5.3, Gaussian16_A) with a destabilization of the lowest CT excitation by 0.25-0.30 eV (compare table 2.5). This effect might be due to the inability of the fast share of the solvation to screen the strong polarization of the CT. Perturbational state-specific corrections (ptSS) to the excitation energies as implemented in QChem 5.3 diminish the effect of C-PCM on local excitations but show no effect at all on the CT states. This might be due to the very strong change in density from ground to excited state which might exceed the limits of an perturbational approach. In a benchmark on different additions to zeroth order solvation, Mewes et al. also advised against the use of the ptSS approach with spatially extended CT states.[119] Therefore, the default non-equilibrium solvation model is used in this study.

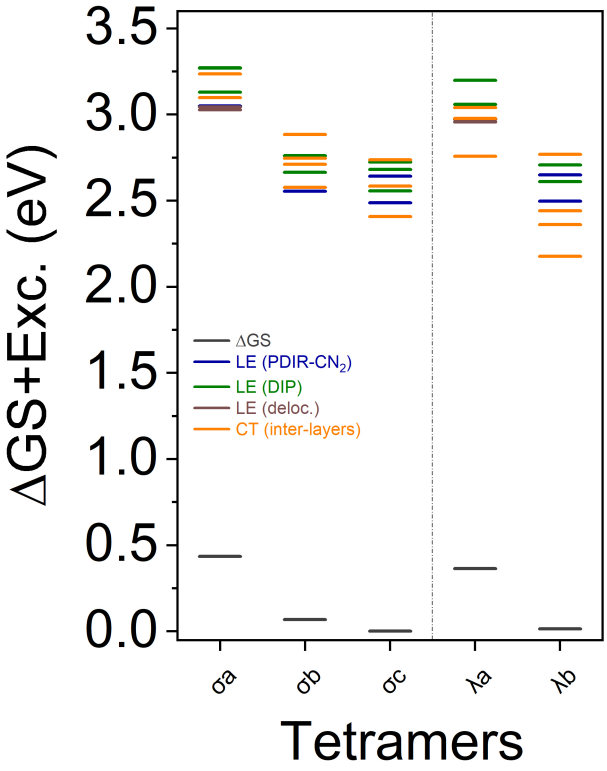

Figure 2.4: Excited states calculated (ωB97X-D3/def2-SVP/ω=0.14) on the tetramer structures defined in figure 2.2 with PDIMe-CN_2. The colors indicate the character of the excited state.

Table 2.5: Effect of C-PCM models on the lowest local and CT excitation in DIP:PDIR-CN_2 tetramers. The calulcations were done with ωB97X-D/def2-SVP/ω=0.14 in Gaussian16_A and with ωB97X-D3/def2-SVP/ω=0.14 in ORCA 5.0.0 and QChem 5.3 in vacuum, C-PCM as implemented for vertical excitations and C-PCM with perturbational state-specific corrections (ptSS).

	ORCA 5.0.0		Gaussian16_A		QChem 5.3		
	vac.	C-PCM	vac.	C-PCM	vac.	C-PCM	C-PCM ptSS
CT_1	2.66	2.93	2.70	2.98	2.66	2.93	2.93
LE_1	2.61	2.45	2.63	2.48	-[a]	2.47	2.62

a: The TD-DFT implementation in QChem heavily relies on a HOMO-LUMO guess which tends to miss low-lying Frenkel states if not enough excited states are calculated for a big system.

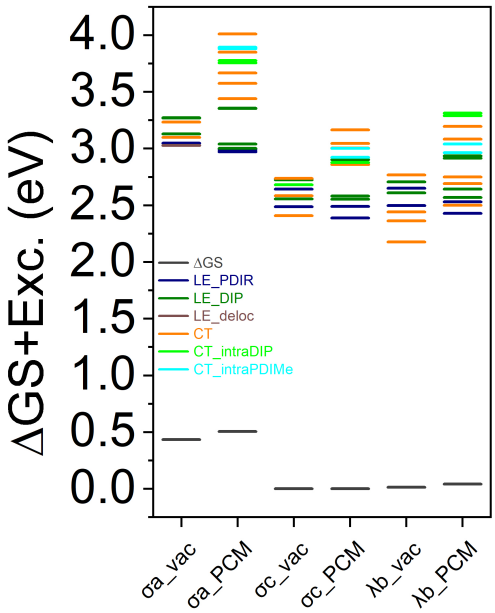

Figure 2.5: Excited states calculated (ωB97X-D3/def2-SVP/ω=0.14/vac. or C-PCM) on tetramer structures defined in figure 2.2 with PDIMe-CN_2. The ground state is shifted to the minimum of the respective method.

Effect of structural relaxation. From the tetramers in 2.4 the most stable geometries (σ_c for the standing up configuration and λ_b for areas which exhibit lying DIP domains in DIP_{LT}) were chosen for further investigations. In addition to vertical excitations we aimed to investigate relaxation effects as presented in reference [85]. This is particularly interesting for interface effects, since relaxations might have distinct influences on Frenkel and CT states. We approximated relaxations of the tetramer by employing the geometries of the relaxed monomers (S_0 to S_1 for Frenkel excitations and S_0 to cation/anion for CT ones). From all possible combinations we chose the ones with the lowest state for each category (CT, Frenkel on DIP, Frenkel on PDIR-CN_2) as the best approximation for further discussion. The chosen arrangements are marked with arrows in figure 2.6 and 2.7.

The calculations on σ-tetramers in a polarizable environment are dominated by low-lying Frenkel excitations for both the relaxed and unrelaxed monomers (compare figures 2.5 and 2.6). Even in the geometry which best approximates the relaxed CT state (or-

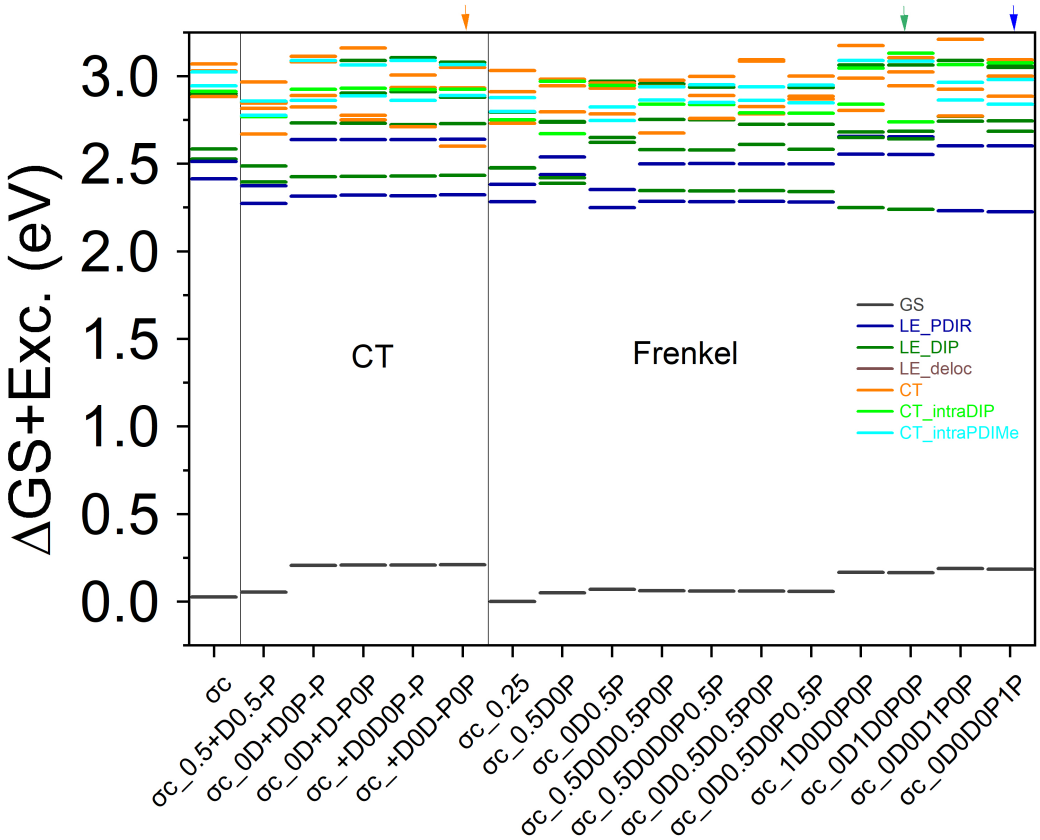

Figure 2.6: Overview over all possible relaxations in the σ_c tetramer with PDIME-CN_2 in our chosen framework. Calculations are done with ωB97X-D/def2-SVP/C-PCM and ω=0.14 as obtained from the tuning of monomers for a first screening. Approximations to the relaxation to a CT state were build by replacing DIP monomers with the optimized structures for cations, PDIR-CN_2 monomers with anions. Relaxed Frenkel geometries were approximated by the use of S_1 optimized monomers. The nomenclature shows the geometry of each monomer (D for DIP and P for PDIR-CN_2) by an added number or sign. "0" signifies a monomer S_0 geometry, "1" S_1 and fractions for interpolated geometries in between S_0 and S_1[85]. Analogously, "+" represents a cationic geometry, "-" an anionic geometry. If only one number is given, all monomers (of this category) are of the same geometry. In the first column all monomers are in S_0 geometry.

ange arrow, figure 2.6), the CT state is still ≈0.3 eV above the lowest Frenkel excitation at this geometry.

In calculations on the λ-tetramers however, the lowest excitation on a CT geometry shows full CT character (orange arrow, figure 2.7). It is obvious that the relaxation of monomers has a strong influence on the position of the states. In the next paragraph additional effects of the aggregate as opposed to monomer effects shall be taken into account.

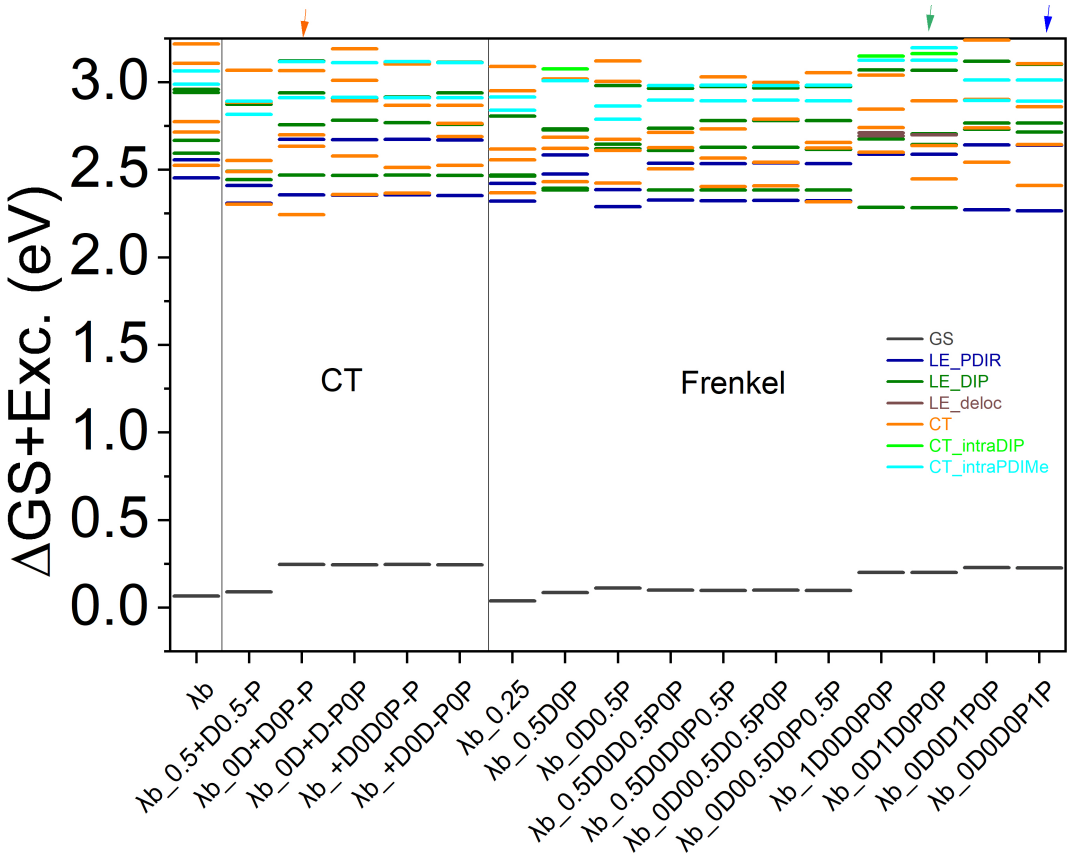

Figure 2.7: Overview over all possible relaxations in the λ_b tetramer with PDIMe-CN_2 in our chosen framework. Calculations are done with ωB97X-D/def2-SVP/C-PCM and ω=0.14 as obtained from the tuning of monomers for a first screening. Approximations to the relaxation to a CT state were build by replacing DIP monomers with the optimized structures for cations, PDIR-CN_2 monomers with anions. Relaxed Frenkel geometries were approximated by the use of S_1 optimized monomers. The nomenclature shows the geometry of each monomer (D for DIP and P for PDIR-CN_2) by an added number or sign. "0" signifies a monomer S_0 geometry, "1" S_1 and fractions for interpolated geometries in between S_0 and S_1[85]. Analogously, "+" represents a cationic geometry, "-" an anionic geometry. If only one number is given, all monomers (of this category) are of the same geometry. In the first column all monomers are in S_0 geometry.

Monomer- vs. aggregate-based tuning. Several studies report the importance of tuning to the correct aggregate.[58;59;120] This is sensible due to the delocalization and stabilization of the frontier orbitals induced by aggregate effects. Therefore, the most stable tetramers were consulted once more and the functional was tuned to these aggregates separately. Results are listed in table 2.2. These results follow an observed trend, which indicates that bigger systems result in a lower ideal RS parameter. Since ω is reciprocal in the spatial space, this is intuitive. Additionally, smaller ω values tend to stabilize all electronic excited states, with a stronger effect on CT excitations.
With these new tuning factors, the main relaxations found in figures 2.6 and 2.7 were reevaluated (see figure 2.8). The trend observed for σ_c in figure 2.6 is affirmed, although the difference between the lowest Frenkel and the first CT state is slightly lowered as expected. For λ_b the new tuning factor is even smaller than for σ_c regardless of the bigger spatial extension of σ_c. This could be due to the higher interaction in between layers in λ_b and results in a bigger change in tuning factors (compare figures 2.7 and 2.8b). CT states are the lowest for each investigated relaxed geometry. While the relaxation to DIP and PDIR-CN_2 S_1 geometries stabilizes local excitations in comparison to CT excitations, this effect is not strong enough to reduce the CT character of the lowest excited state in this tetramer.

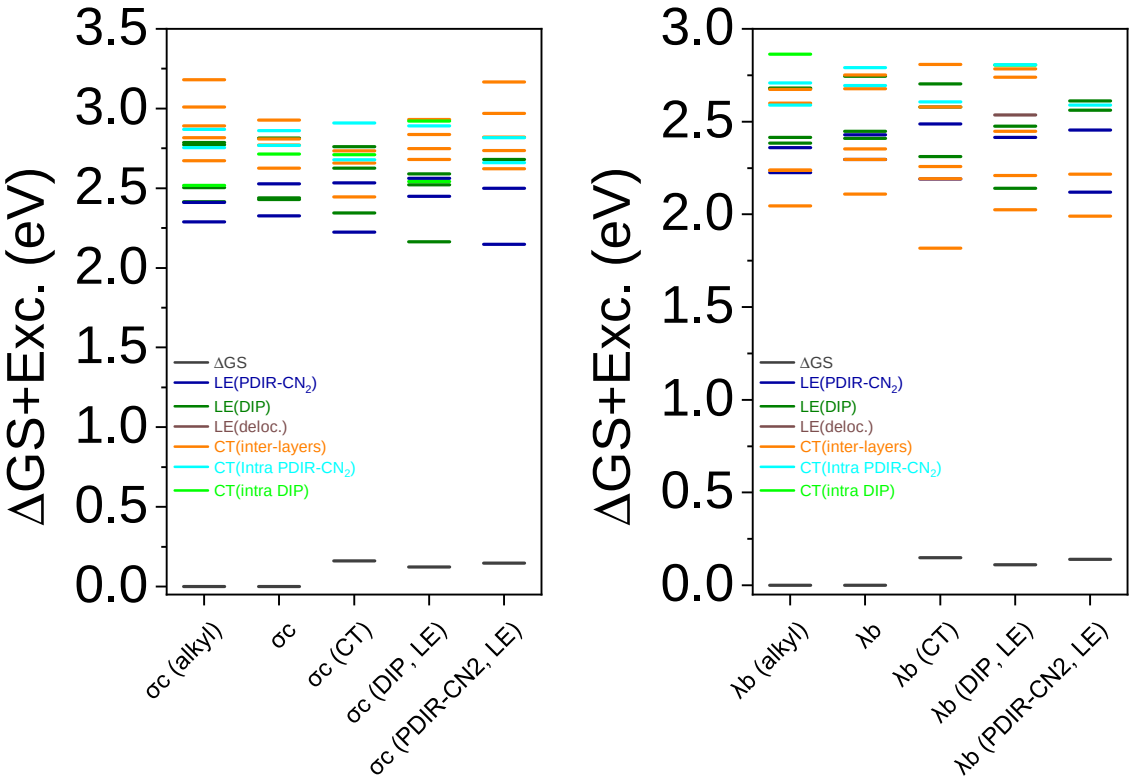

(a) Excited states calculated (ωB97X-D3/def2-SVP/ω=0.12/C-PCM) for σ_c.

(b) Excited states calculated (ωB97X-D3/def2-SVP/ω=0.11 (ω=0.10 for full alkyl-chains)/C-PCM) for λ_b.

Figure 2.8: The first column (σ_c/λ_b (alkyl)) presents calculations on the tetramer with full alkyl-chains. The following ones are based on our usual model system. Columns 3-5 show the best approximations (compare figures 2.6 and 2.7) to the relaxation to a CT (σ_c/λ_b (CT)), local DIP (σ_c/λ_b (DIP, LE)) and local PDIR-CN_2 (σ_c/λ_b (PDIR-CN_2, LE)) state. These states are approximated by relaxation of the monomers to S_1, anion or cation geometry while the positions in the crystal are kept frozen. The colours indicate the character of the excited state.

Effect of the omission of the alkyl-chain of PDIR-CN_2. It is also of interest to reinvestigate the impact of replacing the alkyl-chain in PDIR-CN_2 by a methyl group. The validity was already discussed in the SI of reference [4]. But in that publication, the environment was not mimicked by C-PCM and there was no focus on CT excitations. The main uncertainty might be induced by the change in the cavity of C-PCM when the alkyl-chains are cut.

For this reason, σ_c and λ_b were built with the full PDIR-CN_2 monomer. In the monomer optimization of PDIR-CN_2 the dihedrals were restricted to those from the crystal structure to adopt the flat perylene core and the orientation of the alkyl-chains in the crystal. Both properties are subject to aggregate effects in the thin films. It was however impor-

tant to relax the angles of the nitrile (CN) substituents which were only approximated in the crystal structures and have a pronounced effect on the energetics[1] of the molecule.

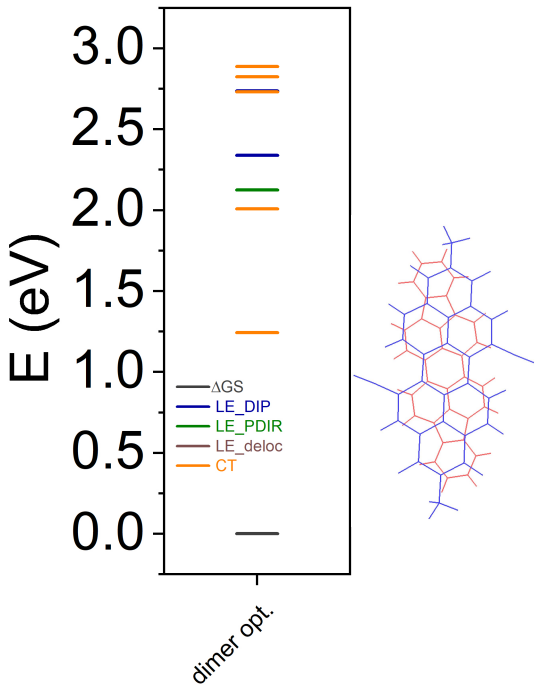

Figure 2.9: Excited states calculated (ωB97X-D3/def2-SVP/ω=0.14/C-PCM) on a fully optimized DIP (red):PDIMe-CN_2 (blue) dimer.

Figure 2.8 shows a very slight difference in the individual excitation energies but no impact on the observed trends. The stabilization of CT excitation by <0.2 eV is the biggest observed effect, but probably has to be attributed to the change in optimal RS factor than to the change in structure. It is not feasible to recreate the relaxed structures with full alkyl-chains since the degree of relaxation which can be accessed by those substituents is highly uncertain.

Effects of highly disordered regions. Following the assumption that interfaces of thin films might exhibit regions were layers consist of both materials, it is reasonable to expect regions were DIP and PDIR-CN_2 are positioned face-to-face. These aggregates are modelled by a full optimization of a heterodimer with ωB97X-D3/def2-SVP in vaccuum starting from a stacked position. This results in a stacked but slightly twisted position as pictured in figure 2.9 with a distance of 3.4 Å in between the flat perylene structures. This face-to-face structure highly stabilizes the CT state in comparison to the edge-on structures of an idealized interface.

[1]The ground state of the structure with constrained CN groups lies 0.3 Hartree above the ground state of the structure which was used in this work. The limitations of the resolution in crystallography were discussed with Katharina Broch (then Universität Tübingen) who advised against the use of the high-energy structure.

2.5 Discussion

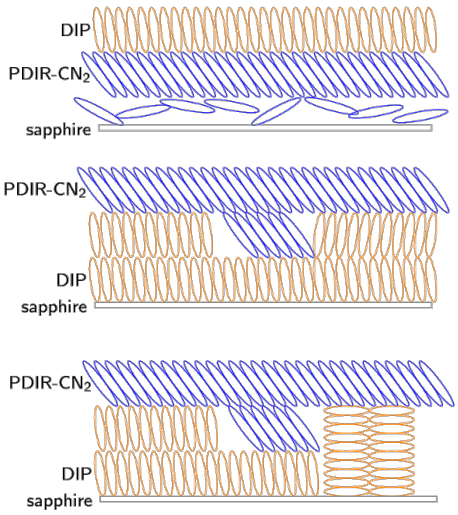

Figure 2.10: Conceptualized sketches of interface structures (DIP:PDIR-CN_2) as used in the experiments by Hänsel et al.[3]

In calculations on the σ-tetramers, the strong edge-on inter-monomer geometries (compare figure 2.10(top, middle)) inhibit stabilization of CT states below Frenkel excitations for both the relaxed and unrelaxed monomers (compare figures 2.8a and 2.6). Even in an aggregate which best approximates the relaxed CT geometry (third column figure 2.8a), the CT state lies ≈0.2 eV above the lowest Frenkel excitation at this geometry. This is in line with the TR-SHG measurements on PDIR-CN_2:DIP_{RT} which show no EFISH effect and therefore no indication for the population of CT states at the interface.[3]

For structures with DIP_{LT} as approximated by the λ tetramers, the first excited state has pronounced CT character for relaxed and unrelaxed monomers (figure 2.8b). These states can be populated if the interface is reached by the excitons and therefore greatly enhance the signal for PDIR-CN_2:DIP_{LT} bilayers as pictured in figure 2.10(bottom), Hänsel reports a stark energy dependence of the EFISH signal as reproduced in table 2.1. This can be explained by closer inspection of the energy levels and used pump energies. In the single layers, the pump pulse with a wavelength of 610 nm can only populate trap states[4]. Excitons can therefore not reach the interface. Directly at the interface population of CT states at favourable configurations would be energetically possible. The position of the lowest CT state in the full λ-tetramer is calculated at 2.05 eV while experimental excitation takes place at 610 nm (2.14 eV). However, those CT excitations are dark and cannot be directly populated. This explains the absence of an increased signal at 610 nm.

With an excitation energy of 580 nm regular states in PDIR-CN_2[4] can be populated and those excitons can therefore reach the interface. There, CT states can be populated as long as DIP exhibits its lying configuration (λ tetramers). In the DIP layer itself only low-lying trap states can be populated[4]. Excitation with a pump pulse of 550 nm results in the strongest signal experimentally.[3] At 2.25 eV states in DIP can be populated from which exciton diffusion towards the interface is possible. This is probably more efficient than the diffusion process in PDIR-CN_2 due to the lying stacks in DIP_{LT}. These have a bigger $\pi - \pi$ overlap perpendicular to the interface and can

therefore direct the excitons towards the interface. The bigger impact of excitons diffusing towards the interface in comparison to directly populated in CT states is also assumed to induce the ultra-short feature parallel to the interface (see table 2.1)). This signal presumably shows the build-up of CT states and is only visible for excitations with pump-pulses of 550 nm.
Experimentally, a difference in the long excited state decay times depending on the stacking order of the layers was found (table 2.1).[3] While the decay of the signal in DIP on PDIR-CN_2 on sapphire (figure 2.10(top)) can be mirrored by a superposition of the signals in pure DIP and PDIR-CN_2, it was dominated by the decay time found in DIP in the other structures (figure 2.10(middle, bottom)).[3] Since the stacking order does not influence the calculations at all, it has to have a structural influence which was not yet considered. Belova et al. reported that the upper layer in DIP:PDIR-CN_2 tends to adapt the structure of the underlying one.[101] She also detected increased disorder in the first layers of PDIR-CN_2 deposited on silicon oxide.[102] In reference [4] we attributed the faster decay time of PDIR-CN_2 in comparison to DIP at least partly to its higher degree of disorder. The combination of these results suggests that the absence of the faster decay time of PDIR-CN_2 when stacked on top of DIP layers is due to a more ordered structure of the first PDIR-CN_2 (compare figure 2.10).

Measurements by Belova et al.[101] also indicated that DIP exhibits a certain roughness which could result in terrace structures and therefore mixed layers (figure 2.10(middle, bottom)). These impurities where PDIR-CN_2 and DIP can arrange quite freely, were modelled by the calculations on a fully optimized dimer (figure 2.9). In this case the population of low-lying CT states should always be possible at every pump-pulse energy and result in an enhancement of the SHG signal. The absence of this signal at lower energies in PDIR-CN_2:DIP_{LT} could be due to the inability of the excitons to reach these positions as discussed before. However, there is also no signal in PDIR-CN_2:DIP_{RT} bilayers at excitation with 550 nm pump pulses. These should be able to populate Frenkel states in all regions of DIP and PDIR-CN_2 and allow for the diffusion to face-to-face geometries. The missing signals indicates that such terrace geometries are either rather rare, or do not allow for such an optimal arrangement as assumed in the calculations.

2.6 Conclusion

Aggregate based DFT calculations were employed to investigate the position and character of excited states at DIP:PDIR-CN_2 interfaces. IP tuning of the functional improved the results and allowed for a comparison to experimental (absorption and TR-SHG) results. The investigation of multiple different model systems allowed for differentiation between processes in the thin film structures. Reasons for the changes in signals were found and the dependency of the energetic position of CT excitations on structural factors was quantified. The incorporation of lying DIP structures (as experimentally found in DIP_{LT})[2–4] stabilizes CT excitations below the lowest local excited states. This explains the enhancement of the TR-SHG signal. The dependence of the signal on excitation energies[3], was attributed to the energetic position of Frenkel excitations. These are too high in energy to be populated by the pump-pulse of 610 nm if ordered aggregates are investigated.[4] Using the same aggregates, only PDIR-CN_2 can be excited at 580 nm and both materials at 550 nm. Trap states are not included in this description. If populated, these would not allow for diffusion to the interface. This explains the absence of signal enhancement at 610 nm and the increase of the signal with the energy of the pump-pulse.

Chapter 3

Excitations in mixed Donor-Acceptor systems for TADF OLEDs

The results of this chapter are part of a collaboration with Jeannine Grüne and Andreas Sperlich, who did corresponding experiments while all quantum chemical calculations were done by myself. Whenever experimental data was used to reason it is labelled and referenced. This chapter starts with an introduction to the topic and present key points of the aforementioned experiments. I will then expand on the computational methods used in this work, building on chapter 0.3. The computational results are divided according to the investigated pure components and their combinations and are complemented by a short discussion of their implications. The discussion is expanded in the following section in which all sides of the story are interwoven. Concluding remarks complete the chapter.

3.1 Introduction

Statistics from 2011 indicate that one third of electricity was utilized in the field of lighting.[121] Efficiency could be improved by the use of surface lighting techniques such as light-emitting diode (LED) in comparison to incandescent bulbs.[121] OLEDs promise additional improvements regarding sustainability.[121] What remains is the intrinsic, efficiency-limiting problem of LEDs which is rooted in spin statistics. In average only 25 % of charge carriers populate singlet states. The remaining 75 % end up in three degenerate triplet states. In a standard application, only the singlet states contribute to luminescence. It is therefore of great interest to utilize charge carriers (initially) populating triplets. Strategies to this end include the utilization of phosphorescence[122] and triplet-triplet annihilation (TTA)[123;124]. Phosphorescence however needs an emitter

which exhibits significant SOC.[125;126] This is mostly found for components including heavy atoms, which makes those materials both expensive and less sustainable. The downside of TTA is that even when the energetic levels are perfectly aligned the highest theoretical quantum efficiency is 62.5 %, since two populated triplet states amount to only one singlet.[127] A third option which has neither of the aforementioned drawbacks is called TADF.[128–130] In systems where the populated triplet state lies almost degenerate to an emissive singlet one, a thermally-induced transition can be possible.[128–130] This allows theoretically for a 100 % quantum efficiency.
A closer inspection of the approximated TADF rate[122]

$$k(TADF) \propto \sum_n \frac{\langle T_n | H_{SOC} | S_1 \rangle}{\Delta E_{S_1 - T_n}} \tag{3.1}$$

serves as a reminder that we cannot ignore SOC, since a symmetry forbidden transition just like in phosphorescence is utilized.[125;126] Contrary to phosphorescence, the energy difference in question is the much smaller one between S_1 and T_n ($\Delta E_{S_1-T_n}$) instead of $\Delta E_{S_0-T_1}$. $\Delta E_{S_1-T_n}$ in efficient TADF emitters is usually below 0.2 eV; in systems where donor (D) and acceptor (A) are located at different molecules, it is reduced to several meV.[127] This allows for a reasonable TADF rate even in purely organic systems with a small (but non-zero) $\langle T_n | H_{SOC} | S_1 \rangle$ element.[129;130]
It is possible to utilize multiple triplet states T_n to ease the passage from the initially populated triplet to emissive singlet or to open an additional pathway.[131–133] The following discussion however focuses on the $T_1 \rightarrow S_1$ transition to sketch the dominating challenges in the design of TADF emitters: Assuming that S_1 and T_1 are based on the same orbital transitions, $\Delta E_{S_1-T_1}$ amounts to two times the exchange energy (J).[127;134] J is exponentially dependent on the distance of the involved wavefunctions.[127;135–137] It is therefore especially small for CT excitations.[127;134] This can be achieved by including electron-withdrawing and donating moieties in the emitter.[138] The separation of the moieties can be enhanced by twists within the molecules.[10;139] Another strategy is to use a blend of distinct donor- and acceptor- molecules, which results in strong exciplex character and extremely small $\Delta E_{S_1-T_1}$ values.[140] The drawback of the latter and generally of materials with extremely pure and isolated CT states are however two-fold. Firstly, El-Sayed's rule states that ISC occurs more readily when the transition in question "involves a change in orbital type".[141] This is due to a strengthening of the SOC element by orbital motion.[142] If both S_1 and T_1 are pure CT states, no such change in orbital type is present. The second problem arises from the CT character of S_1 which results in a low transition dipole moment to a (neutral) singlet ground state.[127] Both issues can be circumnavigated by a fine tuning of close-lying excitations.

The former might be lifted by either mixing with local triplets (although this can also result in a higher non-radiative decay rate) [143] or made obsolete by an energy gap small enough to enable a hyperfine interaction (HFI) induced transition. [144;145] The latter can be diminished by delocalized frontier orbitals [127] or the absence of loss channels [146] which leaves fluorescence as the only option of deactivation even at slow rates.

3.2 Experimental Background

The experiments of Grüne et al. [5;14;147] focus on two donor-acceptor systems. Namely m-MTDATA(D):3TPYMB(A) and m-MTDATA(D):BPhen(A); the monomers are pictured in figure 3.1. Both systems can be utilized as TADF emitters for OLEDs. In this section I give some details on the investigated systems and the methods employed by the experimentalists.

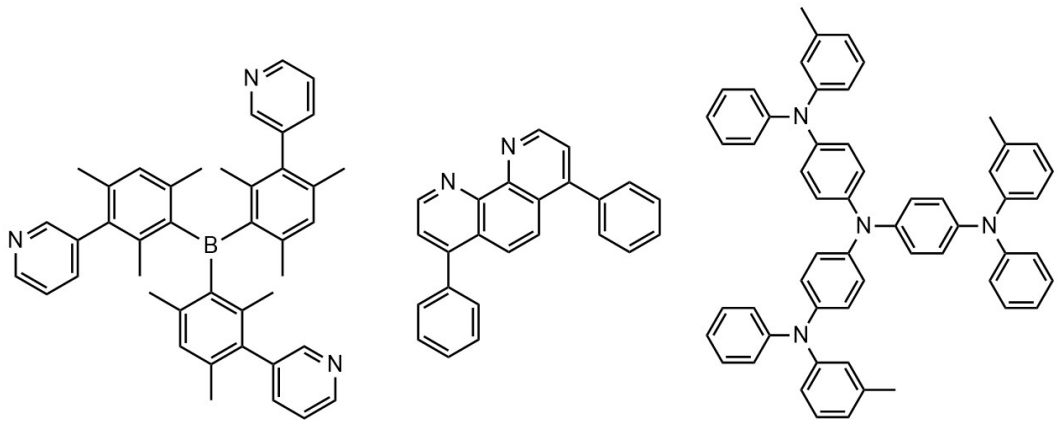

Figure 3.1: Chemical structures of 3TPYMB (left), BPhen (middle) and m-MTDATA (right).

3.2.1 Materials

The D:A system m-MTDATA:3TPYMB is widely researched for its property as an exciplex TADF emitter. [5;6;130;140;143;148] m-MTDATA:BPhen also clearly shows exciplex emission including a TADF signature. [7;140;149] Initial PLDMR studies [6] and the position of the molecular triplet of BPhen [149;150] as calculated from phosphorescence spectroscopy [151] indicate additional pathways in the latter combination which makes it interesting for further investigations. [7]

The emitting layer in the OLED devices used by Grüne et al. consists of thin film of the blend of materials deposited in a vacuum chamber for thermal evaporation. [5] Additionally, photo-luminescence experiments were done on spin-coated films on glass. [5]

3.2.2 Spectroscopic Methods

The experimentalists working on this project combine insights of several spectroscopic methods to create a dense net of information. As a starting point serve absorption and emission spectra, which are easily detectable and can be used to verify the computational ansatz. At the heart of the project are transient optically detected magnetic resonance (trODMR) measurements, more detailed PLDMR and ELDMR. These methods use microwave pulses of milliseconds to create time-dependent spectra.[14] The spectra mirror of the fingerprints caused by triplets and their involvement in the mechanisms in OLEDs and OPVs.[14;152] trODMR spectra and the resulting conclusions were complemented by trEPR measurements. This is a superior combination of experiments since trODMR can probe all spin-carrying excited states which participate in luminescence with the increased sensitivity inherent to optical detection.[14] trEPR on the other hand, gives additional information about states not directly involved in the process leading to luminescence.[16] The latter method is however not as sensitive to short-lived photoexcitations.[14;15] trODMR is also advantageous in the entangling of superimposed signals and allows for the detection of CT states with spatially strongly separated electron and hole which results in a negligible value for the zero-field splitting (D).[14;17;152]

3.3 Computational Details

All DFT calculations in this work were conducted using the ORCA program package (v.4.2 and 5.0.0).[78;153] Geometries were optimized with ωB97X-D3/def2-SVP[67;116] in its original form if not denoted otherwise. For optimization of bigger aggregates, GFN2-xTB as implemented for use in ORCA 4.2 was employed.[154] Energies for ground and excited states were calculated with an optimally tuned version of this functional, following the approach as proposed by Stein, Kronik et al.[69] This allows for a more balanced description of local and charge-transfer (CT) excitations. For details on the tuning process see chapter 0.3. For the vertical calculation of triplet and singlet excitation energies, the TDA[35] was added, whenever a comparison in-between multiplicities was conducted. Additionally, SOCs[83] and zero-field splitting parameters D and D/E values[155] were calculated within the TD-DFT framework as implemented in ORCA 5.0.0. While the effects in the amorphous systems were mainly investigated by calculations on fully optimized donor:acceptor (D:A) complexes (heterodimers), the electronic screening of the environment was approximated using the conductor-like polarizable continuum model (CPCM)[117], were the dielectric screening constant and the refractive

index were approximated to 3.00 and 1.73, respectively. CT character and root-mean-squared electron-hole distances (RMSehs) are calculated using TheoDORE2.4[93;156].

3.3.1 Choice of Method and the Effect of IP Tuning

Due to the size of the systems the natural method of choice was a DFT functional with a double-zeta basisset, preferably a range-separated hybrid for an improved description of CT excitations. Since ωB97X-D/cc-pVDZ proved to be a valuable combination for the description of OSCs,[157] initial calculations were done with this method in Gaussian16_A.[73] The adiabatic excitation energies for m-MTDATA and 3TPYMB with this method are however up to 0.7 eV too high in energy in comparison to reported experimental values (compare table 3.1).[148;158;159] While this might be (at least

Table 3.1: Adiabatic excitation energies ($E_{ad.}$) of m-MTDATA and 3TPYMB from calculations (ωB97X-D/cc-pVDZ, ΔSCF for T_1 and TD-DFT for S_1) and onset of luminescence spectra of thin films.

$E_{ad.}$[eV]	$S_{1,\text{m-MTDATA}}$	$T_{1,\text{m-MTDATA}}$	$S_{1,\text{3TPYMB}}$	$T_{1,\text{3TPYMB}}$
exp. (thin film)	3.10[148]	2.67[148]	3.54[148]	2.95[159]
calc. (vacuum)	3.75	3.00	3.81	3.46

partly) rationalized as a general trend and improved by the application of a solvation model, excited state calculations on the heterodimers called for a more severe change in methodology. The main feature of the experiments[6;7;148], the CT state which results in a pronounced red-shift of the emission was not present in the first 30 excited states (singlets and triplets) calculated (TDA/ωB97X-D/cc-pVDZ) on the neutral ground state structure of the m-MTDATA:3TPYMB heterodimer. These calculations went up to 4.32 eV while the experiment detects emission from the exciplex at $\approx$2.2 eV.[6;7] Even excited state calculations on a fragment based optimization of the first excited singlet with a CT guess (cationic m-MTDATA and anionic 3TPYMB as guess population) did not find any excited state with a CT value exceeding 0.1 in the energetic range up to 4.16 eV.

IP tuning, as introduced in section 0.3.2 seemed promising as it was shown to improve the description of CT states and balance it with regard to local ones, which mostly results in a stabilization of CT states.[69;160] During this change of methods, we also switched to the newer implementation of the functional in ORCA[78;153] (ωB97X-D3)[67] in combination with a basisset of similar quality but designed especially for DFT (def2-SVP)[116] which resulted in an improved convergence behaviour. The optimal ω-values obtained from the tuning procedure (see table3.2) are significantly lower than those of the original functionals (ωB97X-D: 0.20; ωB97X-D3: 0.25) which already indicates

Table 3.2: Optimal values for the range-separation factor ω for different systems.

m-MTDATA	0.12
3TPYMB	0.12
BPhen	0.16
m-MTDATA:3TPYMB (S0_4)[a]	0.10
m-MTDATA:BPhen (S0_3)[a]	0.12

[a]Tuning procedure was done on an exemplary heterodimer each, nomenclature is given in table A.2

that the original ones overestimate energies of CT states for the systems at hand. CT geometries are in the following approximated by a ground state optimization with triplet multiplicity after verifying by the use of spin-densities that those are indeed CT triplets involving the HOMO and the LUMO orbital. Optimizing triplets was not also the more reliable method to find CT states in comparison to the fragment based method but is also reasonable since they present a main focus of the investigation of TADF materials. After all TADF describes the transfer of energy from a low-lying populated triplet to the emissive singlet in energetic vicinity.

Tables 3.3 and 3.4 show that the positioning of CT excitations calculated with the

Table 3.3: Vertical excitation energies on m-MTDATA:3TPYMB heterodimers (S0_4 and T1_3) calculated with the tuned and original version of ωB97X-D3/def2-SVP in a polarizable environment or vacuum. The columns are named by geometry in the first row and tuning factor and environment in the second row. Excitation energies are calculated vertically within the TDA framework and given in eV. CT excitations are here defined by CT>0.5 as calculated by TheoDORE.

	S0_4			T1_3		
state	0.10, C-PCM	0.10, vac.	0.25, vac.	0.10, C-PCM	0.10, vac.	0.25, vac.
S_1	3.36	3.20	4.23	2.53	2.26	3.84
$S_{n,CT}$	3.36	3.20	4.80	2.53	2.26	3.84
T_1	3.17	3.16	3.43	2.53	2.26	3.12
$T_{n,CT}$	-	3.19	-	2.53	2.26	3.85

original functional is still extremely overestimated (0.8-1.6 eV) in comparison to the experimental value of $\approx$2.2 eV for both systems.[6;7] Decreasing the value of the range-separation factor as proposed by IP tuning, has a stark influence on the energetic position of these states and reduces the error to less than 0.2 eV with m-MTDATA:3TPYMB slightly over- and m-MTDATA:BPhen undershooting. This indicates that the error is probably not in the method but rather in the approximation of the thin films. C-PCM as applied in the vertical excitation framework has a small effect in the opposite direction. This is due to the strong dipole moment of the systems which cannot be fully

compensated by the fast share of environmental polarization. Full equilibrium solvation of the excited state as is adequate for the calculation of emission annihilates this issue as can be seen in table 3.8. For this reason, calculations in C-PCM were used to investigate state specific excitations which allow for an equilibrium solvation and for absorption where non-equilibrium solvation is deemed correct. Calculations in vacuum are employed to compare between vertical excitations on different geometries.

Table 3.4: Vertical excitation energies on m-MTDATA:BPhen heterodimers (S0_3 and T1_3) calculated with the tuned and original version of ωB97X-D3/def2-SVP in a polarizable environment or vacuum. The columns are named by geometry in the first row and tuning factor and environment in the second row. Excitation energies are calculated vertically within the TDA framework and given in eV. CT excitations are here defined by CT>0.5 as calculated by TheoDORE.

	S0_3			T1_3		
state	0.12, C-PCM	0.12, vac.	0.25, vac.	0.12, C-PCM	0.12, vac.	0.25, vac.
S_1	3.10	3.07	4.11	2.12	2.00	3.02
$S_{n,CT}$	3.10	3.07	4.29	2.12	2.00	3.02
T_1	3.04	3.03	3.30	2.12	2.00	2.76
$T_{n,CT}$	3.04	3.03	-	2.12	2.00	2.96

3.4 Results and Implications

In this section I present the results of my computational work and draw connections to the experimental work by Grüne et al.[5–7;10;14;147] wherever appropriate.

3.4.1 Pure Materials

The effects of interest in this study are mainly exhibited by donor:acceptor complexes in the blend. It is however important to verify the quality of the methods used to calculate those. Absorption and emission spectra are easiest to interpret and can therefore be used to test the methodology with regard to excitation energies. To a first approximation, absorption is often calculated as vertical excitations at the ground state geometry ($R(S_0)$). This assumption is based on the FC principle. In cases where the geometry of the first excited singlet ($R(S_1)$) is either geometrically or energetically close to $R(S_0)$, this does not strictly hold. Especially for extended π-systems, we found several cases with an absorption spectrum dominated by the $0-0$ transition,[58;85] which can be approximated by the adiabatic excitation energy, rather than the vertical one, if frequencies are not accessible. For this system we do not expect an active

$0-0$ band since the geometries are energetically divided (compare table 3.5) and are sterically hindered. Instead we expect an effect induced by disorder. In an amorphous

Table 3.5: Energy difference of S_0 between its minimum and the minimum geometry of the lowest triplet for m-MTDATA, 3TPYMB and BPhen. Geometries were optimized with ωB97X-D3/def2-SVP, energies calculated with the tuned version of the functional in C-PCM.

	m-MTDATA (ω=0.12)	3TPYMB (ω=0.12)	BPhen (ω=0.16)
ΔE_{S_0}(R(S_0)-R(T_1))[eV]	0.44	1.22	0.56

thin film, monomers cannot fully equilibrate at evaporation. As MD simulations would have exceeded the scope of this work, we approximated differences in structure using $R(S_1)$ and $R(T_1)$ as extreme cases of twisted ground state geometries.
The most important values are listed in table 3.6. $E_v(R(S_0))$ lists the first three excitation energies to singlet states calculated vertically at the S_0 geometry. These are the ones which are normally used to approximate absorption. m-MTDATA exhibits three low-lying singlets, with especially strong absorption coefficient in the second and third. 3TPYMB absorbs at slightly higher energies and with a lower oscillator strength than m-MTDATA. Its two first singlet excitations are almost degenerate at this geometry and show similiar absorption strengths. BPhen was calculated to absorb at the highest energy, 0.66 eV higher than m-MTDATA. Its first excitation is almost dark (f=0.008), and the second and third degenerate, with only the second showing non-negligible absorption. The first triplet is strongly stabilized in comparison to S_1 and lies in the same energetic region for all components, $\Delta E_{S_1-T_1}$ amounts to 0.3-0.4 eV for m-MTDATA and 3TPYMB and almost 0.9 eV for BPhen. In figure 3.2 the excitation energies calculated on monomers are plotted against the photoluminescence/-excitation spectra of thin films. Vertical excitation energies at ground state geometry $E_v(R(S_0))$ as discussed above are plotted in dark blue. Here I used the first five singlets. It is apparent that the calculated absorption energies fall in the region of strong absorption of the thin films, but the measured spectra show an onset at significantly lower energies. This difference amounts to 0.4-0.5 eV in m-MTDATA and 3TPYMB and is especially stark for BPhen with a difference of more than 0.8 eV. This could indicate that the methodology cannot accurately describe the monomer excitations, but it could also be due to disorder and aggregate effects. The first hypothesis can be debunked by looking at monomer spectra. Absorption in solution for m-MTDATA shows a peak at ≈3.54 eV (in toluene) or ≈3.59 eV (in THF),[161] which is in very good agreement with the calculated energies

of 3.58-3.62 eV for the first excitations.[1] Further absorption spectra in solution are not available, but the calculated emission also backs the reliability of the computational method. Emission is by default calculated as the vertical excitation energy of S_1 at its minimum geometry R(S_1). In figure 3.2 they are indicated by a orange dotted line. For BPhen and 3TPYMB the calculated emission is blue-shifted by less than 0.1 eV in comparison to the thin film emission.

The emission of m-MTDATA is calculated to be lower than in the acceptor compounds but still considerably higher (≈0.35 eV) in energy than the peak of the measured thin film emission. This could either be caused by computation of a local minimum geometry of S_1 or an emission which is not mostly induced by the monomer. Stojanović and Crespo-Otero examined relaxation pathways in propeller shaped compounds, where the excitonic coupling is very small in comparison to the monomeric relaxation energy similar to the molecules in this work.[162] They report a significant influence on the emission behaviour by blocked large-amplitude motions[162], a so-called aggregation-induced emission (AIE) effect.[162;163] Such effects can also attribute to a red-shift of the emission, when motions that interrupt the conjugation wavelength of a system are inhibited.[163]

Table 3.6: Excitation energies calculated on monomers for m-MTDATA, 3TPYMB and BPhen with ωB97X-D3/def2-SVP/C-PCM tuned on the monomers as defined in chapter 0.3. Singlet excitations were calculated with TD-DFT, triplets with ground state DFT calculations. The optimizations were done with ωB97X-D3/def2-SVP.

		m-MTDATA (ω=0.12)		3TPYMB (ω=0.12)		BPhen (ω=0.16)	
		eV	f	eV	f	eV	f
	S_1	3.58	0.265	3.84	0.188	4.24	0.008
$E_v(R(S_0))^a$	S_2	3.62	1.026	3.85	0.189	4.32	0.239
	S_3	3.62	0.623	4.17	0.037	4.32	0.001
$E_v(R(S_0))$	T_1	3.25		3.40		3.37	
$E_v(R(S_1))^b$	S_1	3.21	0.502	3.34	0.178	3.28	0.016
E_a	S_1	3.41		3.60		3.85	
E_a	T_1	2.90		2.99		2.75	
$E_v(R(T_1))$	T_1	2.46		1.77		2.20	

a: used to approximate absorption; b: used to approximate emission[3]; E_v: vertical excitation energy; E_a: adiabatic excitation energy

[1] While the contents of table 3.6 are calculated in C-PCM with $\epsilon = 3$ and a refraction index of $\sqrt{3}$, a calculation of the same type with the parameters for toluene results in only sligthly modified results for m-MTDATA. S_1: ΔE=3.58 eV, f=0.196; S_2: ΔE=3.62 eV, f=0.655; S_3: ΔE=3.63 eV, f=0.997

[2] All calculations in this picture are done with non-equilibrium solvation for the excited states as is fitting for absorption. To correctly describe emission one would have to equilibrate solvation to the excited state only. This is however not expected to have a big influence on the position of the state since solvation generally has no big influence on local excitations and emission energies for S_1 in vacuum differ by less than 0.15 eV in comparison to the pictured ones.

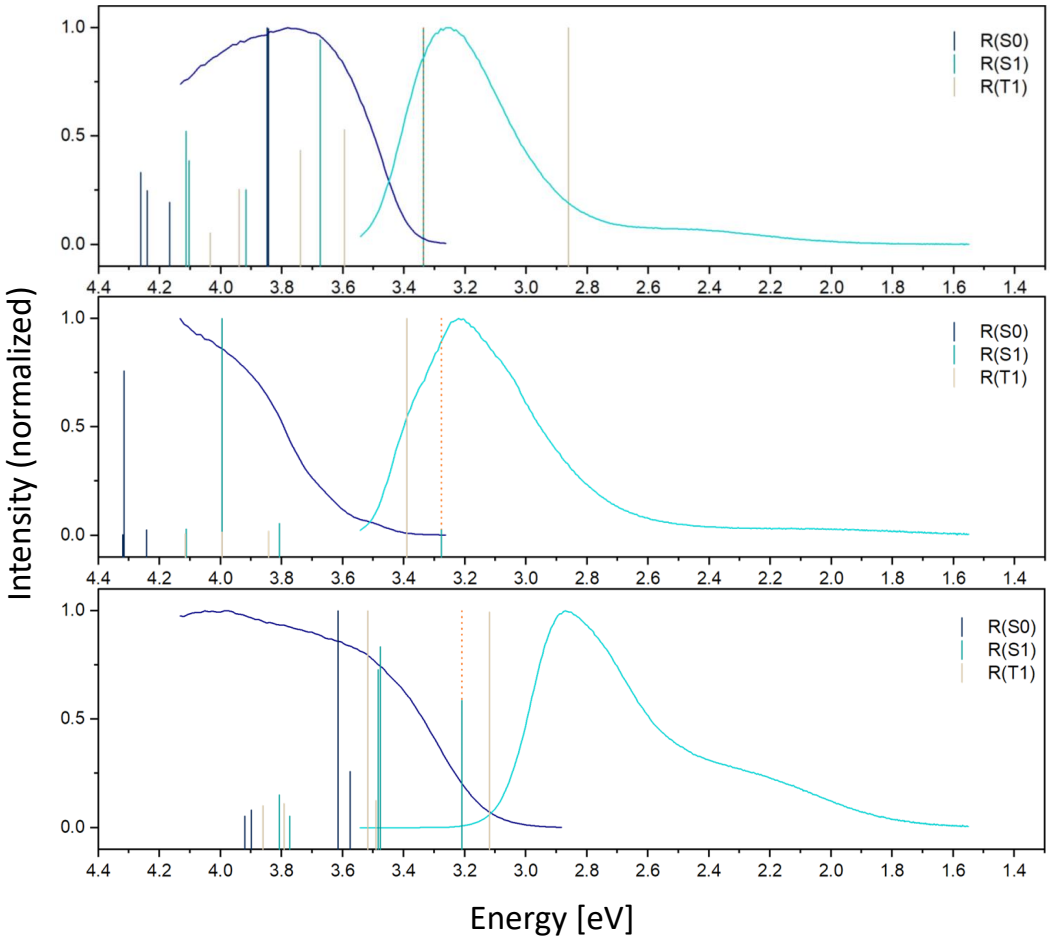

Figure 3.2: top: 3TPYMB; middle: BPhen; bottom: m-MTDATA: photoluminescence/-excitation spectra (lines) + vertical excitations (TD-DFT IP-tuned ωB97X-D3/def2-SVP in PCM) calculated on the monomer. The monomer was optimized to the singlet ground state (R(S0)), first excited singlet state (R(S1)) and the lowest triplet (R(T1)). Vertical excitations on S_0 are a valid approximation for absorbance under ideal conditions. Emission can be approximated by the vertical excitation to S_1 at R(S1) (dotted orange line)[2]. In amorphous systems we also expect molecules which exhibit a geometry which is twisted towards R(S1) or R(T1). To estimate this effect, the excitations on these geometries were added as limiting cases for absorption. Calculated intensities on R(S0) and R(S1) are normalized separately. The experimental spectra where provided by Jeannine Grüne and are measured on thin film systems.

Concluding from this subchapter it is possible to reproduce the main features of emission and absorption of the pure materials by investigation of single molecules with a tuned RS-hybrid functional in a C-PCM environment. The continuum model reflects the dielectric screening in the amorphous film. Splitting of states as found in homodimer and aggregate calculations in other works[85;86;164] is not prominent for the systems investigated here (compare table 3.7). Deviations from the experiment are

Table 3.7: Vertical excitation energies calculated with TDA-DFT IP-tuned ωB97X-D3/def2-SVP on monomers and dimers to investigate state splitting in TADF materials. The molecules in this work are bulky and cannot align closely, which results in a splitting of states of less than 0.05 eV.

	BPhen (ω=0.16)			m-MTDATA (ω=0.12)			3TPYMB (ω=0.12)		
	Monomer	Dimer		Monomer	Dimer		Monomer	Dimer	
	eV	eV	P_R	eV	eV	P_R	eV	eV	P_R
T_1	3.23	3.21	1.01	3.11	3.20	1.02	3.39	3.33	1.00
		3.22	1.01		3.23	1.02		3.35	1.00
S_1	4.20	4.15	1.04	3.66	3.73	1.51	3.89	3.81	1.01
		4.18	1.02		3.76	1.58		3.87	1.02

attributed to disorder and aggregate effects and do not diminish the quality of the model.

3.4.2 Mixed Materials

Photoluminescence and –excitation spectra show clearly that the emission of the blends is red-shifted in comparison to the emission of the pure films.[6;7] This indicates that the molecules interact strongly in the emissive state. We found that the spectra of the pure components can be approximated by vertical excitations calculated on different geometries of the monomers in a continuum model (compare figure 3.2). To investigate the interactions in the blends, we fully optimized dimers consisting of one donor (m-MTDATA) and one acceptor (BPhen/3TPYMB) molecule each. This was done from several starting points to get a rough estimate of the influence of amorphism in the thin films. MD simulations by Liu et al.[165] investigated this influence in more detail for the m-MTDATA:3TPYMB system. The following discussion will focus on exemplary heterodimers (details on the distinct ground state geometries are given in the Appendix, table A.2); but will be generalized to account for the effects of disorder. The arrangement of molecules at absorption is approximated by heterodimers optimized to their ground state geometry with vertical excitations calculated on top. Emission was modelled by a ground state optimization at triplet multiplicity. It was verified

[3]For details on emission in C-PCM, please refer to footnote 2.

that the lowest singlet and triplet both represent the same CT state and a ground state optimization of T_1 is both more accurate and computationally cheaper than a TD-DFT optimization of S_1 with CT character.[166;167]

m-MTDATA:3TPYMB

The peak of emission of a blended m-MTDATA:3TPYMB film is measured to be at 2.25 eV and strongly red-shifted in comparison to the films of the pure materials.[6] This indicates a strong exciplex state.[5;6] The computational investigations in the following review this assumption, examine this excitation and other low-lying states in detail and are used to complete the picture drawn by the experiments.

Energetic position and CT character of excited states. It is apparent (compare table 3.8) that the lowest singlet excitations exhibit charge-transfer character mirrored by their very low transition dipole moment. The first absorbing state is the S_3 and corresponds to a local transition on m-MTDATA (compare table 3.6). This explains why the absorption spectrum of the blend can be roughly approximated by a superposition of the pure films and is not red-shifted.[5–7] At emission, the interaction between donor and acceptor shows pronounced effects on the spectra.[5–7] We modelled this situation by a ground-state optimization of the lowest (CT) triplet. This is a good approximation to the lowest (CT) singlet since both T_1 and S_1 mirror the HOMO-LUMO transition. Since the frontier orbitals are spatially separated, the exchange contribution is negligible and T_1 and S_1 are energetically almost degenerate. The natural transition orbitals (NTOs) for these states are pictured in figure 3.3.

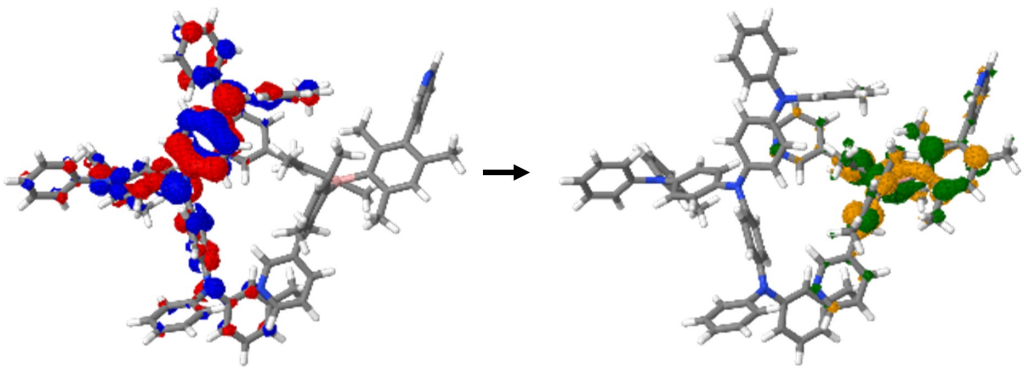

Figure 3.3: Natural transition orbitals (NTOs) to T_1 and S_1 in m-mTDATA:3TPYMB at the relaxed ct geometry $T1_3$. Calculated with ωB97X-D3/def2-SVP/ω=0.10.

The calculated singlet-triplet gap (ΔE_{ST}) for these states at CT amounts to only 2 meV, which is in perfect agreement with the result by Liu et al. based on MD simulated amorphous structures.[165] The experimental estimate derived from ELDMR data is at 16 meV[6] almost an order of magnitude bigger than the value provided by the calculations but with an error of less than 0.02 eV clearly within the error-bars of TD-DFT.[157] The oscillator strength of this lowest singlet state is small, as it denotes a symmetry forbidden transition from the CT S_1 to the neutral S_0. Emission takes place from this state nevertheless since it is highly stabilized in comparison to local singlet states. Comparing the vertical excitation energy of the local singlet on m-MTDATA at its minimum geometry (E_v(S_1, m-MTDATA)=3.26 eV) with the vertical excitation energy of the CT singlet at the relaxed CT geometry T1_3 (compare figure 3.4) (2.53 eV), the stabilization amounts to 0.7 eV.[4] After relaxation to a CT geometry (T1_x) the difference between S_1 and the first local (m-MTDATA) singlet state increases to >0.8 eV (compare figure 3.4).

Table 3.8: Excitation energies on a m-MTDATA:3TPYMB heterodimer optimized with ωB97X-D3/def2-SVP/CPCM; energy calculations were done with the respective tuned range separation factor (ω=0.10). Triplet energies were calculated by ground state calculations, excited singlets with TD-DFT.

		eV	f	CT
Absorption (vertical)$^{(a)}$	S_1	3.34	0.003	0.98 CT
	S_2	3.62	0.012	0.94 CT
	S_3	3.62	0.401	0.02 CT ($LE_{\text{m-MTDATA}}$)
Emission (vertical)[5]$^{(b)}$	S_1	2.12$^{(c)}$	0.001$^{(d)}$	0.99 CT$^{(e)}$
	T_1	2.12		0.99 CT$^{(e)}$
	ΔE_{ST}	2 meV		

(a): E_{vert}(R(S_0)) on S0_4; (b): E_{vert}(R(T_1)) on T1_3; (c) Excitation energy taken from ΔSCF(T_1) + $\Delta E_{T_1-S_1}$(TDA); (d) Taken from TD-DFT calculations on R(T_1); (e) Calculated with TDA-DFT to yield values of comparable quality for S_1 and T_1.

The geometries in figure 3.4 are quite different which is mirrored by their intermolecular distances and relative ground state energies in table 3.9. Nevertheless, important trends persists which increases the credibility of the previously discussed model cases. In neutral geometries (S0_x) a huge number of local triplets lies below the first CT

[4] All calculations for these comparisons are done with ωB97X-D3/def2-SVP/ω=0.12/vac.

[5] For details on emission in C-PCM, please refer to footnote 2. Due to the CT character of the excitation in question, the effect might be bigger than for the monomers if the wrong state is set in equilibrium solvation (compare table 3.3 for the effect of solvation on CT states). But it should also be noted that in this case full equilibrium solvation was used for both states which cancels a large part of the error.

triplet, with the lowest ones localized on m-MTDATA. The first three local singlets are equally localized on m-MTDATA with a vertical excitation energy of 3.6-3.8 eV. In all but one of the neutral geometries, this is higher than the lowest CT singlet (and triplet). Optimization to a CT triplet stabilizes all investigated states relative to S_0 but its influence is way more pronounced on the CT excitations than on the local ones which results in S_1 and T_1 of exclusively CT character (>0.99 CT), well separated from the lowest local triplets. Optimization of a local triplet was not possible due to convergence issues.

Table 3.9: Intermolecular distances (calculated from the center of mass of the monomers) and relative ground state energies of m-MTDATA:3TPYMB heterodimers calculated with ωB97X-D3/def2-SVP/$\omega = 0.12$.

geometry	S0_1	S0_2	S0_3	S0_4	S0_5	T1_1	T1_2	T1_3
dist.[Å]	7.12	8.00	8.97	6.40	5.78	8.18	8.20	7.99
ΔGS[eV]	0.00	0.14	0.27	0.34	0.52	0.61	0.62	0.97

The high CT character of the lowest singlet excitation (S_1) and the closest triplet (T_{close}) is mirrored in the very low SOC elements (last columns in table 3.10) in between these states. Although those elements are usually low for purely organic compounds (compare monomer values in table 3.10, they are even lower if the transitions have the same character, i.e. no change in angular momentum).[141]

Table 3.10: Spin-orbit coupling matrix elements (SOCME) of 3TPYMB and m-MTDATA in S_0 and T_1 (CT for heterodimers) geometry. Calculated with tuned ωB97X-D3/ def2-SVP in C-PCM.

	m-MTDATA (ω=0.12)		3TPYMB (ω=0.12)	
	S_0	T_1	S_0	T_1
S_1-	(0.00,-0.20)	(0.00,-0.80)	(0.00,0.02)	(0.00,-0.08)
T_{close}	(0.00,0.02)	(0.00,0.04)	(0.00,0.18)	(0.00,-0.16)
	(-0.00,-0.38)	(-0.00,0.11)	(-0.00,-0.19)	(-0.00,0.19)

	3TPYMB: (ω=0.10)	m-MTDATA
	S0_4	T1_3
S_1-	(0.00,0.05)	(0.00,-0.00)
T_{close}	(0.00,-0.07)	(0.00,-0.00)
	(-0.00,0.12)	(-0.00,-0.00)

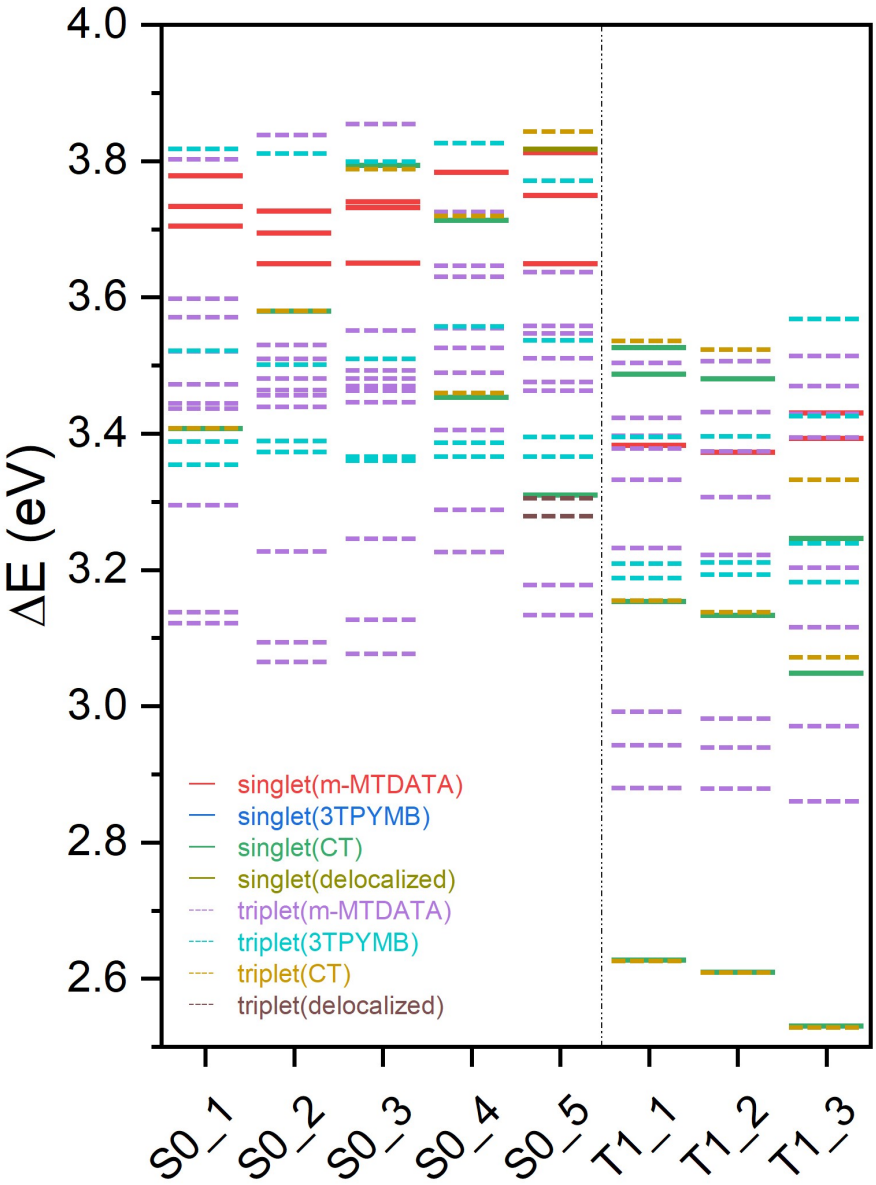

Figure 3.4: Vertical excitation energies (ΔE) calculated on various dimer structures of m-MTDATA:3TPYMB, TD-DFT calculations are done with the tuning factor obtained from the monomers ($\omega = 0.12$) for better comparison in between structures. Excitation energies calculated on singlet structures (S0_x) approximate the situation at absorption, those on triplet structures (T1_x) the situation at emission. The details on the distinct ground state geometries are given in the Appendix, table A.2. Colors indicate the character of the states.

Electron-hole separation and exciton size. EPR based techniques obtain little information about the energetic position of the populated excited states, but their D-value provides a good tool to estimate exciton sizes. While the D-value can be directly calculated in a relativistic framework, it comes with large uncertainties when scalar-relativistic DFT is the best method that could be employed due to cost limits.[168] Instead the approximate exciton size is directly calculated from the transition density as the RMSeh as implemented in TheoDORE.[169;170] For LEs, the exciton size in this

Table 3.11: Root-mean-squared electron-hole distances (RMSeh [Å]) which are used to approximate the exciton size for the first excited singlet (S_1) and first triplet (T_1) state. Calculations are done with ωB97X-D3/def2-SVP/ω=0.12(monomers)/ω=0.10(heterodimer) with TDA-DFT in C-PCM on geometries of the singlet (S_0/S0_4) and triplet (T1_3) ground state of the systems.

geometry		m-MTDATA	3TPYMB	m-MTDATA:3TPYMB			
		S_0	S_0	S0_4	T1_3	T1_3+2 Å	T1_3+5 Å
state	S_1	4.70	3.79	7.62	8.26	9.90	5.99
	T_1	3.98	3.26	4.01	8.25	8.66	4.43
	T_{CT}	-	-	5.82[a]			12.70

a: mixed character, 0.4 CT.

model is limited by the molecule size. This is mirrored by the RMSeh values for excitations on the monomers (m-MTDATA > 3TPYMB). In the m-MTDATA:3TPYMB heterodimers such a local excitation is found for T_1 calculated on the neutral geometry, which is a transition on m-MTDATA. All other excitations on heterodimers in table 3.11 posses CT character. For those excitations, the distance between donor and acceptor is an additional factor which influences the exciton size and especially their energetic position as pictured in figure 3.5. At slightly increased distances[6] between the molecules (+2 Å) the heterodimer still possesses a low-lying CT-triplet state in close vicinity to the S_1 as expected for TADF activity. At even bigger distances RMSeh values for CT states increase further. These are however no longer mirrored by T_1 and S_1, localized excitations are lower in energy than the CT states for those geometries.

Modelling the blends by heterodimers limits the size of excitons to precisely this aggregate. It is therefore of interest to expand the investigation to bigger systems. Due to limitations in computational ressources, trimers were optimized with GFN2-xTB as available as add-on for ORCA 4.2. GFN2-xTB was proven to outperform the accuracy of similarly cheap semiempiric methods for optimization even in compli-

[6]The intramonomer degrees of freedom were frozen and only the distance in between the center of masses of the monomers increased.

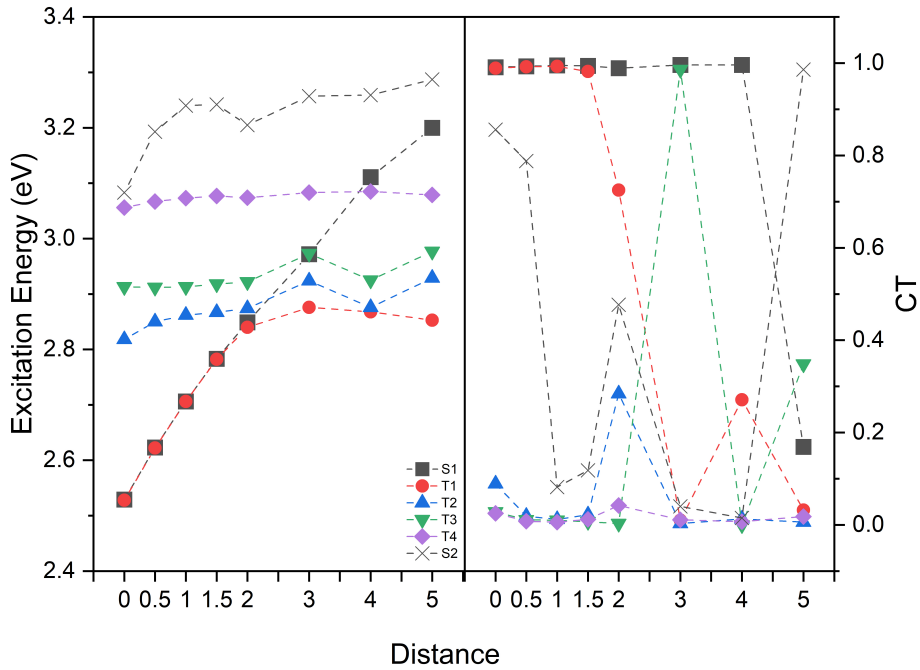

Figure 3.5: Vertical excitation energies and CT character of the lowest excited states on a m-MTDATA:3TPYMB heterodimer (T1_3) at different intermonomer distances. '0' refers to the optimized dimer, for the following data points the intramonomer degrees of freedom were frozen and only the distance increased by the given value in Å.

cated cases.[171] Excitation energies on these aggregates were calculated with ωB97X-D3/def2-SVP/ω=0.12 in the same fashion as on the DFT optimized dimers. Starting points for the optimization were created as an alternating stack of molecules. For resulting structures compare figure 3.6.

Closer investigation of the lowest local and CT triplets (tables 3.12 and 3.13), which are most likely to induce signals in the experiments by Grüne et al.[5–7;10;14;147], provides no evidence for delocalization which exceeds the one calculated on the dimer. The RMSeh values correspond to the ones in monomers and dimers. However, since this value represents only the mean separation of electron and hole, it cannot be used as the only measure for delocalization in trimers. Participation ratios (P_Rs) and transition matrices support the investigation. The P_R gives the mean delocalization of electron and hole over defined fragments, and is close to one in both local triplets in tables 3.12 and 3.13 and the CT triplet of m-MTDATA:3TPYMB:m-MTDATA. This means that both electron and hole are localized on one fragment. For the CT triplet in 3TPYMB:m-MTDATA:3TPYMB the P_R amounts to 1.36, which indicates a delocalization of either electron and/or hole. The transition matrix of that state shows that this is due to a delocalization of the electron. Transition matrices present the

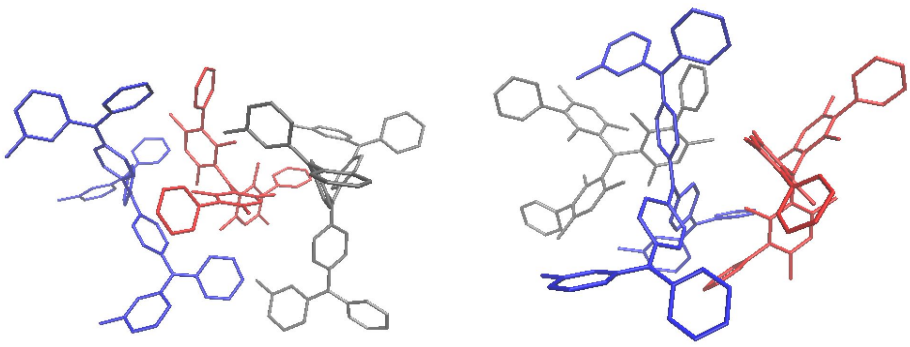

Figure 3.6: Trimers from m-MTDATA:3TPYMB optimized by GFN2-xTB. Left: m-MTDATA (blue, fragment 1):3TPYMB (red, fragment 3):m-MTDATA (grey, fragment 2); right: 3TPYMB (red, fragment 2):m-MTDATA (blue, fragment 1):3TPYMB (grey, fragment 3). The distance between center of masses of the fragments amounts to (left) dist.$_{1-2}$=6.44 Å, dist.$_{2-3}$=6.42 Å and (right) dist.$_{1-2}$=6.50 Å, dist.$_{1-3}$=7.03 Å. Hydrogen atoms are omitted for clarity.

fragments occupied by the hole on the x-axis and the electron on the y-axis. The darkness of the colored squares indicates the proportion of the labeled transition. T_{CT} of 3TPYMB:m-MTDATA:3TPYMB is therefore a transition that starts on fragment 1 (m-MTDATA) and is partly a local excitation (to fragment 1) and partly a CT state with the electron localized on fragment 3 (3TPYMB). However it does not show participation of both acceptor molecules.

To summarize this, no evidence was found that the description of the m-MTDATA: 3TPYMB blend by heterodimers is not sufficient, since excitations are localized on at most one donor and one acceptor molecule in the investigated cases. This could be induced by the non-symmetric arrangement in the aggregates, as pictured in figure 3.6.

Table 3.12: Lowest local and CT triplets on a m-MTDATA (fragment 1):3TPYMB (fragment 3):m-MTDATA (fragment 2) trimer. Optimization was done with GFN2-xTB, excited state calculation with ωB97X-D3/def2-SVP/ω=0.12.

state	ΔE(eV)	P_R	CT	RMSeh [Å]	trans. matrix
T_{CT}	3.14	1.09	0.92	7.29	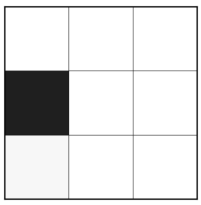
T_{LE}	2.96	1.03	0.03	4.33	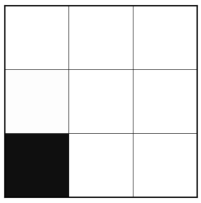

Table 3.13: Lowest local and CT triplets on a 3TPYMB (fragment 2):m-MTDATA (fragment 1):3TPYMB (fragment 3) trimer. Optimization was done with GFN2-xTB, excited state calculation with ωB97X-D3/def2-SVP/ω=0.12.

state	ΔE(eV)	P_R	CT	RMSeh [Å]	trans. matrix
T_{CT}	3.03	1.36	0.71	7.04	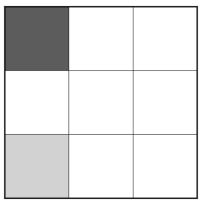
T_{LE}	2.92	1.06	0.05	4.39	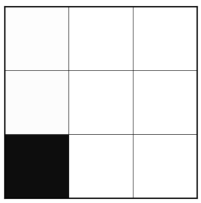

m-MTDATA:BPhen

This blend exhibits a lot of similarities to the one discussed previously. It is therefore processed in a similar manner with special attention to the differences between the systems. Emission of this blend was measured to be most intense at 2.21 eV, indicating a strong exciplex state.[7]

Energetic position and CT character of excited states. The excitation energies in table 3.14 at the neutral and CT geometry closely resemble those of m-MTDATA: 3TPYMB (compare table 3.8) and likewise explain the strong red-shift of emission in comparison to the pure materials while the absorption spectrum of the blend resembles a superposition of these as discussed in the section on m-MTDATA:3TPYMB. The CT excitations at neutral geometries are lower in energy due to BPhen being less bulky than 3TPYMB which allows for a more compact alignment of the donor:acceptor complex as can be seen from intermolecular distances in table 3.15 in comparison to table 3.9. The compact packing is also visualized in figure 3.7 which pictures the NTOs of the lowest singlet and triplet excitation at CT geometry. The involved orbitals are the HOMO and the LUMO of the heterodimer and present a CT excitation.

Table 3.14: Excitation energies on a m-MTDATA:BPhen heterodimer optimized with ωB97X-D3/def2-SVP/C-PCM; energy calculations were done with the respective tuned range separation factor (ω=0.12). Triplet energies were calculated by ground state calculations, excited singlets with TD-DFT.

		eV	f	CT
Absorption (vertical)$^{(a)}$	S_1	3.10	0.009	0.96 CT
	S_2	3.24	0.004	0.96 CT
	S_3	3.59	0.113	0.06 CT ($LE_{\text{m-MTDATA}}$)
Emission (vertical)[7]$^{(b)}$	S_1	2.04$^{(c)}$	0.003$^{(d)}$	0.98 CT$^{(e)}$
	T_1	2.03		0.97 CT$^{(e)}$
	ΔE_{ST}	8 meV		

(a): $E_{vert}(R(S_0))$ on S0_3; (b): $E_{vert}(R(T_1))$ on T1_3; (c) Excitation energy taken from $\Delta SCF(T_1) + \Delta E_{T_1-S_1}(TDA)$; (d) Taken from TD-DFT calculations on $R(T_1)$; (e) Calculated with TDA-DFT to yield values of comparable quality for S_1 and T_1.

[7]For details on emission in C-PCM, please refer to footnote 2. Due to the CT character of the excitation in question, the effect might be bigger than for the monomers if the wrong state is set in equilibrium solvation (compare table 3.4 for the effect of solvation on CT states). But it should also be noted that in this case full equilibrium solvation was used for both states which cancels a large part of the error.

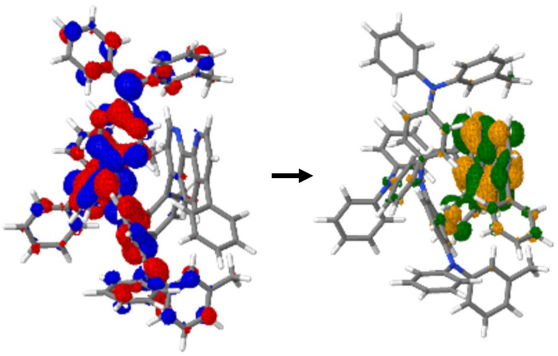

Figure 3.7: NTOs to T_1 and S_1 in m-MTDATA:BPhen at the relaxed CT geometry T1_3. Calculated with ωB97X-D3/def2-SVP/ω=0.12.

The calculated singlet-triplet gap (ΔE_{ST}) for these states at CT geometry amounts to 8 meV, the activation energy (E_A) for TADF was approximated to 58 meV from the ELDMR data.[7] An error of 0.05 eV is low for calculations which utilize TD-DFT.[157] Also, the zero-point energy (ZPE) for these states could not be calculated due to the size of the aggregate which alters energy differences by up to 0.1 eV for perylene based OSCs.[4] Nonetheless, it can not be ruled out at this point that E_A is higher than ΔE_{ST} due to the involvement of additional barriers that need to be overcome for the population of the CT singlet. This singlet is proposed to be the emissive one due to its energetic position although its oscillator strength is low. It is highly stabilized in comparison to local excitations. The difference between the vertical excitation energy of the local singlet on m-MTDATA at its minimum geometry (E_v(S1, m-MTDATA)=3.33 eV) with the vertical excitation energy of the CT singlet at the relaxed CT geometry T1_3 (compare figure 3.8) (2.17 eV), the stabilization amounts to almost 1.1 eV.[8] At CT geometries this difference is higher than 1 eV and goes up to 1.5 eV for geometry T1_5 (figure 3.8) which makes it an effective trap state and inhibits other radiative deexcitation pathways.

Table 3.15: Intermolecular distances (calculated from the center of mass of the monomers) and relative ground state energies of m-MTDATA:BPhen heterodimers calculated with ωB97X-D3/def2-SV/ω=0.14.

geometry	S0_1	S0_2	S0_3	S0_4	T1_1	T1_2	T1_3	T1_4	T1_5	T1_6
dist.[Å]	3.85	3.86	3.47	5.66	3.58	4.98	3.36	3.37	5.01	3.74
ΔGS[eV]	0.00	0.00	0.11	0.35	0.58	0.72	0.74	0.76	0.98	0.51

The geometries in figure 3.8 differ strongly in their intermolecular distances and relative ground state energies as reported in table 3.15. However important trends persists, not

[8] All calculations for these comparisons are done with ωB97X-D3/def2-SVP/ω=0.14/vac.

only between geometries for m-MTDATA:BPhen but also compared to m-MTDATA:-3TPYMB. In neutral geometries (S0_x) some local triplets lie below the first CT triplet, with the lowest ones localized on m-MTDATA. The first three local singlets are equally localized on m-MTDATA with a vertical excitation energy of 3.7-3.8 eV. In all geometries, this is higher than the lowest CT singlet (and triplet). Optimization to a CT triplet stabilizes all investigated states relative to S_0 but its influence is significantly stronger on the CT excitations than on the local ones which results in S_1 and T_1 of exclusively CT character (>0.99 CT), well separated from the lowest local triplets. T1_6 marks a special case where it was possible to optimize a local triplet (on BPhen). At this geometry, the vertical excitation energy to the local triplet lies only slightly above the vertical excitation energy of CT states at T1_1. When the differences in GS energies are taken into consideration (table 3.15) and adiabatic excitation energies are compared, the local triplet is almost degenerate to the lowest CT state at all CT geometries. The implications of this observation will be discussed in section 3.5.

Similarly to m-MTDATA:3TPYMB, the high CT character of the lowest singlet excitation (S_1) and the closest triplet (T_{close}) is mirrored in the very low SOC elements (last columns in table 3.16) in between these states. This is inline with predictions for the transitions of the same character according to El-Sayed's rule.[141]

Table 3.16: Spin-orbit coupling matrix elements (SOCME) of BPhen and m-MTDATA in S_0 and T_1 (CT for heterodimers) geometry. Calculated with tuned ωB97X-D3/ def2-SVP in C-PCM.

	m-MTDATA (ω=0.12)		BPhen (ω=0.16)	
	S_0	T_1	S_0	T_1
S_1-	(0.00,-0.20)	(0.00,-0.80)	(0.00,-0.44)	(0.00,0.05)
T_{close}	(0.00,0.02)	(0.00,0.04)	(0.00,0.12)	(0.00,0.28)
	(-0.00,-0.38)	(-0.00,0.11)	(-0.00,-0.04)	(-0.00,-0.17)

	BPhen:m-MTDATA (ω=0.12)	
	S0_4	T1_3
S_1-	(0.00,-0.01)	(0.00,0.00)
T_{close}	(0.00,-0.02)	(0.00,-0.00)
	(-0.00,0.06)	(-0.00,0.00)

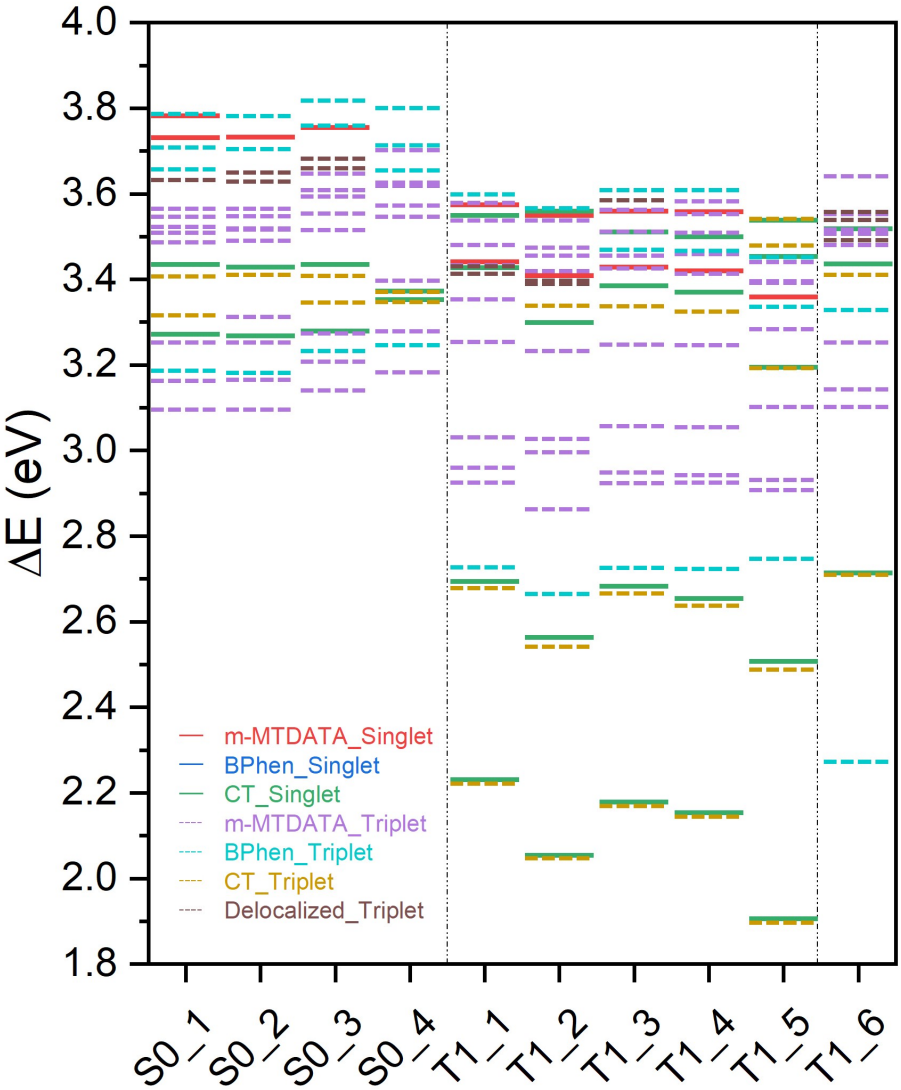

Figure 3.8: Vertical excitation energies (ΔE) calculated on various dimer structures of m-MTDATA:BPhen, TD-DFT calculations are done with the tuning factor obtained from the monomers ($\omega = 0.14$) for better comparison in between structures. Excitation energies calculated on singlet structures (S0_x) approximate the situation at absorption, those on triplet structures (T1_x) the situation at emission. The details on the distinct ground state geometries are given in the Appendix, table A.2. Colors indicate the character of the states.

Electron-hole separation and exciton size. The exciton size is directly approximated from the transition density as the root-mean-square electron-hole separation (RMSeh) as implemented in TheoDORE.[169;170] For LEs, the exciton size in this model

Table 3.17: Root-mean-squared electron-hole distances (RMSeh [Å]) which are used to approximate the exciton size for the first singlet (S_1) and first triplet (T_1) excited state. Calculations are done with ωB97X-D3/def2-SVP/ω=0.12(m-MTDATA):ω=0.16(BPhen):ω=0.12(heterodimer) with TDA-DFT in C-PCM on geometries of the singlet (S_0/S0_3) and triplet (T1_3) ground state of the systems.

geometry		m-MTDATA	BPhen	m-MTDATA:BPhen			
		S_0	S_0	S0_4	T1_3	T1_3+3 Å	T1_3+5 Å
state	S_1	4.70	3.34	6.25	5.89	8.17	9.86
	T_1	3.98	2.95	5.42	5.87	8.11[a]	3.19
	T_{CT}	-	-				10.00

a: energetically degenerate to a local triplet with a RMSeh of 3.34.

is limited by the molecule size. This is mirrored by the RMSeh values for excitations on the monomers (m-MTDATA > 3TPYMB > BPhen) (compare tables 3.11 and 3.17). All excitations on heterodimers at equilibrium in table 3.17 posses CT character. For those excitations the distance between donor and acceptor is an additional factor which influences the exciton size and especially their energetic position as pictured in figure 3.9. At slightly increased distances[9] between the molecules (+3 Å) the heterodimer still possesses a low-lying CT-triplet state in close vicinity to the S_1 as expected for TADF activity. At even bigger distances RMSeh values for CT states increase further. However, localized excitations are lower in energy than the CT states for those geometries, which is mirrored by the RMSeh for T_1. At 3.19 Å, the exciton size of this state clearly states its localization on BPhen.

The investigation was expanded to trimers by optimization with GFN2-xTB. Excitation energies on these aggregates were calculated with ωB97X-D3/def2-SVP/ω=0.14 in the same fashion as on the DFT optimized dimers. Starting points for the optimization were created as an alternating stack of molecules. For resulting structures compare figure 3.10.

[9]The intramonomer degrees of freedom were frozen and only the distance in between the center of masses of the monomers increased.

Table 3.18: Lowest local and CT triplets on a m-MTDATA (fragment 1):BPhen (fragment 2):m-MTDATA (fragment 3) trimer. Optimization was done with GFN2-xTB, excited state calculation with ωB97X-D3/def2-SVP/ω=0.14.

state	ΔE(eV)	P_R	CT	RMSeh [Å]	trans. matrix
T_{CT1}	2.90	1.29	0.79	5.84	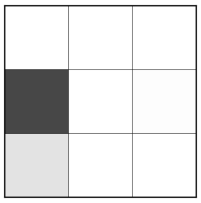
T_{CT2}	2.93	1.49	0.64	5.62	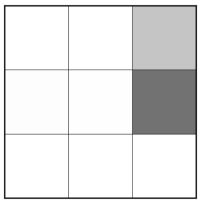
T_{LE}	3.05	1.23	0.18	4.53	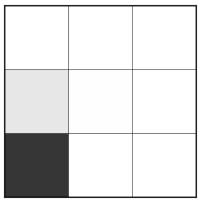

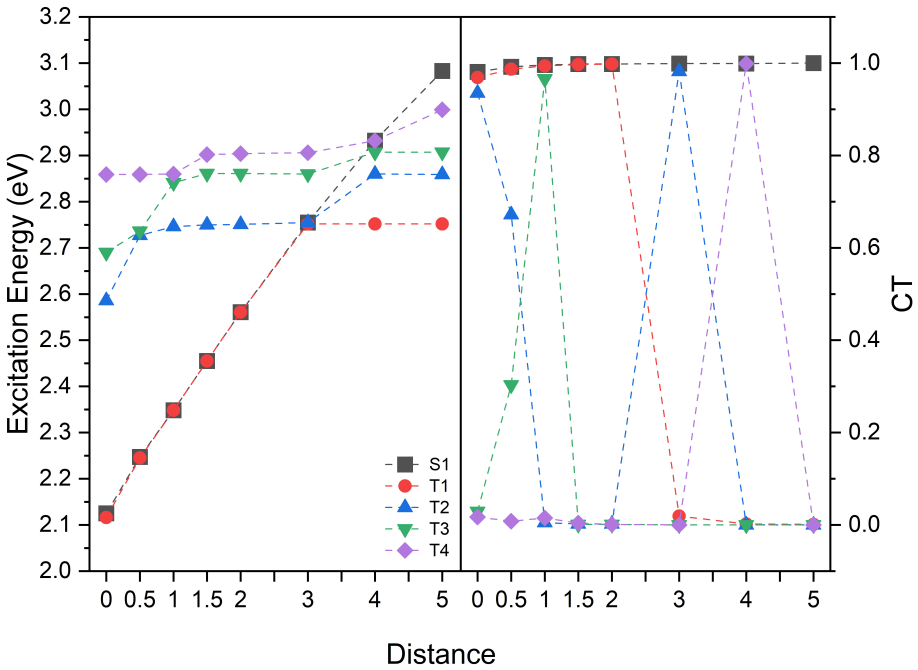

Figure 3.9: Vertical excitation energies and CT character of the lowest excited states on a m-MTDATA:BPhen heterodimer (T1_3) at different intermonomer distances. '0' refers to the optimized dimer, for the following data points the intramonomer degrees of freedom were frozen and only the distance increased by the given value in Å.

Following the reasoning of the previous section on m-MTDATA:3TPYMB, the CT triplets on the BPhen:m-MTDATA:BPhen (compare table 3.19; P_R and transition matrix) show pronounced delocalization of the hole. Therefore, heterodimers might underestimate the exciton size in the m-MTDATA:BPhen blend, if several BPhen monomers are closely aggregated in close proximity to a donor molecule.

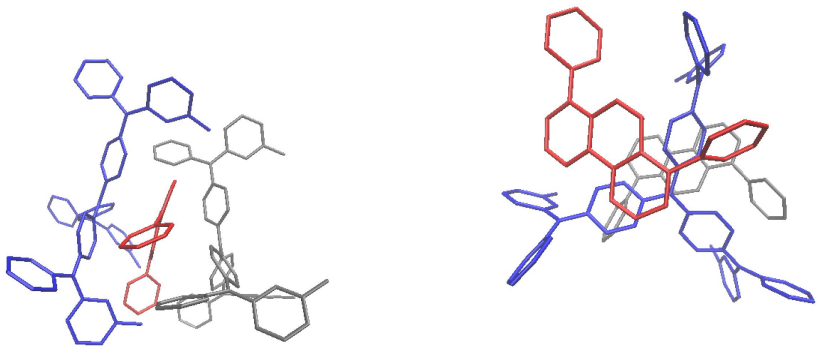

Figure 3.10: Trimers from m-MTDATA:BPhen optimized by GFN2-xTB. Left: m-MTDATA (blue, fragment 1):BPhen (red, fragment 2):m-MTDATA (grey, fragment 3); right: BPhen (red, fragment 2):m-MTDATA (blue, fragment 1):BPhen (grey, fragment 3). Hydrogen atoms are omitted for clarity.

Table 3.19: Lowest local and CT triplets on a BPhen (fragment 2):m-MTDATA (fragment 1):BPhen (fragment 3) trimer. Optimization was done with GFN2-xTB, excited state calculation with ωB97X-D3/def2-SVP/ω=0.14.

state	ΔE(eV)	P_R	CT	RMSeh [Å]	trans. matrix
T_{CT1}	2.88	1.96	0.59	5.53	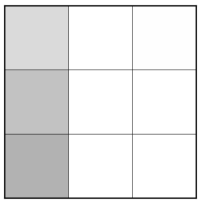
T_{CT2}	2.94	1.58	0.86	6.08	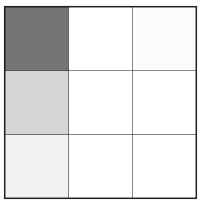
T_{LE}	3.03	1.39	0.27	4.70	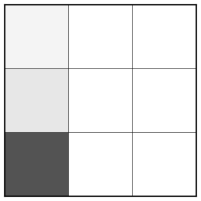

3.5 Discussion

The expectation to find low-lying triplet states in a relaxed D:A heterodimer is confirmed by the calculations, as apparent from tables 3.8 and 3.14. In all investigated dimers this lowest triplet becomes a CT state at geometrical relaxation - with one exception: For m-MTDATA:BPhen we could optimize a triplet dimer geometry (T1_6, R(T_{LE})) which exhibits a lowest triplet localized on BPhen instead of the expected CT triplet (R(T_{CT})) (figure 3.9). The existence of this low-lying triplet in the energetic range of the relaxed CT triplets is also apparent from the monomer calculations (table 3.6). Similarly, Liu et al. found an overlap of the energetic positions of the CT-triplet and the lowest m-MTDATA triplet in 3TPYMB:m-MTDATA.[165] This is matches the monomer calculations 3.6, although the local triplet for this blend was not computationally accessible.

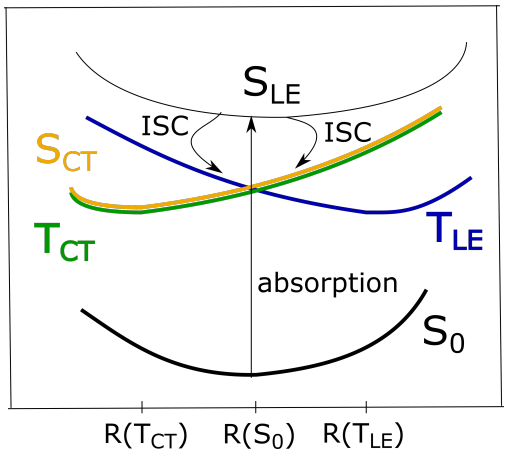

Figure 3.11: Triplet states involved in the TADF dynamics.

Excitons in the blend after optical excitation can thus either relax to a local or a CT triplet state as shown in figure 3.11, depending for example on the initial geometry of heterodimers in the film. rISC to the CT singlet is however only possible at R(T_{CT}) because of the inherent sequence of states: Calculated singlet-triplet gaps (ΔE_{ST}) for the lowest excitations at CT geometries amount to less than 0.01 eV. This allows for an effective rISC regardless of the SOC (compare tables 3.10 and 3.16). At R(T_{LE}) the lowest triplet lies almost 0.5 eV below the CT states (figure 3.9), which inhibits rISC processes to the emissive singlet. This fits the experiments by Grüne et al.[5–7;14;147] which indicate population of local triplets after optical excitation but show no involvement of those states in processes leading to luminescence.

Among the central results of the experimental study by optically detected magnetic resonance (ODMR) are two signals in trPLDMR but only one in trELDMR.[5–7;14;147] The broader signal in trPLDMR indicates an electron-hole separation[10] of $r_{e-h} \geq 1.0$ nm (m-MTDATA:3TPYMB)[6] and $r_{e-h} \geq 0.9$ nm (m-MTDATA:BPhen)[147]. While this

[10]Electron-hole separations are estimated from EPR spectra by $r_{e-h}[\mathrm{nm}] = \sqrt[3]{\frac{2.785}{D[\mathrm{mT}]}}\,\mathrm{nm}$, where D is the dipolar-coupling.

signal was formerly attributed to a local triplet,[6] the calculated RMSeh values suggest that this is indeed a compact CT triplet. New trEPR measurements back the new assignment.[147] TrEPR show an additional considerably broader signal (smaller exciton) which is attributed to a local triplet but is not apparent in the optical response in trPLDMR.[14;147] The narrow signal in trPLDMR and the main signal in trELDMR presumably stem from the same process (same trend in behaviour at varying temperatures and magnetic fields) and yield electron-hole separations of $r_{e-h} \geq 1.2\,\mathrm{nm}$ (electrical generation) or $r_{e-h} \geq 1.4\,\mathrm{nm}$ (optical generation) in m-MTDATA:3TPYMB.[6] The narrow signal from m-MTDATA:BPhen indicates $r_{e-h} = 1.1\,\mathrm{nm} - 1.2\,\mathrm{nm}$ (electrical generation).[172] These signals are attributed to non-geminate exciplexes. After electrical generation this can be explained by charge carriers which undergo rISC as soon as they get in contact as ΔE_{ST} becomes infinitely small for CT states and large HOMO-LUMO separations. In optical experiments diffusion is postulated to take place after population of the CT states which triggers a process similar to that after electrical excitation.

At this point, seemingly two discrepancies between calculations and experimental findings remain: For intermolecular distances increased by more than 2.0 Å, we calculate various local triplet states to be found below the CT-triplet and singlet (compare figures 3.5 and 3.9) although the exciton size found experimentally indicates such long distances between monomers. However, CT singlet and triplet are almost degenerate for those systems ($\Delta E < 0.002\,\mathrm{eV}$). Since recombination/population of a local triplet might not be possible at these distances, rISC might still happen between $T_{n,CT}$ and S_1. Additionally, the calculated S_1 lies too high in energy for stretched excitons in comparison to the experiment. This reinforces the idea that prior to emission from the S_1, the distance between the electrons must be diminished to facilitate a non-zero transition moment, which than results in emission from a lower point of the S_1 surface.

3.6 Conclusion

The investigations on monomers, neutral heterodimers and CT heterodimers match the experimental results and can expand the robustness and accuracy of models on exciton dynamics in OLED devices. To obtain sufficient precision in the calculations, the method and environment need to be chosen carefully. In this case and for other OSC materials (compare chapter 2), IP tuning presents a very beneficial compromise of accuracy and cost.

It is apparent from the sequence of excited states (figures 3.5 and 3.9) that optical

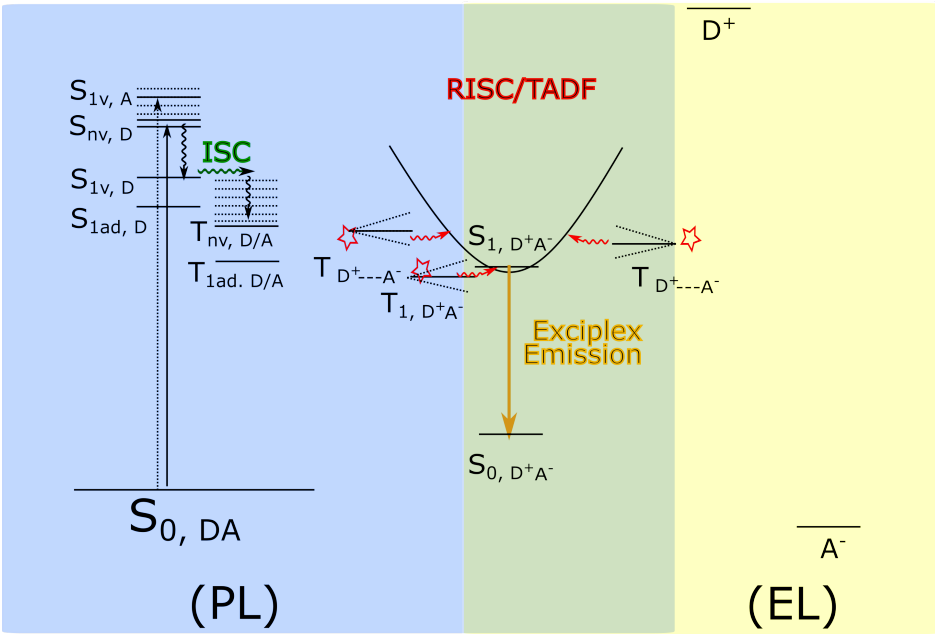

Figure 3.12: Processes after excitation in TADF D:A complexes.

excitation of the lowest singlets in the donor (and acceptor, depending on the wavelength of the pump-pulse) facilitates the population of local triplet states. These states are not expected to be populated after electrical excitation, the standard work-mode of an OLED. Results of optical experiments can therefore not be directly transferred to obtain knowledge of optimized OLED devices. Nevertheless it is of interest to unravel the processes after optical excitations. Optical spectroscopic results can often be modelled by quantum chemical calculations and serve as benchmarks. These can therefore provide a reliable basis for theoretical investigations to tackle less transparent problems.

For the investigated system, ODMR measurements were dominated by two signals after optical excitation and one after electrical excitation.[6;7;14;147] The signal in ELDMR resembles the narrower one of PLDMR in width, shape and temperature dependence and was therefore experimentally attributed to the same process.[6] The calculated results on model D:A dimers are attributed to the broader signal of PLDMR. The calculated RMSeh values for an optimized triplet are 0.8 nm (m-MTDATA:3TPYMB, table 3.11, experimentally 1.0 nm) and 0.6 nm (m-MTDATA:BPhen, table 3.11, experimentally 0.9 nm). The broader signal showed a stronger dependence on the choice of acceptor molecule[6;147] than the narrow signal, which is mirrored by the optimized model heterodimers. BPhen is smaller than 3TPYMB and allows for a more compact packing if a full geometrical relaxation is possible. Less system dependence of the narrower/ELDMR signal indicates that this is induced by stretched dimers (i.e. charge

carriers interacting across a distance) and could be approximated by variation of the distance of the monomers in model systems (tables 3.11 and 3.17). A local excitation was calculated to result in a RMSeh of at most 0.3 nm (BPhen), 0.4 nm (3TPYMB) and 0.5 nm (m-MTDATA). Also these states were calculated to be energetically strongly separated from the emissive singlet at exciplex geometries. It is therefore proposed that local triplet excitations do not directly influence emission dynamics in the investigated D:A systems but might rather result in radiation-less deexcitation when populated.

Chapter 4

Investigation of organometallic bismuth radicals

This collaborative work reports the generation of a new species, a non-stabilized organometallic bismuthidene. Our computational work fused the various spectroscopic investigations to provide a clear picture of involved configurations and vibronic states. In contrast to the previous chapters, the difficulties in describing the systems under investigation are not caused by their size. There is however a new computational bottleneck which arises from the heaviness of bismuth and the subsequent need to include relativistic effects in the theoretical treatment.[75;76] An overview of the treatment of relativistic effects employed in this work can be found in chapter 0.3.4, for further reading please refer to the references mentioned therein and in the paper. As a compromise between accuracy, computational resources and availability of methods, we resorted to scalar relativistic DFT with an all-electron treatment for most optimizations and all frequency calculations.[80;173;174] It was shown before that DFT can provide very accurate structures even for complicated electronic configurations,[175] while lacking some accuracy in the computation of excitation energies.[176] Therefore, we supplemented these results by excitation energies and benchmark geometry optimizations calculated by NEVPT2 in the same scalar relativistic framework. This framework allows for the inclusion of effects introduced by relativistic mass increase of electrons which are responsible for the contraction/expansion of orbitals.[43]

Within this framework we were able to reproduce single-molecule photoelectron spectra and determine the geometries of decay products. The focus of the investigations was on $BiCH_3$. In accord with the experimental results we found the ground state of this species to be a triplet and therefore a biradical. Closer inspection of the photoelectron spectrum of this species revealed a further anomaly. The spectrum could not be modelled taking into account only the ground state vibrations of the cationic species. In

the neutral species the two singly occupied orbitals mainly resemble the p_x/p_y-orbitals of bismuth (the Bi-C bond is assumed to lie in z-direction). After ionization the degeneracy of this orbitals is lifted due to a Jahn-Teller distortion. This results in two distinct excited states with an energy gap calculated to be only 50 meV. Combining the vibronic features of both low-lying cationic states allows for the calculation of the full photoelectron spectrum.

This paper was published in D. P. Mukhopadhyay, D. Schleier, S. Wirsing, J. Ramler, D. Kaiser, E. Reusch, P. Hemberger, T. Preitschopf, I. Krummenacher, B. Engels, et al., *Methylbismuth: an organometallic bismuthinidene biradical*, Chemical Science **11**, 7562–7568 (2020). Reprinted from reference [24] with permission from the Royal Society of Chemistry.

Chemical Science

ROYAL SOCIETY OF CHEMISTRY

EDGE ARTICLE

View Article Online
View Journal | View Issue

Check for updates

Cite this: *Chem. Sci.*, 2020, **11**, 7562

All publication charges for this article have been paid for by the Royal Society of Chemistry

Methylbismuth: an organometallic bismuthinidene biradical†

Deb Pratim Mukhopadhyay,[a] Domenik Schleier,[a] Sara Wirsing,[a] Jacqueline Ramler,[b] Dustin Kaiser,[a] Engelbert Reusch,[a] Patrick Hemberger,[c] Tobias Preitschopf,[a] Ivo Krummenacher,[b] Bernd Engels,*[a] Ingo Fischer*[a] and Crispin Lichtenberg*[b]

Received 28th April 2020
Accepted 2nd June 2020

DOI: 10.1039/d0sc02410d

rsc.li/chemical-science

We report the generation, spectroscopic characterization, and computational analysis of the first free (non-stabilized) organometallic bismuthinidene, BiMe. The title compound was generated *in situ* from $BiMe_3$ by controlled homolytic Bi–C bond cleavage in the gas phase. Its electronic structure was characterized by a combination of photoion mass-selected threshold photoelectron spectroscopy and DFT as well as multi-reference computations. A triplet ground state was identified and an ionization energy (IE) of 7.88 eV was experimentally determined. Methyl abstraction from $BiMe_3$ to give $[BiMe_2]^\bullet$ is a key step in the generation of BiMe. We reaveal a bond dissociation energy of 210 ± 7 kJ mol^{-1}, which is substantially higher than the previously accepted value. Nevertheless, the homolytic cleavage of Me–$BiMe_2$ bonds could be achieved at moderate temperatures (60–120 °C) in the condensed phase, suggesting that $[BiMe_2]^\bullet$ and BiMe are accessible as reactive intermediates under these conditions.

Introduction

Low-valent molecular compounds of group 15 elements, E–R, with the central atom E in the oxidation state of +1 are highly reactive, electron-deficient species (E = N–Bi; R = monoanionic ligand).[1] In principle, they can adopt either singlet or triplet electronic ground states, which strongly influences their physical and chemical properties (Scheme 1). Thus, understanding their (electronic) structures is key to rationalizing the reactivity of these species, which represent important intermediates in fundamental transformations such as insertion and ring expansion reactions.[2] The isolation of such compounds, in which the group 15 atom is bound to only one additional atom, is extremely challenging and has only recently been achieved for the lightest congeners in landmark contributions (E = N, P, Scheme 1a).[2,3] Access to the heavier homologues is increasingly difficult due to their tendency to undergo degradation reactions such as oligomerization, disproportionation, and bond activation processes. For the heaviest group 15 element bismuth, mononuclear organometallic compounds with the metal atom in the oxidation state of +1 (so-called bismuthinidenes) could so far only be accessed by stabilization through adduct formation with Lewis bases (Scheme 1b).[4–9] Very recently, the intriguing properties of such bismuthinidenes have been exploited for (electro-)catalytic and photophysical applications: a Bi^{I}/Bi^{III} redox couple has been proposed to be a key component in bismuth-catalyzed transfer hydrogenation reactions with ammonia borane.[10] In addition, Bi^{I} oxalates have been suggested to be involved in the electrochemical reduction of carbon dioxide at bismuth electrodes.[11] When embedded in host materials such as zeolites, $[Bi^{I}]^{+}$ centers show intriguing photophysical properties such as ultrabroad near-infrared emission.[12,13] Without any exceptions, the isolable, Lewis-base-stabilized bismuthinidenes reported to date show singlet ground states. This situation changes, when non-stabilized, (so far) non-isolable, electron-deficient molecular bismuthinidenes, Bi–R, are targeted. To date, only inorganic species Bi–X have been reported and were accessed by comproportionation (*e.g.* at high temperature in the melt) or by reaction of Bi atoms with reactive species such as F_2 in the gas phase (X = H, F–I, $AlCl_4$).[14–18] Importantly, these synthetic routes did not allow to study the reactivity of bismuthinidenes, they did not allow to work in conventional solvents at moderate temperature, and they did not allow to access compounds with tunable substituents R, such as organometallic bismuthinidenes Bi–R (R = alkyl, aryl; Fig. 1c).

[a]*Institute of Physical and Theoretical Chemistry, University of Würzburg, Am Hubland, D-97074 Würzburg, Germany. E-mail: bernd.engels@uni-wuerzburg.de; ingo.fischer@uni-wuerzburg.de*

[b]*Institute of Inorganic Chemistry, University of Würzburg, Am Hubland, D-97074 Würzburg, Germany. E-mail: crispin.lichtenberg@uni-wuerzburg.de*

[c]*Laboratory for Femtochemistry and Synchrotron Radiation, Paul Scherrer Institut (PSI), CH-5232 Villigen, Switzerland. E-mail: patrick.hemberger@psi.ch*

† Electronic supplementary information (ESI) available. CCDC 1991253. For ESI and crystallographic data in CIF or other electronic format see DOI: 10.1039/d0sc02410d

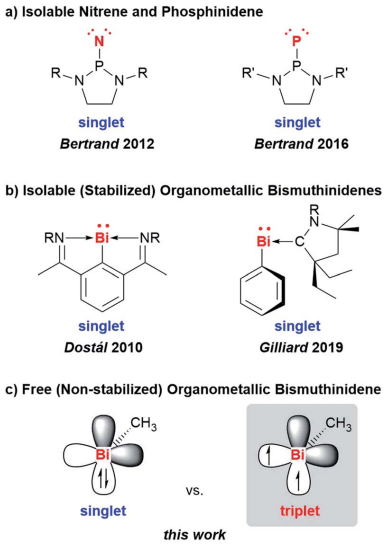

Scheme 1 Low-valent group 15 compounds: (a) isolable nitrene and phosphinidene (singlet ground state). (b) stabilized organometallic bismuthinidenes (singlet ground state; occupied bismuth 6s-orbital omitted for clarity); (c) free (non-stabilized) singlet and triplet species that may be envisaged for BiMe (only two bismuth p-orbitals shown; p-orbital used for Bi–Me bonding and occupied s-orbital are omitted for clarity). R = 2,6-Me_2-C_6H_3; 2,6-iPr_2-C_6H_3; R′ = 2,6-[(4-*t*Bu-C_6H_4)$_2$CH]$_2$-4-Me-C_6H_3.

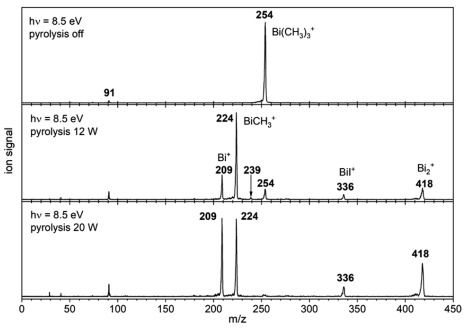

Fig. 1 Photoionization mass spectra recorded at 8.5 eV without pyrolysis (top trace), low pyrolysis power ($T \approx 470$ K, center trace) and medium pyrolysis power ($T \approx 600$ K, bottom trace). The signal at $m/z = 91$ is due to a background signal from previous experiments.

Here we report the generation and characterization of the first free (*i.e.* non-stabilized) organometallic bismuthinidene methylbismuth, BiMe, in a gas-phase reaction with implications for related reactions in condensed phase at moderate temperature. In addition, dimethylbismuth, $[BiMe_2]^{\bullet}$ was studied to determine the Bi–CH_3 bond dissociation energy in $BiMe_3$.

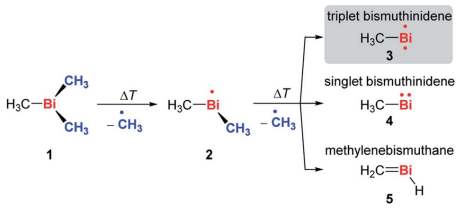

Scheme 2 Controlled, stepwise abstraction of CH_3 radicals from **1** in the gas phase by flash pyrolysis.

Results and discussion

In order to access the elusive class of non-stabilized organometallic bismuthinidenes, we aimed at a "top-down approach", more specifically the homolytic cleavage of Bi–C bonds from the well-defined organometallic precursor $BiMe_3$ (**1**) as shown in Scheme 2. The long-known $BiMe_3$ has been investigated from many different perspectives,[19–21] including its application in chemical vapor deposition, where the abstraction of all its methyl groups is targeted.[22,46]

In a recent study, it was demonstrated that the abstraction of a single methyl group can be achieved by dissociative photoionization of **1**, *i.e.* the Bi–C bond cleavage of the $[BiMe_3]^{\bullet+}$ cation in the gas phase.[23] Under these conditions, only a single methyl group was abstracted, yielding the cation $[BiMe_2]^+$. Here we attempt a thermally-induced, controlled and stepwise abstraction of methyl groups from neutral $BiMe_3$. Thus, a sample of $BiMe_3$ diluted in Ar was pyrolysed in a microreactor and analyzed by photoelectron–photoion coincidence spectroscopy (PEPICO) using synchrotron radiation.[24] This method permits to record photoion mass-selected threshold photoelectron spectra (ms-TPE) for each species by correlating ions and electrons produced in a single photoionization event. Isomer-selective information is then obtained from an analysis of the photoelectron spectrum based on computations.

Fig. 1 shows mass spectra under various pyrolysis conditions. Without pyrolysis (top trace) only the parent ion $\mathbf{1}^{\bullet+}$ is visible, thus dissociative photoionization is irrelevant under our experimental conditions. Already at low pyrolysis power (center trace) a stepwise methyl loss down to atomic Bi occurs, associated with formation of **2** and one of the products **3–5**. The small intensity of $m/z = 239$ ($[Bi(CH_3)_2]^+$) compared to $m/z = 224$ ($[BiCH_3]^{\bullet+}$) indicates that cleavage of the second methyl group is more facile than the first. In addition, Bi_2 is visible at $m/z = 418$, due to dimerization of bismuth atoms (see ESI, Fig. S4†). In some experiments a further peak appeared at $m/z = 478$ and is most likely due to Me_2Bi–$BiMe_2$. Note that CH_3 is not observed due to its ionization energy of 9.83891 eV.[25,26] Traces of BiI from the synthesis are also present in the spectrum.

When the pyrolysis power is further increased (bottom trace) the precursor is fully converted and experimental conditions are suitable for studying the molecule formed after loss of two methyl groups. Three structures are possible for $m/z = 224$, the bismuthinidenes **3** (triplet)/**4** (singlet) or the methylenebismuthane **5**. Threshold photoelectron spectroscopy provides structural isomer-selective information through comparison with Franck–Condon-simulated or reference spectra. Fig. 2 represents the ms-TPE spectrum of a species with the composition $BiCH_3$ at $m/z = 224$. The first major band at 7.88 eV is assigned to the adiabatic ionization energy (IE_{ad}). It is followed by several smaller bands that are *ca.* 40–50 meV apart. Simulations based on DFT and multi-reference calculations were carried out for **3**, **4** and **5**. While DFT often provides very accurate geometries and frequencies even for molecules with complicated electronic structures,[48] it is in many cases less accurate for the computation of energy surfaces or excitation energies.[49] Hence, the ωB97X-D3 [50] functional was employed for frequency computations, but the multi-reference NEVPT2 [51] approach was used to determine geometrical changes and to compute ionization energies as well as the energy difference between the two relevant states of the $[BiCH_3]^{\bullet+}$ cation (*vide infra*). Both methods (DFT and multi-reference) were combined with a scalar relativistic approach and with the SARC-ZORA-TZVP basis set which allows for an all-electron treatment of bismuth[52] (for computational details, see ESI†). Bismuthinidene **3** with a C_{3v} symmetry and an $X\,^3E$ (T_0) triplet ground state is the lowest-energy structure ($\Delta E = 0$ kJ mol^{-1}). The computations on the NEVPT2-level show a very good agreement with the experimentally determined IE of 7.88 eV ($IE_{calc} = 7.98$ eV for the $X^+\,^2A'' \leftarrow X\,^3E$ transition (*vide infra*)), as compared to singlet bismuthinidene **4** ($\Delta E = +0.78$ eV/+75 kJ mol^{-1}; $IE_{calc} = 7.21$ eV) and methylenebismuthane **5** ($\Delta E = +0.91$ eV/+88 kJ mol^{-1}; $IE_{calc} = 8.68$ eV; for energy values obtained through DFT calculations see ESI†). This shows, that the ground state (electronic) structure of species with the sum formula ECH_3 are fundamentally different, depending on the choice of the element E. For E = Bi the triplet bismuthinidene **3** is energetically favored and observed (*vide supra*), whereas for the lighter congeners (E = N, P), the formation of the methylene species $HN{=}CH_2$ and $HP{=}CH_2$ has been determined to be more favorable.[27–32,53]

Upon photoionization of **3**, one electron is removed from either of the two degenerate SOMOs, which correspond in first approximation to the p_x and p_y orbital on the Bi center. The computations for the ionic ground state, $[BiCH_3]^{\bullet+}$ ($\mathbf{3}^{\bullet+}$), yielded a shortening of the Bi–C bond (from 2.27 Å in **3** to 2.21 Å in $\mathbf{3}^{\bullet+}$) and a deformation of the methyl group with a tilt angle of 4° relative to the Bi–C axis. This was ascribed to antibonding interactions between the unpaired electron and the bonding electrons of the two C–H groups, which are approximately aligned with the singly occupied p-type orbital of bismuth (Table S18†). This leads to a loss of the C_3 axis and a reduction to C_s symmetry. As a consequence of this Jahn–Teller distortion, the ^2E state in the C_{3v} symmetric cation splits into a $X^+\,^2A''$ and a $A^+\,^2A'$ component. The computations indicate an energy difference of only 50 meV between the two states at the geometry of the $X^+\,^2A''$. Thus, transitions into both states contribute

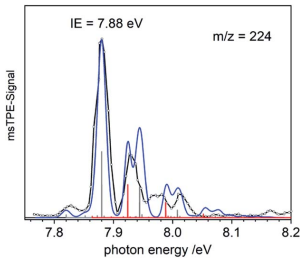

Fig. 2 Mass-selected threshold photoelectron spectrum of $m/z = 224$. The simulation based on **3** as the carrier (blue line) fits the experiment well. Transitions into the $X^+\,^2A''$ ground state of the ion are given as grey bars, transitions into the $A^+\,^2A'$ state as red bars.

to the spectrum and have to be included in the simulation in Fig. 2 (blue curve). Transitions from the T_0 ground state of neutral **3** into the $X^+\,^2A''$ ionic ground state are given as grey bars, while transitions into the $A^+\,^2A'$ excited state are shown as red bars. In addition, there is a vibrational structure evident in the spectrum with a spacing of around 50 meV, including a hot band transition at 7.83 eV, which is assigned to the Bi–C stretching motion (corresponding to $\nu'' \approx 50$ meV). Vibrational activity is expected due to the reduction of the Bi–C bond lengths in the cation by > 0.06 Å (see ESI† for all geometry parameters). Franck–Condon simulations based on computations of isomer **5** further support the triplet bismuthinidene **3** as the carrier of the spectrum (Fig. S3†). First, the computed IE of **5** is 0.80 eV higher than the experimental value, and second, a more pronounced vibrational progression with a maximum intensity for a transition into an excited vibrational state would be expected for **5**. Thus a contribution of **5** to the spectrum can be ruled out.

The computed IE of **3** (for the lowest state of $\mathbf{3}^{\bullet+}$) and the relative energies for the two states of the cation $\mathbf{3}^{\bullet+}$ are in excellent agreement with the corresponding experimental data. This indicates that the neglected spin–orbit effects[33] do not play a key role for the determination of the ionization energies, possibly because they are similar in magnitude for all involved states. While the experimental and calculated IEs nicely agree, deviations were observed in the shape of the spectra and were ascribed to the flatness of the potential energy surface (PES) of the cation. Two factors mainly contribute to the flatness of this PES: (i) the $X^+\,^2A''$ state is threefold degenerate due to facile rotation around the Bi–C bond. (ii) The shape of the PES going from the equilibrium geometry of the $X^+\,^2A''$ towards the equilibrium geometry of the $A^+\,^2A'$ state is expected to be non-harmonic. Efforts to obtain a better description of the surface were so far unsuccessful due to strong correlations of the various internal coordinates, so that high dimensional surfaces would be necessary for an appropriate description.

To gain additional information on the formation of BiMe (**3**) by stepwise abstraction of methyl groups from $BiMe_3$ (**1**), an ms-TPE spectrum of $[BiMe_2]^{\bullet}$ (**2**) ($m/z(\mathbf{2}^+) = 239$) was recorded at

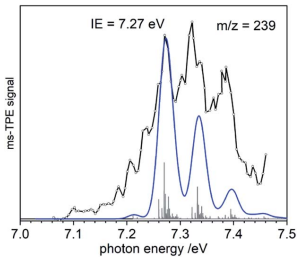

Fig. 3 Ms-TPE spectrum of $Bi(CH_3)_2$, $m/z = 239$. The vibrational progression is due to the symmetric bismuth–carbon stretch and its combination with torsional motion. The blue line represents the simulated spectrum based on **2**.

a low pyrolysis temperature (Fig. 3; *cf.* Fig. 1). Simulations of the spectrum based on DFT calculations indicate C_{2v} symmetry for both **2** and $\mathbf{2}^+$ as well as a $X^+\,{}^1A_1 \leftarrow X\,{}^2B_1$ transition in $[BiMe_2]^\bullet$ (**2**). The first major band at 7.27 eV is assigned to the IE, in excellent agreement with the computed value of 7.35 eV at the NEVTP2 level of theory. A vibrational progression with a spacing of 60 meV is visible and is dominated by the symmetric Bi–C stretching mode in the cation. Additional torsional modes of the CH_3 groups may lead to a broadening of the bands. While there is a good agreement between simulation and experiment, the vibrational intensities (including hot bands) are somewhat underestimated in the simulations. This indicates a slightly larger change of the Bi–C bond length upon ionization than the computed shortening of 0.05 Å (see ESI† for all geometry parameters).

Bond dissociation energies (BDEs) can be determined *via* thermochemical cycles that combine appearance energies (AE) and ionization energies. The zero Kelvin appearance energy AE_{0K} for the abstraction of the first methyl radical from **1** has been determined with very high accuracy, $AE_{0K}(Bi(CH_3)_3, Bi(CH_3)_2^+) = 9.445 \pm 0.064$ eV.[23] According to computations, the methyl loss in the cation is a simple homolytic bond cleavage without a reverse barrier. Combined with the IE of **2**, the Me_2Bi–CH_3 bond dissociation energy in **1**, $BDE(Me_2Bi–CH_3)$, can be derived:

$$BDE(Me_2Bi–CH_3) = AE_{0K}(BiMe_3, [BiMe_2]^{\bullet+}) - IE([BiMe_2]^\bullet) \quad (1)$$

From eqn (1) a value of 210 ± 7 kJ mol^{-1} is obtained for $BDE(Me_2Bi–CH_3)$. The bond dissociation energy of the first Bi–CH_3 bond in $BiMe_3$ ($BDE(Me_2Bi–CH_3)$) can be expected to be the highest of the three Bi–CH_3 BDEs in this molecule[34] and is thus crucial for any type of reaction initiation *via* Bi–CH_3 homolysis. However, the value of $BDE(Me_2Bi–CH_3)$ has never been determined explicitly in the primary literature. Based on previous investigations into the thermal decomposition of **1**,[34–36] an estimation of $BDE(Me_2Bi–CH_3)$ can be made, which yields a value of 182 kJ mol^{-1} as the upper limit that would be possible for this parameter.[37] Thus, our results substantially revise the bond dissociation energy of the first Bi–Me bond in **1**, which is

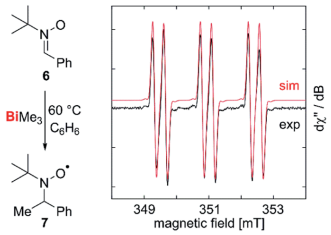

Fig. 4 Abstraction and spin trapping of methyl radicals from $BiMe_3$.

key to the radical chemistry of **1** and related bismuth compounds. The calculated isodesmic reaction provides a value of 226 kJ mol^{-1} in good agreement with the experimental findings.

Our correction of the BDE in a fundamentally important organometallic compound such as $BiMe_3$ raised the question, whether homolytic Bi–C bond cleavage is possible at moderate reaction temperatures in the condensed phase, making this process relevant for synthetic chemistry under conventional experimental conditions. To test for methyl radical abstraction from $BiMe_3$, a benzene solution of $BiMe_3$ and the radical trap **6** was heated to 60 °C and subsequently analyzed by EPR spectroscopy (Fig. 4). Indeed, a resonance was detected with $g_{iso} = 2.006$ and $a(^{14}N) = 41.6$ MHz, $a(^1H) = 9.63$ MHz, $a(^{13}C) = 12.9$ MHz, indicating the formation of **7** by methyl radical transfer.[38,54,55]

In order to gain further hints at the generation and subsequent trapping of BiMe in the condensed phase, neat $BiMe_3$ was

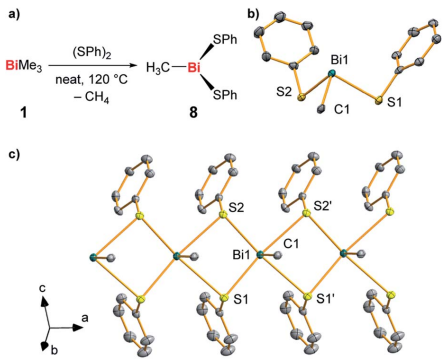

Fig. 5 (a) Synthesis of $BiMe(SPh)_2$ (**8**) from $BiMe_3$ and $(SPh)_2$ with methane as a detected by-product. (b and c) Molecular structure of **8** in the solid state with one formula unit shown in (b) and a cutout of the coordination polymer shown in (c). Displacement ellipsoids are shown at the 50% probability level. Hydrogen atoms and one set of split positions of disordered atoms are omitted for clarity. For detailed discussion of structural parameters see ESI.† Selected bond lengths (Å) and angles (°): Bi1–C1, 2.208(10); Bi1–S1, 2.736(2); Bi1–S2, 2.699(2); C1–Bi1–S1, 89.6(3); C1–Bi1–S2, 89.4(3); S1–Bi1–S2, 93.18(7).

reacted with stoichiometric amounts of $(PhS)_2$ at 120 °C (Fig. 5a). $BiMe(SPh)_2$ (**8**)[39–41] was isolated as the product of this reaction in 41% yield and fully characterized (Fig. 5b and c; for details see ESI†). Methane was detected in the headspace of the reaction by IR spectroscopy (Fig. S5†), suggesting the appearance of methyl radicals in this reaction.

This – together with literature reports[42] – supports the potential of BiMe to act as a transient reactive species in this reaction. The thioether MeSPh was also detected, suggesting that methyl radical attack at sulfur or σ-bond metathesis/disproportionation sequences may also be operative as a parallel reaction pathway.[41] In the solid state, compound **8** forms a coordination polymer through bridging coordination modes of the thiolate ligands (Fig. 5c). This is a unique structural feature within the small number of literature-known compounds $BiR(SR')_2$ (R, R′ = aryl, alkyl; for details see ESI†).[42–45]

Conclusions

In conclusion, we have generated methylbismuth (BiMe), a fundamental organometallic compound and the first example of an organometallic non-stabilized bismuthinidene. BiMe was accessed *via* controlled thermal homolysis in the gas phase. The title compounds shows a triplet (biradical) ground state and an ionization energy of 7.88 eV, as revealed by combination of photoelectron spectroscopy and computations. The homolytic dissociation of the first $Me_2Bi–CH_3$ bond in $BiMe_3$ is crucial to the radical chemistry of this compound (and related species) and is the initiating step in the formation of BiMe. Our results reveal a $Me_2Bi–CH_3$ homolytic bond dissociation energy of 210 ± 7 kJ mol^{-1}, *i.e.* the previously reported value is revised by more than +15% (+28 kJ mol^{-1}). Nevertheless, reactions in the condensed phase demonstrate that the abstraction of methyl radicals from $BiMe_3$ is possible at moderate reaction conditions and suggest that BiMe may act as an intermediate in reactions with suitable trapping reagents. Future research will be directed towards the generation of non-stabilized bismuthinidenes and their exploitation in synthetic chemistry.

Methods and experimental

Details of experimental conditions for synchrotron experiments, for calculations with DFT and multi-reference methods, for the preparation of compounds **1** and **8** (including two methods for the preparation of **1** [19]), and for IR and EPR spectroscopic experiments are given in the ESI.†

All calculations were performed with the ORCA program package, version 4.1.1 and 4.2.[56]

The spectroscopic experiments were carried out at the VUV beamline of the Swiss Light Source (SLS) at the Paul-Scherrer Institute, Villigen/CH. In most experiments the photon energy was scanned in 5 meV steps and calibrated using autoionization resonances in Ar. The ionization energies reported in the main paper are accurate to within ±20 meV and were corrected for the Stark-shift by the extraction field (8–9 meV). Note that in some experiments 10 meV steps were used. A detailed description of the beamline is given in the literature.[47]

[$MeBi(SPh)_2$] (8).[39]

Neat trimethyl bismuth (100 mg, 0.394 mmol) and diphenyl disulfide (85.9 mg, 0.393 mmol) were heated to 120 °C for 3 d. After cooling to ambient temperature, a green solid was obtained, which was dissolved in benzene (1.5 mL) and layered with *n*-pentane (1.5 mL). After 16 h at ambient temperature, the product could be isolated by filtration and dried *in vacuo* as yellow needles. Yield: 70.8 mg, 0.160 mmol, 41%.

^{1}H NMR (500 MHz, C_6D_6): $\delta = 0.94$ (s, 3H, CH_3), 6.86 (dd, 2H, $^3J_{HH} = 7.4$ Hz, $^3J_{HH} = 7.5$ Hz, *p*-C_6H_5), 7.03 (t, 4H, $^3J_{HH} = 7.6$ Hz, *m*-C_6H_5), 7.48 (d, 4H, $^3J_{HH} = 7.8$ Hz, *o*-C_6H_5) ppm.

^{13}C NMR (126 MHz, C_6D_6): $\delta = 40.40$ (br, CH_3), 127.29 (s, *p*-C_6H_5), 128.60 (s, *m*-C_6H_5), 135.62 (s, *o*-C_6H_5), 136.06 (s, *ipso*-C_6H_5) ppm.

Elemental analysis: anal. calc. for: [$C_{13}H_{13}BiS_2$] (442.35 g mol^{-1}): C 35.30, H 2.96, S 14.50; found: C: 35.12, H 2.90, S 14.40.

Conflicts of interest

There are no conflicts to declare.

Author contributions

DPM, DS, ER and PH carried out the synchrotron radiation experiments, JR carried out all synthetic work, SW and DK performed the computations, IK performed the ESR and TP the IR spectroscopy. IF, BE and CL planned the project, contributed to the interpretation of the results and wrote the manuscript.

Acknowledgements

Funding by the DFG (funding to CL, IF (FI575/13-1) and through GRK2112), by the Swiss Federal Office for Energy (BFE Contract Number SI/501269-01), and the FCI (PhD and Liebig scholarships to DK and CL) are gratefully acknowledged. CL thanks Prof. Holger Braunschweig for continuous support. The spectroscopic experiments were performed at the VUV beamline of the Swiss Light Source, located at the Paul Scherrer Institute (PSI).

Notes and references

1 L. Dostál, *Coord. Chem. Rev.*, 2017, **353**, 142–158.
2 F. Dielmann, O. Back, M. Henry-Ellinger, P. Jerabek, G. Frenking and G. Bertrand, *Science*, 2012, **337**, 1526–1528.
3 L. Liu, D. A. Ruiz, D. Munz and G. Bertrand, *Chem*, 2016, **1**, 147–153.
4 P. Šimon, F. de Proft, R. Jambor, A. Růžička and L. Dostál, *Angew. Chem., Int. Ed.*, 2010, **49**, 5468–5471.
5 I. Vranova, M. Alonso, R. Lo, R. Sedlak, R. Jambor, A. Ruzicka, F. De Proft, P. Hobza and L. Dostál, *Chem.–Eur. J.*, 2015, **21**, 16917–16928.

6 I. Vranova, M. Alonso, R. Jambor, A. Ruzicka, M. Erben and L. Dostál, *Chem.–Eur. J.*, 2016, **22**, 7376–7380.
7 G. C. Wang, L. A. Freeman, D. A. Dickie, R. Mokrai, Z. Benkő and R. J. Gilliard, *Chem.–Eur. J.*, 2019, **25**, 4335–4339.
8 C. Lichtenberg, *Angew. Chem., Int. Ed.*, 2016, **55**, 484–486.
9 A. M. Arif, A. H. Cowley, N. C. Norman and M. Pakulski, *J. Am. Chem. Soc.*, 1985, **107**, 1062–1063.
10 F. Wang, O. Planas and J. Cornella, *J. Am. Chem. Soc.*, 2019, **141**, 4235–4240.
11 M. C. Thompson, J. Ramsay and J. M. Weber, *Angew. Chem., Int. Ed.*, 2016, **55**, 15171–15174.
12 H. T. Sun, Y. Matsushita, Y. Sakka, N. Shirahata, M. Tanaka, Y. Katsuya, H. Gao and K. Kobayashi, *J. Am. Chem. Soc.*, 2012, **134**, 2918–2921.
13 H. T. Sun, Y. Sakka, N. Shirahata, Y. Matsushita, K. Deguchi and T. Shimizu, *J. Phys. Chem. C*, 2013, **117**, 6399–6408.
14 E. H. Fink, K. D. Setzer, D. A. Ramsay, M. Vervloet and J. M. Brown, *J. Mol. Spectrosc.*, 1990, **142**, 108–116.
15 J. D. Corbett, *J. Am. Chem. Soc.*, 1958, **80**, 4257–4260.
16 P. Kuijpers and A. Dymanus, *Chem. Phys. Lett.*, 1976, **39**, 217–220.
17 E. H. Fink, K. D. Setzer, D. A. Ramsay and M. Vervloet, *Chem. Phys. Lett.*, 1991, **179**, 95–102.
18 R. A. Lynde and J. D. Corbett, *Inorg. Chem.*, 1971, **10**, 1746–1749.
19 K. Schäfer and F. Hein, *Z. Anorg. Allg. Chem.*, 1917, **100**, 249–303.
20 S. Schulz, A. Kuczkowski, D. Bläser, C. Wolper, G. Jansen and R. Haack, *Organometallics*, 2013, **32**, 5445–5450.
21 J. M. Herbelin, R. Klingberg, D. J. Spencer, M. A. Kwok, H. Bixler, R. Ueunten, R. Cook and W. Hansen, *Opt. Commun.*, 1981, **36**, 475–476.
22 S. W. Kang, K. M. Jeon, J. S. Shin, J. R. Chun, Y. H. Kim, S. J. Lee and J. Y. Yun, *Chem. Vap. Deposition*, 2013, **19**, 61–67.
23 B. Hornung, A. Bodi, C. I. Pongor, Z. Gengeliczki, T. Baer and B. Sztáray, *J. Phys. Chem. A*, 2009, **113**, 8091–8098.
24 T. Baer and R. P. Tuckett, *Phys. Chem. Chem. Phys.*, 2017, **19**, 9698–9723.
25 B. K. Cunha de Miranda, C. Alcaraz, M. Elhanine, B. Noller, P. Hemberger, I. Fischer, G. Garcia, H. Soldi-Lose, B. Gans, L. A. Viera Mendez, S. Boye-Peronne, S. Douin, J. Zabka and P. Botschwina, *J. Phys. Chem. A*, 2010, **114**, 4818–4830.
26 A. M. Schulenburg, C. Alcaraz, G. Grassi and F. Merkt, *J. Chem. Phys.*, 2006, **125**, 104310.
27 H. Bock and R. Dammel, *Chem. Ber.*, 1987, **120**, 1961–1970.
28 F. Holzmeier, M. Lang, K. Hader, P. Hemberger and I. Fischer, *J. Chem. Phys.*, 2013, **138**, 214310.
29 S.-J. Kim, T. P. Hamilton and H. F. Schaefer III, *J. Phys. Chem.*, 1993, **97**, 1872–1877.
30 S. Lacombe, D. Gonbeau, J.-L. Cabioch, B. Pellerin, J.-M. Denis and G. Pfister-Guillouzo, *J. Am. Chem. Soc.*, 1988, **110**, 6964–6967.
31 S. Y. Liang, P. Hemberger, J. Levalois-Grützmacher, H. Grützmacher and S. Gaan, *Chem.–Eur. J.*, 2017, **23**, 5595–5601.
32 S. Y. Liang, P. Hemberger, N. M. Neisius, A. Bodi, H. Grützmacher, J. Levalois-Grützmacher and S. Gaan, *Chem.–Eur. J.*, 2015, **21**, 1073–1080.
33 G. Herzberg, *Molecular Spectra and Molecular Structure*, Krieger, Malabar/FL, 1966.
34 S. J. W. Price and A. F. Trotman-Dickenson, *Trans. Faraday Soc.*, 1958, **54**, 1630–1637.
35 L. H. Long and J. F. Sackman, *Trans. Faraday Soc.*, 1954, **50**, 1177–1182.
36 S. J. W. Price, in *Comprehensive Chemical Kinetics*, ed. C. H. Bamford and C. F. H. Tipper, Elsevier, 1972, vol. 4, pp. 197–257.
37 The average bond dissociation energy for a Bi–CH_3 bond in **1** has been reported to be 33.8 kcal mol^{-1} (141 kJ mol^{-1}) (ref. 35). The sum of the bond dissociation energies associated with the cleavage of the second and the third Bi–CH_3 bond in **1** (BDE(MeBi–CH_3) plus BDE(Bi–CH_3)) was estimated to be at least 57.8 kcal mol^{-1} (242 kJ mol^{-1}) (ref. 34). This gives a maximum value of 43.6 kcal mol^{-1} (182 kJ mol^{-1}) for the bond dissociation energy of the first Bi–CH_3 bond in **1**.
38 D. L. Haire, U. M. Oehler, P. H. Krygsman and E. G. Janzen, *J. Org. Chem.*, 1988, **53**, 4535–4542.
39 In a different synthetic approach, compound **8** has previously been obtained from reaction of *in situ* generated [MeBi$(OEt)_2$] with two equiv. HSPh: M. Wieber and U. Baudis, *Z. Anorg. Allg. Chem.*, 1976, **423**, 40–46.
40 A. G. Davies and S. C. W. Hook, *J. Chem. Soc. B*, 1970, 735–737.
41 M. Wieber and I. Sauer, *Z. Naturforsch., B: Anorg. Chem., Org. Chem.*, 1984, **39**, 1668–1670.
42 P. Simon, R. Jambor, A. Ruzicka and L. Dostál, *Organometallics*, 2013, **32**, 239–248.
43 M. Dräger and B. M. Schmidt, *J. Organomet. Chem.*, 1985, **290**, 133–145.
44 K. M. Anderson, C. J. Baylies, A. H. M. Monowar Jahan, N. C. Norman, A. G. Orpen and J. Starbuck, *Dalton Trans.*, 2003, 3270–3277.
45 P. Šimon, R. Jambor, A. Růžička and L. Dostál, *J. Organomet. Chem.*, 2013, **740**, 98–103.
46 For reactions of the related precursor Sb_2Me_4 under near-chemical vapor deposition conditions see: N. Bahlawane, F. Reilmann, S. Schulz, D. Schuchmann and K. Kohse-Höinghaus, *J. Am. Soc. Mass Spectrom.*, 2008, **19**, 1336–1342.
47 M. Johnson, A. Bodi, L. Schulz and T. Gerber, *Nucl. Instrum. Methods Phys. Res., Sect. A*, 2009, **610**, 597–603.
48 (*a*) E. Welz, J. Böhnke, R. D. Dewhurst, H. Braunschweig and B. Engels, *J. Am. Chem. Soc.*, 2018, **140**, 12580–12591; (*b*) J. Böhnke, T. Dellermann, M. A. Celik, I. Krummenacher, R. D. Dewhurst, S. Demeshko, W. C. Ewing, K. Hammond, M. Heß, E. Bill, E. Welz, M. I. S. Röhr, R. Mitrić, B. Engels, F. Meyer and H. Braunschweig, *Nat. Commun.*, 2018, **9**, 1197.
49 V. Settels, W. Liu, J. Pflaum, R. F. Fink and B. Engels, *J. Comput. Chem.*, 2012, **33**, 1544–1553.
50 (*a*) J.-D. Chai and M. Head-Gordon, *J. Chem. Phys.*, 2008, **128**, 084106; (*b*) S. Grimme, J. Antony, S. Ehrlich and H. Krieg, *J. Chem. Phys.*, 2010, **132**, 154104.

51 (*a*) C. Angeli, R. Cimiraglia, S. Evangelisti, T. Leininger and J.-P. Malrieu, *J. Chem. Phys.*, 2001, **114**, 10252–10264; (*b*) C. Angeli, R. Cimiraglia and J.-P. Malrieu, *Chem. Phys. Lett.*, 2001, **350**, 297–305; (*c*) C. Angeli, R. Cimiraglia and J.-P. Malrieu, *J. Chem. Phys.*, 2002, **117**, 9138–9153.

52 D. A. Pantazis and F. Neese, *Theor. Chem. Acc.*, 2012, **131**, 1292.

53 It should be noted that methyl nitrene (N–CH_3) and methyl phosphinidene (P–CH_3) also have triplet ground states. But the structures with methylene (rather than methyl) functional groups, *i.e.* HN=CH_2 and HP=CH_2, are energetically favored over N–CH_3 and P–CH_3. See ref. 27–32 and A. G. Kutateladze, *Computational Methods in Photochemistry*, CSC Press Taylor and Francis Group, 2019.

54 Bismuth-containing radical species were not detected under these conditions. It has been reported that even persistent dialkyl bismuth radicals may not be detectable by EPR spectroscopy, which has been ascribed to fast relaxation as a result of spin orbit coupling: S. Ishida, F. Hirakawa, K. Furukawa, K. Yoza and T. Iwamoto, *Angew. Chem., Int. Ed.*, 2014, **53**, 11172–11176.

55 Trapping of alkyl radical species in reactions of bismuth compounds has been reported: J. Ramler, I. Krummenacher and C. Lichtenberg, *Angew. Chem., Int. Ed.*, 2019, **58**, 12924–12929.

56 (*a*) F. Neese, *Wiley Interdiscip. Rev.: Comput. Mol. Sci.*, 2012, **2**, 73–78; (*b*) F. Neese, *Wiley Interdiscip. Rev.: Comput. Mol. Sci.*, 2018, **8**, e1327.

Summary

In the first part of this work (reference [4]), excitations in aggregates of DIP and PDIR-CN_2 are calculated and characterised in order to assign signals in experimental TR-SHG spectra and explain underlying processes. The first chapter focuses on the evolution of excited state populations in the individual materials. Those present mainly Frenkel character and could therefore be modeled with a standard RS functional. The environment was modelled by atomic point charges. Absorption spectra could be assigned, although a systematic shift remained. This was discussed in terms of aggregate size, relaxation effects and the inherent error of description by an approximated DFT functional. Features in the TR-SHG spectra were mainly assigned to aggregate effects. These include (de-)localization processes, population of low-lying trap states and relaxation to the ground state. Additionally, we could explain the vibrational feature by vibrations of the monomers.
In the second part of this chapter (reference [85]) the focus lies on geometrical relaxation and its effect on the positioning and character of excited states. We found that the first excited state in DIP is stabilized by localization on and relaxation of a single molecule as compared to a delocalized exciton. However, the effect on higher lying excitations did not parallel this observation. Further investigations showed that this effects add up to several tenths of eV and are not generizable. It is therefore mandatory to include such investigations in aggregate-based calculations if a precise description of excited states is aspired.
The second chapter focused on interface systems of DIP and PDIR-CN_2. These can be used as OPV materials. A special interest lies in the position of CT states and their dependence on arrangements at the interface. This is due to the central role of CT states in the generation of free charge carriers.[3] CT excitations demanded a change in methodology. It was found that the energetic position can only be determined with satisfying quality with DFT if a RS functional is IP tuned. IP tuning also influences excitation energies of Frenkel excitations towards the experimental values in comparison to the approach in chapter 1. Additionally, relaxation effects were investigated and it was found that their influence on CT excitations is stronger than for local excita-

tions. Using this methodology on tetramers consisting of two DIP and two PDIR-CN_2 molecules from a idealized interface structure, it was possible to affirm and explain the experimental data by Hänsel et al.[3].
In the third chapter a project on TADF OLEDs was covered with reference to EPR data by Grüne et al.[6;7;14;147]. Position and characteristics of excited states were determined with the same approach as in chapter 2 due to a similar importance of CT excitations. In contrast to the former chapter, triplet excitations cannot be neglected in this project. Results were therefore expanded by TDA and ΔSCF calculations. Additionally, disorder is of higher importance in this project, since the molecules are bulkier, can align less closely and blends are used instead of interfaces. For this reason, a collection of fully optimized D:A aggregates was used for the investigations. Since the calculated energetic levels matched the experiments well, further characterisations were used to interpret more opaque spectroscopic features. A useful metric was the RMSeh, which is directly related to the experimentally measured D-value. This calculations strongly indicated that both experimental features can be attributed to CT excitations and not a monomer localized Frenkel as proposed earlier.[6;10] SOC calculations were less insightful, since the character of excitations could already be used to predict the very small matrix elements between states of the same character. This is directly related to the reverse inter-system crossing (rISC) which induces the delayed fluorescence and happens between an exciplex triplet and a singlet of the same character. Calculations on D:A complexes with an increased intermonomer distance were used to approximate disorder and diffusion effects. In this stretched dimers, the singlet-triplet gap is further decreased. This is due to the vanishing electron-hole overlap and can facilitate HFI transitions which do not depend on the SOC. This route is also proposed to be the preferred route for deexcitation after electrical excitation. In conclusion, model systems were found which match the experiment well and could be used to expand the understanding of the emission process and the involved excited states.
The last chapter (reference [24]) reports the investigation of methylbismuth, the first reported free organometallic bismuthidene. In addition to MR calculations to provide accurate energies and geometries, it was also necessary to include a second excited state to reproduce a msTPE spectrum. The combination with a ZORA hamiltonian and DFT based frequencies, allowed for the identification of all involved compounds.

Zusammenfassung

Im ersten Teil dieser Arbeit (Referenz [4]) wurden Anregungen in DIP und PDIR-CN_2 Aggregaten berechnet und charakterisiert, um Signale experimenteller TR-SHG Spektren zuzuweisen und zugrundeliegende Prozesse aufzuklären. Der Fokus des ersten Kapitels liegt auf der zeitlichen Entwicklung der Populationen der angeregten Zusände in den individuellen Materialien. Diese Anregungen haben Frenkel Charakter und konnten deswegen mit standard RS-Funktionalen beschrieben werden. Die Umgebung wurde durch atomare Punktladungen modelliert. Absoptionsspektren konnten zugewiesen werden, allerdings mit einer systematischen Abweichung in den Anregungsenergien. Diese Zuweisung wurde diskutiert mit Blick auf Größe der untersuchten Aggregate, Relaxationseffekte und den Funktional-inherenten Fehler. Die Signale in den TR-SHG Spektren wurden hauptächlich auf Aggregateffekte zurückgeführt. Dazu gehören (De-)Lokalisierungsprozesse, Population von tiefliegenden Fallenzuständen und Relaxation zum Grundzustand. Zusätzlich konnten wir Vibrationsprogressionen durch Schwingungen der Monomere erklären.
Im zweiten Teil dieses Kapitels (Referenz [85]) liegt der Schwerpunkt auf der geometrischen Relaxation der untersuchten Systeme und deren Auswirkung auf die Position und den Charakter der angeregten Zustände. Wir konnten feststellen, dass der erste angeregte Zustand in DIP durch die Lokalisierung auf ein Monomer und dessen Relaxation stabilisiert wird. Diese Effekte waren jedoch nicht für alle Anregungen gleich. Es ist daher erforderlich, solche Untersuchungen in aggregatbasierte Berechnungen einzubeziehen, wenn eine genaue Beschreibung der angeregten Zustände angestrebt wird.
Das zweite Kapitel konzentriert sich auf Grenzflächensysteme von DIP und PDIR-CN_2. Diese können als OPV-Materialien verwendet werden. Ein besonderes Interesse gilt dabei der Lage der CT-Zustände und deren Abhängigkeit von der relativen Anordnung an der Grenzfläche. Dies ist auf die zentrale Rolle der CT Zustände bei der Erzeugung von freien Ladungsträgern zurückzuführen,[3] was eine Anpassung der Methodik erforderte. Es zeigte sich, dass die energetische Lage nur dann mit zufriedenstellender Qualität mit DFT bestimmt werden kann, wenn ein IP-getunetes RS-Funktional verwendet wird. IP-Tuning beeinflusst auch die Anregungsenergien von Frenkel-Anregungen und verbessert

die Beschreibung in Richtung der experimentellen Werte im Vergleich zum Ansatz in Kapitel 1. Zusätzlich wurden Relaxationseffekte untersucht. Es konnte festgestellt werden, dass ihr Einfluss auf CT-Anregungen stärker ist als bei lokalen Anregungen. Durch Anwendung dieser Methode auf Tetramere - die aus zwei DIP und zwei PDIR-CN_2 Molekülen bestehen und einer idealisierten Grenzflächenstruktur entsprechen - war es möglich, die experimentellen Daten von Hänsel et al.[3] zu bestätigen und zu erklären. Im dritten Kapitel wurde ein Projekt über TADF-OLEDs unter Bezugnahme auf EPR-Daten von Grüne et al.[6;7;14;147] behandelt. Position und Eigenschaften der angeregten Zustände wurden mit dem gleichen Ansatz wie in Kapitel 2 bestimmt, da die CT-Anregungen eine ähnliche Bedeutung haben. Im Gegensatz zum ersten Kapitel können Triplett-Anregungen in diesem Projekt nicht vernachlässigt werden. Die Ergebnisse wurden daher durch TDA- und ΔSCF-Rechnungen erweitert. Außerdem ist Unordnung in diesem Projekt von größerer Bedeutung, da die Moleküle voluminöser sind, sich weniger eng anordnen können und anstelle von Grenzflächen Blends in den Experimenten verwendet wurden. Aus diesem Grund wurde eine Anzahl von verschiedenen vollständig optimierter D:A-Aggregate für die Untersuchungen verwendet. Da die berechneten energetischen Energieniveaus gut mit den Experimenten übereinstimmten, wurden weitere Charakterisierungen zur Interpretation der undurchsichtigen experimentellen Ergebnisse herangezogen. Eine nützliche Metrik ist der RMSeh-Wert, der in direktem Zusammenhang mit dem mit dem experimentell gemessenen D-Wert steht. Diese Berechnungen zeigten deutlich, dass beide experimentelle Signale auf CT-Anregungen und nicht, wie zuvor vermutet, auf eine monomer lokalisierte Frenkel Anregung zurückzuführen sind.[6;10] SOC-Berechnungen waren weniger aufschlussreich, da der Charakter der Anregungen bereits zur Vorhersage der sehr kleinen Matrixelemente zwischen Zuständen desselben Charakters ausgereicht hätte. Diese Matrixelemente stehen in direktem Zusammenhang mit rISC, das verzögerter Fluoreszenz zugrunde liegt. Berechnungen an D:A-Komplexen mit einem vergrößerten Abstand zwischen den Monomeren wurden verwendet, um Unordnung und Diffusionseffekte zu approximieren. In diesen gestreckten Dimeren ist die Singulett-Triplett-Lücke weiter verringert. Dies ist auf den verschwindend geringen Elektron-Loch-Überlapp zurückzuführen und kann HFI-Übergänge erleichtern. Dieser Weg wird daher als der bevorzugte Weg für die Deexzitation nach elektrischer Anregung vorgeschlagen. Zusammenfassend lässt sich sagen, dass Modellsysteme gefunden wurden, die gut mit dem Experiment übereinstimmen und die zum besseren Verständnis des Emissionsprozesses und der beteiligten angeregten Zustände beitragen.

Das letzte Kapitel (Referenz [24]) berichtet über die Untersuchung von Methylbismut, dem ersten nachgewiesenen unstabilisierten metallorganischen Bismutiniden. Energi-

en und Geometrien mussten mit MR-Ansätzen berechnet werden; außerdem war es notwendig, einen zweiten elektronisch angeregten Zustand miteinzubeziehen um ein msTPE-Spektrum zu reproduzieren. Die Kombination mit einem ZORA-Hamiltonian und DFT-basierten Frequenzen ermöglichte die Identifizierung aller am Spektrum beteiligter Komponenten.

Acknowledgment

First I would like to thank my supervisor Prof. Dr. Bernd Engels for the opportunity to work in his group. Thank you for all the discussions and ideas, the support and the nice working atmosphere. Special thanks also to my co-supervisor Prof. Dr. Volker Engel for accepting this role and all the support. The position was provided by the DFG as part of the GRK2112; its academic and financial support is gratefully acknowledged.
A big part of the motivation to always keep going came from the great people in the Engels group who I had the pleasure to work with. Special mentions deserve (in alphabetical order): Dr. Daniel Bellinger, Julian Erdmannsdörfer, Dr. Anna Heilos, Dr. Dustin Kaiser, Dr. Thien Anh Le, Dr. Eileen Welz and of course the current members Luca Craciunescu, Alexander Geis, Christoph Herok and Jessica Meyr who additionally were of great help spotting typos and inconsistencies in this work. Also - Ursula Rüppel, thank you for all the support both regarding the bureaucratic stuff and (even more importantly) by just being an awesome human being.
Thanks to all my collaborators, especially Prof. Dr. Petra Tegeder, Prof. Dr. Ingo Fischer and his group, Prof. Dr. Crispin Lichtenberg, Dr. Jacqueline Rammler, PD habil. Dr Andreas Sperlich and Jeannine Grüne. Thank you for the fruitful discussions and for teaching me about the various spectroscopic methods.
Through the years I had the pleasure to mentor various research interns and a master student. Thanks to Maximilian Asbach, Luca Craciunescu, Christin Fernholz, Klaus Hofmann, Jonas Klopf, Eric Macholdt, Lisa Partholl, Jonas Weiser, Raphael Wichary for your motivation, the support of my projects, and the very helpful discussions.
Conferences are not only a great way to exchange knowledge but also to meet awesome people. Thanks to Federica, Simon, Rodrigo and Petros for providing a very valuable non-Würzburg perspective to my work and especially for being awesome friends!
Biggest thanks also to all the awesome non-TC people out there who kept me sane during the last years. The friends I met during my studies and those of you who might not care about chemistry at all.
Finally, the biggest shout-out to my awesome family and partner. Mama, Papa, Regina, Kilian and Chris - I love you.

Bibliography

[1] Z. B. Henson, K. Müllen, and G. C. Bazan, *Design strategies for organic semiconductors beyond the molecular formula*, Nature chemistry **4**, 699–704 (2012).

[2] M. Hänsel, V. Belova, A. Hinderhofer, F. Schreiber, K. Broch, and P. Tegeder, *Ultrafast Excited State Dynamics in Diindenoperylene Films*, J. Phys. Chem. C **121**, 17900–17906 (2017).

[3] M. Hänsel. *Ultrafast Excited State Dynamics and Functional Interfaces Probed by Second Harmonic Generation.* phdthesis, University of Heidelberg, (2017).

[4] S. Wirsing, M. Hänsel, V. Belova, F. Schreiber, K. Broch, B. Engels, and P. Tegeder, *Excited-state dynamics in perylene-based organic semiconductor thin films: Theory meets experiment*, The Journal of Physical Chemistry C **123**, 27561–27572 (2019).

[5] J. Grüne, N. Bunzmann, M. Meinecke, V. Dyakonov, and A. Sperlich, *Kinetic modeling of transient electroluminescence reveals TTA as an efficiency-limiting process in exciplex-based TADF OLEDs*, The Journal of Physical Chemistry C **124**, 25667–25674 (2020).

[6] N. Bunzmann, S. Weissenseel, L. Kudriashova, J. Grüne, B. Krugmann, J. V. Grazulevicius, A. Sperlich, and V. Dyakonov, *Optically and electrically excited intermediate electronic states in donor: acceptor based OLEDs*, Materials Horizons **7**, 1126–1137 (2020).

[7] N. Bunzmann, D. L. Baird, H. Malissa, S. Weissenseel, C. Boehme, V. Dyakonov, and A. Sperlich, *Thermal Activation Bottleneck in TADF OLEDs based on m-MTDATA: BPhen*, arXiv preprint arXiv:2008.05781 (2020).

[8] Y.-J. Cheng, S.-H. Yang, and C.-S. Hsu, *Synthesis of conjugated polymers for organic solar cell applications*, Chemical reviews **109**, 5868–5923 (2009).

[9] Y. Yamashita, *Organic semiconductors for organic field-effect transistors*, Science and technology of advanced materials **10**, 024313 (2009).

[10] S. Weissenseel, N. A. Drigo, L. G. Kudriashova, M. Schmid, T. Morgenstern, K.-H. Lin, A. Prlj, C. Corminboeuf, A. Sperlich, W. Brütting, et al., *Getting the right twist: influence of donor–acceptor dihedral angle on exciton kinetics and singlet–triplet gap in deep blue thermally activated delayed fluorescence emitter*, The Journal of Physical Chemistry C **123**, 27778–27784 (2019).

[11] J. Lauth, G. Grimaldi, S. Kinge, A. J. Houtepen, L. D. Siebbeles, and M. Scheele, *Ultrafast Charge Transfer and Upconversion in Zinc β-Tetraaminophthalocyanine-Functionalized PbS Nanostructures Probed by Transient Absorption Spectroscopy*, Angewandte Chemie **129**, 14249–14253 (2017).

[12] R. Shivanna, S. Shoaee, S. Dimitrov, S. K. Kandappa, S. Rajaram, J. R. Durrant, and K. Narayan, *Charge generation and transport in efficient organic bulk heterojunction solar cells with a perylene acceptor*, Energy & Environmental Science **7**, 435–441 (2014).

[13] C. Zhang, Y. Zhang, Z. Wang, Y. Su, Z. Wei, J. Hou, S. He, K. Wu, C. He, J. Zhang, et al., *Probing molecular orientation at bulk heterojunctions by polarization-selective transient absorption spectroscopy*, Science China Chemistry **64**, 1569–1576 (2021).

[14] J. Grüne, V. Dyakonov, and A. Sperlich, *Detecting triplet states in opto-electronic and photovoltaic materials and devices by transient optically detected magnetic resonance*, Materials Horizons **8**, 2569–2575 (2021).

[15] V. Dyakonov, N. Gauss, G. Rösler, S. Karg, W. Rieß, and M. Schwoerer, *Electron spin resonance in PPV-photodiodes: detection via photoinduced current*, Chemical Physics **189**, 687–695 (1994).

[16] S. Weissman, *Recent Developments in Electron Paramagnetic Resonance: Transient Methods*, Annual Review of Physical Chemistry **33**, 301–318 (1982).

[17] F. Kraffert, R. Steyrleuthner, S. Albrecht, D. Neher, M. C. Scharber, R. Bittl, and J. Behrends, *Charge separation in PCPDTBT: PCBM blends from an EPR perspective*, The Journal of Physical Chemistry C **118**, 28482–28493 (2014).

[18] P. A. Franken, A. E. Hill, C. W. Peters, and G. Weinreich, *Generation of Optical Harmonics*, Phys. Rev. Lett. **7**, 118–119 (1961).

[19] B. Levine and C. G. Bethea, *Second and third order hyperpolarizabilities of organic molecules*, The Journal of Chemical Physics **63**, 2666–2682 (1975).

[20] S. Difley, L.-P. Wang, S. Yeganeh, S. R. Yost, and T. V. Voorhis, *Electronic properties of disordered organic semiconductors via QM/MM simulations*, Accounts of chemical research **43**, 995–1004 (2010).

[21] C. Brückner, F. Würthner, K. Meerholz, and B. Engels, *Structure–property relationships from atomistic multiscale simulations of the relevant processes in organic solar cells. I. thermodynamic aspects*, The Journal of Physical Chemistry C **121**, 4–25 (2017).

[22] D. Fazzi, M. Barbatti, and W. Thiel, *Hot and cold charge-transfer mechanisms in organic photovoltaics: insights into the excited states of donor/acceptor interfaces*, The journal of physical chemistry letters **8**, 4727–4734 (2017).

[23] W. Liu, *Essentials of relativistic quantum chemistry*, The Journal of Chemical Physics **152**, 180901 (2020).

[24] D. P. Mukhopadhyay, D. Schleier, S. Wirsing, J. Ramler, D. Kaiser, E. Reusch, P. Hemberger, T. Preitschopf, I. Krummenacher, B. Engels, et al., *Methylbismuth: an organometallic bismuthinidene biradical*, Chemical science **11**, 7562–7568 (2020).

[25] E. Reusch, D. Kaiser, D. Schleier, R. Buschmann, A. Krueger, T. Hermann, B. Engels, I. Fischer, and P. Hemberger, *Pentadiynylidene and its methyl-substituted derivates: Threshold photoelectron spectroscopy of R1-C5-R2 triplet carbon chains*, The Journal of Physical Chemistry A **123**, 2008–2017 (2019).

[26] V. Bonačić-Koutecký, J. Koutecký, and J. Michl, *Neutral and charged biradicals, zwitterions, funnels in S1, and proton translocation: their role in photochemistry, photophysics, and vision*, Angewandte Chemie International Edition in English **26**, 170–189 (1987).

[27] M. Bendikov, H. M. Duong, K. Starkey, K. Houk, E. A. Carter, and F. Wudl, *Oligoacenes: theoretical prediction of open-shell singlet diradical ground states*, Journal of the American Chemical Society **126**, 7416–7417 (2004).

[28] C. Saalfrank, F. Fantuzzi, T. Kupfer, B. Ritschel, K. Hammond, I. Krummenacher, R. Bertermann, R. Wirthensohn, M. Finze, P. Schmid, et al., *cAAC-stabilisierte 9, 10-Diboraanthracene–offenschalige Singulettbiradikale*, Angewandte Chemie **132**, 19502–19507 (2020).

[29] Z. Sun, Z. Zeng, and J. Wu, *Zethrenes, extended p-quinodimethanes, and periacenes with a singlet biradical ground state*, Accounts of chemical research **47**, 2582–2591 (2014).

[30] S. Ito and M. Nakano, *Theoretical molecular design of heteroacenes for singlet fission: Tuning the diradical character by modifying π-conjugation length and aromaticity*, The Journal of Physical Chemistry C **119**, 148–157 (2015).

[31] R. Calvo, E. C. Abresch, R. Bittl, G. Feher, W. Hofbauer, R. A. Isaacson, W. Lubitz, M. Y. Okamura, and M. L. Paddock, *EPR study of the molecular and electronic structure of the semiquinone biradical QA-• QB-• in photosynthetic reaction centers from Rhodobacter sphaeroides*, Journal of the American Chemical Society **122**, 7327–7341 (2000).

[32] G. I. Roshchupkina, A. A. Bobko, A. Bratasz, V. A. Reznikov, P. Kuppusamy, and V. V. Khramtsov, *In vivo EPR measurement of glutathione in tumor-bearing mice using improved disulfide biradical probe*, Free Radical Biology and Medicine **45**, 312–320 (2008).

[33] I. Fischer and S. T. Pratt, *Photoelectron Spectroscopy in Molecular Physical Chemistry*, Physical Chemistry Chemical Physics (2022).

[34] D. Kaiser, E. Reusch, P. Hemberger, A. Bodi, E. Welz, B. Engels, and I. Fischer, *The ortho-benzyne cation is not planar*, Physical Chemistry Chemical Physics **20**, 3988–3996 (2018).

[35] S. Hirata and M. Head-Gordon, *Time-dependent density functional theory within the Tamm–Dancoff approximation*, Chemical Physics Letters **314**, 291–299 (1999).

[36] J. Gräfenstein and D. Cremer, *Can density functional theory describe multireference systems? Investigation of carbenes and organic biradicals*, Physical Chemistry Chemical Physics **2**, 2091–2103 (2000).

[37] Y. Shao, M. Head-Gordon, and A. I. Krylov, *The spin–flip approach within time-dependent density functional theory: Theory and applications to diradicals*, The Journal of chemical physics **118**, 4807–4818 (2003).

[38] C. Angeli, R. Cimiraglia, and J.-P. Malrieu, *n-electron valence state perturbation theory: A spinless formulation and an efficient implementation of the strongly contracted and of the partially contracted variants*, The Journal of chemical physics **117**, 9138–9153 (2002).

[39] C. Angeli, R. Cimiraglia, and J.-P. Malrieu, *N-electron valence state perturbation theory: a fast implementation of the strongly contracted variant*, Chemical physics letters **350**, 297–305 (2001).

[40] C. Angeli, R. Cimiraglia, S. Evangelisti, T. Leininger, and J.-P. Malrieu, *Introduction of n-electron valence states for multireference perturbation theory*, The Journal of Chemical Physics **114**, 10252–10264 (2001).

[41] A. Szabo and N. S. Ostlund, *Modern quantum chemistry: introduction to advanced electronic structure theory*, Courier Corporation (2012).

[42] T. Tsuneda, *Density Functional Theory in Quantum Chemistry*, Springer Japan (2014).

[43] P. Norman, K. Ruud, and T. Saue, *Principles and practices of molecular properties: Theory, modeling, and simulations*, John Wiley & Sons (2018).

[44] M. A. Marques, N. T. Maitra, F. M. Nogueira, E. K. Gross, and A. Rubio, *Fundamentals of time-dependent density functional theory*, Springer Science & Business Media (2012).

[45] M. Stott and E. Zaremba, *Linear-response theory within the density-functional formalism: Application to atomic polarizabilities*, Physical Review A **21**, 12 (1980).

[46] P. Hohenberg and W. Kohn, *Density functional theory (DFT)*, Phys. Rev **136**, B864 (1964).

[47] E. Runge and E. K. U. Gross, *Density-Functional Theory for Time-Dependent Systems*, Phys. Rev. Lett. **52**, 997–1000 (1984).

[48] P. Norman, D. M. Bishop, H. J. A. Jensen, and J. Oddershede, *Nonlinear response theory with relaxation: The first-order hyperpolarizability*, The Journal of chemical physics **123**, 194103 (2005).

[49] V. A. Goncharov and K. Varga, *Real-space, real-time calculation of dynamic hyperpolarizabilities*, The Journal of chemical physics **137**, 094111 (2012).

[50] L. González and R. Lindh, *Quantum Chemistry and Dynamics of Excited States: Methods and Applications*, John Wiley & Sons (2020).

[51] M. Petersilka, U. Gossmann, and E. Gross, *Excitation energies from time-dependent density-functional theory*, Physical review letters **76**, 1212 (1996).

[52] M. Petersilka and E. Gross, *Spin-multiplet energies from time-dependent density functional theory*, International journal of quantum chemistry **60**, 1393–1401 (1996).

[53] T. Ando, *Inter-subband optical absorption in space-charge layers on semiconductor surfaces*, Zeitschrift für Physik B Condensed Matter **26**, 263–272 (1977).

[54] M. E. Casida. *Time-Dependent Density Functional Response Theory for Molecules*, pages 155–192. World Scientific, (1995).

[55] Y. Tawada, T. Tsuneda, S. Yanagisawa, T. Yanai, and K. Hirao, *A long-range-corrected time-dependent density functional theory*, The Journal of Chemical Physics **120**, 8425–8433 (2004).

[56] F. Neese, F. Wennmohs, U. Becker, and C. Riplinger, *The ORCA quantum chemistry program package*, The Journal of Chemical Physics **152**, 224108 (2020).

[57] Y. Shao, Z. Gan, E. Epifanovsky, A. T. Gilbert, M. Wormit, J. Kussmann, A. W. Lange, A. Behn, J. Deng, X. Feng, D. Ghosh, M. Goldey, P. R. Horn, L. D. Jacobson, I. Kaliman, R. Z. Khaliullin, T. Kuś, A. Landau, J. Liu, E. I. Proynov, Y. M. Rhee, R. M. Richard, M. A. Rohrdanz, R. P. Steele, E. J. Sundstrom, H. L. W. III, P. M. Zimmerman, D. Zuev, B. Albrecht, E. Alguire, B. Austin, G. J. O. Beran, Y. A. Bernard, E. Berquist, K. Brandhorst, K. B. Bravaya, S. T. Brown, D. Casanova, C.-M. Chang, Y. Chen, S. H. Chien, K. D. Closser, D. L. Crittenden, M. Diedenhofen, R. A. D. Jr., H. Do, A. D. Dutoi, R. G. Edgar, S. Fatehi, L. Fusti-Molnar, A. Ghysels, A. Golubeva-Zadorozhnaya, J. Gomes, M. W. Hanson-Heine, P. H. Harbach, A. W. Hauser, E. G. Hohenstein, Z. C. Holden, T.-C. Jagau, H. Ji, B. Kaduk, K. Khistyaev, J. Kim, J. Kim, R. A. King, P. Klunzinger, D. Kosenkov, T. Kowalczyk, C. M. Krauter, K. U. Lao, A. D. Laurent, K. V. Lawler, S. V. Levchenko, C. Y. Lin, F. Liu, E. Livshits, R. C. Lochan, A. Luenser, P. Manohar, S. F. Manzer, S.-P. Mao, N. Mardirossian, A. V. Marenich, S. A. Maurer, N. J. Mayhall, E. Neuscamman, C. M. Oana, R. Olivares-Amaya, D. P. O'Neill, J. A. Parkhill, T. M. Perrine, R. Peverati, A. Prociuk, D. R. Rehn, E. Rosta, N. J. Russ, S. M. Sharada, S. Sharma, D. W. Small, A. Sodt, T. Stein, D. Stück, Y.-C. Su, A. J. Thom, T. Tsuchimochi, V. Vanovschi, L. Vogt, O. Vydrov, T. Wang, M. A. Watson, J. Wenzel, A. White, C. F. Williams, J. Yang, S. Yeganeh, S. R. Yost, Z.-Q. You, I. Y. Zhang, X. Zhang, Y. Zhao, B. R. Brooks, G. K. Chan, D. M. Chipman, C. J. Cramer, W. A. G. III, M. S. Gordon, W. J. Hehre, A. Klamt, H. F. S. III, M. W. Schmidt, C. D.

Sherrill, D. G. Truhlar, A. Warshel, X. Xu, A. Aspuru-Guzik, R. Baer, A. T. Bell, N. A. Besley, J.-D. Chai, A. Dreuw, B. D. Dunietz, T. R. Furlani, S. R. Gwaltney, C.-P. Hsu, Y. Jung, J. Kong, D. S. Lambrecht, W. Liang, C. Ochsenfeld, V. A. Rassolov, L. V. Slipchenko, J. E. Subotnik, T. V. Voorhis, J. M. Herbert, A. I. Krylov, P. M. Gill, and M. Head-Gordon, *Advances in molecular quantum chemistry contained in the Q-Chem 4 program package*, Molecular Physics **113**, 184–215 (2015).

[58] L. Craciunescu, S. Wirsing, S. Hammer, K. Broch, A. Dreuw, F. Fantuzzi, V. Sivanesan, P. Tegeder, and B. Engels, *Accurate Polarization-Resolved Absorption Spectra of Organic Semiconductor Thin Films Using First-Principles Quantum-Chemical Methods: Pentacene as a Case Study*, The Journal of Physical Chemistry Letters **13**, 3726–3731 (2022).

[59] B. Alam, A. F. Morrison, and J. M. Herbert, *Charge Separation and Charge Transfer in the Low-Lying Excited States of Pentacene*, The Journal of Physical Chemistry C **124**, 24653–24666 (2020).

[60] R. Gaudoin and K. Burke, *Lack of Hohenberg-Kohn Theorem for Excited States*, Phys. Rev. Lett. **93**, 173001 (2004).

[61] W. Kohn and L. J. Sham, *Self-Consistent Equations Including Exchange and Correlation Effects*, Phys. Rev. **140**, A1133–A1138 (1965).

[62] L. Goerigk and S. Grimme, *A thorough benchmark of density functional methods for general main group thermochemistry, kinetics, and noncovalent interactions*, Phys. Chem. Chem. Phys. **13**, 6670–6688 (2011).

[63] J. P. Perdew and M. Levy, *Physical Content of the Exact Kohn-Sham Orbital Energies: Band Gaps and Derivative Discontinuities*, Phys. Rev. Lett. **51**, 1884–1887 (1983).

[64] A. Seidl, A. Görling, P. Vogl, J. A. Majewski, and M. Levy, *Generalized Kohn-Sham schemes and the band-gap problem*, Phys. Rev. B **53**, 3764–3774 (1996).

[65] T. Leininger, H. Stoll, H.-J. Werner, and A. Savin, *Combining long-range configuration interaction with short-range density functionals*, Chemical Physics Letters **275**, 151–160 (1997).

[66] T. Yanai, D. P. Tew, and N. C. Handy, *A new hybrid exchange–correlation functional using the Coulomb-attenuating method (CAM-B3LYP)*, Chemical physics letters **393**, 51–57 (2004).

[67] Y.-S. Lin, G.-D. Li, S.-P. Mao, and J.-D. Chai, *Long-Range Corrected Hybrid Density Functionals with Improved Dispersion Corrections*, Journal of Chemical Theory and Computation **9**, 263–272 (2013).

[68] J. Toulouse and A. Savin, *Local density approximation for long-range or for short-range energy functionals?*, Journal of Molecular Structure: THEOCHEM **762**, 147–150 (2006).

[69] T. Stein, L. Kronik, and R. Baer, *Reliable Prediction of Charge Transfer Excitations in Molecular Complexes Using Time-Dependent Density Functional Theory*, Journal of the American Chemical Society **131**, 2818–2820 (2009).

[70] C.-O. Almbladh and U. von Barth, *Exact results for the charge and spin densities, exchange-correlation potentials, and density-functional eigenvalues*, Physical Review B **31**, 3231 (1985).

[71] E. U. Condon, *The Franck-Condon principle and related topics*, American journal of physics **15**, 365–374 (1947).

[72] S. Gozem and A. I. Krylov, *The ezSpectra suite: An easy-to-use toolkit for spectroscopy modeling*, WIREs Computational Molecular Science **n/a**, e1546 (2021).

[73] M. J. Frisch, G. W. Trucks, H. B. Schlegel, G. E. Scuseria, M. A. Robb, J. R. Cheeseman, G. Scalmani, V. Barone, G. A. Petersson, H. Nakatsuji, X. Li, M. Caricato, A. V. Marenich, J. Bloino, B. G. Janesko, R. Gomperts, B. Mennucci, H. P. Hratchian, J. V. Ortiz, A. F. Izmaylov, J. L. Sonnenberg, D. Williams-Young, F. Ding, F. Lipparini, F. Egidi, J. Goings, B. Peng, A. Petrone, T. Henderson, D. Ranasinghe, V. G. Zakrzewski, J. Gao, N. Rega, G. Zheng, W. Liang, M. Hada, M. Ehara, K. Toyota, R. Fukuda, J. Hasegawa, M. Ishida, T. Nakajima, Y. Honda, O. Kitao, H. Nakai, T. Vreven, K. Throssell, J. A. Montgomery, Jr., J. E. Peralta, F. Ogliaro, M. J. Bearpark, J. J. Heyd, E. N. Brothers, K. N. Kudin, V. N. Staroverov, T. A. Keith, R. Kobayashi, J. Normand, K. Raghavachari, A. P. Rendell, J. C. Burant, S. S. Iyengar, J. Tomasi, M. Cossi, J. M. Millam, M. Klene, C. Adamo, R. Cammi, J. W. Ochterski, R. L. Martin, K. Morokuma, O. Farkas, J. B. Foresman, and D. J. Fox. *Gaussian~16 Revision C.01*, (2016). Gaussian Inc. Wallingford CT.

[74] F. Neese, *The ORCA program system*, Wiley Interdisciplinary Reviews: Computational Molecular Science **2**, 73–78 (2012).

[75] P. Pyykkö, *Relativistic Effects in Chemistry: More Common Than You Thought*, Annual Review of Physical Chemistry **63**, 45–64 (2012).

[76] J. Autschbach, *Perspective: Relativistic effects*, The Journal of Chemical Physics **136**, 150902 (2012).

[77] T. Saue, *Relativistic Hamiltonians for chemistry: A primer*, ChemPhysChem **12**, 3077–3094 (2011).

[78] F. Neese, *Software update: the ORCA program system, version 4.0*, Wiley Interdisciplinary Reviews: Computational Molecular Science **8**, e1327 (2018).

[79] M. Reiher, *Relativistic Douglas–Kroll–Hess theory*, WIREs Computational Molecular Science **2**, 139–149 (2012).

[80] E. van Lenthe, J. G. Snijders, and E. J. Baerends, *The zero-order regular approximation for relativistic effects: The effect of spin–orbit coupling in closed shell molecules*, The Journal of Chemical Physics **105**, 6505–6516 (1996).

[81] E. v. Lenthe, E. J. Baerends, and J. G. Snijders, *Relativistic regular two-component Hamiltonians*, The Journal of Chemical Physics **99**, 4597–4610 (1993).

[82] C. van Wüllen, *Molecular density functional calculations in the regular relativistic approximation: Method, application to coinage metal diatomics, hydrides, fluorides and chlorides, and comparison with first-order relativistic calculations*, The Journal of Chemical Physics **109**, 392–399 (1998).

[83] B. de Souza, G. Farias, F. Neese, and R. Izsák, *Predicting Phosphorescence Rates of Light Organic Molecules Using Time-Dependent Density Functional Theory and the Path Integral Approach to Dynamics*, Journal of Chemical Theory and Computation **15**, 1896–1904 (2019).

[84] G. Baryshnikov, B. Minaev, and H. Ågren, *Theory and calculation of the phosphorescence phenomenon*, Chemical reviews **117**, 6500–6537 (2017).

[85] M. Deutsch, S. Wirsing, D. Kaiser, R. Fink, P. Tegeder, and B. Engels, *Geometry relaxation-mediated localization and delocalization of excitons in organic semiconductors: A quantum chemical study*, The Journal of Chemical Physics **153**, 224104 (2020).

[86] B. Engels and V. Engel, *The dimer-approach to characterize opto-electronic properties of and exciton trapping and diffusion in organic semiconductor aggregates and crystals*, Physical Chemistry Chemical Physics **19**, 12604–12619 (2017).

[87] D. Bellinger, J. Pflaum, C. Brüning, V. Engel, and B. Engels, *The electronic character of PTCDA thin films in comparison to other perylene-based organic semi-conductors: ab initio-, TD-DFT and semi-empirical computations of the opto-electronic properties of large aggregates*, Phys. Chem. Chem. Phys. **19**, 2434–2448 (2017).

[88] A. Schubert, V. Settels, W. Liu, F. Würthner, C. Meier, R. F. Fink, S. Schindlbeck, S. Lochbrunner, B. Engels, and V. Engel, *Ultrafast exciton self-trapping upon geometry deformation in perylene-based molecular aggregates*, The journal of physical chemistry letters **4**, 792–796 (2013).

[89] V. Settels, A. Schubert, M. Tafipolski, W. Liu, V. Stehr, A. K. Topczak, J. Pflaum, C. Deibel, R. F. Fink, V. Engel, et al., *Identification of ultrafast relaxation processes as a major reason for inefficient exciton diffusion in perylene-based organic semiconductors*, Journal of the American Chemical Society **136**, 9327–9337 (2014).

[90] T. M. Clarke and J. R. Durrant, *Charge Photogeneration in Organic Solar Cells*, Chem. Rev. **110**, 6736–6767 (2010).

[91] A. A. Bakulin, A. Rao, V. G. Pavelyev, P. H. M. van Loosdecht, M. S. Pshenichnikov, D. Niedzialek, J. Cornil, D. Beljonne, and R. H. Friend, *The Role of Driving Energy and Delocalized States for Charge Separation in Organic Semiconductors*, Science **16**, 1340–1344 (2012).

[92] K. Vandewal, *Interfacial charge transfer states in condensed phase systems*, Annual review of physical chemistry **67**, 113–133 (2016).

[93] F. Plasser and H. Lischka, *Analysis of Excitonic and Charge Transfer Interactions from Quantum Chemical Calculations*, Journal of Chemical Theory and Computation **8**, 2777–2789 (2012).

[94] F. Plasser, *TheoDORE: A toolbox for a detailed and automated analysis of electronic excited state computations*, The Journal of Chemical Physics **152**, 084108 (2020).

[95] K. W. Guo, *Green nanotechnology of trends in future energy: a review*, International Journal of Energy Research **36**, 1–17 (2012).

[96] M. A. Green and S. P. Bremner, *Energy conversion approaches and materials for high-efficiency photovoltaics*, Nature materials **16**, 23–34 (2017).

[97] S. Shoaee, T. M. Clarke, C. Huang, S. Barlow, S. R. Marder, M. Heeney, I. McCulloch, and J. R. Durrant, *Acceptor Energy Level Control of Charge Photogeneration in Organic Donor/Acceptor Blends*, Journal of the American Chemical Society **132**, 12919–12926 (2010).

[98] A. Armin, W. Li, O. J. Sandberg, Z. Xiao, L. Ding, J. Nelson, D. Neher, K. Vandewal, S. Shoaee, T. Wang, et al., *A History and Perspective of Non-Fullerene Electron Acceptors for Organic Solar Cells*, Advanced Energy Materials **11**, 2003570 (2021).

[99] J. Nelson, J. Kirkpatrick, and P. Ravirajan, *Factors limiting the efficiency of molecular photovoltaic devices*, Phys. Rev. B **69**, 035337 (2004).

[100] M. Musiał. *Equation-of-Motion Coupled-Cluster Models*, chapter 4, pages 77–108. John Wiley & Sons, Ltd, (2020).

[101] V. Belova, P. Beyer, E. Meister, T. Linderl, M.-U. Halbich, M. Gerhard, S. Schmidt, T. Zechel, T. Meisel, A. V. Generalov, A. S. Anselmo, R. Scholz, O. Konovalov, A. Gerlach, M. Koch, A. Hinderhofer, A. Opitz, W. Brütting, and F. Schreiber, *Evidence for Anisotropic Electronic Coupling of Charge Transfer States in Weakly Interacting Organic Semiconductor Mixtures*, Journal of the American Chemical Society **139**, 8474–8486 (2017).

[102] V. Belova, B. Wagner, B. Reisz, C. Zeiser, G. Duva, J. Rozbořil, J. Novák, A. Gerlach, A. Hinderhofer, and F. Schreiber, *Real-Time Structural and Optical Study of Growth and Packing Behavior of Perylene Diimide Derivative Thin Films: Influence of Side-Chain Modification*, The Journal of Physical Chemistry C **122**, 8589–8601 (2018).

[103] S. Kowarik, A. Gerlach, S. Sellner, L. Cavalcanti, O. Konovalov, and F. Schreiber, *Real-time X-ray diffraction measurements of structural dynamics and polymorphism in diindenoperylene growth*, Applied Physics A **95**, 233–239 (2009).

[104] S. Kowarik, A. Gerlach, S. Sellner, F. Schreiber, L. Cavalcanti, and O. Konovalov, *Real-time observation of structural and orientational transitions during growth of organic thin films*, Physical review letters **96**, 125504 (2006).

[105] A. C. Dürr, N. Koch, M. Kelsch, A. Rühm, J. Ghijsen, R. L. Johnson, J.-J. Pireaux, J. Schwartz, F. Schreiber, H. Dosch, and A. Kahn, *Interplay between morphology, structure, and electronic properties at diindenoperylene-gold interfaces*, Phys. Rev. B **68**, 115428 (2003).

[106] M. A. Heinrich, J. Pflaum, A. K. Tripathi, W. Frey, M. L. Steigerwald, and T. Siegrist, *Enantiotropic Polymorphism in Di-indenoperylene*, Journal of Physical Chemistry C **111**, 18878–18881 (2007).

[107] L. Ferlauto, F. Liscio, E. Orgiu, N. Masciocchi, A. Guagliardi, F. Biscarini, P. Samorì, and S. Milita, *Enhancing the Charge Transport in Solution-Processed Perylene Di-imide Transistors via Thermal Annealing of Metastable Disordered Films*, Advanced Functional Materials **24**, 5503–5510 (2014).

[108] J. F. McGilp, *A review of optical second-harmonic and sum-frequency generation at surfaces and interfaces*, J. Phys. D: Appl. Phys. **29**, 1812–1821 (1996).

[109] Y. R. Shen, *Surface properties probed by second-harmonic and sum-frequency generation*, Nature **337**, 519 (1989).

[110] P. Guyot-Sionnest, W. Chen, and Y. R. Shen, *General considerations on optical second-harmonic generation from surfaces and interfaces*, Phys. Rev. B **33**, 8254–8263 (1986).

[111] C. H. Lee, R. K. Chang, and N. Bloembergen, *Nonlinear Electroreflectance in Silicon and Silver*, Phys. Rev. Lett. **18**, 167–170 (1967).

[112] J. I. Dadap, P. T. Wilson, M. H. Anderson, M. C. Downer, and M. ter Beek, *Femtosecond carrier-induced screening of dc electric-field-induced second-harmonic generation at the Si(001)-SiO_2 interface*, Opt. Lett. **22**, 901–903 (1997).

[113] M. Schulze, M. Hänsel, and P. Tegeder, *Hot Excitons Increase the Donor/Acceptor Charge Transfer Yield*, J. Phys. Chem. C **118**, 28527–28534 (2014).

[114] C. R. Groom, I. J. Bruno, M. P. Lightfoot, and S. C. Ward, *The Cambridge Structural Database*, Acta Crystallographica Section B Structural Science, Crystal Engineering and Materials **72**, 171–179 (2016).

[115] C. Grebner, J. Becker, D. Weber, D. Bellinger, M. Tafipolski, C. Brückner, and B. Engels. *CAST: A new program package for the accurate characterization of large and flexible molecular systems*, (2014).

[116] F. Weigend and R. Ahlrichs, *Balanced basis sets of split valence, triple zeta valence and quadruple zeta valence quality for H to Rn: Design and assessment of accuracy*, Phys. Chem. Chem. Phys. **7**, 3297–3305 (2005).

[117] S. Miertuš, E. Scrocco, and J. Tomasi, *Electrostatic interaction of a solute with a continuum. A direct utilizaion of AB initio molecular potentials for the prevision of solvent effects*, Chemical Physics **55**, 117 – 129 (1981).

[118] D. Bellinger, V. Settels, W. Liu, R. F. Fink, and B. Engels, *Influence of a polarizable surrounding on the electronically excited states of aggregated perylene materials*, Journal of computational chemistry **37**, 1601–1610 (2016).

[119] J.-M. Mewes, Z.-Q. You, M. Wormit, T. Kriesche, J. M. Herbert, and A. Dreuw, *Experimental benchmark data and systematic evaluation of two a posteriori, polarizable-continuum corrections for vertical excitation energies in solution*, The Journal of Physical Chemistry A **119**, 5446–5464 (2015).

[120] Z. Wong, W. Fan, and T. Chwee, *Computational modelling of singlet excitation energy transfer: a DFT/TD-DFT study of the ground and excited state properties of a syn bimane dimer system using non-empirically tuned range-separated functionals*, New Journal of Chemistry **42**, 13732–13743 (2018).

[121] N. T. Kalyani and S. Dhoble, *Organic light emitting diodes: Energy saving lighting technology—A review*, Renewable and Sustainable Energy Reviews **16**, 2696–2723 (2012).

[122] D. S. M. Ravinson and M. E. Thompson, *Thermally assisted delayed fluorescence (TADF): fluorescence delayed is fluorescence denied*, Mater. Horiz. **7**, 1210–1217 (2020).

[123] Y. Luo and H. Aziz, *Correlation between triplet–triplet annihilation and electroluminescence efficiency in doped fluorescent organic light-emitting devices*, Advanced Functional Materials **20**, 1285–1293 (2010).

[124] D. Y. Kondakov, *Triplet–triplet annihilation in highly efficient fluorescent organic light-emitting diodes: current state and future outlook*, Philosophical Transactions of the Royal Society A: Mathematical, Physical and Engineering Sciences **373**, 20140321 (2015).

[125] N. J. Turro, V. Ramamurthy, and J. C. Scaiano, *Modern Molecular Photochemistry of Organic Molecules*, Photochemistry and Photobiology **88**, 1033–1033 (2012).

[126] A. Köhler and H. Bässler, *Electronic processes in organic semiconductors: An introduction*, John Wiley & Sons (2015).

[127] Z. Yang, Z. Mao, Z. Xie, Y. Zhang, S. Liu, J. Zhao, J. Xu, Z. Chi, and M. P. Aldred, *Recent advances in organic thermally activated delayed fluorescence materials*, Chem. Soc. Rev. **46**, 915–1016 (2017).

[128] A. Endo, M. Ogasawara, A. Takahashi, D. Yokoyama, Y. Kato, and C. Adachi, *Thermally Activated Delayed Fluorescence from Sn4+–Porphyrin Complexes and Their Application to Organic Light Emitting Diodes — A Novel Mechanism for Electroluminescence*, Advanced Materials **21**, 4802–4806 (2009).

[129] A. Endo, K. Sato, K. Yoshimura, T. Kai, A. Kawada, H. Miyazaki, and C. Adachi, *Efficient up-conversion of triplet excitons into a singlet state and its application for organic light emitting diodes*, Applied Physics Letters **98**, 083302 (2011).

[130] H. Uoyama, K. Goushi, K. Shizu, H. Nomura, and C. Adachi, *Highly efficient organic light-emitting diodes from delayed fluorescence*, Nature **492**, 234–238 (2012).

[131] C. Rothe and A. Monkman, *Regarding the origin of the delayed fluorescence of conjugated polymers*, The Journal of chemical physics **123**, 244904 (2005).

[132] T. Hosokai, H. Matsuzaki, H. Nakanotani, K. Tokumaru, T. Tsutsui, A. Furube, K. Nasu, H. Nomura, M. Yahiro, and C. Adachi, *Evidence and mechanism of efficient thermally activated delayed fluorescence promoted by delocalized excited states*, Science advances **3**, e1603282 (2017).

[133] W. Sotoyama, *Simulation of Low-Lying Singlet and Triplet Excited States of Multiple-Resonance-Type Thermally Activated Delayed Fluorescence Emitters by Delta Self-Consistent Field (ΔSCF) Method*, The Journal of Physical Chemistry A **125**, 10373–10378 (2021).

[134] M. Klessinger and J. Michl, *Excited states and photochemistry of organic molecules*, VCH publishers (1995).

[135] H. Yersin, *Highly efficient OLEDs: Materials based on thermally activated delayed fluorescence*, John Wiley & Sons (2019).

[136] A. Köhler and H. Bässler, *Triplet states in organic semiconductors*, Materials Science and Engineering: R: Reports **66**, 71–109 (2009).

[137] A. Köhler and D. Beljonne, *The singlet–triplet exchange energy in conjugated polymers*, Advanced Functional Materials **14**, 11–18 (2004).

[138] H. Tanaka, K. Shizu, H. Miyazaki, and C. Adachi, *Efficient green thermally activated delayed fluorescence (TADF) from a phenoxazine–triphenyltriazine (PXZ–TRZ) derivative*, Chemical Communications **48**, 11392–11394 (2012).

[139] Q. Zhang, B. Li, S. Huang, H. Nomura, H. Tanaka, and C. Adachi, *Efficient blue organic light-emitting diodes employing thermally activated delayed fluorescence*, Nature Photonics **8**, 326–332 (2014).

[140] M. Sarma and K.-T. Wong, *Exciplex: An Intermolecular Charge-Transfer Approach for TADF*, ACS Applied Materials & Interfaces **10**, 19279–19304 (2018).

[141] M. A. El-Sayed, *Triplet state. Its radiative and nonradiative properties*, Accounts of chemical research **1**, 8–16 (1968).

[142] M. Baba, *Intersystem Crossing in the 1nπ* and 1$\pi\pi$* States*, The Journal of Physical Chemistry A **115**, 9514–9519 (2011).

[143] K. Goushi and C. Adachi, *Efficient organic light-emitting diodes through up-conversion from triplet to singlet excited states of exciplexes*, Applied Physics Letters **101**, 023306 (2012).

[144] A. J. Gillett, C. Tonnelé, G. Londi, G. Ricci, M. Catherin, D. M. Unson, D. Casanova, F. Castet, Y. Olivier, W. M. Chen, et al., *Spontaneous exciton dissociation enables spin state interconversion in delayed fluorescence organic semiconductors*, Nature communications **12**, 1–10 (2021).

[145] A. Koptyug, V. Saik, O. Animisov, and Y. N. Molin, *Spin-locking in concentration-narrowed OD ESR spectra*, Chemical physics **138**, 173–178 (1989).

[146] K.-H. Kim, S.-J. Yoo, and J.-J. Kim, *Boosting triplet harvest by reducing nonradiative transition of exciplex toward fluorescent organic light-emitting diodes with 100% internal quantum efficiency*, Chemistry of Materials **28**, 1936–1941 (2016).

[147] J. Grüne, S. Wirsing, V. Dyakonov, B. Engels, and A. Sperlich, *The different role of triplet states in photo- and electroluminescence of (TADF) donor:acceptor systems.*, to be submitted (2022).

[148] K. Goushi, K. Yoshida, K. Sato, and C. Adachi, *Organic light-emitting diodes employing efficient reverse intersystem crossing for triplet-to-singlet state conversion*, Nature Photonics **6**, 253–258 (2012).

[149] L. Zhu, K. Xu, Y. Wang, J. Chen, and D. Ma, *High efficiency yellow fluorescent organic light emitting diodes based on m-MTDATA/BPhen exciplex*, Frontiers of Optoelectronics **8**, 439–444 (2015).

[150] P. Yuan, X. Qiao, D. Yan, and D. Ma, *Magnetic field effects on the quenching of triplet excitons in exciplex-based organic light emitting diodes*, Journal of Materials Chemistry C **6**, 5721–5726 (2018).

[151] Q. Xin, W. L. Li, W. M. Su, T. L. Li, Z. S. Su, B. Chu, and B. Li, *Emission mechanism in organic light-emitting devices comprising a europium complex as emitter and an electron transporting material as host*, Journal of Applied Physics **101**, 044512 (2007).

[152] I. Sudakov, M. Van Landeghem, R. Lenaerts, W. Maes, S. Van Doorslaer, and E. Goovaerts, *The Interplay of Stability between Donor and Acceptor Materials in a Fullerene-Free Bulk Heterojunction Solar Cell Blend*, Advanced Energy Materials **10**, 2002095 (2020).

[153] T. Petrenko, S. Kossmann, and F. Neese, *Efficient time-dependent density functional theory approximations for hybrid density functionals: Analytical gradients and parallelization*, The Journal of chemical physics **134**, 054116 (2011).

[154] C. Bannwarth, S. Ehlert, and S. Grimme, *GFN2-xTB—An Accurate and Broadly Parametrized Self-Consistent Tight-Binding Quantum Chemical Method with Multipole Electrostatics and Density-Dependent Dispersion Contributions*, Journal of Chemical Theory and Computation **15**, 1652–1671 (2019).

[155] F. Neese, *Calculation of the zero-field splitting tensor on the basis of hybrid density functional and Hartree-Fock theory*, The Journal of chemical physics **127**, 164112 (2007).

[156] F. Plasser. *TheoDORE 1.4: a package for theoretical density, orbital relaxation, and exciton analysis.* programme package, (2016).

[157] C. Brückner and B. Engels, *Benchmarking singlet and triplet excitation energies of molecular semiconductors for singlet fission: Tuning the amount of HF exchange and adjusting local correlation to obtain accurate functionals for singlet–triplet gaps*, Chemical Physics **482**, 319–338 (2017).

[158] D. Graves, V. Jankus, F. B. Dias, and A. Monkman, *Photophysical Investigation of the Thermally Activated Delayed Emission from Films of m-MTDATA:PBD Exciplex*, Advanced Functional Materials **24**, 2343–2351 (2014).

[159] D. Tanaka, T. Takeda, T. Chiba, S. Watanabe, and J. Kido, *Novel electron-transport material containing boron atom with a high triplet excited energy level*, Chemistry letters **36**, 262–263 (2007).

[160] N. Kuritz, T. Stein, R. Baer, and L. Kronik, *Charge-transfer-like $\pi \rightarrow \pi^*$ excitations in time-dependent density functional theory: A conundrum and its solution*, Journal of chemical theory and computation **7**, 2408–2415 (2011).

[161] W. Stampor and W. Mróz, *Electroabsorption in triphenylamine-based hole-transporting materials for organic light-emitting diodes*, Chemical Physics **331**, 261–269 (2007).

[162] L. Stojanović and R. Crespo-Otero, *Aggregation-Induced Emission in the Tetraphenylthiophene Crystal: The Role of Triplet States*, The Journal of Physical Chemistry C **124**, 17752–17761 (2020).

[163] J. Mei, N. L. C. Leung, R. T. K. Kwok, J. W. Y. Lam, and B. Z. Tang, *Aggregation-Induced Emission: Together We Shine, United We Soar!*, Chemical Reviews **115**, 11718–11940 (2015).

[164] L. E. Aguilar Suarez, C. de Graaf, and S. Faraji, *Influence of the crystal packing in singlet fission: one step beyond the gas phase approximation*, Phys. Chem. Chem. Phys. **23**, 14164–14177 (2021).

[165] Y. Liu, Z. Zheng, V. Coropceanu, J.-L. Brédas, and D. S. Ginger, *Lower limits for non-radiative recombination loss in organic donor/acceptor complexes*, Materials Horizons (2021).

[166] T. Baruah, M. Olguin, and R. R. Zope, *Charge transfer excited state energies by perturbative delta self consistent field method*, The Journal of Chemical Physics **137**, 084316 (2012).

[167] J. Cullen, M. Krykunov, and T. Ziegler, *The formulation of a self-consistent constricted variational density functional theory for the description of excited states*, Chemical Physics **391**, 11–18 (2011).

[168] L. Ress, D. Kaiser, J. Grüne, M. Gerlach, E. Reusch, T. Brixner, A. Sperlich, B. Engels, and I. Fischer, *Femtosecond dynamics of diphenylpropynylidene in ethanol and dichloromethane*, Spectrochimica Acta Part A: Molecular and Biomolecular Spectroscopy **254**, 119606 (2021).

[169] S. A. Mewes, J.-M. Mewes, A. Dreuw, and F. Plasser, *Excitons in poly (para phenylene vinylene): a quantum-chemical perspective based on high-level ab initio calculations*, Physical Chemistry Chemical Physics **18**, 2548–2563 (2016).

[170] S. A. Mewes, F. Plasser, and A. Dreuw, *Universal exciton size in organic polymers is determined by nonlocal orbital exchange in time-dependent density functional theory*, The journal of physical chemistry letters **8**, 1205–1210 (2017).

[171] M. Bursch, H. Neugebauer, and S. Grimme, *Structure optimisation of large transition-metal complexes with extended tight-binding methods*, Angewandte Chemie International Edition **58**, 11078–11087 (2019).

[172] S. Weissenseel, A. Gottscholl, R. Bönnighausen, V. Dyakonov, and A. Sperlich, *Long-lived spin-polarized intermolecular exciplex states in thermally activated delayed fluorescence-based organic light-emitting diodes*, Science advances **7**, eabj9961 (2021).

[173] D. A. Pantazis, X.-Y. Chen, C. R. Landis, and F. Neese, *All-Electron Scalar Relativistic Basis Sets for Third-Row Transition Metal Atoms*, Journal of Chemical Theory and Computation **4**, 908–919 (2008).

[174] D. A. Pantazis and F. Neese, *All-electron scalar relativistic basis sets for the 6 p elements*, Theoretical Chemistry Accounts **131**, 1–7 (2012).

[175] E. Welz, J. Böhnke, R. D. Dewhurst, H. Braunschweig, and B. Engels, *Unravelling the Dramatic Electrostructural Differences Between N-Heterocyclic Carbene-and Cyclic (Alkyl)(amino) carbene-Stabilized Low-Valent Main Group Species*, Journal of the American Chemical Society **140**, 12580–12591 (2018).

[176] V. Settels, W. Liu, J. Pflaum, R. F. Fink, and B. Engels, *Comparison of the electronic structure of different perylene-based dye-aggregates*, Journal of computational chemistry **33**, 1544–1553 (2012).

Appendix A

Structural Details

A.1 Nomenclature of Aggregates in Chapter 2

Table A.1: Numeration of monomers in DIP/PDIR-CN_2 aggregates as used in the original calculations and backed-up data.

name in this work	numeration in original data
σ_a	13, 19, 3, 7
σ_b	14, 19, 2, 6
σ_c	19, 24, 2, 3
λ_a	A, C, b, e
λ_b	A, C, C, e

A.2 Nomenclature of Heterodimers in Chapter 3

Table A.2: Definition of the ground state geometries used in chapter 3. Nomenclature follows the backed-up data.

	m-MTDATA:3TPYMB				m-MTDATA:BPhen			
name	ground state	ω(TD)	ω(opt.)	starting point	ground state	ω(TD)	ω(opt.)	starting point
S0_1	S_0	0.12	0.12	S0_4	S_0	0.14	0.14	S0_3
S0_2	S_0	0.12	0.25	stacked	S_0	0.14	0.14	random (ω=0.10 opt.)
S0_3	S_0	0.12	0.12	random (ω=0.09 opt.)	S_0	0.14	0.25	random
S0_4	S_0	0.12	0.25	random	S_0	0.14	0.25	stacked
S0_5	S_0	0.12	0.25	random (ω=0.09 opt.)	-	-	-	-
T1_1	T_1	0.12	0.12	random (ω=0.09 opt.)	T_1	0.14	0.14	T1_3
T1_2	T_1	0.12	0.12	T1_3	T_1	0.14	0.14	random (ω=0.10 opt.)
T1_3	T_1	0.12	0.25	random	T_1	0.14	0.25	random
T1_4					T_1	0.14	0.25	random[a]
T1_5					T_1	0.14	0.25	stacked
T1_6					T_1	0.14	0.14	random (ω=0.10 opt.[b])

a: preoptimized with Gaussian16_A ωB97X-D/cc-pVDZ; b: guess orbitals from ω=0.10 optimization.

Appendix B

Supporting Information

B.1 Chapter 1

Supporting Information for chapter 1 can be found under `https://pubs.acs.org/doi/abs/10.1021/acs.jpcc.9b07511` and `https://aip.scitation.org/doi/suppl/10.1063/5.0028943`.

B.2 Chapter 4

Supporting Information for chapter 4 can be found under `https://pubs.rsc.org/en/content/articlelanding/2020/SC/D0SC02410D`.

Appendix C

Copyright Clearance and Author Contributions

C.1 Copyright Clearance for Included Articles

For the articles in this thesis which were previously published in peer reviewed journals, the necessary copyright clearences were obtained as follows:

Chapter 1:
S. Wirsing, M. Hänsel, V. Belova, F. Schreiber, K. Broch, B. Engels, and P. Tegeder, *Excited-State Dynamics in Perylene-Based Organic Semiconductor Thin Films: Theory Meets Experiment*, The Journal of Physical Chemistry C **123**, 27561–27572 (2019). Reprinted from reference [4] with permission from 2021 American Chemical Society.
M. Deutsch, S. Wirsing, D. Kaiser, R. Fink, P. Tegeder, and B. Engels, *Geometry relaxation-mediated localization and delocalization of excitons in organic semiconductors: A quantum chemical study*, The Journal of Chemical Physics **153**, 224104(2020). Reprinted from reference [85] with permission from 2021 American Chemical Society.

Chapter 4:
D. P. Mukhopadhyay, D. Schleier, S. Wirsing, J. Ramler, D. Kaiser, E. Reusch, P. Hemberger, T. Preitschopf, I. Krummenacher, B. Engels, et al., *Methylbismuth: an organometallic bismuthinidene biradical*, Chemical Science **11**, 7562–7568 (2020). Reprinted from reference [24] with permission from the Royal Society of Chemistry.

C.2 Listings of Author Contributions

Erklärung zur Autorenschaft
Excited-State Dynamics in Perylene-Based Organic Semiconductor Thin Films: Theory Meets Experiment, Wirsing, Sara and Hänsel, Marc and Belova, Valentina and Schreiber, Frank and Broch, Katharina and Engels, Bernd and Tegeder, Petra, The Journal of Physical Chemistry C, 2019, 123, 45, 27561-27572
Titel der Arbeit, Titel, Autoren/innen, Zeitschrift, Jahr, Ausgabe, Seiten

Detaillierte Darstellung der Anteile an der Veröffentlichung (in %)
Angabe Autoren/innen (ggf. Haupt- / Ko- / korrespondierende/r Autor/in) mit Vorname Nachname (Initialen)

Sara Wirsing (SW), Marc Hänsel (MH), Valentina Belova (VB), Frank Schreiber (FS), Katharina Broch (KB), Bernd Engels (BE), Petra Tegeder (PT)

Autor	SW	MH	VB	FS	KB	BE	PT	∑ in Prozent
Durchführung ab-initio Berechnungen	100%							20%
Deutung ab-initio Berechnungen	75%					25%		15%
Durchführung der Messungen		100%						15%
Auswertung der Messungen		75%					25%	15%
Herstellung der Proben			75%	10%	15%			5%
Charakterisierung der Proben			75%	10%	15%			5%
Verfassen der Veröffentlichung	33%					33%	33%	10%
Korrektur der Veröffentlichung	50%			5%	5%	20%	20%	10%
Koordination der Veröffentlichung	25%			5%	5%	25%	40%	5%
Summe	40.8%	26.3%	7.5%	1.8%	2.3%	10.3%	11.1%	100.00%

Die Mitautoren der in dieser (teil-)kumulativen Dissertation verwendeten Manuskripte sind sowohl über die Nutzung als auch über die angegebenen Eigenanteile informiert und stimmen dem zu.

*Angabe Autorenschaft: Anwählen Dropdownmenü / Autorenunterschrift **oder** Angabe Verweis: Kontrollkästchen über Eigenschaften aktivieren !*

Erklärung zur Autorenschaft

Geometry relaxation-mediated localization and delocalization of excitons in organic semiconductors: A quantum chemical study, Marian Deutsch, Sara Wirsing, Dustin Kaiser, Reinhold F. Fink, Petra Tegeder, Bernd Engels, The Journal of Chemical Physics, 2020, 153, 22, 224104

Detaillierte Darstellung der Anteile an der Veröffentlichung (in %)
Angabe Autoren/innen (ggf. Haupt- / Ko- / korrespondierende/r Autor/in) mit Vorname Nachname (Initialen)

Autor/in 1 (Marian Deutsch), Autor/in 2 (Sara Wirsing), Autor/in 3 (Dustin Kaiser), Autor/in 4 (Reinhold F. Fink), Autor/in 5 (Petra Tegeder), Autor/in 6 (Bernd Engels)

Autor	A1	A2	A3	A4	A5	A6	∑ in Prozent
Konzeption und Idee des Forschungsvorhabens	5%	5%	5%	15%	15%	55%	100%
Hauptautorenschaft: Quantenchemische Rechnungen zum Einfluss der Geometrieverzerrung auf PBI-Dimere	0%	0%	100%	0%	0%	0%	100%
Hauptautorenschaft: Benchmark von Anregungsenergien des PBI-Monomers	100%	0%	0%	0%	0%	0%	100%
Hauptautorenschaft: Analyse von DIP & PDIR-CN2 Monomer- & Tetramer-Aggregaten	0%	100%	0%	0%	0%	0%	100%
Verfassen des Teils: „Intra-monomer relaxation effects in PBI aggregate structures“	0%	0%	90%	0%	0%	10%	100%
Verfassen des Teils: „Benchmark for vibrationally resolved absorption spectra of perylene-based organic semi-conductors“	90%	0%	0%	0%	0%	10%	100%
Verfassen des Teils: „Intra-monomer relaxation effects in DIP aggregate structures“	0%	90%	0%	0%	0%	10%	100%
Zusammenführung & Verbinden der Einzelbereiche	10%	10%	10%	20%	20%	30%	100%
Korrektur der Publikation	23%	23%	23%	10%	10%	10%	100%
Diskussion der Ergebnisse	23%	23%	23%	10%	10%	10%	100%

Julius-Maximilians-
UNIVERSITÄT
WÜRZBURG

Fakultät für
CHEMIE UND
PHARMAZIE

Erklärung zur Autorenschaft

Methylbismuth: an organometallic bismuthinidene biradical
D. P. Mukhopadhyay, D. Schleier, S. Wirsing, J. Ramler, D. Kaiser, E. Reusch, P. Hemberger, T. Preitschopf, I. Krummenacher, B. Engels, I. Fischer, C. Lichtenberg
Chem. Sci., **2020**, *11*, *7562-7568*.

Detaillierte Darstellung der Anteile an der Veröffentlichung (in %)
Angabe Autoren/innen (ggf. Haupt- / Ko- / korrespondierende/r Autor/in) mit Vorname Nachname (Initialen)

Autor/in 1 (D. P. M.), Autor/in 2 (D. S.), Autor/in 3 (S. W.), Autor/in 4 (J. R.), Autor/in 5 (D. K.), Autor/in 6 (E. R.), Autor/in 7 (P. H.), Autor/in 8 (T. P.), Autor/in 9 (I. K.), Autor/in 10 (B. E.), Autor/in 11 (I. F.), Autor/in 12 (C. L.)

Autor	A1	A2	A3	A4	A5	A6	A7	A8	A9	A10	A11	A12	∑ in Prozent
Synthesis of all compounds, including analytical data				100%									100%
X-ray crystallography				40%								60%	100%
Theoretical calculations			60%		40%								100%
IR spectroscopy				30%				70%					100%
EPR spectroscopy				10%					80%			10%	100%
Synchrotron radiation experiments	20%	20%				20%	20%				20%		100%
Conception of the publication										20%	40%	40%	100%
Writing the publication										20%	40%	40%	100%
Correcting the manuscript	8%	8%	8%	8%	8%	8%	8%	8%	8%	8%	8%	8%	100%
Coordination of the publication										33%	34%	33%	100%
Summe	8%	8%	12%	8%	6%	8%	4%	3%	3%	10%	15%	15%	100%